Theoretical Insights in 2D Defect Engineering and van der Waals Heterostructures for Optical and Catalytic Applications

by

Arunima Singh

Department of Physics

Submitted
in fulfillment of the requirements of the degree of Doctor of Philosophy
to the

Indian Institute of Technology Delhi
April 2023

Dedicated to my family

Certificate

This is to certify that the thesis entitled "**Theoretical Insights in 2D Defect Engineering and van der Waals Heterostructures for Optical and Catalytic Applications**" being submitted by **Arunima Singh**, to the Indian Institute of Technology Delhi, for the award of the degree of **Doctor of Philosophy** in Physics is a record of bonafide research work carried out by her under my supervision and guidance. She has fulfilled the requirements for the submission of the thesis, which to the best of my knowledge has reached the required standard. The material contained in the thesis has not been submitted in part or full to any other University or Institute for the award of any degree or diploma.

Prof. Saswata Bhattacharya
Thesis Supervisor
Department of Physics,
Indian Institute of Technology Delhi,
Hauz Khas, New Delhi 110016, India.
Date:.....
Place: New Delhi

Acknowledgements

My most profound appreciation goes to my supervisor Prof. Saswata Bhattacharya. His expertise, punctuality and prompt decision-making ability have been inspiring throughout my Ph.D. tenure and will remain my motivation. Through him, I have also learned the importance of planning and research in any area of work and life. His persistent advice and guidance have impacted me significantly. His wisdom has exemplified the adept execution of a thought or goal. His enthusiasm for physics is a virtue to be learned. I sincerely thank him for consistently believing in my endeavours.

I am thankful to my student research committee: Prof. Pankaj Srivastava, Prof. Rajendra Singh, and Prof. M. Ali Haider for their constructive feedback and inspiration.

I thank my colleagues from my research group DISCERE: Dr. Shikha Saini, Dr. Pooja Basera, Dr. Ekta Arora, Dr. Manish Kumar, Deepika Gill, Manjari Jain, Preeti Bhumla, Sajjan Sheoran, Ankita Phutela, Sanchi Moonga, Ruman Moulik, Riya Gupta and Shantanu Pathak. I thank Shikha Di, who has been there to support, uplift, and respect my capabilities. I thank my friend Pooja for all the discussions regarding life and work. You had shared the warmth when I needed it. I extend my thanks to Manish, Deepika and Preeti. I have found Manjari backing my decisions and thank you for the same. I thank Sajjan, Ankita, Ruman and Sanchi for giving different perspective in my work, continuous support and encouragement. I have had good time in my interactions with Riya and Shantanu. My best wishes to all my colleagues.

I shall thank my other collaborators: Prof. Jitendra Pratap Singh, Prof. Manjeet Jassal, Prof. Ashwini K. Agrawal, Prof. John Mondal, Prof. Rajendra Singh, Prof. Bikas C. Das, Prof. Sameer Sapra, for strengthening the experimental insights in work.

My association with SPIC MACAY club has strengthened me. I express my gratitude to Padma Shri Prof. Kiran Seth for instilling confidence in my personality. I thank Dr. Pragya Jain and Dr. Rachna Prasad for always supporting me as an anchor at various performances and

concerts. I also thank my friends from the club: Dr. Chetan, Dr. Kritika, Dr. Aparna, Dr. Sanchayan, Laxman, Hardik, and Pranav.

I thank my Lecturer Ms. Jyoti Kapil for her guidance in every walk of my life.

A special thanks to my friends Aysha, Ruchi and Pooja, without which my Ph.D. journey would have been arduous. I thank my Delhi University friends (Garima, Tanvi, Surbhi, Himanshi, Manaya, Deepti, Nutan, and Devesh) for believing that I can endure the challenges. I also thank my dearest school friends, Aakansha and Sumit, who have consistently supported me till now.

Last but not least, I acknowledge my parents and brother. Their contribution and sacrifices for me have instilled in me the values that matter in life. They are my strength.

Arunima Singh

Abstract

Transition metal dichalcogenides (TMD) are part of the 2D material family with profound scientific interest. They exhibit direct bandgap, conducive electronic and mechanical properties, and atomic-scale thickness, making them suitable for fundamental studies. Their applicability is evident in diverse fields of high-end electronics, optoelectronics, spintronics, flexible electronics, and energy harvesting. MoS_2 being abundant becomes the obvious choice to understand the TMD family. In this thesis, we attempt to tune MoS_2 by defect engineering and designing van der Waals heterostructures (vdW HTSs). In case of defect engineering, we intend to analyse the thermodynamic stability of native point defects using density functional theory (DFT). In addition, the van der Waals interactions do affect the stability and mobility of the point defects in the semiconductors. Hence, the thesis includes comparative analysis of two-body van der Waals and many body dispersion that affect the defect states leading to a change in the free energy of formation and hence, in the stability. Further, moisture plays a significant role in the emergence of negative differential resistance (NDR) in our devices as the defect sites on the MoS_2 nanoflakes readily adsorb water, facilitating electrochemical redox reactions. Therefore, it is imperative to understand the mechanism behind the same.

In the case of designing vdW HTSs, we have focused on photocatalytic and electrocatalytic hydrogen evolution reactions (HER). vdW HTSs have immense scope in this field as the lubricity due to weak vdW forces facilitates the interlayer movement that assists in photocatalysis. As no extensive study on MoS_2 (and MoSSe) based bilayer vdW HTSs with transition metal oxides (TMOs, viz. HfO_2, T-PtO_2, T-SnO_2) and TMDs (viz. HfS_2, ZrS_2, TiS_2) as the second layer has been performed so far, we have attempted to understand the same for Z-scheme photocatalytic application. Subsequently, we move towards electrocatalytic study where the electronegativity difference between the constituent monolayers actuates electron transfer, thereby affecting the HER. Even if the constituent monolayers have inactive sites, the resulting vdW HTS can be obtained as an active electrocatalyst due to an inbuilt electric field at the interface. We explore

Boron Phosphide (BP) monolayer, MoS_2/BP and MoSSe/BP vdW HTSs for HER. BP monolayer has been reported with low carrier effective mass, high carrier mobility, good mechanical strength, and stability in water environments. Since the lattice parameters of MoS_2 and BP are similar, the MoS_2/BP vdW HTS becomes a plausible system with minimal lattice mismatch. In addition, we have also analyzed MoSSe/BP vdW HTS. Any prior investigations for HER on these systems are hitherto unknown; hence we have considered these systems for our work.
We have followed first-principles based approach with the DFT formalism to conduct the studies. Under its aegis, we have employed hybrid density functional theory and density functional perturbation theory (DFPT). The stability and the excited state properties have been predicted by *ab initio* atomistic thermodynamics and many-body perturbation theory (MBPT: G_0W_0, BSE and model-BSE (mBSE)), respectively. Further, to find the saddle points and minimum energy paths between known reactants and products, the climbing image nudged elastic band (CI-NEB) method is incorporated.

सार

ट्रैंज़िशन मेटल डाईचैलकोजेनॉइड्स (TMD) गहन वैज्ञानिक रुचि वाले 2D परिवार का हिस्सा हैं। MoS_2 का प्रचुर मात्रा में होना TMD परिवार को समझने का स्पष्ट विकल्प बन जाता है। इस शोध प्रबन्ध में, हम "डीफ़ेक्ट एंजिनीरिंग" और "वैन डर वॉल्ज़ हेटरोस्ट्रक्चर (vdW HTS)" की रचना कर MoS_2 के गुणो को परिवर्तित करने का प्रयास करते हैं। "डीफ़ेक्ट एंजिनीरिंग" के मामले में, हम "घनत्व-फ़लन सिद्धांत (DFT)" का उपयोग करके पदार्थ के मूल दोषों की थर्मोडायनामिक स्थिरता का विश्लेषण करना चाहते हैं। इसके उपरांत, "वैन डर वॉल्ज़" इंटरैक्शन सेमीकंडक्टर में मूल दोषों की स्थिरता और गतिशीलता को प्रभावित करते हैं। इसलिए, इस शोध प्रबन्ध में टू-बॉडी वैन डर वॉल्ज़ और मेनी-बॉडी डिस्पर्शन का तुलनात्मक विश्लेषण शामिल है, जो मूल दोषों को प्रभावित कर उसके फ़्री एनर्जी ओफ़ फ़ॉर्मेशन को परिवर्तित करता है। इस कारण पदार्थ की स्थिरता भी प्रभावित होती है। इसके अतिरिक्त, नमी हमारे उपकरणों में एक महत्वपूर्ण भूमिका निभाती है। MoS_2 नैनोफ्लेक्स के मूल दोष आसानी से पानी के अणु को अधिशोषित कर, विद्युत रासायनिक रेडॉक्स अभीक्रियाएं में सहायता करते है। इस हेतु, ऋणात्मक विभेदी प्रतिरोधक (NDR) के MoS_2 नैनोफ्लेक्स में प्रभाव के पीछे के तंत्र को समझना अनिवार्य है।

vdW HTS डिजाइन करने के मामले में, हमने फोटोकैटलिटिक और इलेक्ट्रोकैटलिटिक हाइड्रोजन इवोल्यूशन रिएक्शन (HER) पर ध्यान केंद्रित किया है। vdW HTS का विस्तृत कार्य क्षेत्र और स्नेहक निष्पादन, Z-स्कीम फोटोकैटलिसिस में सहायता करती है। इस हेतु, MoS_2 (और MoSSe) आधारित बाइलेयर vdW HTS पर ट्रैंज़िशन मेटल ऑक्सायड्ज़ (TMOs, अर्थात HfO_2, T-PtO_2, T-SnO_2) और TMDs (अर्थात HfS_2, ZrS_2, TiS_2) की दूसरी परत के रूप में अब तक फोटोकैटलिटिक एप्लिकेशन के लिए कोई व्यापक अध्ययन नहीं किया गया है। इसके बाद, हम इलेक्ट्रोकैटलिटिक अध्ययन की ओर बढ़ते हैं, जहां मोनोलेयर्स के बीच इलेक्ट्रोनगेटिविटी अंतर इलेक्ट्रॉन हस्तांतरण को सक्रिय करता है, जिससे HER प्रभावित होता है। मोनोलयर्स में निष्क्रिय कैटलिटिक साइटों के बावजूद, उससे निर्मित vdW HTS के इंटरफेस में एक अंतर्निर्मित इलेक्ट्रिक फील्ड के कारण, यह सक्रिय इलेक्ट्रोकैटलिस्ट के रूप में प्राप्त किया जा सकता है। हमने HER के लिए बोरॉन फास्फाइड (BP) मोनोलेयर, MoS_2/BP और MoSSe/BP vdW HTS पर क्षोध कीया है। BP मोनोलेयर को अच्छी यांत्रिक शक्ति और पानी के वातावरण में स्थिरता के साथ सूचित किया गया है। चूँकि MoS_2 और BP के लैटिस पैरामीटर समान हैं, MoS_2 /BP vdW HTS न्यूनतम बेमेल लैटिस के साथ एक प्रशंसनीय उदाहरण बन जाती है। इसके अलावा, हमने

MoSSe/BP vdW HTS का भी विश्लेषण किया है। इनपर HER के लिए कोई पूर्व जांच अब तक अज्ञात है; इसलिए हमने इन्हें अपने क्षोध हेतु माना है।

हमने अध्ययन करने के लिए DFT के साथ आदितः परिकलन का पालन किया है। इसके तत्वावधान में, हमने हाइब्रिड DFT और डेंसिटी फंक्शनल पर्टर्बेशन सिद्धांत (DFPT) को नियोजित किया है। स्थिरता और इक्सायटेड-स्टेट के गुणों का विश्लेषण क्रमशः आदितः परिकलन और मेनी-बॉडी पर्टर्बेशन सिद्धांत (MBPT: G_0W_0, BSE और model-BSE (mBSE)) द्वारा किया गया है। इसके अलावा, ज्ञात अभिकारकों और उत्पादों के बीच सैडल पॉइंट और न्यूनतम ऊर्जा पथ खोजने के लिए, क्लाइमिंग इमिज नज्ड इलास्टिक बैंड (CI-NEB) विधि को शामिल किया गया है।

List of Publications

1. **Arunima Singh**, Pooja Basera, Shikha Saini, Manish Kumar, Saswata Bhattacharya, "Importance of Many-Body Dispersion in the Stability of Vacancies and Antisites in Free-Standing Monolayer of MoS_2 from First-Principles Approaches".
   The Journal of Physical Chemistry C, **124**, 1390 (2020)

2. **Arunima Singh**, Manjari Jain, Saswata Bhattacharya, "MoS_2 and Janus (MoSSe) Based 2D van der Waals Heterostructures: Emerging Direct Z-scheme Photocatalysts".
   Nanoscale Advances, **3**, 2837, (2021)

3. **Arunima Singh**, Manjari Jain, Preeti Bhumla, Saswata Bhattacharya, "Electrocatalytic Study for Hydrogen Evolution Reaction on MoS_2/BP and MoSSe/BP in Acidic Media".
   arXiv:2208.07971 (manuscript under review)

4. Litty Thomas Manamel, **Arunima Singh**, Puranjay Saha, Saswata Bhattacharya, Bikas C. Das, "Probing High Conductance and Negative Differential Resistance Property of Nanoconfined Water".
   (manuscript under review)

5. Ekta Arora, Shikha Saini, Pooja Basera, Manish Kumar, **Arunima Singh**, Saswata Bhattacharya, "Elucidating the Role of Temperature and Pressure to the Thermodynamic Stability of Charged Defects in Complex Metal-Hydrides: A Case Study of $NaAlH_4$".
   Journal of Physical Chemistry C, **123**, 62 (2019)

6. Pooja Basera, Shikha Saini, Ekta Arora, **Arunima Singh**, Manish Kumar, Saswata Bhattacharya , "Stability of Non-Metal Dopants to Tune the Photo-Absorption of TiO_2 at Realistic Temperatures and Oxygen Partial Pressures: A Hybrid DFT Study".
   Scientific Reports, **9**, 11427 (2019).

7. Manjari Jain, **Arunima Singh**, Pooja Basera, Manish Kumar, Saswata Bhattacharya, "Understanding the Role of Sn Substitution and Pb-Vacancy in Enhancing the Stability of $CH(NH_2)_2Pb_{1-X-Y}$ $Sn_XVac_YBr_3$: A hybrid Density Functional Approach".
   Journal of Materials Chemistry C, **8**, 10362 (2020)

8. Manish Kumar, Manjari Jain, **Arunima Singh**, Saswata Bhattacharya, "Sublattice Mixing in $Cs_2AgInCl_6$ for Enhanced Optical Properties from First-principles"
   Applied Physical Letters, **118**, 021901 (2021)

9. Pooja Basera, **Arunima Singh**, Deepika Gill, Saswata Bhattacharya, "Capturing excitonic and polaronic effects in lead iodide perovskites from many-body perturbation theory".
   Journal of Materials Chemistry C, **9**, 17113 (2021)

10. Hardeep S. Jhinjer, **Arunima Singh**, Saswata Bhattacharya, Manjeet Jassal, Ashwini K. Agrawal, "Metal-Organic Frameworks Functional Smart Textiles for Capture of Harmful Aromatic Pollutants from Ambient Air".
    Journal of Hazardous Materials, **411**, 125056 (2021)

11. Pinki Devi, **Arunima Singh**, Karan Malik, Anil Verma, Saswata Bhattacharya, Jitendra Pratap Singh, "Role of Oxygen Vacancy Defects in the Regeneration of Deactivated CuO-Cu_2O/In_2O_3 Nanocomposite Catalyst for Selective Electrochemical Reduction of CO2 to CO".
    Journal of Electrochemical Society, **168**, 066518 (2021)

12. Manish Kumar, **Arunima Singh**, Deepika Gill, Saswata Bhattacharya, "Optoelectronic Properties of Chalcogenide Perovskites from Many-body Perturbation Theory".
    The Journal of Physical Chemistry Letters, **12**, 5301 (2021)

13. Deepika Gill, **Arunima Singh**, Manjari Jain, Saswata Bhattacharya, "Exploring Exciton and Polaron Dominated Photo-physical Phenomena in $Ba_{n+1}Zr_nS_{3n+1}$ (n=[1,3]) Ruddlesden Popper Phases from Many-body Perturbation Theory".
    The Journal of Physical Chemistry Letters, **12**, 6698 (2021)

14. Ratul Paul[a], S. C. Shit[a], **Arunima Singh**[a], R. J. Wong, D. Q. Dao, Boby Joseph, Wen Liu, Saswata Bhattacharya, John Mondal, "Organogel-assisted porous organic polymer

embedding Cu NPs for selectivity control in the semi hydrogenation of alkynes". Nanoscale, **14**, 1505, (2022), [a]Equally contributed

15. Madan Sharma, **Arunima Singh**, A.K. Kapoor, Shuchi Kaushik, Bhera Ram Tak, Saswata Bhattacharya, Rajendra Singh, "van der Waals Integration of Trilayer MoS_2 Film with β-Ga_2O_3/muscovite Heteroepitaxy for Flexible Photodetectors having High-Temperature Functionalities".
(Accepted- DOI: 10.1021/acsaelm.3c00120)

Contents

List of Figures

List of Tables

CHAPTER 1

Introduction

1.1 2D materials

Can we imagine a world without smartphones? Semiconductors drive the innovation in smartphones or, in generic terms, electronic devices. Research on 2D materials is the new trend that can make them more nimble. Extending the applicability of 2D materials to our environment, surroundings, and body can tackle many issues such as global warming, pollution and environment degradation. In materials science, we deal with materials classified based on dimensions. When we reduce the dimensions to the nm scale, we come under the regime of nanomaterials. If one dimension is in nm (i.e., d$\leq$100 nm), it is 2D material; if two, then 1D material, and if three, then 0D material. Using graphite as an example, we see 0D fullerene, 1D nanotubes, 2D graphene, and 3D (bulk) graphite, possessing various properties.

Role of 2D materials in sustainable development goals: The varied facets of human development, including economy, social stature, education, and science, provide the blueprint for prosperity and development. In this purview, the 2D materials provide substantive support in the specific areas of affordable and clean energy, industry and innovation, and climate action. The existing reports discussed herein have built onto further research. For instance, in the regime of energy storage applications such as supercapacitors, graphene, reduced graphene oxide (rGO), 2D MnO_2, MoS_2/rGO heterostructure, and Co_3O_4 nanosheet have been reported as promising alternatives for an electrode [3]. Further, emerging technologies and startups have been devising solutions using 2D materials. Some industry-ready solutions are hexa-boron nitride for highly conductive inks, nanofluids as a coolant, and nano-chips for transmission electron microscopy (TEM) heating solutions. Hence, working on varied 2D material aspects includes fundamental electronic and structural property studies, thermal and mechanical studies, and industry-ready applicability or device-based study.

Types of 2D materials: Graphene has been a cutting edge material that opened new possibilities for a range of materials [4, 5]. The combination of its dimensionality and behaviour of electrons as relativistic particles make it extraordinary. Being a zero band gap semimetal, graphene is highly sensitive to change such as mechanical deformations, external electric field etc. However, its restricted use in the semiconductor and/or photovoltaic industry due to zero band gap and engineering required for the same, opened new avenues of various other 2D materials [6, 7, 8]. The transition metal dichalcogenides (TMDs) gained special interest due to their lamellar structures similar to that of graphite. In addition, they are naturally abundant and their monolayers exhibit band gap. TMDs are a versatile group of 2D materials family where the bulk property range from semiconductors (MoS_2, WS_2), metal (NbS_2), semimetals (WTe_2, $TiSe_2$) to insulators (HfS_2). The general classification of 2D materials are as follows [9, 10]:

- Graphene family: This include graphene and its derivatives, whereby derivatives mean heterogeneous atoms and hybridized C atoms. For e.g. fluoro-graphene, chlorographene, and graphene oxide.
- Xenes: This is monoelement material with trigonal and hexagonal lattices. These are made from group IIIA, IVA, and VA elements (e.g. silicene, gemanene, borophene). These structures include out of plane arrangements rather than ideal flat structure.
- MXenes (Transition metal carbides and nitrides): $M_{n+1}X_n$ (n=1-3) where M is early transition metal and X is carbon or nitrogen. These are arranged in the form of $[MX]_nM$.
- TMDs: These are three atomic layer arrangement where transition metal layer is in between the two chalcogen layers (MX_2: e.g HfS_2, MoS_2).
- 2D Oxides: These broadly include lead oxides, phosphorous oxides and transition metal oxides. These have strong chemical bonding within a layer. These form highly chemically active interface.
- Synthetic 2D vdW materials: The generic formula MA_2Z_4 belongs to these materials. These materials are formed by passivating non-layered materials with the layered counterparts.
- vdW Heterostructures: These are formed by vertically layering the monolayers where there are van der Waals forces in between the two layers. These open wide range of tunable properties for varied applications.

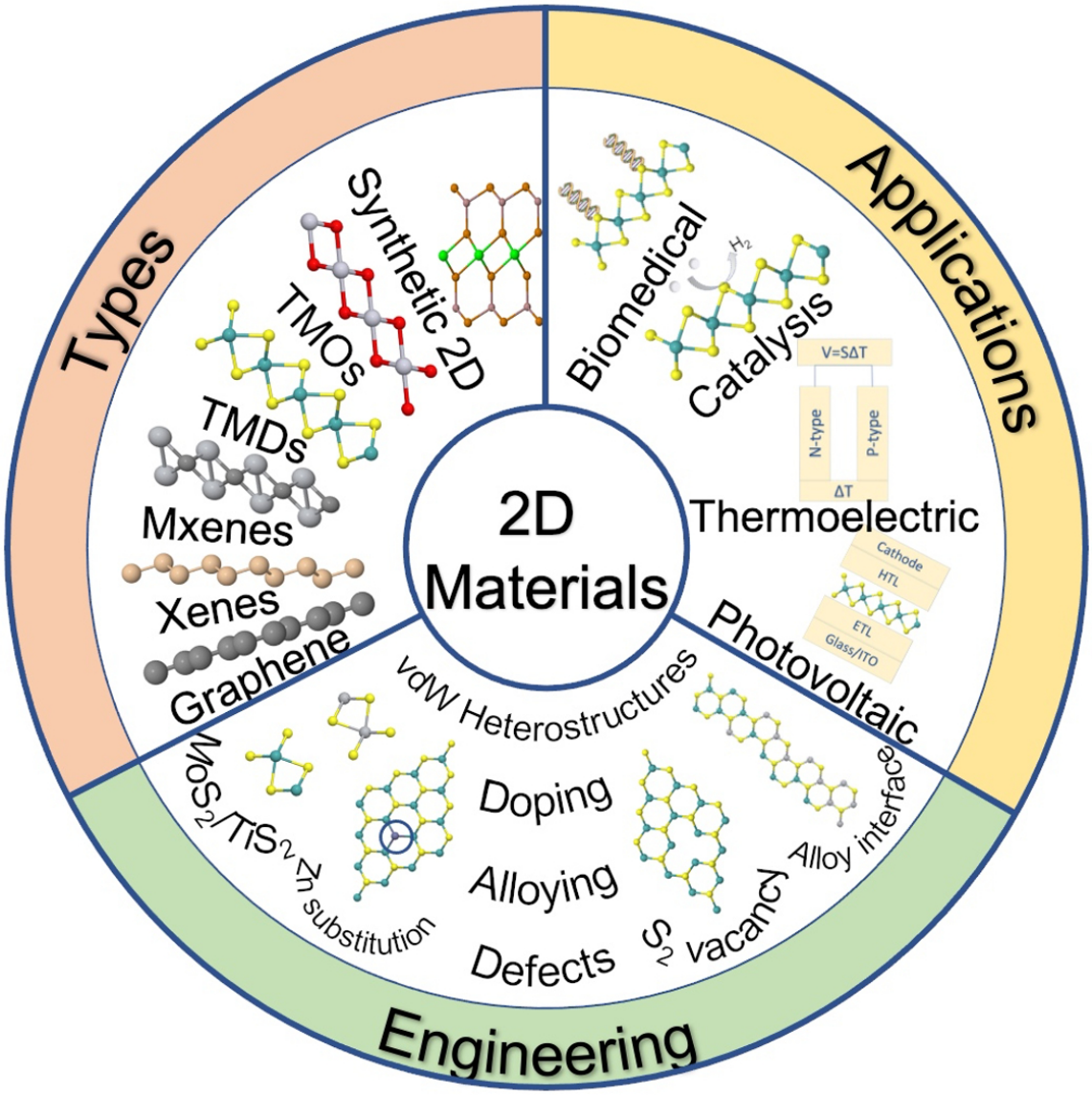

Figure 1.1: Schematic illustration of types of 2D materials.

Now, let us understand, how property of the material changes as we go from bulk to 2D. Whenever, we reduce the dimension of a material, the change in the electrical, optical, mechanical and chemical properties are bound to happen. Therefore, this affects the transparency, conductivity, hardness and reactivity of the materials. The consequence of reduction in dimension is quantum tunnelling. In nanometre scale, we observe wavelength of the particle comparable to the thickness of the energy barrier. Moreover, the electrons are confined in a space as compared to that in bulk. Finally, there is increased surface to volume ratio. Hence, property change is evident in 2D as compared to bulk. We can understand this by considering an example of "particle in a box problem", with the following energy equations that corresponds to the 0D, 1D

and 2D cases:

$$E_n = \left[\frac{\pi^2\hbar^2}{2mL^2}\right](n_x^2 + n_y^2 + n_z^2) \tag{1.1}$$

$$E_n = \left[\frac{\pi^2\hbar^2}{2mL^2}\right](n_x^2 + n_y^2) \tag{1.2}$$

$$E_n = \left[\frac{\pi^2\hbar^2}{2mL^2}\right](n_x^2) \tag{1.3}$$

1.2 TMDs

MoS_2, $MoSe_2$, WS_2 and WSe_2 are the widely studied TMDs. These are isolated by chemical and mechanical exfoliation. There band gaps transit from indirect (bulk) to direct (monolayer) indicating the effect of quantum confinement, interlayer interaction and long range Coulomb effects. Direct band gaps are at near-infrared and visible energy spectrum. The TMD layer fabrication is comparatively low-priced due to the presence of weak vdW interaction. Their optical properties are largely affected by the reduced 2D screening, resulting into tightly bound excitons. Hence, they are explored for (opto)electronics, valleytronics and (opto)spintronics applications.

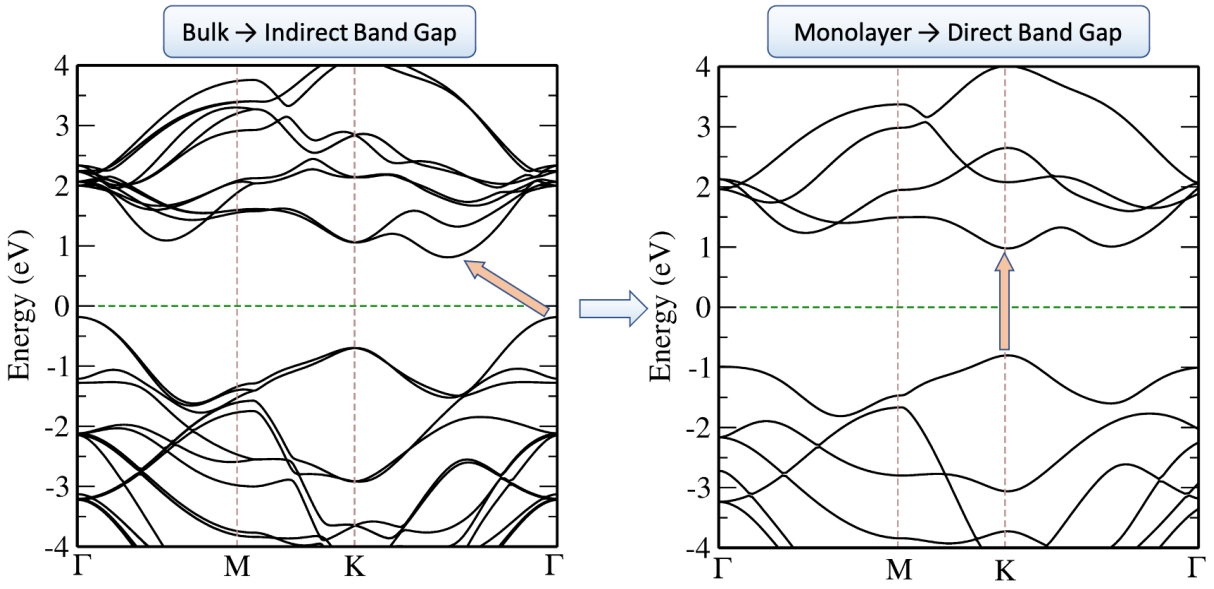

Figure 1.2: Bandstructure from bulk to 2D.

The crystal structure of bulk TMD (consider MoS_2 as a prototype) exists in 1T (trigonal, space group: $P\bar{3}m1$, point group: D_{6d}), 2H (hexagonal, space group: $P6_3/mmc$, point group: D_{6h})

and 3R (rhombohedral, space group: R3m, point group: C_{3V}) polytypes [11]. The digits in the polytypes represent number of monolayers in the unit cell. The 1T phase has octahedral Mo-S coordination whereas the other two phases have trigonal prismatic coordination. The naturally occurring molybdenite is thermodynamically stable in the 2H phase. The corresponding monolayer is 1H phase with trigonal prismatic coordination. The point group is now D_{3h} with no inversion symmetry. All the study in this thesis has been undertaken in this phase. In the bandstructure, Mo 3d contributes to the conduction band (CB) and S 2p to the valence band (VB).

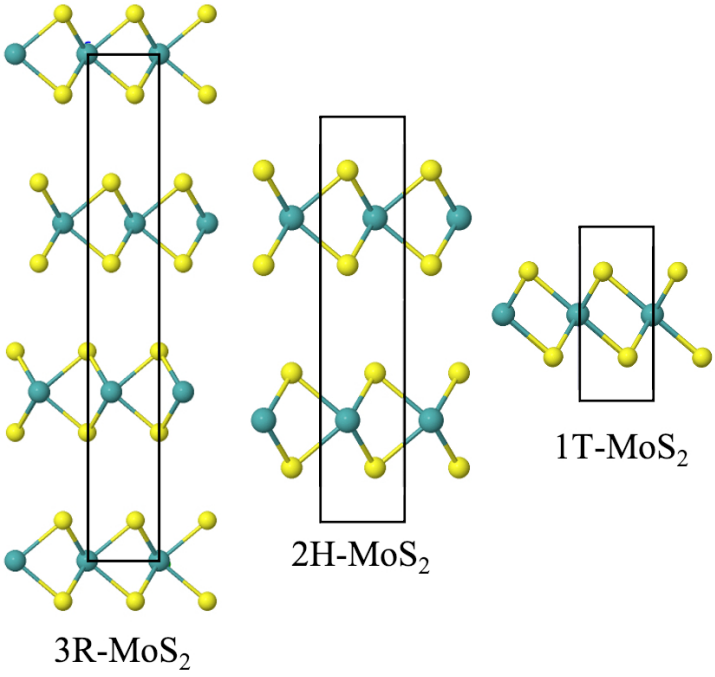

Figure 1.3: Prototypes of bulk MoS_2

1.3 Applications

Energy related issues and environmental problems such as pollution and global warming are alarming to the humanity. In the last decade, the large increase in world population has led to a significant increase of the emission of greenhouse gases from fossil fuels. In this context, clean and renewable energy, and in particular harnessing solar energy is the most promising solution. In view of this, the widely researched area for 2D materials have been photovoltaics, thermoelectrics and catalysis.

- Photovoltaic: Owing to their unique electronic, optical and structural properties, TMDs can be utilized as an absorber and transparent electrodes [12]. Their monolayers exhibit direct bandgap and excellent light absorption, making them promising candidates for photoelectrochemical and photovoltaic applications. The bandgaps of these are in the range 1.0–2.0 eV, which is in the visible region solar spectrum window. The other materials with the comparable bandgaps are Si (1.1 eV), CdTe (1.5 eV) and GaAs (1.4 eV) [13, 14, 15, 16].

- Thermoelectric: The electrical and thermal conductivity of the material can be independently modulated for thermoelectric applications [17]. TMDs possess relatively high electrical conductivity and low thermal conductivity, thereby, being plausible option for heat and electricity conversion [18].

- Catalysis: The TMD monolayers in general exhibit chemical stability, large surface area and large number of active sites. Hence, they can be utilized as electrocatalysts. Moreover, the water splitting redox level potential is 1.23 eV and therefore, as previously discussed TMDs with band gap around this value that straddles the redox potential is used as photocatalysts.

Now, utilizing the TMD monolayers simply for these applications is not practical. Many factors come into play such as defects, strain and substrates, that significantly affect their electronic and optical properties. Therefore, we can purposely utilize these in monolayers to achieve desirable properties for suitable applications. In this thesis, we have engineered MoS_2 monolayer by defects and designed the van der Waals heterostructures (vdW HTSs) for the same. These have tuned their optical properties and catalytic properties. Let us now understand why defects are crucial for study and why there is a need to design vdW HTSs?

1.4 Point defects

Imperfections (or defects) are inevitable in solids and refer to any arrangement of atoms/ions than the perfect crystalline order. The defects are classified as per the dimensions with one or two atomic positions as the point defects, one dimensional as the linear defects and two dimensional as the interfacial or the boundaries. The thesis incorporates the point defects (vacancies and antisites). As per the thermal equilibrium phenomenon, the presence of vacancies

are normal. Since, probing these defects is not always experimentally feasible, first-principles computations are crucial to understand the same [19, 20, 21, 22, 23, 24, 25].

Let us now understand the presence of the same thermodynamically. The entropy increases with the defects in the system thereby making them entropically favourable. Hence, the perfect crystal growth is not favourable due to the enthalpy and entropy. We can understand this as per the Boltzmann equation [26]:

$$\Delta S = k_B \ln \omega \tag{1.4}$$

where ω is number of possible ways elements are arranged in a system. Considering N as total number of sites available and n being the number of vacancies on those sites, we have $\omega = \frac{N!}{(N-n)!n!}$. Therefore, entropy is:

$$\Delta S = k_B \ln \frac{N!}{(N-n)!n!} \tag{1.5}$$

Now, any stable system requires minimizing the change in Gibbs free energy ΔG which further corroborates with increase in ΔS

$$\Delta G = \Delta H - T\Delta S \tag{1.6}$$

Therefore, no vacancies (i.e. n=0) results to $\Delta S = 0$ and Gibbs free energy is not reduced. Hence, defects are inevitable in a system to ensure its stability.

Further, the defect concentrations, howsoever small, have ability to influence the properties of material that control the transport of matter such as electronic conduction and thermal conductivity, along with optical properties. As indicated in the previous section, defects can also be engineered to tune the properties for application in optoelectronic and electronic devices.

1.5 van der Waals heterostructures

Since the bulk and surface are the two faces of the same coin, their usage and properties are drastically different [27]. Surface reconstruction and interaction lead to different properties related to the interfaces. The surface is termed a solid and vacuum interface, whereas, the interfaces constitute two materials. The monolayer comes under the regime of surfaces whereas the heterostructures are altered due to interfacial effects. In this thesis, vdW HTSs are considered. The vdW HTSs have been described as atomic scale lego [10] with vertical stacking of

different monolayers on top of each other, where the planar stability is due to covalent bonds and between two monolayers there are van der Waals interactions. The monolayers with different properties can be chosen to obtain the required property in the vdW HTS, along with keeping their original electronic structure and hence the properties intact. Experimentally these are realized by deterministic transfer techniques [28]. Since, the database of 2D materials is increasing, we have high flexibility and control over engineering the heterostructures as per the required applications. These are broadly utilized in electronic, optoelectronic and energy storage industry.

Richard P. Feynman once said, "There is plenty of room at the bottom", and vdW HTSs is exactly the envision of the same. One can achieve myriad of properties such as interlayer excitons, superconducting states, Hofstadter's butterfly and moiré patterns. This is due to the atomically sharp interfaces resulting into electrons' correlation with phonons and spins, thereby affecting the charge transfer and energy. The properties of the vdW HTSs formed are affected by the stacking order, lattice mismatch, supercell and twisting angle. The material synthesis of these is challenging specifically the monolayers of the non-layered system [29, 30].

1.6 TMDs for catalysis

Let us first discuss what is catalysis? Catalysis represents accelerating reactions and reducing the energy required for the same. In 1835, the term catalyst was coined by J. J. Berzelius for the materials that do not consume itself while facilitating a reaction [31, 32]. Another significant timeline is 1912 when the Nobel Prize was awarded to Paul Sabatier for his work on Ni and Co catalysts for the hydrogenation of ethylene and CO. Further, the chronology includes the study of adsorbed species, configuration of materials, reactivity patterns, defects and surface. The computational insights on the active sites and reaction path have sufficed experimental realizations. Catalytic processes constitute around 85% of the industrial products [33]. They are indispensable for environment and energy related issues such as pollutant degradation, transportation fuels and manufacturing chemicals. The catalysis is mainly classified as homogeneous catalysis, heterogeneous catalysis and enzymatic catalysis (Fig. 1.4). Amongst them, the heterogeneous catalysis pathway is preferred due to separable reactants and products that can be reused. In this thesis, we study the same for hydrogen evolution reaction (HER) by electrocatalysis and photocatalysis (Fig. 1.5).

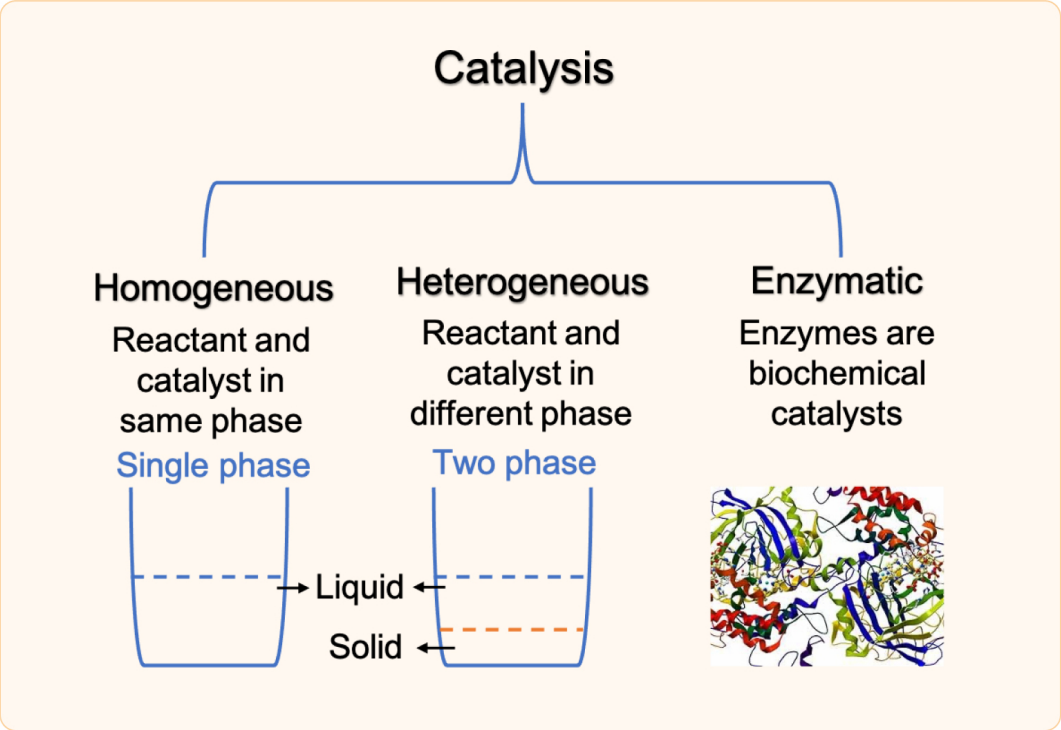

Figure 1.4: Types of catalysis

Since, precious metals (Pt and Pd) are the most efficient electrocatalysts, there is dire need to replace them by TMDs owing to their abundance and low cost [34]. Literature have reported TMDs to be sustainable for HER. Over the time, continuous advancement in synthesis techniques have led to the production of stable monolayers thus enhancing the interest in these materials. The stability is supported by the increased surface to volume ratio and availability of active sites. TMDs in the forms of defected sheet, alloyed sheet, HTSs (vertical and lateral), Janus sheets, heteroatom-doped sheets and crystal phase based structures (1T, 1T', and their HTSs) are utilized for the same.

Photocatalysis utilizes solar energy in visible range to generate electrons (e^-) and holes (h^+) at conduction band minima (CBm) and valence band maxima (VBM), respectively, for reaction. In case of electrocatalysis, external voltage initiates the reaction. These electrochemical interactions and reactions are boon to the aim of green sustainable energy requirements. These reactions need to be catalyzed to reduce the potential requirements for the same. Therefore, it is of utmost importance to look for better catalyst. The vdW HTSs have been chosen for the application, due to spatial separation of e^--h^+ at different monolayers and actuation of e^- transfer due to electronegativity difference. Now, vdW HTSs as an electrode for HER can be divided into two domains: graphene based vdW HTSs and non-graphene based TMD vdW

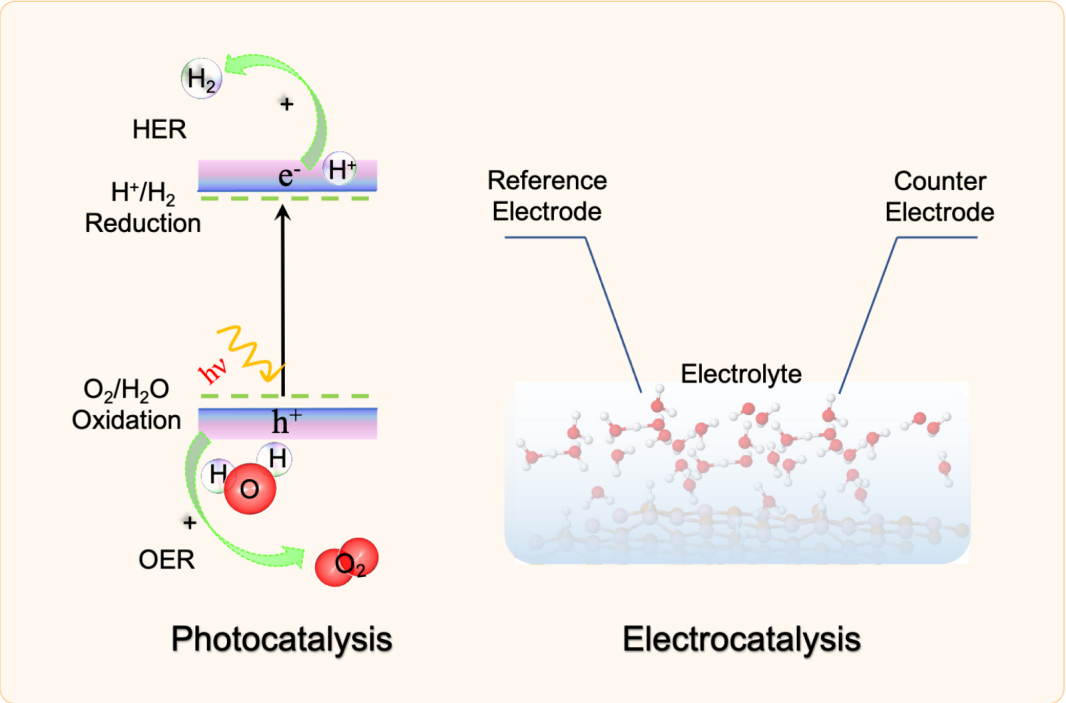

Figure 1.5: Photocatalysis and Electrocatalysis

HTS [35, 36, 37, 38, 39]. Majorly, these attempts are experimental on vdW HTSs such as ZnO/WS_2, CdS/g-C_3N_4, MoS_2/Gr, $MoSe_2/WS_2$. These have shown less overpotential for the HER. However, expanding the current library should be the focus as despite the advances in experiments, discussion on feasible reaction pathways is missing.

1.7 Problems and Challenges

Choosing a suitable type of 2D material and engineering it for required application is a humongous task. Factors that affect it are huge theoretical database, cost, abundance, experimental growth or exfoliation techniques, defects and stability. Existing studies have construed TMDs (especially MoS_2) as versatile family of 2D materials. Experimentally, one of the challenges faced by MoS_2 is its scalable growth with control over defects. Defects, henceforth, is important to understand for tuning the properties. First-principles study is an effective strategy as experimental workflow for every 2D structure is not conducive practically. The same is true for designing vdW HTSs.

In 20th century, greatest mind emphasized on the fundamental concepts pertaining to the defect-free crystals. The discussions on any kind of perturbations were qualitative and not analytically tried by the tools of quantum mechanics [40]. Defects were not prominent topic of study, which

was exemplified by the Pauli's comment on the Peierl's manuscript (in 1931) that stated "the residual resistivity is caused by dirt and one should not dwell in dirt". It is the prominence of Ge and Si in the rising semiconductor industry, that accelerated the need to control the electrical properties. Hence, dopants and defects were studied especially vacancies and interstitials. Theoretical studies gained momentum with challenge to understand doping mechanism. Density functional theory (DFT) referred as "first-principles" provided superior attempt in understanding defects. Since, defects significantly affect the 2D with respect to their 3D counterpart, the exchange-correlation (xc) functionals, supercell sizes and k-point sampling is crucial to adjust. The presence of defects affect carrier mobility and are characterized by strong localization. Subsequently, problem lies in determining, which kind of defects is stable and/or prominent in the system. We saw, vacancies are intrinsic as per thermodynamics, whereas other kind of point defects can arise due to synthesis, alloying and crystallography. Assuring reduced defect electrostatic interaction by varying supercell size in the model is therefore first step to conduct a defect-study via "first-principles". However, resources for computation restricts the convergence limit. Finally, effect of finite temperature and pressure is incorporated as formulated in ab-initio atomistic thermodynamics.

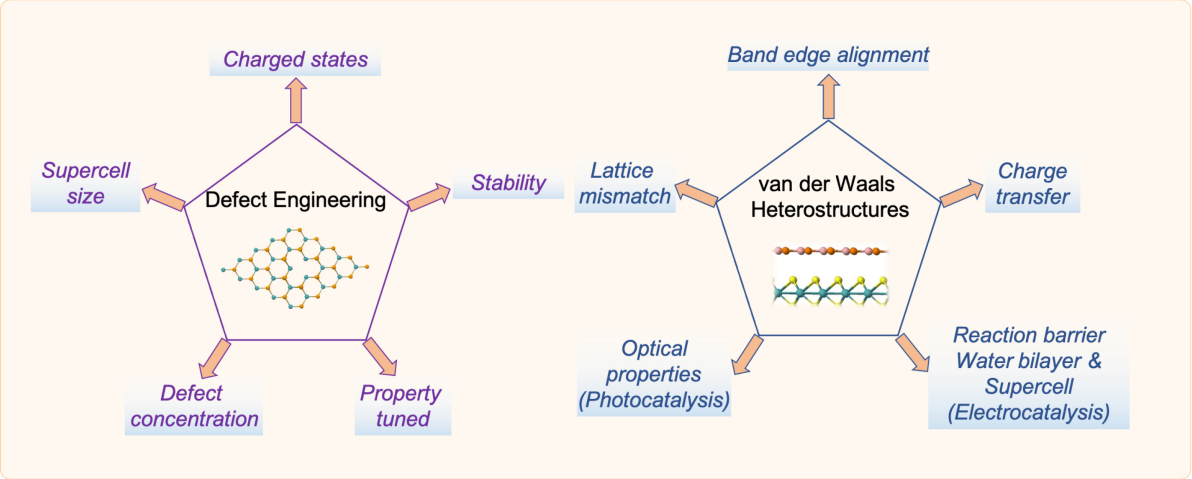

Figure 1.6: Illustration of the approaches (i) Defect engineering and (ii) van der waals heterostructures for tuning the properties

Now, when a study aims to understand excited state properties, the quasiparticle calculations are undertaken which are based on Green's function methods. These come under the regime of many-body perturbation theory (MBPT) with GW and Bethe-Salpeter equation approaches. This further aggravates the memory and cost requirements for the calculations. These require-

ments also depend on the number of atoms in the systems. Similar challenge is also experienced in the Climbing image - nudged elastic band calculations (CI-NEB) that is undertaken to find the saddle points and minimum energy paths between known reactants and products. In this thesis the aforementioned points have been tackled while undertaking defect study and designing the vdW HTSs for optical and catalytic applications.

Now, designing a vdW HTS starts by choosing materials/monolayers such that their lattice mismatch is minimum so as to form commensurate HTSs. Secondly, as per the requirement, the band edge alignment of monolayer should be checked because the band edges of the vdW HTSs are at similar level with as predicted in their constituent monolayer due to van der Waals forces in play. Finally, an apt model for further calculations should be chosen based on minimum energetic stacking configuration. In this thesis, we have designed the vdW HTS for HER through photocatalysis or electrocatalysis. In the photocatalytic study all the previously mentioned factors of supercell size, k-point sampling, MBPT calculations, planar averaged charged density plot, carrier mobility and Gibbs free energy (ab-initio thermodynamics) have been systematically conducted. Subsequently, the electrocatalytic study for HER in acidic media required electrical double layer kind of approach. Now, the challenge here is the model of water bilayer along with vdW HTSs for increasing supercell sizes upto 4x4, that significantly increase the number of atoms in the system. We choose vdW HTSs for the study because even if the constituent monolayers have inactive sites, the resulting vdW HTS can be obtained as an active electrocatalyst due to an inbuilt electric field at the interface [41].

1.8 A short overview of the thesis

- **Chapter 2:** This chapter put forths the methodology employed in the work. It explains the fundamentals behind the DFT through which we can find the ground state properties. The excited state properties as achieved by MBPT (GW and BSE) are discussed. Thereafter, density functional perturbation theory (DFPT) is discussed that caters to the lattice dynamics. Ab-initio atomistic thermodynamics and CI-NEB is also briefly introduced for understanding the stability and minimum energy path for a reaction, respectively.

- **Chapter 3:** In this chapter, we intend to analyse the thermodynamic stability of native point defects, where we have calculated the formation energies of the charged point defects i.e., Mo, S and S_2 vacancies, and S_{Mo}, $S_{2_{Mo}}$, Mo_S, Mo_{S_2} and $2Mo_{S_2}$ antisites. It is

of paramount importance to include vdW interaction that originates due to polarization (refers to induced dipole) and this have been incorporated as (i) the two-body van der Waals and (ii) many-body dispersion (MBD). We have obtained the phase diagrams for the most stable defect configurations with PBE and HSE06 functionals. The phase diagram infers the stable defect states as acceptors or donors. If a defect accepts electron to gain stability, it will have negative charge associated with it and hence will act as electron acceptors. Similarly, we can interpret for positive charged defects. Moreover, when $\Delta\mu_{\mathrm{e}}$ is close to CBm or VBM, the situation can be stated as either n-type or p-type MoS_2 monolayer. The results have supported the dependence of many body dispersion on the stability of defect configurations and therefore, for accurate experimental correlation this should be incorporated in the studies. The V_S^{-2}, V_{Mo}^{-2} and S_{Mo}^{-2}, V_S^{+2}, V_{Mo}^{+2} and $S_{2_{Mo}}^{+2}$ are the most probable defect states (HSE06+MBD). Inclusion of finite temperature using *ab inito* atomistic thermodynamics approach have shown significant defect concentration in the temperature range of 50-1000 K. Further, red shift is observed in the optical response of S_{Mo}^{-2} and $S_{2_{Mo}}^{+2}$ as their band gap are tuned in the range 1.1 to 1.8 eV. Harnessing these defect states instead of pristine monolayer is considerable for absorption in photovoltaics.

- **Chapter 4:** In this chapter, we intend to understand the mechanism behind the observed negative differential resistance (NDR) in the few-layer MoS_2 as grown by bi-phasic method under liquid phase exfoliation. The synthesis route plays a massive role in the formation and type of these defects. In either case, S vacancies (V_S) are prominent in MoS_2 monolayer and bulk. We have obtained the optimized structure of the adsorbed H^+ and OH^- at the defect sites, respectively. The V_S^{+2} being abundant and stable with +2 charged state adsorbs OH^-. Hence, this charged state leads to the dissociation of H_2O to H^+ and OH^-. The corresponding oxidation and reduction equations are:
  $2H_2O \rightarrow O_2{+}4H^+{+}4e^-$
  $2H_2O{+}2e^- \rightarrow H_2{+}4OH^-$
  The H^+ exists in the form of hydronium (H_3O^+) in the water layer. Thus, active sites prefer OH^- adsorption, thereby facilitating the H^+ to transfer and conduct between electrodes through the water molecular chain. This defect mediated H^+ transfer creates a gradient between OH^- and H_3O^+ species, thus supporting NDR effect in MoS_2 device in the presence of adsorbed water molecules. Proton conductors are usually solid material of various types which contain protons (H^+) as the primary charge carriers. On the

other hand, the proton transport in an aqueous medium containing hydronium (H_3O^+) and hydroxide (OH^-) ions is also an interesting phenomenon resulting in the high conductivity of water. The previous studies have also indicated the dissociation of H_2O and adsorption of OH^- on the O vacancy sites, that facilitates the proton conduction, thereby affecting the NDR seen in the system.

- **Chapter 5:** An exhaustive study has been undertaken for understanding different MoS_2 and MoSSe based vdW HTSs. As per the band edge alignment, it is observed that these vdW HTSs does not facilitate the normal photocatalytic process as they do not straddle the redox potential. However, these are predicted to be implementing the natural photocatalysis by Z-scheme. The band edge alignment of the MoSSe vdW HTSs has inferred large band gap in configuration III than in case of configuration II. This has been attributed to the additional anionic potential gradient due to Se atomic layer at the interface in configuration II. Moreover, since we are considering Z-scheme photocatalysis, we require monolayer with lesser recombination as compared to that of their corresponding vdW HTSs. In order to review this we have checked the variance of D values around 1 for monolayers and vdW HTSs. Therefore, the vdW HTSs with lesser variance as compared to that of their respective monolayer can be considered probable for Z-scheme photocatalysis. As per the discussed approach, we have deduced MoSSe/ZrS_2 (configuration II and III), MoSSe/HfS_2 (configuration II), MoSSe/TiS_2 (configuration III), MoS_2/SnO_2 and MoSSe/SnO_2 (configuration II and III) as the probable Z-scheme vdW HTSs. Amongst these, the MoS_2/SnO_2, MoSSe/HfS_2 (configuration II) and MoSSe/TiS_2 (configuration III) have shown least variance from 1. Their respective carrier mobilities have been approximately calculated. Moreover, their exciton binding energy is estimated using BSE@GW@HSE06 which showed comparatively smaller exciton binding energy of vdW HTSs as compared to that of MoS_2 and MoSSe monolayers. The absorption spectra further confirms the response of these vdW HTSs and hence, their applicability in photocatalytic devices. Finally, the H_2O adsorption and HER indicates their interaction with water, thus, helping in the photocatalytic process.

- **Chapter 6:** We have modelled a dynamically stable MoS_2/BP and MoSSe/BP vdW HTSs for studying HER by computational hydrogen electrode model as proposed by Norskov *et al.* [42]. The underlying approximation considers solvated proton upto first

bilayer. We have initially discussed the stacking configuration and electronic structure. We then conduct HER study by initially constituting 2×2, 3×3 and 4×4 supercells. The optimized structure with the water layer showed a significant potential drop at the surface-water interface. The electrostatic potential is further affected by the proton solvated in water layer and the H_{ads} constituting coverage over the surface. 2×2 and 4×4 supercell with 25% H coverage and 3×3 supercell with 11% H coverage have been deduced for the calculations. Thereafter, we have discussed the optimized systems consisting of water layer (water-solid interface with 3 Å thick water layer) without and with solvated protons (i.e., H^+). The corresponding H_2O molecules in the water layer are varied, thereby constituting 1/3 (i.e., 1 H^+/3H_2O) and 1/4 (i.e., 1 H^+/4H_2O) H^+ conc. The configuration corresponding to 3×3 supercell size has been studied for 1/8 (i.e., 1 H^+/8H_2O) H^+ conc. The MoS_2/BP and MoSSe/BP vdW HTSs show reduced barrier height for both Tafel and Heyrovsky reactions in comparison to the BP monolayer.The Heyrovsky reaction barrier, is lower in case of MoSSe/BP than MoS_2/BP vdW HTS, as observed from the minimum energy reaction paths. On comparing the supercells (and hence different coverages) with respect to the same H^+ conc., we observe high coverage to favour low H^+ conc. and vice versa for reduced reaction barrier. Finally, as per the extrapolation approach for ΔE_R vs ΔU, the Heyrovsky reaction mechanism is plausible.

- **Chapter 7:** This chapter sums up the important conclusions of the present thesis. The future scope of the present work is also suggested in this chapter.

CHAPTER 2

Theoretical methodology

2.1 Computational physics

In the present context, the ubiquity of computer simulation is unquestionable. Historically, the prominence of simulations rose after the second world war. Some examples that mark the breakthroughs are Electronic Numerical Integrator and Compiler (ENIAC) for mathematical modeling in the 1940s, Monte-Carlo techniques in the 1960s for particle physics, modeling in architecture in the 1980s, and the Paris-Durham model in astrophysics from the 1980s. The usage gained interest from the field of computational physics to the domain of architectural design. In material science, the extent of computational power utilization is being tested every time new ways have emanated by exploiting the tools of quantum mechanics. Computer simulations use mathematical models for physical, engineering, chemical, economic, astrophysics, and manufacturing systems.

In industry, too, the modeling and simulations are the basis of the formulation and performance of the product. The field is rather interdisciplinary, where the process is an amalgamation of numerical methods, user interfaces, and model formalism. It is in the model formalism where the physical or chemical processes are considered. The progression of any process is associated with a length and time scale, where the corresponding input and output decide the type of simulation. The different levels of the same are classified as (i) atomistic simulation, where the structures of the system determine the relationship of structure-property (e.g., Electronic structure methods, Monte Carlo, Molecular dynamics), (ii) mesoscale simulation pertains to the evolution of the system as a function of time (e.g., Phase field, Dislocation dynamics) and (iii) macroscale or continuum simulation ascertains phase diagrams, morphological stability, interfacial tensions, and flow characteristics (e.g., Computational fluid dynamics). This constitution of multi-scale computations allow the utilization of results from one level to another,

thereby predicting the material specific properties. Now, the determination of these fundamental principles behind the system is crucial for experimental advancement. Therefore, improving the quantum mechanical models and the computational infrastructure are necessities of parallel research. In this area, yet another challenge is the interface of classical atomistic simulation techniques and quantum mechanical methods. From a broader perspective, these constitute coupled methods for two or more temporal and spatial scales. Hence, the methods at different levels are being updated and ever-evolving.

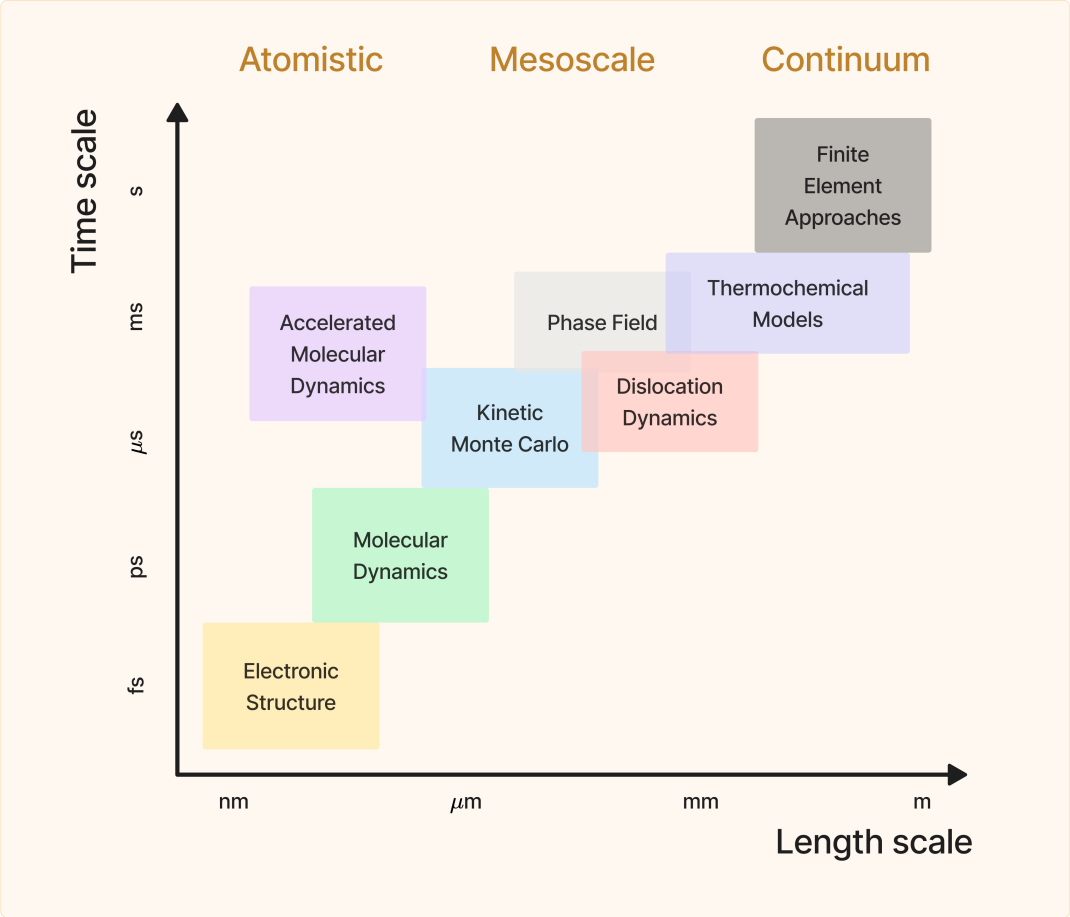

Figure 2.1: Different length and time scales of multi-scale simulations.

In this thesis, we discuss the frameworks corroborating the atomistic simulations. The first-principles based approaches have been employed to understand optical and catalytic properties. The layout of the present chapter initiates with the ideation of first-principles calculation. Subsequently, the density functional theory (DFT) analysis for many-electron quantum systems is discussed. For excited state properties, the approach is many body perturbation theory (MBPT). Further, for the reaction pathway, chapter explains the climbing image nudged elastic band method (CI-NEB). Finally, a discussion on the solid-water interfacial model for electro-

catalysis is presented.

2.2 First-principles calculations

The foundation of first-principles calculation is the mathematical equations that define physical laws with no empirical parameters (i.e., *ab initio*). The electrons and nuclei that constitute matter are the fundamental particles. Their interactions determine the nature of chemical and molecular bonding in the system. Hence, the intricate physical processes should naturally arise in the calculations if we can accurately characterize these interactions. Theoretical frameworks based on the approximation that explain various phenomena largely depend on electron-electron interactions. Some approximations that assisted the theory of electrons are the free electron approximation (discreteness of ions is neglected), the independent electron approximation (electron-electron interaction is neglected), the Self-Consistent Field (SCF) (electrons' motion in the mean field of other ions and electrons) and Landaus Fermi liquid (interacting electrons description by the quasi-particle). However, detailed descriptions of the interacting electrons must outwith these approximations as strong correlations and exchange energy play a significant role. The quantum mechanical formalism that governs electron dynamics lays its basis on the Schrödinger equation. However, the dimensionality of the problem for a many-electron system complicates the equation. Thus, efficient computational techniques seek more research and development.

In addition, the equation of state describes the fundamental quantities for condensed matter and is a function of pressure and temperature. The properties of the material for a given P and T is determined by its stable structure. Electronic structure calculations are carried at fixed volume. Therefore, the total energy E at T=0 as a function of volume Ω is an apt quantity to determine the properties. The fundamental quantities that can be determined are energy E, pressure P, bulk modulus B and higher derivatives of the energy.

2.3 The many-body problem

The interacting electrons and nuclei govern the many-body problem under the Coloumb potential and, in a non-relativistic regime, is formulated as a time-independent Schrödinger equation.

$$\hat{H}\Psi_k\left(r_1, r_2, \ldots, r_N, R_1, R_2, \ldots, R_M\right) = E_k\Psi_k\left(r_1, r_2, \ldots, r_N, R_1, R_2, \ldots, R_M\right) \tag{2.1}$$

Here, for a system of N electrons and M nuclei, $\hat{H}$ is the Hamiltonian operator. The corresponding expression is as follows:

$$\begin{aligned}\hat{H} = &-\sum_{i=1}^{N}\frac{\hbar^2}{2m_e}\nabla_i^2 - \sum_{I=1}^{M}\frac{\hbar^2}{2M_I}\nabla_I^2 - \sum_{i=1}^{N}\sum_{I=1}^{M}\frac{Z_I e^2}{|R_I - r_i|} \\ &+ \frac{1}{2}\sum_{i=1}^{N}\sum_{j\neq i}^{N}\frac{e^2}{|r_i - r_j|} + \frac{1}{2}\sum_{I=1}^{M}\sum_{J\neq I}^{M}\frac{Z_I Z_J e^2}{|R_I - R_J|}\end{aligned} \tag{2.2}$$

On representing the operator as:

$$\hat{H} = \hat{T}_e + \hat{T}_n + \hat{V}_{en} + \hat{V}_{ee} + \hat{V}_{nn} \tag{2.3}$$

$\hat{T}_e$ and $\hat{T}_n$ are the kinetic energy operators of electron and nuclei respectively. The $\hat{V}_{en}$, $\hat{V}_{ee}$ and $\hat{V}_{nn}$ account for the electron-nuclear Coulombic interaction, electronic and nuclear Coulombic repulsions. The r_i, e, R_I and Z_Ie are electronic coordinate, electronic charge, nuclei coordinate and nucleic charge, respectively. The $\frac{1}{M_I}$ term as per the Born-Oppenheimer approximation is small and the $\hat{V}_{nn}$ term is a constant term that can be added. Hence, the Hamiltonian becomes

$$\hat{H} = \hat{T}_e + \hat{V}_{en} + \hat{V}_{ee} \tag{2.4}$$

The Born-Oppenheimer approximation separates the nuclei and electronic degrees of freedom. The nuclei have heavier mass than the electrons and have different time scales of motion. The approximation assumes electrons' adiabatic motion following the nucleic movement. The total wave function, therefore, becomes:

$$\begin{aligned}\Psi_k\left(r_1, r_2, \ldots, r_N, R_1, R_2, \ldots, R_M\right) = \Psi_e\left(r_1, r_2, \ldots, r_N; R_1, R_2, \ldots, R_M\right) \\ \times\Psi_n\left(R_1, R_2, \ldots, R_M\right)\end{aligned} \tag{2.5}$$

Hamiltonian is thus written into two parts (Ψ_e electronic and Ψ_n nuclear) where the electronic wave function corresponds to a fixed nuclear geometry and hence depends parametrically on the nuclear positions.

Considering the atomic units $\hbar = m_e = e = \frac{4\pi}{\epsilon_0} = 1$, the terms are:

$$\hat{T}_e = -\sum_{i=1}^{N}\frac{1}{2}\nabla_i^2 \tag{2.6}$$

$\hat{V}_{en}$ is the potential acting on the electrons due to the nuclei,

$$\hat{V}_{en} = \sum_{i=1}^{N} \sum_{I=1}^{M} V_I \left(|r_i - R_I| \right) \tag{2.7}$$

and $\hat{V}_{ee}$ is the electron-electron interaction,

$$\hat{V}_{ee} = \frac{1}{2} \sum_{i=1}^{N} \sum_{j \neq i}^{N} \frac{1}{|r_i - r_j|} \tag{2.8}$$

Even after the Born-Oppenheimer approximation, the large dimensionality hinders the exact solution and is tractable only for some simple cases. Hence, we graduate towards other approximations. Amongst different *ab initio* approaches, the thesis discusses the wave function based methods, DFT and MBPT.

2.4 Wavefunction based methods

2.4.1 Hartree approximation

Under Hartree approximation the electronic wavefunction is written as:

$$\Psi \left(\mathbf{r}_1, \mathbf{r}_2, \ldots, \mathbf{r}_N \right) = \phi_1 \left(\mathbf{r}_1 \right) \phi_2 \left(\mathbf{r}_2 \right) \ldots \phi_N \left(\mathbf{r}_N \right) \tag{2.9}$$

The assumption being independent electrons interact under the averaged density of electrons, the electronic Hamiltonian corresponds to:

$$\hat{H_{el}} = \sum_i \hat{h_i} + \hat{V_{ee}} \tag{2.10}$$

where

$$\hat{h_i} = \frac{-1}{2} \nabla_i^2 + \hat{v_i} \tag{2.11}$$

The $\hat{h_i}$ depends solely on the coordinates of $\mathbf{r}_i$ (i-th electron). Each electron behaves under an effective potential of other electrons. The V_{ee} therefore is the interaction between individual electron and the averaged density of N-1 electrons.

$$\hat{g_k}(\mathbf{r}) = \int \rho^k(\mathbf{r}) \frac{1}{|\mathbf{r} - \mathbf{r'}|} d\mathbf{r} \tag{2.12}$$

$$\hat{V_{ee}} \approx \sum_{i=1}^{N} \hat{g}_i(\mathbf{r}) \tag{2.13}$$

where

$$\rho^{(k)}(\mathbf{r}) = \sum_{\substack{i=1 \\ i\neq k}}^{N} |\phi_i(\mathbf{r})|^2 \tag{2.14}$$

is the k-th electron interaction with the total density of electrons and excluding its own density. Hence, we now have N independent single electron equations:

$$\hat{H}_{el} \approx \sum_{i=1} \hat{g}_i(\mathbf{r}) + \hat{v}_i - \frac{1}{2}\nabla_i^2 \tag{2.15}$$

$$\hat{H}_{el}\phi_i(\mathbf{r}) = \epsilon_i \phi_i(\mathbf{r}) \tag{2.16}$$

Thereafter, Hartree potential for each electron is computed and solved.

$$\frac{\delta}{\delta\psi}|\langle\psi|H|\psi\rangle - E\langle\psi|\psi\rangle| = 0 \tag{2.17}$$

The comparison of states with the trial states we obtain the new guess state and the iteration continues until convergence. A major drawback is that it fails to satisfy the anti-symmetry of a wave function describing fermions, with the interchange of space-spin coordinates.
We find out the total energy E of the ground state.

$$E = \sum_{i=1}^{N} \epsilon_i - \frac{1}{2}\sum_{i=1}^{N}\sum_{j\neq i}^{N} J_{ij} \tag{2.18}$$

where J_{ij} is the Coulomb interaction between electron i and j. These Coulomb integrals are given by

$$J_{ij} = \int\int \frac{\rho_i(\mathbf{r}_1)\,\rho_j(\mathbf{r}_2)}{|\mathbf{r}_1 - \mathbf{r}_2|} d\mathbf{r}_1 d\mathbf{r}_2 = \int\int |\phi_i(\mathbf{r}_1)|^2 \frac{1}{|\mathbf{r}_1 - \mathbf{r}_2|} |\phi_j(\mathbf{r}_2)|^2 d\mathbf{r}_1 d\mathbf{r}_2 \tag{2.19}$$

$$J_{ij} = \int\int \phi_i^*(\mathbf{r}_1)\,\phi_i(\mathbf{r}_1)\,\frac{1}{|\mathbf{r}_1 - \mathbf{r}_2|}\phi_j^*(\mathbf{r}_2)\,\phi_j(\mathbf{r}_2)\,d\mathbf{r}_1 d\mathbf{r}_2 \tag{2.20}$$

2.4.2 Hartree-Fock (HF) approximation

The variational wave function here is in the form of slater determinant satisfying the antisymmetric condition. Pauli exclusion principle corroborates to the antisymmetric condition.
The Slater determinant for N-electron system is as follows:

$$\psi(r_1, r_2, r_3, \ldots, r_n) = \frac{1}{\sqrt{N!}} \begin{vmatrix} \phi_1(x_1) & \cdots & \phi_n(x_1) \\ \vdots & \vdots & \vdots \\ \phi_1(x_n) & \cdots & \phi_n(x_n) \end{vmatrix} \tag{2.21}$$

Here, $\phi_n(x_j)$ denotes the j-th electron occupying the n-th orbital.

HF equation :

$$[\hat{h_1} + \sum_i (\hat{J}_i - \hat{K}_i)]\phi_k = \sum_i \lambda_{ki}\phi_i \tag{2.22}$$

Here, $\hat{J}$ constitutes direct term and the operator corresponds to the $|\phi_i|^2$ and $|\phi_k|^2$ classical interactions. The $\hat{K}$ is called the exchange term and is a direct result of the antisymmetry property of the wavefunction. The Fock operator is defined as:

$$\begin{aligned} \hat{F} &= \hat{h_1} + \sum_i (\hat{J}_i - \hat{K}_i) \\ \hat{F}\phi_k = \sum_{i=1} \lambda_{ki}\phi_i \;&\rightarrow\; \lambda_{ki} = \delta_{ki}\epsilon_k \\ \hat{F}\phi_k &= \epsilon_k\phi_k \end{aligned} \tag{2.23}$$

Here, eigenvalues ϵ_k are the energy levels of an interacting system. Now, when we compare the energy of N-electron system with the N-1 electrons system, the energy required to remove an electron is given by:

$$E_{HF}(N-1) - E_{HF}(N) = -\epsilon_n \tag{2.24}$$

This brings us to the Koopman's theorem that states, each eigenvalue of the Fock operator provides the energy required to remove an electron from the corresponding single electron state. Negative of the orbital energy of highest occupied molecular orbital (HOMO) is the first ionization energy.

2.5 Density functional theory

As the name entails, the fundamental entity behind the theory is electron density and it is a scalar function of position. In this case the use of electron density rather than the wave function reduces the dimensionality of the many-electron system problem from $3N$ to 3.

The change in number of electrons in the system, does not alter the three-dimensionality of the electron density. Thus DFT is employable for many atoms at a low computing cost. DFT is therefore frequently employed to study many-electron systems, including atoms, molecules, and solids. It primarily serves to describe the functionals of electron density that define the ground-state features of the systems. The following sections provide a description of how DFT evolved.

2.5.1 Thomas-Fermi-Dirac approximation

Thomas and Fermi independently prescribed energy calculations of many-electron system apropos electronic density as the fundamental variable [43, 44]. They proposed kinetic energy expression as a functional of electron density of the many-electron system. The theory is based on the assumption of the non-interacting system with the uniformly distributed electronic equal to the local density. The fermion statistical mechanics is the tool behind the kinetic energy expression for uniform electron gas.

$$T_{TF}\left[n\right] = C_1 \int n^{\frac{5}{3}}\left(\mathbf{r}\right) d\mathbf{r} \tag{2.25}$$

In atomic units, $C_1 = \frac{3}{10}\left(3\pi^2\right)^{\frac{2}{3}} n(\mathbf{r})$ = 2.871. Here, $n\left(\mathbf{r}\right)$ represents the electronic density for a uniform electron gas. Note that the exchange and correlated electronic interactions are neglected here. However, Slater's expression can be incorporated under local approximation for accounting exchange interactions.

$$E_X\left[n\right] = C_2 \int n^{\frac{4}{3}}\left(\mathbf{r}\right) d\mathbf{r} \tag{2.26}$$

In atomic units, $C_2 = -\frac{3}{4}\left(\frac{3}{\pi}\right)^{\frac{1}{3}}$ = 0.739. Now, with the external potential $V_{ext}\left(\mathbf{r}\right)$, the energy functional for electrons is:

$$\begin{aligned} E_{TFD}\left[n\right] = C_1 \int n^{\frac{5}{3}}\left(\mathbf{r}\right) d^3r + \int V_{ext}\left(\mathbf{r}\right) n\left(\mathbf{r}\right) d^3r + C_2 \int n^{\frac{4}{3}}\left(\mathbf{r}\right) d^3r \\ + \frac{1}{2}\int \frac{n\left(\mathbf{r}\right) n\left(\mathbf{r}'\right)}{\left|\mathbf{r}-\mathbf{r}'\right|} d^3r d^3r' \end{aligned} \tag{2.27}$$

where the last term is the classical electrostatic Hartree energy. The introduction of exchange interaction terms the theory as *Thomas-Fermi-Dirac* (TFD).

Minimization of the functional $E[n]$ for all possible $n\left(\mathbf{r}\right)$, with the constraint of integrated charge being equal to the number of electrons in the system, deduces the ground-state density and hence, the energy.

$$\int n\left(\mathbf{r}\right) d^3r = N \tag{2.28}$$

Subsequently, using the method of Lagrange multipliers, the solution can be found by an unconstrained minimization of the function where the Lagrange multiplier μ is the Fermi energy.

$$\Omega_{TF}\left[n\right] = E_{TF}\left[n\right] - \mu\left\{\int n\left(\mathbf{r}\right) d^3r - N\right\} \tag{2.29}$$

This leads to the expression

$$\frac{1}{2}\left(3\pi^2\right)^{\frac{2}{3}} n^{\frac{2}{3}}\left(\mathbf{r}\right) + V\left(\mathbf{r}\right) - \mu = 0 \tag{2.30}$$

where $V(\mathbf{r}) = V_{ext}(\mathbf{r}) + V_{Hartree}(\mathbf{r}) + V_x(\mathbf{r})$ is the total potential.

This model is not apt for execution as the requisite fundamentals such as correlation interactions, binding of molecules and shell structures of atoms are absent.

2.5.2 The Hohenberg-Kohn theorems

Hohenberg and Kohn [45] formulated the density functional theory that is applicable to any system of interacting particles. They proposed two theorems that lays the tenet of DFT.

Theorem I: *For any system of interacting electrons in an external potential $V_{ext}(\mathbf{r})$, the potential $V_{ext}(\mathbf{r})$ is determined uniquely, apart from a trivial additive constant, by the electronic ground-state density $n(\mathbf{r})$.*

Proof: Let us start by assuming two different potentials $V_{ext}(\mathbf{r})$ and $V'_{ext}(\mathbf{r})$, for a system with same ground-state density $n(\mathbf{r})$. They correspond to the Hamiltonians H and H', with the obtained wave functions Ψ and Ψ', respectively. Hence, their ground-state energies are: $E = \langle\Psi|H|\Psi\rangle$ and $E' = \langle\Psi'|H'|\Psi'\rangle$. We have put forth the consideration of the non-degenerate case; however, the deduction can extend to the degenerate case [27]. Now, employing variational principle we have:

$$\begin{aligned} E < \langle\Psi'|H|\Psi'\rangle &= \langle\Psi'|H'|\Psi'\rangle + \langle\Psi'|H - H'|\Psi'\rangle \\ &= E' + \int n(\mathbf{r})\left[V_{ext}(\mathbf{r}) - V'_{ext}(\mathbf{r})\right] d\mathbf{r} \end{aligned} \tag{2.31}$$

On a similar note, solving for E' we obtain:

$$\begin{aligned} E' < \langle\Psi|H'|\Psi\rangle &= \langle\Psi|H|\Psi\rangle + \langle\Psi|H' - H|\Psi\rangle \\ &= E + \int n(\mathbf{r})\left[V'_{ext}(\mathbf{r}) - V_{ext}(\mathbf{r})\right] d\mathbf{r} \end{aligned} \tag{2.32}$$

On adding Equations 2.31 and 2.32, we obtain

$$E + E' < E + E' \tag{2.33}$$

The expression is contradictory, thereby, establishing the initial assumption to be wrong. Hence, the ground-state density uniquely determines the potential.

Corollary I: Since $n(\mathbf{r})$ uniquely determines $V_{ext}(\mathbf{r})$, in turn, $V_{ext}(\mathbf{r})$ fixes the Hamiltonian and hence, the many-body wave functions are determined. Therefore, all the properties of the system are determined provided only the ground-state density $n(\mathbf{r})$.

Theorem II: *A universal energy functional $E[n]$ using density $n(\mathbf{r})$ can be defined, valid for any number of particles and any external potential $V_{ext}(\mathbf{r})$. For a given potential $V_{ext}(\mathbf{r})$, the*

$E[n]$ equals the correct ground-state energy of the system which is the global minimum value for the correct ground-state density $n(\mathbf{r})$.

Proof: In these theorems, the ground state density of the system corroborate to an external potential and hence, space of such densities is referred as "V-representable". Specifying $n(\mathbf{r})$ in a system uniquely determines the properties of the system that can be expressed as functional of $n(\mathbf{r})$. Similarly, the energy functional can be written as universal functional of $n(\mathbf{r})$:

$$\begin{aligned} E_{HK}[n] &= T[n] + E_{int}[n] + \int V_{ext}(\mathbf{r})\, n(\mathbf{r})\, d\mathbf{r} \\ &= F_{HK}[n] + \int V_{ext}(\mathbf{r})\, n(\mathbf{r})\, d\mathbf{r} \end{aligned} \tag{2.34}$$

where

$$F_{HK}[n] = T[n] + E_{int}[n] \tag{2.35}$$

The expression includes kinetic and interaction energy of electrons. $V_{ext}(\mathbf{r})$ is specific to a system as it is dependent on the nuclear coordinates. Considering the potential $V^1_{ext}(\mathbf{r})$ with corresponding ground-state density $n_1(\mathbf{r})$ and ground state wave function Ψ_1, we obtain the energy as:

$$E_1 = E_{HK}[n_1] = \langle \Psi_1 | H | \Psi_1 \rangle \tag{2.36}$$

Sunsequently, consider different density $n_2(\mathbf{r})$ corresponding to different wave function Ψ_2. On application of variational principle we obtain:

$$E_1 = E_{HK}[n_1] = \langle \Psi_1 | H | \Psi_1 \rangle < \langle \Psi_2 | H | \Psi_2 \rangle = E_{HK}[n_2] = E_2 \tag{2.37}$$

Hence, the Hohenberg-Kohn functional corroborates the true ground-state density with the ground-state energy. The appropriate functional $F_{HK}[n]$ and subsequent minimization of total energy with respect to (w.r.t) variations in $n(\mathbf{r})$, the exact ground-state energy and density can be determined.

Corollary II: Note that the functional only determines the ground state properties; it does not provide any guidance concerning excited states.

Even though these theorems prove the existence of a universal functional $F_{HK}[n]$, there is no prescription for its determination. The Kohn-Sham ansatz has led to effective approximations to substantiate the Hohenberg-Kohn theorems for practical computations.

2.5.3 The Kohn-Sham ansatz

Kohn and Sham attempted to determine the functional $F_{HK}[n]$ [46], by introducing a non-interacting particle system (auxiliary) with the same ground-state density as the primary in-

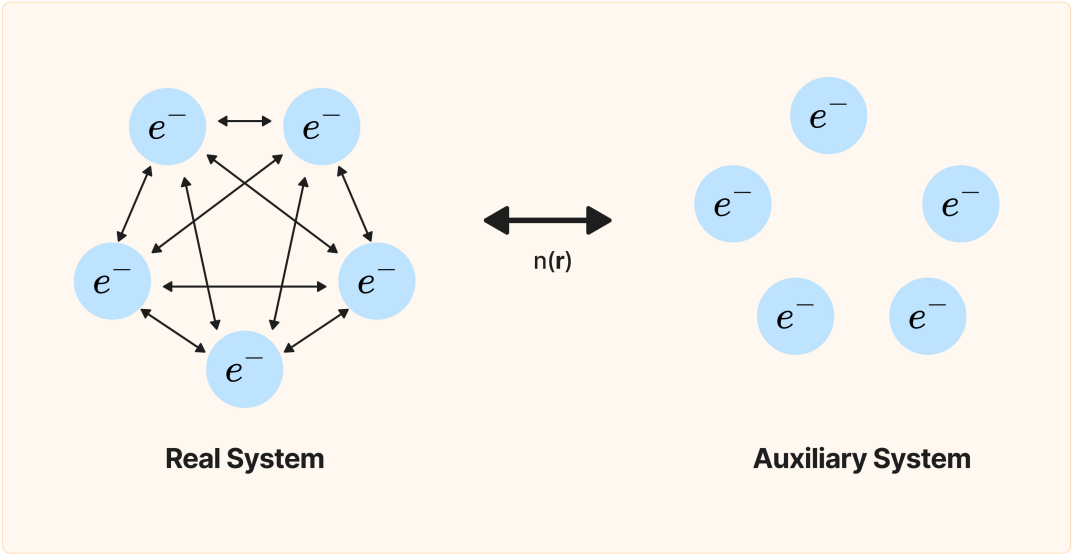

Figure 2.2: Depiction of interacting and non-interacting many-electron system with same ground-state electron density.

teracting system. Fig. 2.2 provides a schematic representation of the same. The auxiliary Hamiltonian for an electron with spin σ at point $\mathbf{r}$, under the effective local potential $V_{eff}^{\sigma}(\mathbf{r})$ is expressed as:

$$\hat{H}_{aux}^{\sigma} = -\frac{1}{2}\nabla^2 + V_{eff}^{\sigma}(\mathbf{r}) \tag{2.38}$$

$\psi_i^{\sigma}(\mathbf{r})$ and ϵ_i^{σ} are the eigenstates and eigenvalues of this Hamiltonian. The density of this auxiliary system (Equation 2.39) would yield exact total energy of the interacting system, if the total energy functional dependency on electron density is comprehended.

$$n(\mathbf{r}) = \sum_{\sigma} n(\mathbf{r}, \sigma) = \sum_{\sigma} \sum_{i=1}^{N^{\sigma}} |\psi_i^{\sigma}(\mathbf{r})|^2 \tag{2.39}$$

The corresponding kinetic energy T_s of the auxiliary system is expressed as:

$$T_s = -\frac{1}{2} \sum_{\sigma} \sum_{i=1}^{N^{\sigma}} \langle \psi_i^{\sigma} | \nabla^2 | \psi_i^{\sigma} \rangle = \frac{1}{2} \sum_{\sigma} \sum_{i=1}^{N^{\sigma}} \int |\nabla \psi_i^{\sigma}(\mathbf{r})|^2 d\mathbf{r} \tag{2.40}$$

The Hartree energy defined as the classical Coulomb interaction energy of the electron density $n(\mathbf{r})$ interacting with itself is given by:

$$E_{Hartree}[n] = \frac{1}{2} \int \frac{n(\mathbf{r})\, n(\mathbf{r}')}{|\mathbf{r} - \mathbf{r}'|} d\mathbf{r} d\mathbf{r}' \tag{2.41}$$

Hence, the total energy functional under the Kohn-Sham ansatz is:

$$E_{KS} = T_s[n] + \int V_{ext}(\mathbf{r})\, n(\mathbf{r})\, d\mathbf{r} + E_{Hartree}[n] + E_{xc}[n] \tag{2.42}$$

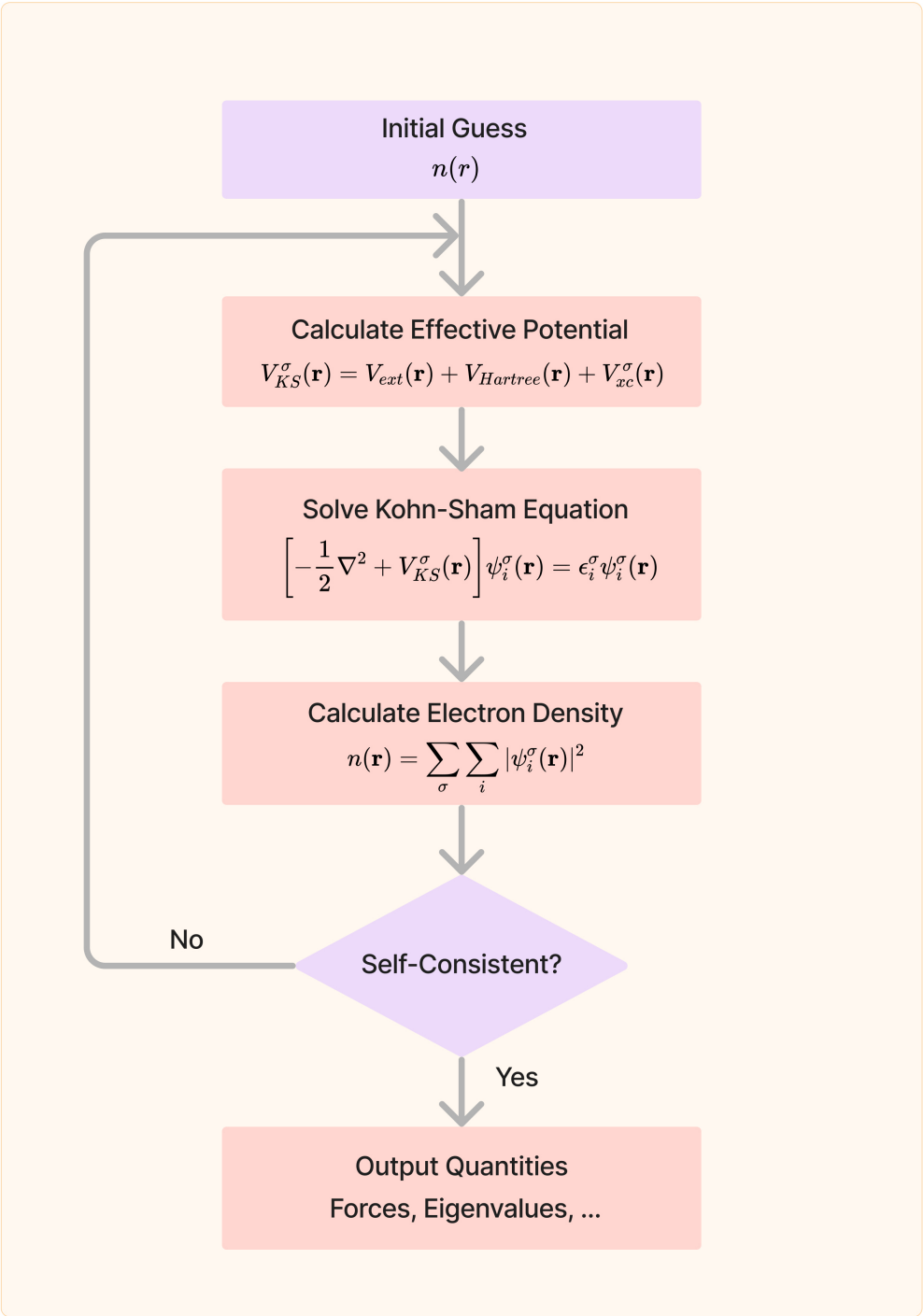

Figure 2.3: Flow chart for self-consistent solution of Kohn-Sham equations.

The exchange-correlation energy E_{xc} encompasses the exchange and correlation many-body interactions. Now, we can express $F_{HK}[n]$ as:

$$E_{xc}[n] = F_{HK}[n] - (T_s[n] + E_{Hartree}[n]) \tag{2.43}$$

$$E_{xc}[n] = \langle\hat{T}\rangle - T_s[n] + \langle\hat{V}_{int}\rangle - E_{Hartree}[n] \tag{2.44}$$

Here, $\langle \hat{T} \rangle$ and $\langle \hat{V}_{int} \rangle$ is the kinetic energy and internal interaction energy of the primary interacting system. $E_{xc}[n]$ accounts for binding among atoms. Hence, the Kohn-Sham Schrödinger equation is expressed as:

$$H_{KS}^{\sigma} \psi_i^{\sigma}(\mathbf{r}) = \epsilon_i^{\sigma} \psi_i^{\sigma}(\mathbf{r}) \tag{2.45}$$

with

$$H_{KS}^{\sigma}(\mathbf{r}) = -\frac{1}{2}\nabla^2 + V_{KS}^{\sigma}(\mathbf{r}) \tag{2.46}$$

and

$$\begin{aligned} V_{KS}^{\sigma}(\mathbf{r}) &= V_{ext}(\mathbf{r}) + \frac{\delta E_{Hartree}}{\delta n(\mathbf{r},\sigma)} + \frac{\delta E_{xc}}{\delta n(\mathbf{r},\sigma)} \\ &= V_{ext}(\mathbf{r}) + V_{Hartree}(\mathbf{r}) + V_{xc}^{\sigma}(\mathbf{r}) \end{aligned} \tag{2.47}$$

Fig. 2.3 shows the self-consistent approach to obtain potential and thus the density. However, the dependence of $E_{xc}[n]$ on the electron density is unknown, and approximations are therefore necessary.

2.5.4 Exchange-correlation functionals

Despite the fact that the exact functional $E_{xc}[n]$ must have complexity, remarkable simple approximations have made significant progress. There are several approximations with differing degrees of accuracy and computational expense. Some of these approximations are known as "empirical" and "semi-empirical" functionals and are based on the experimental input. The category of non-empirical functionals is purely based on the first-principles calculations.

2.5.4.1 Local Density Approximation (LDA)

Kohn-Sham proposed a general inhomogeneous electronic system to be locally homogeneous, thereby interpreting exchange-correlation functional $E_{xc}[n]$ as a local functional of the electron density. This has been the first attempt at exchange-correlation functional formulation.

$$E_{xc}^{LDA}[n] = \int n(\mathbf{r})\, \varepsilon_{xc}^{unif}(n(\mathbf{r}))\, d\mathbf{r} \tag{2.48}$$

where $\varepsilon_{xc}^{unif}(n(\mathbf{r}))$ is the exchange-correlation energy per electron in a locally homogeneous electron gas with uniform density $n(\mathbf{r})$. The validity of LDA is only for slow varying densities.

$$\frac{|\nabla n|}{n} \ll k_F = \left(3\pi^2 n\right)^{\frac{1}{3}} \tag{2.49}$$

and

$$\frac{|\nabla n|}{n} \ll k_S = \frac{2}{\sqrt{\pi}} \left(3\pi^2 n\right)^{\frac{1}{6}} \tag{2.50}$$

where k_F and k_S is the Fermi and Thomas-Fermi wave vector, respectively.

At this point, discussing the electron-correlation hole that represents charge depletion is pertinent. The concept describes that the presence of an electron at a point, decreases the probability of another electron in its vicinity. Since LDA is characterized by uniform density, the electron-correlation hole and the electronic density are centered at the same spatial coordinate.

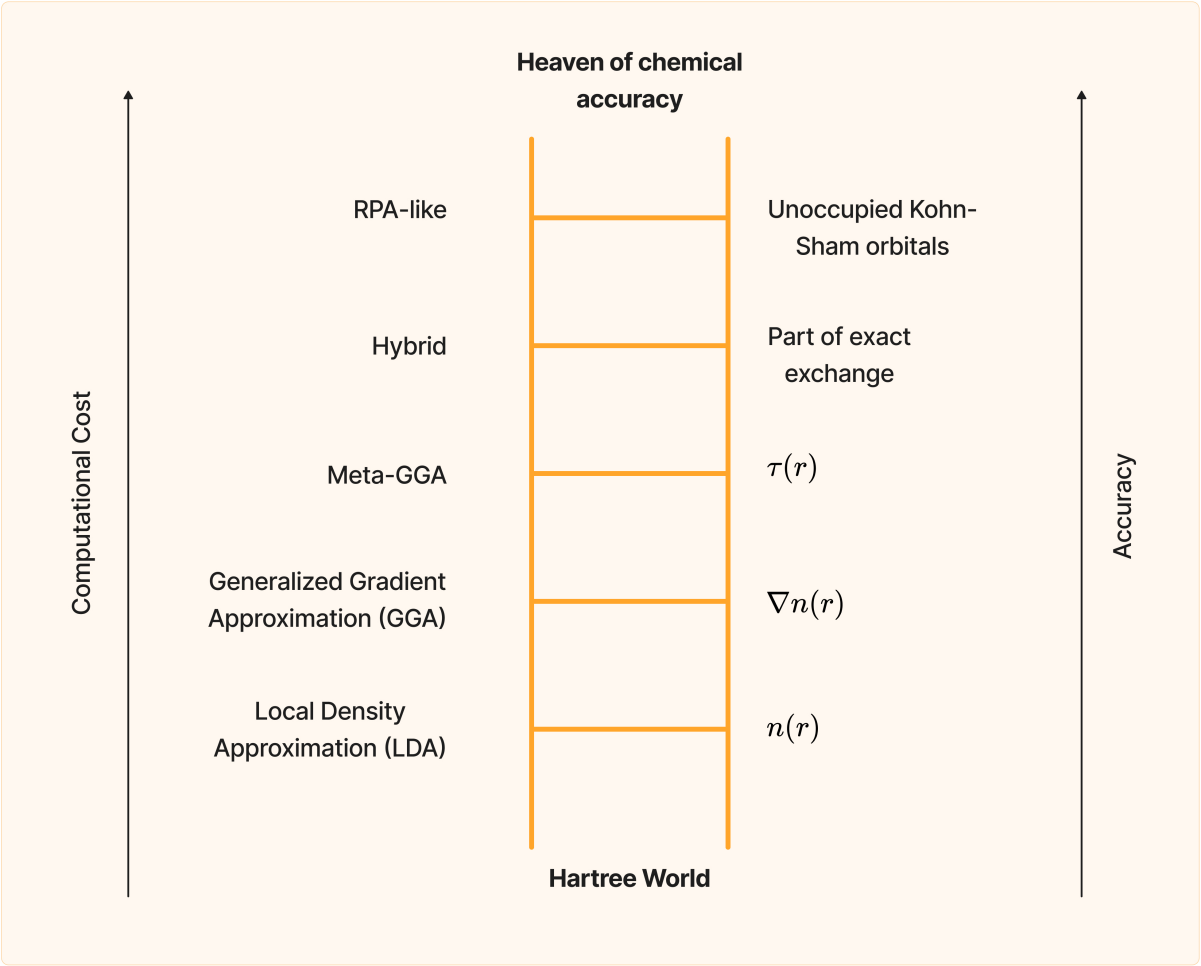

Figure 2.4: Jacob's ladder for exchange and correlation functional approximations under DFT [1]

In case of spin-polarized systems, the LDA is extended to the local spin density approximation (LSDA):

$$E_{xc}^{LSDA}\left[n_{\uparrow}, n_{\downarrow}\right] = \int n\left(\mathbf{r}\right) \varepsilon_{xc}^{unif}\left(n_{\uparrow}\left(\mathbf{r}\right), n_{\downarrow}\left(\mathbf{r}\right)\right) d\mathbf{r} \tag{2.51}$$

LSDA have showcased better accuracies than LDA for ground state spin polarized system, with same ($\uparrow$ and $\downarrow$) spin dependent external potential, i.e., $v_{\uparrow}\left(\mathbf{r}\right) = v_{\downarrow}\left(\mathbf{r}\right) = v\left(\mathbf{r}\right)$. In addition,

for inhomogeneous cases too LSDA works significantly well. Thus, constructing more accurate functionals can be attempted by adding parameters that satisfy the appropriate norms and constraints. Such ideation implies Jacob's ladder for exchange-correlation functional, growing from the Hartree regime to the most accurate functional for chemical accuracy [1]. Jacob's ladder is depicted in Fig. 2.4. It displays the hierarchy of exchange-correlation functional approximations, where the accuracy, complexity, cost, and time increase upwards.

2.5.4.2 Generalized Gradient Approximation (GGA)

Langreth-Mehl proposed the idea for GGA [47].

$$E_{xc}^{GGA}[n] = \int n(\mathbf{r})\, \varepsilon_{xc}^{GGA}(n, |\nabla n|)\, d\mathbf{r} \tag{2.52}$$

Gradient expansion is the core behind these approximations that cater to the issue of inhomogeneous electron density. The expansion can extend to higher-order derivatives. The semi-local approach considers density variation in the vicinity of a point and is unable to capture non-local effects at a larger range. The second-order gradient expansion is valid for slowly varying densities in space. However, this approximation resulted in a significant error in the correlation term. Therefore, to retain the relevance of the expansion, the exact conditions of the exchange-correlation hole, such as negative exchange density, self-interaction, and normalization condition, should be imposed. Gradient expansions incorporating these modifications are termed generalized gradient approximations (GGA's). Perdew, Burke, and Ernzerhof (PBE) have deduced GGA with the consideration of all parameters as fundamental constants and is extensively used [48]. GGA has improved the atomic bonding energies and bond lengths. However, the limitations of GGA include the unaccountability of non-local effects and self-interaction error.

2.5.4.3 Meta-Generalized Gradient Approximation (meta-GGA)

meta-GGA was proposed by Perdew *et. al.* (PZKB) in 1999 with the expression [49]:

$$E_{xc}^{MGGA}[n] = \int n(\mathbf{r})\, \varepsilon_{xc}^{MGGA}(n, |\nabla n|, \tau)\, d\mathbf{r} \tag{2.53}$$

Here, τ is defined as kinetic energy density for the non-interacting system and is given by

$$\tau(\mathbf{r}) = \sum_{i}^{occup} \frac{1}{2} |\nabla \phi_i(\mathbf{r})|^2 \tag{2.54}$$

$$\int \tau\left(\mathbf{r}\right) d\mathbf{r} = T_s\left[n\right] \tag{2.55}$$

τ satisfies some exact constraints that was not possible with GGA.

However, meta-GGA is a semi-local functional and even with the improvement the self-interaction correction is fragmentary. Hence, non-local approximation is requisite for the case of self interaction.

2.5.4.4 Hybrid functionals

The ideation of hybrid density functionals was introduced by Becke in 1993. The concept is to mix a fraction of HF exchange with the GGA exchange and correlation.

$$E_{xc}^{hyb} = \alpha E_x^{HF} + \left(1-\alpha\right) E_x^{GGA} + E_c^{GGA} \tag{2.56}$$

where the coefficient α is either experimentally corroborated or theoretically estimated.

Since the non-local effects are considered, the accuracy of hybrid functionals is high. The HF exchange computations are challenging, specifically for larger systems. The proposed method by Heyd, Scuseria, and Ernzerhof (HSE) [50, 51] have significantly reduced the calculation cost, as here the screened Coulomb potential is used to screen the long-range part of the HF exchange. The Coulomb potential entails the short-range (SR) and long-range (LR) parts

$$\frac{1}{r} = \underbrace{\frac{1-\text{erf}(\omega r)}{r}}_{\text{SR}} + \underbrace{\frac{\text{erf}(\omega r)}{r}}_{\text{LR}} \tag{2.57}$$

The error function is:

$$\text{erf}(\omega r) = \frac{2}{\sqrt{\pi}} \int_0^{\omega r} e^{-x^2} dx \tag{2.58}$$

ω is defined as the screening parameter that represents the range of separation The exchange-correlation energy is thus obtained as:

$$E_{xc}^{HSE} = \alpha E_x^{HF,SR}(\omega) + (1-\alpha) E_x^{PBE,SR}(\omega) + E_x^{PBE,LR}(\omega) + E_c^{PBE} \tag{2.59}$$

where $\alpha = 0.25$ and $\omega = 0.11$ bohr^{-1} are the default values; however, these can be varied. These have predicted the lattice constants, band gaps, enthalpies of formation, electron affinities, and ionization potentials with sufficient accuracy. In the present thesis, we have incorporated GGA by PBE functional and hybrid approximation by HSE06 functional.

2.5.5 Basis set

The electronic structure problem requires wavefunction expansion in terms of a known set of functions, which constitutes the basis. A set of linearly independent vectors that span the space is called a basis. The first step thus in implementing DFT is to ascertain a basis set. The corresponding wavefunctions can be energy independent $\phi_\alpha(\mathbf{r})$ or dependent $\phi_\alpha(E, \mathbf{r})$. Further, the three types basis sets in application are:

1. Plane waves and grids
    - Pseudopotential methods
    - Orthogonalized Plane Wave Method (OPW)
    - Projector Augmented Wave (PAW)
2. Localized atomic-like orbitals
    - Linear Combination of Atomic Orbital [LCAO]
    - Linear Combination of Gaussian Orbital [LCGO]
    - Semi-empirical Tight Binding Method
    - Numerical Approach [Order-N methods]
3. Atomic sphere methods
    - Linearized Method: LMTO, LAPW, ASW
    - Augmented Plane Wave Method

2.5.5.1 Plane waves basis set

Solving the single-particle Kohn-Sham equations for the extended system requires an implementable numerical method. Since plane waves are orthonormal and independent of energy, they are the best choice for the basis function set for extended systems. As a result, the Schrödinger equation is reduced to a simple matrix eigenvalue problem for obtaining the expansion coefficients. The pulay forces are absent because plane waves are independent of the atomic locations. Also, the Hellmann-Feynman theorem can be used to determine atomic forces without further calculation.

The plane wave basis set typically includes plane waves up to a particular wave vector cutoff. The length of the cutoff wave vector serves as the sole parameter for basis set convergence. The valence wave functions in the core region close to nuclei exhibit rapid oscillations, requiring a significant number of plane wave representations. In order to imitate the influence of core electrons, the plane waves are employed in conjunction with the pseudopotentials.
Additionally, the integrals and operations are simpler to execute with the implementation of Fast Fourier Transforms (FFTs) along with plane waves. It enables the application of plane waves in more complex systems. The fundamental terminology for characterizing infinitely extended periodic systems will be introduced in this section. The pseudopotential technique is discussed in the sections that follow.

Supercells

Although the many-body electron issue has been reduced to a set of single-particle equations, it is still difficult to calculate the single-electron wave functions for an infinite system. The infinite system can be represented by regular repetition of unit cells in all three spatial directions to make the solution possible. These repeated unit cells constitute a supercell that defines the same system but with a larger volume. Further, The volume of the cell is given by

$$\Omega_c = |\, \mathbf{a_1} \cdot (\mathbf{a_2} \times \mathbf{a_3})| \tag{2.60}$$

where $\mathbf{a_1}$, $\mathbf{a_2}$, and $\mathbf{a_3}$ are the lattice vectors. Supercells are mainly employed for modeling certain perturbations, surfaces, and point defects. In order to prevent interactions between the periodic images of defects or surfaces, the supercell should be sufficiently large.

Bloch's theorem

As per Bloch's theorem, the eigenstates of the single-particle Hamiltonian in a periodic crystal can be expressed in terms of plane waves as:

$$\psi\left(\mathbf{r} + \mathbf{R}\right) = e^{i\mathbf{k}\cdot\mathbf{R}}\psi\left(\mathbf{r}\right) \tag{2.61}$$

where $\mathbf{R}$ corresponds to the Bravais lattice. $\mathbf{k}$ is the wave vector defined in the reciprocal space. The values of $\mathbf{k}$ are confined within the first Brillouin zone (BZ). There exists different independent eigenstates for a given $\mathbf{k}$, each of which can be identified by a band index of n. Alternatively, Bloch's theorem can be stated as [52]:

$$\psi_{n\mathbf{k}}\left(\mathbf{r}\right) = e^{i\mathbf{k}\cdot\mathbf{r}}u_{n\mathbf{k}}\left(\mathbf{r}\right) \tag{2.62}$$

where

$$u_{n\mathbf{k}}\left(\mathbf{r}+\mathbf{R}\right)=u_{n\mathbf{k}}\left(\mathbf{r}\right) \tag{2.63}$$

The calculations are thus restricted within one unit cell and normalization of eigenfunctions is thus convenient. Further, in reciprocal lattice and **G** as the reciprocal lattice vector Equation 2.62 is represented as:

$$\psi_{n\mathbf{k}}\left(\mathbf{r}\right)=\sum_{\mathbf{G}}c_{n\mathbf{k}}\left(\mathbf{G}\right)e^{i(\mathbf{k}+\mathbf{G})\cdot\mathbf{r}} \tag{2.64}$$

Here, $c_{n\mathbf{k}}\left(\mathbf{G}\right)$ are the plane wave coefficients. Now, the Kohn-Sham equations in the Bloch states representation is given as:

$$\left(-\frac{1}{2}\nabla^2+V_{eff}\left(\mathbf{r}\right)\right)\psi_{i\mathbf{k}}\left(\mathbf{r}\right)=\epsilon_{i\mathbf{k}}\psi_{i\mathbf{k}}\left(\mathbf{r}\right) \tag{2.65}$$

where $V_{eff}\left(\mathbf{r}\right)$ is the effective potential as experienced by electron in the periodic lattice. Here,

$$n\left(\mathbf{r}\right)=2\frac{\Omega_c}{\left(2\pi\right)^3}\sum_i\int_{\mathrm{BZ}}\left|\psi_{i\mathbf{k}}\left(\mathbf{r}\right)\right|^2\Theta\left(\mathrm{E_{Fermi}}-\epsilon_{i\mathbf{k}}\right)d\mathbf{k} \tag{2.66}$$

Electron spin is accounted by the factor two in Equation 2.66. Here, Θ is the step function and $\mathrm{E_{Fermi}}$ represents the Fermi energy.

Now, $V_{eff}\left(\mathbf{r}\right)$ can be expressed as:

$$V_{eff}(\mathbf{r}+\mathbf{T})=V_{eff}(\mathbf{r}) \tag{2.67}$$

Here, the translation vector (**T**) is:

$$\mathbf{T}=N_1\mathbf{a_1}+N_2\mathbf{a_2}+N_3\mathbf{a_3} \tag{2.68}$$

where N_1, N_2, and N_3 are three integers.

The V_{eff} Fourier series expansion is given by

$$V_{eff}(\mathbf{r})=\sum_{\mathbf{G}}V_{eff}(\mathbf{G})e^{i\mathbf{G}\cdot\mathbf{r}}\quad\text{and}\quad V_{eff}(\mathbf{G})=\frac{1}{\Omega_c}\int_{\Omega_c}V_{eff}(\mathbf{r})e^{-i\mathbf{G}\cdot\mathbf{r}}d\mathbf{r} \tag{2.69}$$

In addition, the condition $\mathbf{G}\cdot\mathbf{T}=2\pi M$ is followed, where M is an integer and **T** is a unit cell translation vector.

Employing the plane-wave basis set simplifies the Kohn-Sham equation. On substituting Equation 2.64 to Equation 2.65, we obtain the matrix eigenvalue equation [27]:

$$\sum_{\mathbf{G}}\left(\frac{1}{2}|\mathbf{k}+\mathbf{G}|^2\delta_{\mathbf{G'G}}+V_{eff}\left(\mathbf{G'}-\mathbf{G}\right)\right)c_{\mathbf{G}}^{j\mathbf{k}}=\epsilon_{j\mathbf{k}}c_{\mathbf{G'}}^{j\mathbf{k}} \tag{2.70}$$

In practice, the Fourier expansion significantly depends on the given cutoff value E_{cut}:

$$\frac{1}{2}|\mathbf{k}+\mathbf{G}|^2 \leq E_{\text{cut}} \tag{2.71}$$

The electron density in Fourier representation is expressed as:

$$n(\mathbf{G}) = \frac{2}{N_{\text{kpt}}} \sum_{j\mathbf{k}} f_{j\mathbf{k}} \sum_{\mathbf{G}'} \left(c^{j\mathbf{k}}_{\mathbf{G}'-\mathbf{G}}\right)^* c^{j\mathbf{k}}_{\mathbf{G}'} \tag{2.72}$$

Electron density being proportional to $|\psi|^2$, corroborates the Fourier components extending twice as far in each direction as those needed for ψ.

The double summation in Equation 2.72 scales as N_G^2, where N_G is the number of **G** vectors that describe the electron density. Hence, the calculations get costly for larger systems. Similarly, the Bloch states in real space (N_R) would scale as N_R^2. Employing the fast Fourier transform (FFT), it is possible to transform from one space to another ($N = N_R = N_G$) in $N \ln N$ operations. Hence, implementing the plane waves with FFT expedites the evaluation of the expressions.

Brillouin zone sampling

Bloch's theorem lets one know the finite number of eigenstates for wave vectors **k** within the first Brillouin zone. The improvement appears minimal on the surface because the computations require precise sampling of the Brillouin zone. However, since $u_{n\mathbf{k}}(\mathbf{r})$ is weakly dependent on **k**, Brillouin zone sampling is sufficient with small finite number of **k**-points [53]. As a result, the discrete sum over the chosen N_{kpt} **k**-point mesh can be used to substitute the integral over the Brillouin zone:

$$\frac{\Omega_c}{(2\pi)^3} \int_{\text{BZ}} \ldots \Theta(E_F - \epsilon_{j\mathbf{k}})\, d\mathbf{k} \quad \rightarrow \quad \frac{1}{N_{\text{kpt}}} \sum_{\mathbf{k}} f_{j\mathbf{k}} \ldots \tag{2.73}$$

where $f_{j\mathbf{k}}$ are occupation numbers which are either one or zero. Among various proposed methods for constructing the **k**-point meshes, we have utilized the Monkhorst-Pack scheme for the Brillouin zone sampling [54, 55, 56]. A dense **k**-point mesh can reduce the error introduced by replacing the integral to a discrete sum over a finite number of **k**-points. Since the Brillouin zone of a larger supercell is smaller, a coarser **k**-point mesh reaches convergence. Typically, a coarser and denser **k**-point mesh is required for the insulators and metals, respectively, to obtain precise Fermi surface sampling.

2.5.5.2 Numeric atom-centered basis functions

The numeric atom-centered orbitals (NAOs) have the form:

$$\phi_i(\mathbf{r}) = \frac{u_i(r)}{r} Y_{lm}(\Omega) \tag{2.74}$$

Here, $u_i(\mathbf{r})$ is numerically tabulated and hence, fully flexible. The $Y_{lm}(\Omega)$ represents the real (m=0,...,l) and imaginary parts (m=l,...,1) of the complex spherical harmonics, where l, m are implicit functions of the radial function index i.

The Schrödinger-like radial equations correspond to:

$$\left[-\frac{1}{2}\frac{d^2}{dr^2} + \frac{l(l+1)}{r^2} + v_i(r) + v_{cut}(r)\right] u_i(r) = \epsilon_i u_i(r) \tag{2.75}$$

Here, the potential $v_i(r)$ characterizes the behaviour of $u_i(r)$ and $v_{cut}(r)$ is the confining potential that facilitates smooth decay of the radial function beyond the confining radius r_{cut}. Tha analytical shape of latter is defined as:

$$v_{cut}(r) = \begin{cases} 0 & \text{for } r \leq r_{onset} \\ s.\exp(\frac{w}{r-r_{onset}}).\frac{1}{(r-r_{cut})^2} & \text{for } r_{onset} \leq r \leq r_{cut} \\ \infty & r \geq r_{cut} \end{cases}$$

Here, s is scaling parameter and $w = r_{cut} - r_{onset}$. On setting $v_i(r)$ to the free atom radial potential v_{at}^{free}, Equation 2.75 can include a minimal basis consisting of core and valence functions of spherically symmetric free atoms. This minimum basis naturally considers wave function oscillations close to the nucleus, thereby facilitating the all-electron treatment. Another aspect of these basis sets is the hierarchy between successive basis sets for the same element, with a larger basis set containing all smaller ones. This assures that the total energy convergence is strictly variational.

2.5.5.3 Pseudopotentials

The determination of Kohn-Sham wave functions for N electrons makes the solution computationally challenging. A significant number of plane waves are also necessary to account for the rapidly oscillating valence electron wave functions in the core region and expand the tightly confined core orbitals. A large number of plane-wave basis sets requires considerable computational time for all-electron calculations. Hence, the pseudopotentials are advantageous for

lesser plane-wave basis sets compared to the previous [57]. Most of a solid's physical properties depend on the valence electrons rather than the core electrons. Hence, the pseudopotentials are constructed by replacing the core electrons and strong ionic potential with a weaker pseudopotential. The calculations, thus, are based on the corresponding pseudo wave functions and not on the true valence wave functions. The illustration of the concept is given in Fig. 2.5. The Pauli exclusion principle requires the orthogonality between the core wave functions and the valence wave functions, which is maintained by the rapid oscillations of valence wave functions in the core electrons region. The strong ionic potential in the region occupied by core electrons leads to rapid valence wave function oscillations. As per the Pauli exclusion principle, these oscillations preserve the orthogonality between the core and valence wave functions. Inside the core region (specified by a cutoff radius, r_c), the pseudo wave functions are smooth and nodeless, and outside the core region, they coincide with those of an all-electron calculation (Fig. 2.5). The large r_c corresponds to the softer pseudopotentials requiring a lesser plane-wave basis set for convergence. However, the transferability of these soft pseudopotentials is less. Transferability corresponds to reproducing the valence properties in varied chemical environments. An advantage of pseudopotentials lies in the simultaneous inclusion of relativistic effects with the non-relativistic valence electron treatment.

2.5.5.4 Norm-conserving pseudopotentials

The norm-conserving pseudopotentials are the energy-independent pseudopotentials introduced by Hamann, Schlüter, and Chiang [27, 58] in 1979. These are defined by following properties:

1. The all-electron (AE) and pseudo (PS) valence eigenvalues agree for an atomic configuration.

$$\epsilon_{nl}^{\mathrm{AE}} = \epsilon_{nl}^{\mathrm{PS}} \tag{2.76}$$

   Here, n is the principal quantum number and l is the angular momentum quantum number.

2. The corresponding wave functions are equal for $r \geq r_c$, where r_c is the core radius.

$$\psi_{nl}^{\mathrm{AE}}(r) = \psi_{nl}^{\mathrm{PS}}(r) \tag{2.77}$$

3. Norm conservation: The integrals of AE and PS charge densities are equal for each valence state.

$$\int_0^{r_c} |\phi_{nl}^{\mathrm{AE}}|^2 r^2 dr = \int_0^{r_c} |\phi_{nl}^{\mathrm{PS}}|^2 r^2 dr \tag{2.78}$$

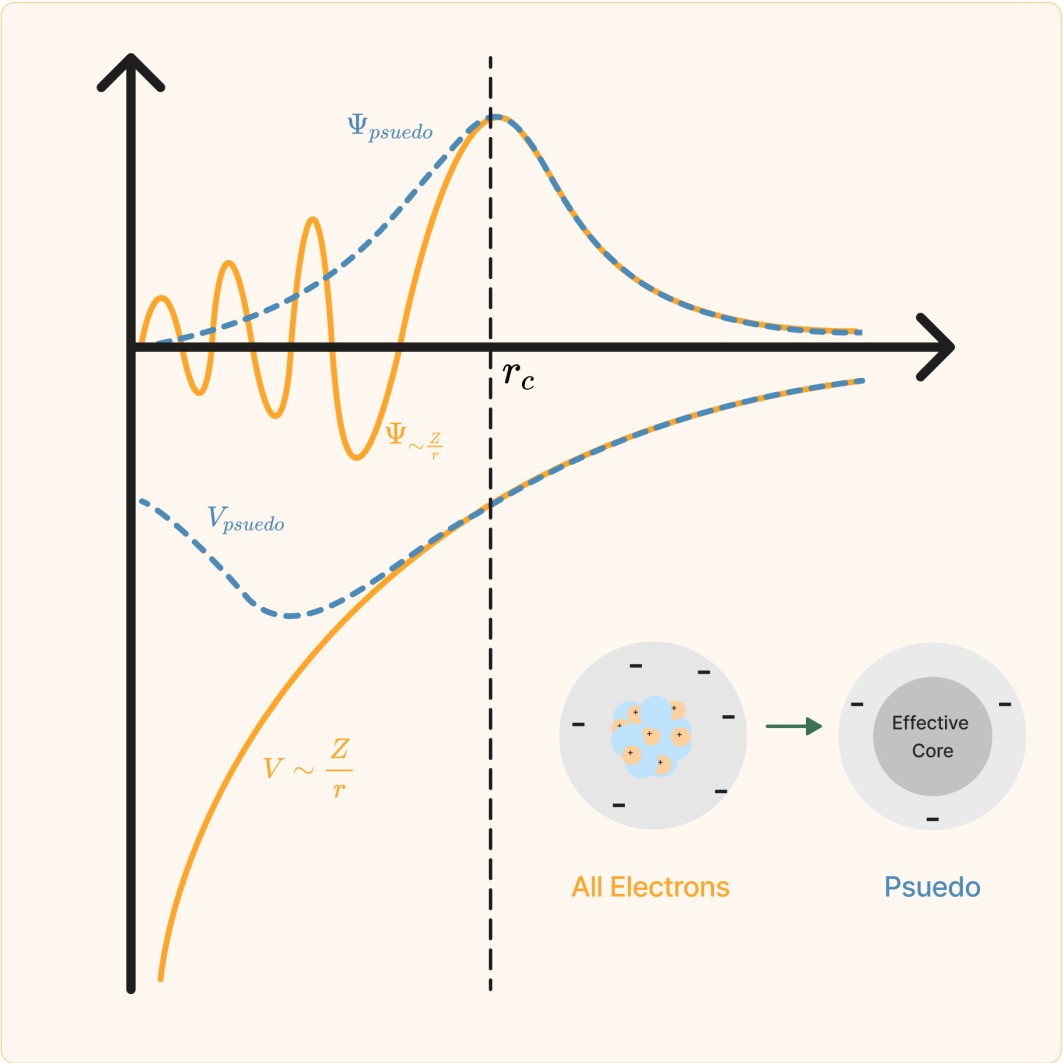

Figure 2.5: Schematic representation of external Coulomb potential, all-electron wave function, pseudopotential and pseudo wave function.

Here, $\phi_{nl}(r)$ correspond to the radial part of the wave function. The condition ensures the identical electrostatic potential for AE and PS charge distributions (Gauss's theorem).

4. The logarithmic derivatives of the wavefunctions and their the first energy derivatives are equal at r_c.

$$\left[\left(r\phi_{nl}^{\mathrm{AE}}(r)\right)^2 \frac{d}{d\epsilon}\frac{d}{dr}\ln\phi_{nl}^{\mathrm{AE}}(r)\right]_{r_c} = \left[\left(r\phi_{nl}^{\mathrm{PS}}(r)\right)^2 \frac{d}{d\epsilon}\frac{d}{dr}\ln\phi_{nl}^{\mathrm{PS}}(r)\right]_{r_c} \tag{2.79}$$

The condition corroborates with the scattering properties of ion cores are reproducible with the minimum error. This is also referred to as the conservation of scattering properties that is obtained from the energy vs. logarithmic derivative curve [59].

Points 1 and 2 extract the pseudopotential conditions. Points 3 and 4 are this approach's crucial

points that account for the transferability among various chemical environments. The process of generating norm-conserving pseudopotential initiates with all-electron atomic calculations. Subsequently, the corresponding pseudopotentials are generated with the identification of core and valence states. The pseudopotential is then unscreened by subtracting Hartree and exchange-correlation potentials from the total potential. The pseudopotential constitutes the local (l-independent) part and the non-local terms. Further, the condition of norm-conservation does not necessitate having one best pseudopotential. In fact, freedom lies in the generation of pseudopotentials based on the following two factors

- Accuracy and transferability leads to the choice of smaller r_c and hard potentials.
- Smoothness leads to the choice of larger r_c and soft potentials.

2.5.5.5 Vanderbilt Ultrasoft pseudopotentials

Limitations in norm-conserving pseudopotentials is due to the difficulty of expressing the pseudo wave function in the plane wave basis set. Hence, its applicability to systems with highly localised valence orbitals, such as $2p$ and $3d$ is restricted. In case of ultrasoft pseudopotentials, the norm-conserving requirement is relaxed and fewer plane waves are needed. The ultrasoft pseudopotential are entirely nonlocal by construction and turn local outside the core [60]. Its transferability is enhanced by the nonlocal ultrasoft peudopotential's self-consistent dependence on the charge density. The smoothness of pseudo wave function can be optimized as the norm-conserving condition is lifted. The pseudo wave function is categorized into two parts:

1. Ultrasoft valence wave function: This violates the norm conservation constraint and significantly lowers the plane wave cutoff energy.

2. The core augmentation charge: This corresponds to the charge deficit in the core region and hence, adds new terms to the Kohn-Sham formalism, thereby complicating the situation and increasing the number of operations required for each computational cycle.

2.5.5.6 Projector augmented-wave (PAW) method

Generalization of pseudopotential and linear augmented plane wave (LAPW) approaches constitute the projector augmented-wave (PAW) method [61, 62]. Blöchl devised the formalism in 1994, where the method directly works on the core and valence wave functions [63]. The

central idea behind the approach is mapping all-electron wave functions onto the pseudo wave functions. Note that the former oscillates in the core region and behaves smoothly beyond a distance. Here the all-electron wave function corresponds to the one-electron Kohn-Sham wave function. Let us consider the Kohn-Sham all-electron wave function $|\phi_s\rangle$, pseudo wave function $|\tilde{\phi}_s^0\rangle$, and linear transformation $\hat{T}$. We have,

$$|\phi_s^0\rangle = \hat{T}|\tilde{\phi}_s^0\rangle \tag{2.80}$$

Now, the linear transformation can be written in terms of atom-centered contributions $\hat{T}^a$ as:

$$\hat{T} = 1 + \sum_a \hat{T}^a \tag{2.81}$$

$\hat{T}^a$ acts in the augmentation region Ω_a enclosing the nuclei and marked out by the cutoff radius r_c^a. The choice of r_c^a should ensure non-overlap of augmentation spheres and beyond Ω_a, $|\tilde{\phi}_s^0\rangle$ should coincide $|\phi_s\rangle$. This augmentation region corresponds to the core region in the pseudopotential method [64].

Considering the all-electron (φ_j^a) and pseudo ($\tilde{\varphi}_j^a$) partial waves, the transformation operator is given by:

$$\hat{T} = 1 + \sum_a \sum_j \left(|\varphi_j^a\rangle - |\tilde{\varphi}_j^a\rangle\right) \langle\tilde{p}_j^a| \tag{2.82}$$

where $|\tilde{p}_j^a\rangle$ are set of projector functions. These projector functions are localized within Ω_a and obey orthonormalization to pseudo partial waves. These probe the wavefunction character such as s, p, and d types. We thus obtain,

$$|\phi_s^0\rangle = |\tilde{\phi}_s^0\rangle + \sum_a \sum_j \left(|\varphi_j^a\rangle - |\tilde{\varphi}_j^a\rangle\right) \langle\tilde{p}_j^a|\tilde{\phi}_s^0\rangle \tag{2.83}$$

The $|\tilde{\phi}_s^0\rangle$ is the variational object that can be expanded using plane waves basis set. In calculations, low energy cutoff can be utilized due to the smoothness. Now, the following conditions pertaning to the all-electron and pseudo wave functions must hold.

(1) Inside the augmentation region

$$\begin{aligned} \phi_s^0(\mathbf{r}) &= \phi_s^a(\mathbf{r}) \\ \tilde{\phi}_s^0(\mathbf{r}) &= \tilde{\phi}_s^a(\mathbf{r}) \end{aligned} \tag{2.84}$$

(2) Outside the augmentation region

$$\begin{aligned} \phi_s^0(\mathbf{r}) &= \tilde{\phi}_s^0(\mathbf{r}) \\ \phi_s^a(\mathbf{r}) &= \tilde{\phi}_s^a(\mathbf{r}) \end{aligned} \tag{2.85}$$

Further, $\phi_s^a(\mathbf{r})$ and $\tilde{\phi}_s^a(\mathbf{r})$ can be expanded with the finite set of local basis functions:

$$\begin{aligned}\phi_s^a(\mathbf{r}) &= \sum_j \varphi_j^a(\mathbf{r})\langle\tilde{p}_j^a|\tilde{\phi}_s^0\rangle \\ \tilde{\phi}_s^a(\mathbf{r}) &= \sum_j \tilde{\varphi}_j^a(\mathbf{r})\langle\tilde{p}_j^a|\tilde{\phi}_s^0\rangle\end{aligned} \tag{2.86}$$

In this thesis, we have employed PAW method under the electronic structure calculations executed by the VASP.

2.5.6 Geometry optimization

The arrangement of atoms in the ground state is its equilibrium configuration, and geometry optimization is performed on the system to obtain the same. The system reaches its minimum energy configuration when the forces per atom is zero or numerically converge within a given value. The atomic motion is driven by the Hellmann-Feynman forces as discussed in the Hellmann-Feynman theorem [65]. As per the theorem, force acting on I-th atom is:

$$\mathbf{F}_I = -\frac{\partial E}{\partial \mathbf{R}_I} \tag{2.87}$$

where $E = \langle\Psi|H|\Psi\rangle$ is the total energy of the system, with the assumption of wave function being normalized ($\langle\Psi|\Psi\rangle = 1$). Hence, we have:

$$\mathbf{F}_I = -\langle\Psi|\frac{\partial H}{\partial \mathbf{R}_I}|\Psi\rangle - \langle\frac{\partial \Psi}{\partial \mathbf{R}_I}|H|\Psi\rangle - \langle\Psi|H|\frac{\partial \Psi}{\partial \mathbf{R}_I}\rangle \tag{2.88}$$

Further, with $|\Psi\rangle$ as an eigenstate of H, we get

$$\begin{aligned}\mathbf{F}_I &= -\langle\Psi|\frac{\partial H}{\partial \mathbf{R}_I}|\Psi\rangle - E\frac{\partial}{\partial \mathbf{R}_I}\langle\Psi|\Psi\rangle \\ &= -\langle\Psi|\frac{\partial H}{\partial \mathbf{R}_I}|\Psi\rangle\end{aligned} \tag{2.89}$$

Now considering the energy expression:

$$E = \langle\hat{T}\rangle + \langle\hat{V}_{int}\rangle + \int d^3r V_{ext}(\mathbf{r})n(\mathbf{r}) + E_{II} \tag{2.90}$$

where $V_{ext}\,(\mathbf{r})$ is the external potential and E_{II} is the nuclei-nuclei interaction, the corresponding force is given as:

$$\mathbf{F}_I = -\int d\mathbf{r}\, n\,(\mathbf{r})\,\frac{\partial V_{ext}\,(\mathbf{r})}{\partial \mathbf{R}_I} - \frac{\partial E_{II}}{\partial \mathbf{R}_I} \tag{2.91}$$

As per the electrostatic theorem of Feynman, the expression (Equation 2.91) essentially equates to the nuclear charge times the electric field caused by the electrons. Hence, in the force

theorem the terms corresponding to the kinetic energy and internal interaction variation with nuclei motion cancel. Further, the basis set dependence on the nuclei position gives rise to the Pulay forces, and this should be corrected to avoid any further errors. The forces pertaining to the non-local potentials, such as pseudopotentials, cannot be fully represented in terms of electron density. Direct derivation of any subsequent expression from the Equation 2.91 is possible. For instance, considering electron density motion in the core region is more physical than considering it to be fixed. So the crucial point is that the change in $V_{ext}\left(\mathbf{r}\right)$ and $n(\mathbf{r})$ do not change the force, but the corresponding change in expression would improve the accuracy and physical interpretation.

2.6 *Ab initio* atomistic thermodynamics

The *ab initio* atomistic thermodynamics is primarily used as a pathway between the microscopic and macroscopic regimes. In the microscopic realm, DFT performs the calculations at zero temperature and zero pressure. The DFT can be used to calculate the potential energy surface (PES), where $E(\mathbf{R}_I)$ represents the atomic configuration. The influence of finite temperature and pressure are taken into account in the *ab initio* atomistic thermodynamics approach by computing appropriate thermodynamic potential functions using the PES, such as the Gibbs free energy. Therefore, one can derive the macroscopic system properties by integrating DFT calculations with thermodynamics. The approach can be extended to the larger systems, thereby dividing into smaller subsystems that are in thermal equilibrium with one another.

2.6.1 Thermodynamic potentials

Thermodynamic potentials represent the state of a system, as a function of natural variables i.e., temperature (T), pressure (p), entropy (S) and volume (V). There are four thermodynamic potentials that characterizes the system: (i) Internal energy U, (ii) enthalpy $H = U + pV$, (iii) Helmholtz free energy $F = U - TS$, and (iv) Gibbs free energy $G = U + pV - TS = H - TS = F + pV$. System with constant T and V, is charcterized by the Helmholtz free energy, whereas that with constant T and p is characterized by Gibbs free energy. Energies obtained from the DFT calculations can be analyzed through Gibbs free energy for the equilibrium states.

2.6.2 Defect formation energy

The presence of defects alter the free energy of a system. These defects can be either native or engineered intentionally as per the environmental conditions. The thermodynamic stability of a defect configuration w.r.t pristine is analyzed by calculating the free energy of formation as follows [66]

$$\mathrm{E_f}(T,p) = \mathrm{E}^{(q)}_{\mathrm{defect}} - \mathrm{E}^{(0)}_{\mathrm{pristine}} \pm \sum \mathrm{N_i}\mu_{\mathrm{i}}(T,p) + q(\mu_{\mathrm{e}}) \tag{2.92}$$

where $\mathrm{E}^{(q)}_{\mathrm{defect}}$ and $\mathrm{E}^{(0)}_{\mathrm{pristine}}$ represent the total energies of the system with and without defect, respectively. These total energies are determined from the DFT calculations. q is the charge state and N_i is the number of atoms of a species i added/removed from the system. $\mu_i(T,p)$ is the corresponding chemical potential of species i as a function of temperature T and partial pressure p and μ_e is the chemical potential of electron that is obtained w.r.t the valence band maximum (VBM) of the host.

2.6.3 Chemical potentials

The atomic chemical potentials in Equation 2.92, is a function of temperature and partial pressure. Hence, varying the chemical potentials can capture the different experimental conditions. These are subject to bounds as chemical potentials represent the reservoir of atoms innvolved in defect creation.

Let us consider S vacancy in MoS_2 monolayer for explaining the concept. Hence, the chemical potential of S, $\mu_{\mathrm{S}}(T,p)$ has to be accounted. This is determined under the ideal gas approximation, thereby treating ideal gas composed of N indistinguishable S_2 molecules. $\mu_{\mathrm{S}}(T,p)$ is given by

$$\mu_{\mathrm{S}}(T,p) = \frac{1}{2}\mu_{\mathrm{S_2}} = \frac{1}{2}\left[\mathrm{E_{S_2}} + \mathrm{E}^{vib}_{\mathrm{S_2}}(0K) + \Delta H(T,p^0) - T\Delta S(T,p^0) + k_B T ln(\frac{p_{S2}}{p^0})\right] \tag{2.93}$$

where k_{B} is the Boltzmann constant. The change in enthalpy ($\Delta H(T,p^0)$) and change in entropy ($\Delta S(T,p^0)$) are obtained from the thermodynamic tables. The partition function of an ideal S_2 gas, considers the translational, rotational, vibrational, electronic and configurational degrees of freedom [67].

$$F(T) = F^{translational}(T) + F^{rotational}(T) + F^{vibrational}(T) + F^{symmetry}(T) + F^{spin}(T) + E^{DFT} \tag{2.94}$$

The individual energy terms are given by

$$\begin{aligned} F^{translational} &= -\frac{3}{2}k_{\mathrm{B}}T\ln\left[\left(\frac{2\pi m k_{\mathrm{B}}T}{h^2}\right)\right] \\ F^{rotational} &= -k_{\mathrm{B}}T\ln\left[8\pi^2\left(\frac{2\pi k_{\mathrm{B}}T}{\sigma h^2}\right)^{\frac{3}{2}}\right] \\ F^{vibrational} &= \sum_{i=1}^{M}\left[\frac{\hbar\omega_i}{2}+k_{\mathrm{B}}T\ln\left(1-\exp\left(-\frac{\hbar\omega_i}{k_{\mathrm{B}}T}\right)\right)\right] \\ F^{symmetry} &= k_{\mathrm{B}}T\ln\sigma \\ F^{spin} &= -k_{\mathrm{B}}T\ln\mathcal{M} \end{aligned} \tag{2.95}$$

Here, m is the mass and I is the moment of inertia of the molecule. σ represents the symmetry number of the molecule, that corresponds to the number of indistinguishable orientations of the molecule (homonuclear diatomic molecules: $\sigma = 2$ and hetronuclear diatomic molecules: $\sigma = 1$). In Equation 2.95, the vibrational term is obtained under the harmonic approximation. M is the number of the vibrational modes of the molecule with corresponding frequencies ω_i. E^{DFT} is the ground-state energy of the S_2 molecule as per DFT calculations. $\mathcal{M}$ is the electronic spin degeneracy of the ground state. Hence, the chemical potential of S is obtained as:

$$\begin{aligned} \mu_{\mathrm{S}_2}(T,p_{\mathrm{S}_2}) = &-\mathrm{k_B}T\ln\left[\left(\frac{2\pi\mathrm{m}}{\mathrm{h}^2}\right)^{\frac{3}{2}}(\mathrm{k_B}T)^{\frac{5}{2}}\right]+\mathrm{k_B}T\ln p_{\mathrm{S}_2} \\ &-\mathrm{k_B}T\ln\left(\frac{8\pi^2\mathrm{I_A}\mathrm{k_B}T}{\mathrm{h}^2}\right)+\mathrm{k_B}T\ln\left[1-\exp\left(-\frac{\mathrm{h}\nu_{\mathrm{SS}}}{\mathrm{k_B}T}\right)\right] \\ &-\mathrm{k_B}T\ln\mathcal{M}+\mathrm{k_B}T\ln\sigma \end{aligned} \tag{2.96}$$

2.7 Many-body perturbation theory (MBPT): Green's function methods

DFT determines the ground state properties of the many-body system. In the previous section, we have understood the association of the Kohn-Sham equation with the single-particle eigenvalues that, simply being a mathematical tool, do not corroborate the excitation energies. Hence, predicting excited state properties (e.g., band gap, optical absorption) is not plausible via DFT [68, 69]. Alternatively, an extension to DFT is the time-dependent DFT (TDDFT) method to ascertain excitations in the system [70]. However, TDDFT faces two significant

challenges, i.e., underestimation of band gap and excitonic effects. These are associated with adiabatic approximation and semilocal xc kernels that are self-consistently derived. Research to derive inexpensive TDDFT methodology is an ongoing issue. The MBPT, thus, remains standard for calculating the excited state properties of the system and is often referred to as beyond DFT approaches [71]. Green's function is primary in the formalism of MBPT methods. The single-particle Green's function (GW approximation) and the two-particle Green's function (Bethe-Salpeter Equation), formulates charged and neutral excitations, respectively.

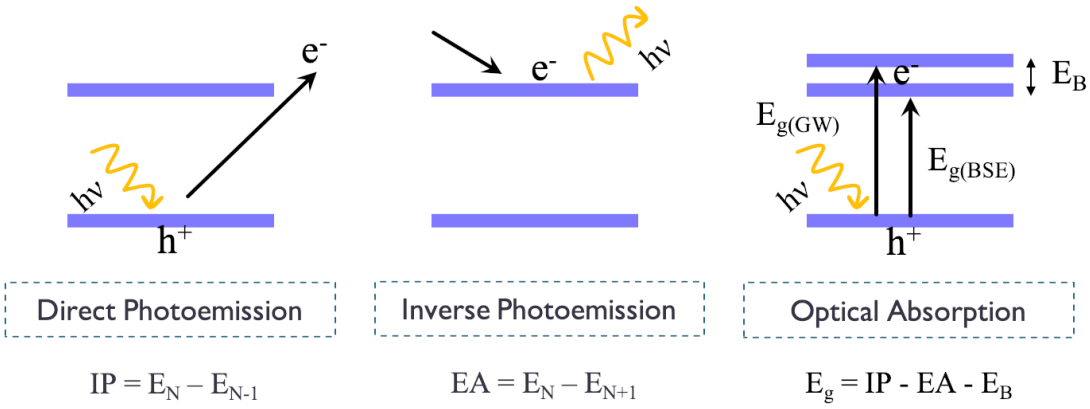

Figure 2.6: Schematic for excited-state spectroscopies viz. direct photoemission, inverse photoemission, and optical absorption.

Spectroscopies experimentally probe the material to measure excited-state properties. The charged excitations corroborate the direct and inverse photoemission spectroscopies. The former ejects an electron on an interaction with the photon (occupied states probed), whereas, in the latter case electron is injected, and the photon is emitted (unoccupied states probed). Therefore, one can calculate ionization potential (IP) from electronic systems with N and N-1 electrons in direct photoemission. Similarly, electron affinity (EA) is determined by the total energy difference between the N and the N+1 electron systems in inverse photoemission. Since excitations of a single charged particle are being studied, single-particle Green's function method is theoretically employed. When we analyze neutral excitations, optical absorption is the corresponding process where an electron is excited to the conduction band from the valence band upon absorption of a photon. The electron and hole pair, thus generated, are in a bound state and cannot be handled independently. The two-particle Green's function method provides a theoretically sound description of the same.

2.7.1 Green's function

If $h\nu$ is the energy of photon, K.E is the kinetic energy of the emitted electrons and E(k) is the excitation spectrum of the system, the expression as per energy and momentum conservation is:

$$h\nu = \text{K.E} + \text{E(k)} \tag{2.97}$$

For direct photoemission ($\epsilon_s < \text{E}_{\text{Fermi}}$: bound state)

$$\text{IP} = -\epsilon_s = h\nu - \text{K.E} - \text{E(k)} \tag{2.98}$$

For inverse photoemission ($\epsilon_s \geq \text{E}_{\text{Fermi}}$: unoccupied state)

$$-\text{EA} = -\epsilon_s = h\nu - \text{K.E} - \text{E(k)} \tag{2.99}$$

Here, E_{Fermi} is the Fermi level. The measured photocurrent during spectroscopy is theoretically represented by the spectral function where ω is the energy (frequency)

$$A(\mathbf{r}, \mathbf{r}', \omega) = \frac{1}{\pi}\text{Im } G(\mathbf{r}, \mathbf{r}', \omega)\text{sgn}(\text{E}_{\text{Fermi}} - \omega) \tag{2.100}$$

The single-particle Green's function contains the data of excitation lifetime and energies. It is expressed as:

$$\begin{aligned} G\left(\mathbf{r}t, \mathbf{r}'t'\right) = &- i\langle\Psi_0^N|\hat{\psi}(\mathbf{r}t)\hat{\psi}^\dagger(\mathbf{r}'t')|\Psi_0^N\rangle\Theta(t-t') \\ &+ i\langle\Psi_0^N|\hat{\psi}^\dagger(\mathbf{r}'t')\hat{\psi}(\mathbf{r}t)|\Psi_0^N\rangle\Theta(t'-t) \end{aligned} \tag{2.101}$$

where

$$\Theta(t-t') = \begin{cases} 1 & \text{if } t > t' \\ 0 & \text{if } t < t' \end{cases}$$

The N-electron ground state is $|\Psi_0^N\rangle$. The field operators $\hat{\psi}^\dagger(\mathbf{r}'t')$ and $\hat{\psi}(\mathbf{r}t)$ describes the creation of electron at time t' (and position $\mathbf{r}'$) and annihilation at time t (and position $\mathbf{r}$), respectively. Hence, the Green's function acts as a propagator.

Now, as previously discussed the excitation energies (ϵ_s) and the transition amplitudes ($(\psi_s(\mathbf{r}))$) from N to N $\pm$ 1 electron system are:

$$\epsilon_s = \begin{cases} E_N - E_{N-1} & \text{for } \epsilon_s < \text{E}_{\text{Fermi}} \\ E_{N+1} - E_N & \text{for } \epsilon_s \geq \text{E}_{\text{Fermi}} \end{cases}$$

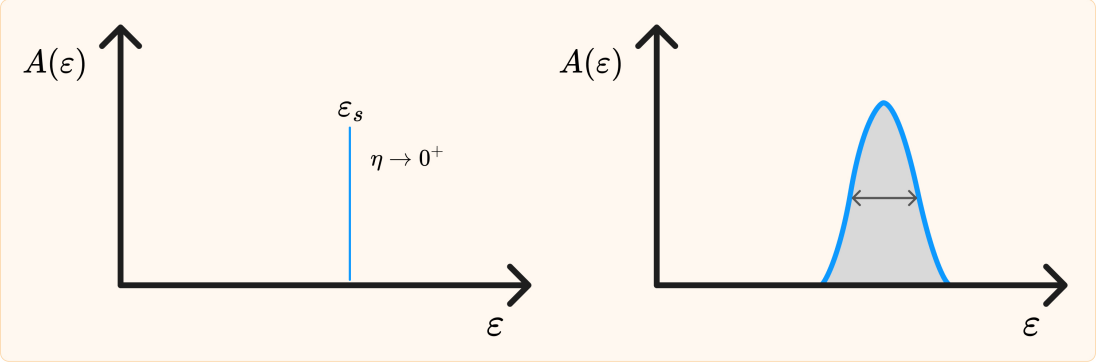

Figure 2.7: Spectral function for electronic excitation (non-interacting) and QP excitation (interacting).

$$\psi_s(\mathbf{r}) = \begin{cases} \langle \Psi_s^{N-1} | \hat{\psi}(\mathbf{r}) | \Psi_0^N \rangle & \text{for } \epsilon_s < \mathrm{E_{Fermi}} \\ \langle \Psi_0^N | \hat{\psi}(\mathbf{r}) | \Psi_s^{N+1} \rangle & \text{for } \epsilon_s \geq \mathrm{E_{Fermi}} \end{cases}$$

The spectral representation of Green's function (Lehman representation) exemplifies the poles of Green's function to corroborate with addition/removal of an electron.

$$G(\mathbf{r}, \mathbf{r}', \omega) = \lim_{\eta \to 0^+} \sum_s \psi_s(\mathbf{r}) \psi_s^*(\mathbf{r}') \times \left[\frac{\Theta(\epsilon_s - \mathrm{E_{Fermi}})}{\omega - (\epsilon_s - i\eta)} + \frac{\Theta(\mathrm{E_{Fermi}} - \epsilon_s)}{\omega - (\epsilon_s + i\eta)} \right] \tag{2.102}$$

The particle lifetime for non-interacting electrons is infinite. Each transition is represented by the delta peaks in the spectral function (Fig. 2.7). On the other hand, a single-particle-like excitation (quasiparticle-QP) corresponds to the experimentally observed finite width at the peak point (Fig. 2.7), that is, further attributed to the combination of many closely spaced delta peaks. In addition, a satellite peak is also detected with a broad peak of minor intensity. Therefore, in summary, a QP sharp peak and a satellite peak are the features of the spectral function. We can obtain excitation lifetime and spectral weight corresponding to the QP from the spectral function, which can also be expressed as:

$$A \approx \frac{1}{\pi} \left| \frac{Z_s}{\omega - (\epsilon_s + i\Gamma)} \right| \tag{2.103}$$

Here, Z_s and Γ is the QP weight and peak width, respectively. When a charged particle is screened, the particle and the polarization cloud constitute the QP. For instance, electron ejection would result in a hole followed by the electrons dynamically screening the hole. This hole, along with electrons screening the same, is a QP. This engenders particle interaction with the self, hence, termed self-energy.

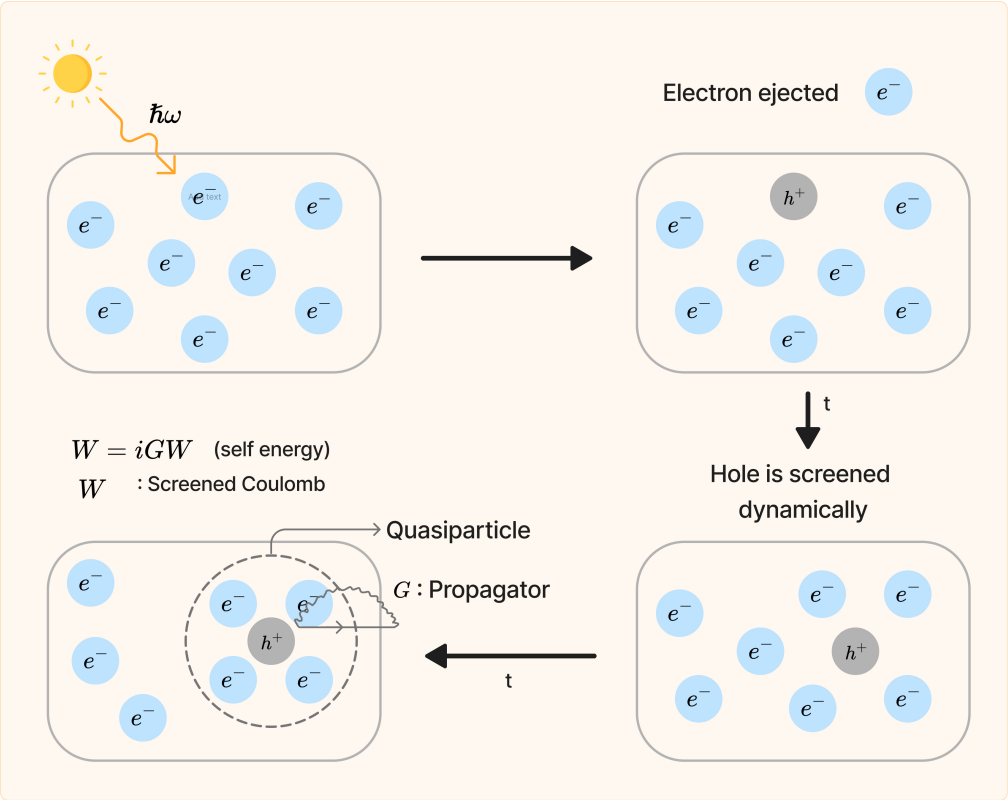

Figure 2.8: The quasiparticle concept

2.7.2 Dyson's and Hedin's equations

The exact Green's function contains the interacting and non-interacting terms, where DFT evaluates the latter. Dyson's equation relates the self energy (Σ) to the Green's function as:

$$G(\mathbf{r},\mathbf{r}',\omega) = G_0(\mathbf{r},\mathbf{r}',\omega) + \int\int G_0(\mathbf{r},\mathbf{r}'',\omega)\Sigma(\mathbf{r}'',\mathbf{r}''',\omega)G(\mathbf{r}''',\mathbf{r}',\omega)d\mathbf{r}''d\mathbf{r}''' \tag{2.104}$$

where $G_0(\mathbf{r},\mathbf{r}',\omega)$ is as determined by Equation 2.102. The Σ is non-Hermitian and depends on energy (frequency). The exchange and correlation effects are incorporated in the self-energy term. This equation is extremely important in many-body physics and associates with the QP equation (i.e., single-particle eigenvalue problem). The effective single-particle reformulation is:

$$\hat{h}_0(\mathbf{r})\psi_s(\mathbf{r}) + \int \Sigma(\mathbf{r},\mathbf{r}',\epsilon_s)\psi_s(\mathbf{r}')d\mathbf{r}' = \epsilon_s\psi_s(\mathbf{r}) \tag{2.105}$$

The orthonormality of wave functions $\psi_s(\mathbf{r})$, which forms a complete set, is not satisfied due to Σ being energy dependent.

In algebraic form the Dyson's equation is:

$$\begin{aligned} G &= G_0 + G_0\Sigma G_0 + G_0\Sigma G_0\Sigma G_0 + ... \\ G &= G_0 + G_0\Sigma G \end{aligned} \tag{2.106}$$

The multiple instantaneous scattering processes during excitations are incorporated in Dyson's equation (refer Equation 2.106). The self-energy is the total of all single scattering processes. Now, a system experiences infinite scattering events during the excitation process, and it is challenging to consider every such process to calculate the self-energy. Hence, approximations are required to calculate the same.

2.7.2.1 Hedin's equation

To evaluate the Green function and the self-energy, Lars Hedin published a set of equations in 1965 that are self-consistent and are known as Hedin's equations[72]. Hedin's equations approach the many-body issue with quantities such as screened Coulomb interaction W. The quantities (polarizability (P), W, Σ and vertex function (Γ)) defined in Equation 2.107 are the mathematical tools for self-consistent evaluation of G and Σ.

$$\begin{aligned} G(1,2) &= G_0(1,2) + \int d(3,4)G_0(1,3)\Sigma(3,4)G(4,2) \\ P(1,2) &= -i\int d(3,4)G(2,3)G(4,2^+)\Gamma(3,4;1) \\ W(1,2) &= v(1,2) + \int d(3,4)W(1,3)P(3,4)v(4,2) \\ \Sigma(1,2) &= i\int d(3,4)G(1,4)W(1^+,3)\Gamma(4,2;3) \\ \Gamma(1,2;3) &= \delta(1,2)\delta(1,3) + \int d(4,5,6,7)\frac{\delta\Sigma(1,2)}{\delta G(4,5)}G(4,6)G(7,5)\Gamma(6,7;3) \end{aligned} \tag{2.107}$$

Here, $1 = (\mathbf{r}_1, t_1)$, $1^+ = (\mathbf{r}_1, t_1 + \eta)$ (η is positive infinitesimal) and v is the bare Coulomb interaction. Among the aforementioned equations, the vertex function consists of the functional derivative of self-energy and is challenging to compute. The approximations, thus, employed in Hedin's equations are as follows:

- Hartree approximation ($\Sigma = 0$): This approximation does not ascribe Pauli exclusion principle for exchange interactions.
- Hartree-Fock approximation: This approximation negates the polarization ($P = 0$), equates W to the bare interaction ($W(1,2) = v(1,2)$) and constrains the vertex function to the zeroth order component

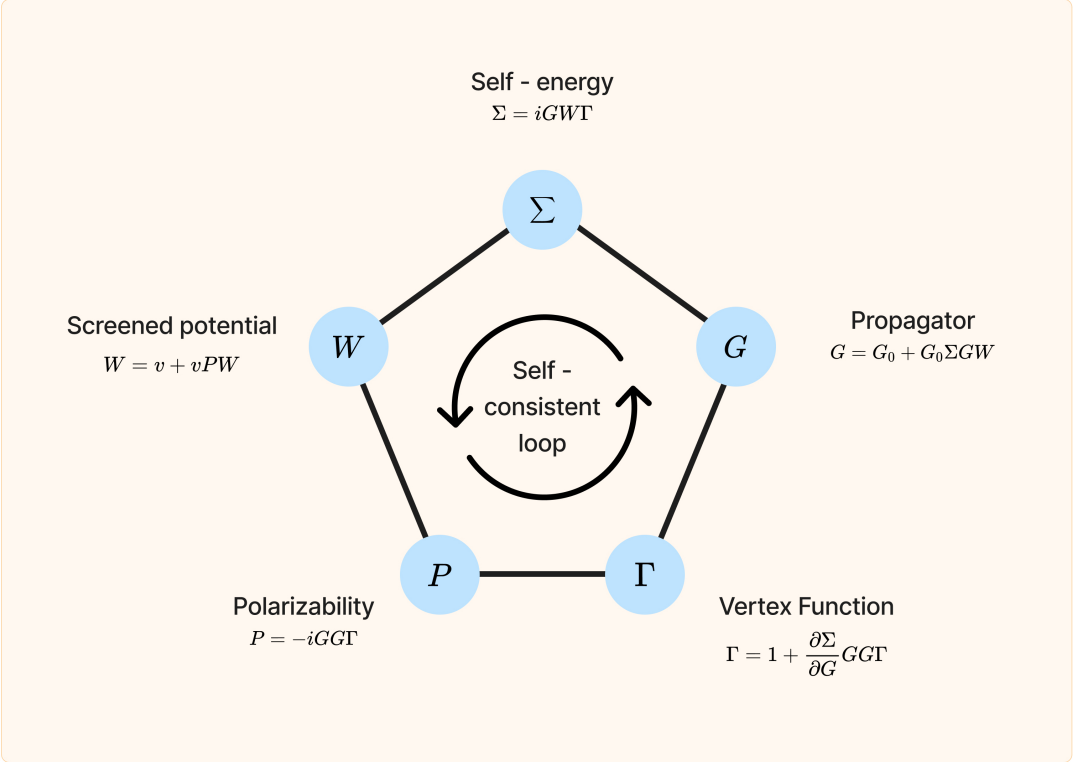

Figure 2.9: The Hedin's pentagon

- GW approximation: Now, incorporating the screening between the electrons by replacing the $v(1,2)$ to W at first order the self-energy equates as product of G and W. Hence, the name GW approximation.

Therefore, now the Hedin's equations reduce to:

$$\begin{aligned} \Gamma(1,2;3) &= \delta(1,2)\delta(1,3) \\ P(1,2) &= -iG(1,2^+)G(2,1) \\ \Sigma(1,2) &= iG(1,2)W(1^+,2) \end{aligned} \tag{2.108}$$

2.7.3 Implementation of G_0W_0

The complexity of the self-consistent Hedin's equations in computation has led to the treatment of Γ and Green's function in a non-self-consistent approach (G_0W_0 approach). The implementation of the G_0W_0 approach is discussed herein (Fig. 2.10). The G_0W_0 is referred as single-shot GW as only one GW iteration is executed. The calculation is initiated on top of Kohn-Sham eigenvalues (ϵ_s^{KS}) and eigenstates (ϕ_s^{KS}) from the DFT calculation. Thereafter, the Kohn-Sham Green's function is set with subsequent calculations of polarizability (P), Dielec-

tric function, W and Σ for solving the QP equation. The corresponding flow chart is shown in Fig. 2.10, where Σ_s^x is the exchange part of self-energy and is directly obtained from DFT. The corresponding eigenvalues of the QP equation are complex. The real part and imaginary part corresponds to the QP energy (ϵ_s^{QP}) and the QP lifetime, respectively. Analogous to the Kohn-Sham equation, here, the difference between the exchange-correlation potential and the self-energy operator is treated as a perturbation to update the QP energies:

$$\epsilon_i^{QP} = \epsilon_i^{\mathrm{KS}} + \langle \psi_i^{\mathrm{KS}} | \Sigma(\epsilon_i^{\mathrm{QP}}) - V_{xc} | \psi_i^{\mathrm{KS}} \rangle \tag{2.109}$$

The Taylor series expansion of self-energy around ϵ_s^{KS} linearizes the same along with the assumption of a minute difference between the ϵ_s^{KS} and ϵ_s^{QP}. The approach is executed as the energy dependence of Σ is unknown.

$$\Sigma(\epsilon_s^{\mathrm{QP}}) \approx \Sigma(\epsilon_s^{\mathrm{KS}}) + (\epsilon_s^{\mathrm{QP}} - \epsilon_s^{\mathrm{KS}}) \frac{\partial \Sigma(\epsilon)}{\partial \epsilon}\bigg|_{\epsilon=\epsilon_s^{\mathrm{KS}}} \tag{2.110}$$

QP energies correspond to:

$$\epsilon_i^{QP} = \epsilon_i^{\mathrm{KS}} + Z_i \langle \psi_i^{\mathrm{KS}} | \Sigma(\epsilon_i^{\mathrm{KS}}) - V_{xc} | \psi_i^{\mathrm{KS}} \rangle \tag{2.111}$$

where Z_i is the renormalization factor given as:

$$Z_i = \left(1 - \langle \psi_i^{\mathrm{KS}} | \frac{\partial \Sigma(\epsilon)}{\partial \epsilon}\bigg|_{\epsilon=\epsilon_s^{\mathrm{KS}}} | \psi_i^{\mathrm{KS}} \rangle \right)^{-1} \tag{2.112}$$

As previously seen, the method initiates with the DFT (LDA/PBE/HSE06) and the corresponding xc-functional are chosen carefully, since the QP energies depend on it. The G_0W_0 band gap is often in sync with the experimental measurements [73, 74]. Moreover, in principle a self-consistent GW (scGW) approach can be implemented, however imposing the same in absence of vertex correction severely affects the corroboration with the experiments [75, 76]. In the present work, we have used the single-shot GW.

2.7.4 Bethe-Salpeter equation (BSE)

In neutral, electron-hole (e^- - h^+) excitations (e.g., optical absorption, electron energy loss), the total number of electrons in the system remains unchanged. These excitations are represented by the two-particle Green's function, i.e., the Bethe-Salpeter equation (BSE) [77, 78] (Equation 2.113).

$$L(1,2,1',2') = L_0(1,2,1',2') + \int d(3,4,5,6) L_0(1,4,1',3) K(3,5,4,6) L(6,2,5,2') \tag{2.113}$$

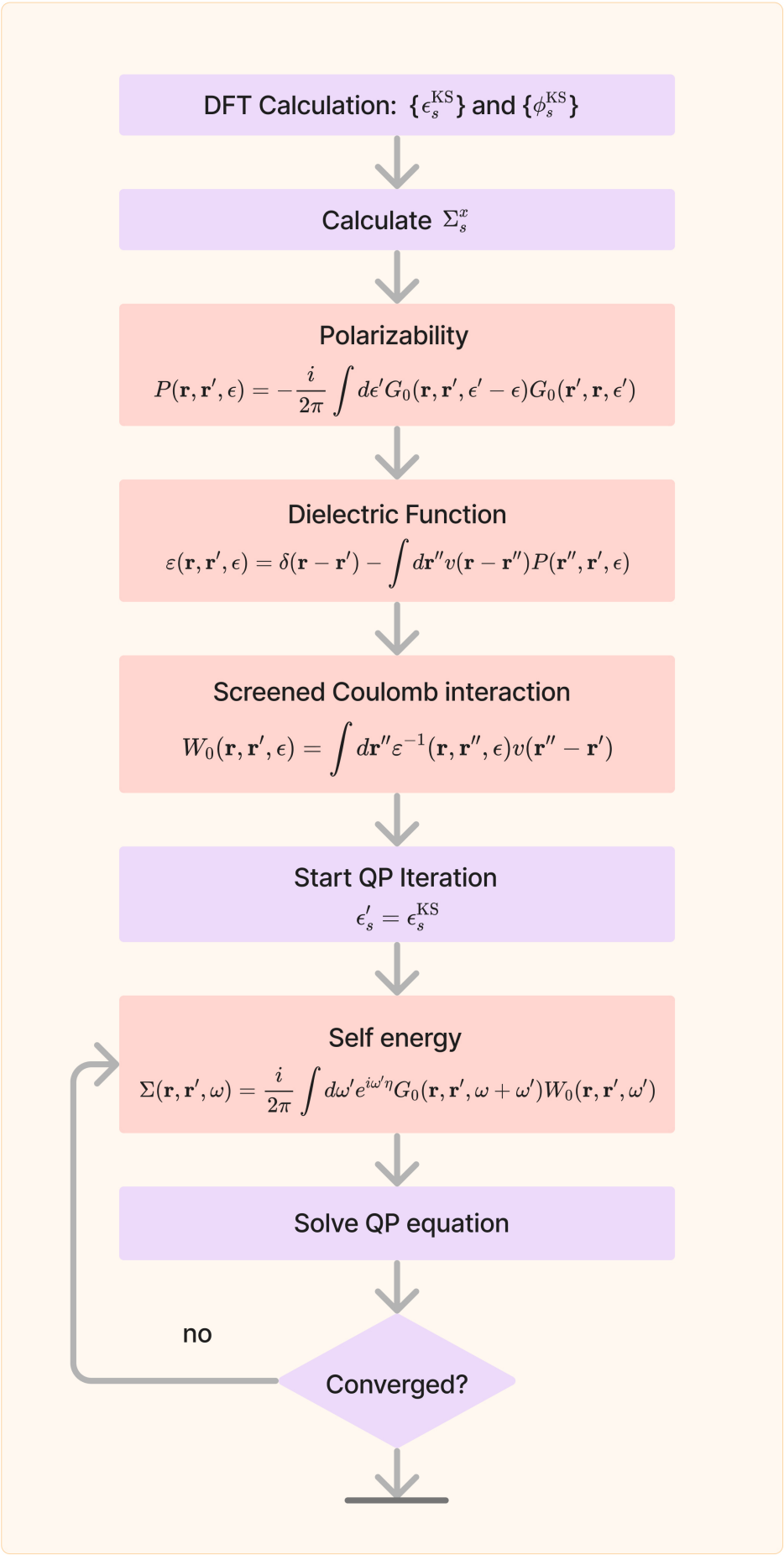

Figure 2.10: Schematic representation of the G_0W_0 implementation.

Here, the $L(1,2,1',2')$ and $K(3,5,4,6)$ represent the e^- - h^+ correlation function and the e^- - h^+ interaction kernel, respectively. The BSE links the non-interacting and interacting four point correlation function. The $L_0(1,2,1',2') = G(1,2')G(2,1')$ corresponds to the propagation of electrons and holes freely i.e., without interaction ($K = 0$). L is a function of four time variables, that corresponds to two creation and annihilation processes. In present context, the consideration of simultaneous creation and annihilation leads to two independent time variables and the time-energy Fourier transformation to $L(1,2,1',2',\omega)$ converts the correlation function in the energy space.

Therefore, in energy space we now have L_0 as:

$$L_0(1,2,1',2',\omega) = i\sum_{v,c}\left[\frac{\psi_c(\mathbf{r}_1)\psi_v^*(\mathbf{r}_1')\psi_v(\mathbf{r}_2)\psi_c^*(\mathbf{r}_2')}{\omega-(E_c-E_v)} - \frac{\psi_v(\mathbf{r}_1)\psi_c^*(\mathbf{r}_1')\psi_c(\mathbf{r}_2)\psi_v^*(\mathbf{r}_2')}{\omega+(E_c-E_v)}\right] \tag{2.114}$$

The v and c traverse the occupied states (hole) and unoccupied states (electron), respectively. For ease in representation the imaginary infinitesimals in the denominator is not included here. On inclusion of e^- - h^+ interaction, the correlation function L becomes:

$$L(1,2,1',2',\omega) = i\sum_{S}\left[\frac{\chi_S(\mathbf{r}_1,\mathbf{r}_1')\chi_S^*(\mathbf{r}_2',\mathbf{r}_2)}{\omega-\Omega_S} - \frac{\chi_S(\mathbf{r}_2,\mathbf{r}_2')\chi_S^*(\mathbf{r}_1',\mathbf{r}_1)}{\omega+\Omega_S}\right] \tag{2.115}$$

where S represents the correlated e^- - h^+ states with the Ω_S as the corresponding excitation energies. In Equation 2.115, χ_S represents the e^- - h^+ amplitudes that is evaluated as:

$$\begin{aligned}\chi_S(\mathbf{r},\mathbf{r}') &= -\langle N,0|\psi^\dagger(\mathbf{r}')\psi(\mathbf{r})|N,S\rangle \\ &= \sum_{v}^{\text{occ}}\sum_{c}^{\text{unocc}} A_{vc}^S\psi_c(\mathbf{r})\psi_v^*(\mathbf{r}') + B_{vc}^S\psi_v(\mathbf{r})\psi_c^*(\mathbf{r}')\end{aligned} \tag{2.116}$$

Here, $|N,0\rangle$ is the N-electron ground state and $|N,S\rangle$ is correlated e^- - h^+ state. The A_{vc}^S and B_{vc}^S are the coupling coefficients, and no terms for two occupied or unoccupied states appear int he equation. Now, considering the Equations 2.114, 2.115, and 2.116, the BSE (Equation 2.113) is now expressed as:

$$\begin{aligned}&(E_c-E_v)A_{vc}^S + \sum_{v',c'}K_{vc,v'c'}^{AA}(\Omega_S)A_{v'c'}^S + \sum_{v',c'}K_{vc,v'c'}^{AB}(\Omega_S)B_{v'c'}^S = \Omega_S A_{vc}^S\,, \\ &\sum_{v',c'}K_{vc,v'c'}^{BA}(\Omega_S)A_{v'c'}^S + (E_c-E_v)B_{vc}^S + \sum_{v',c'}K_{vc,v'c'}^{BB}(\Omega_S)B_{v'c'}^S = -\Omega_S B_{vc}^S\end{aligned} \tag{2.117}$$

where

$$K_{vc,v'c'}^{AA}(\Omega_S) = i\int d(3,4,5,6)\psi_v(\mathbf{r}_4)\psi_c^*(\mathbf{r}_3)K(3,5,4,6,\Omega_S)\psi_{v'}^*(\mathbf{r}_5)\psi_{c'}(\mathbf{r}_6) \tag{2.118}$$

$$K^{AB}_{vc,v'c'}(\Omega_S) = i \int d(3,4,5,6)\psi_v(\mathbf{r}_4)\psi^*_c(\mathbf{r}_3)K(3,5,4,6,\Omega_S)\psi^*_{v'}(\mathbf{r}_6)\psi_{c'}(\mathbf{r}_5) \tag{2.119}$$

Similar expressions is obtained for K^{BA} and K^{BB}. The $(E_c - E_v)$, K^{AA} and K^{BB} constitute the diagonal elements, whereas the K^{AB} and K^{BA} are the off-diagonal terms of the corresponding matrix of Equation 2.117. Generally, the off-diagonal blocks can be neglected as they are found to be small (i.e., $K^{AB} = K^{BA} = 0$). Hence, the Equation 2.117 decouples to two equations of A^S_{vc} and B^S_{vc} with identical excitations. Thus, the eigenvalue equation obtained is:

$$(E_c - E_v)A^S_{vc} + \sum_{v',c'} K^{AA}_{vc,v'c'}(\Omega_S)A^S_{v'c'} = \Omega_S A^S_{vc} \tag{2.120}$$

The correlated e^- - h^+ states can be expanded as:

$$|N,S\rangle = \sum_v^{\text{hole}} \sum_c^{\text{elec}} A^S_{vc}\hat{a}^\dagger_v \hat{b}^\dagger_c |N,0\rangle =: \sum_v^{\text{hole}} \sum_c^{\text{elec}} A^S_{vc}|vc\rangle \tag{2.121}$$

The $\hat{a}^\dagger_v$ and $\hat{b}^\dagger_c$ are the hole and electron creation operators, respectively, in the N-electron ground state $|N,0\rangle$. The expansion of Equation 2.121 is termed as the Tamm-Dancoff approximation.

2.7.4.1 Determination of e^- - h^+ kernel, K

The functional derivative w.r.t G determines the kernel K

$$K(3,4,5,6) = \frac{\delta\left[V_{\text{Coul}}(3)\delta(3,4) + \Sigma(3,4)\right]}{\delta G(6,5)} \tag{2.122}$$

The GW approximation is implemented to determine the self-energy operator Σ and with further negation of the derivative of W w.r.t G, K becomes

$$\begin{aligned} K(3,5,4,6) &= -i\delta(3,4)\delta(5^-,6)v(3,6) + i\delta(3,6)\delta(4,5)W(3^+,4) \\ &=: K^x(3,5,4,6) + K^d(3,5,4,6) \end{aligned} \tag{2.123}$$

The term K^x from the Coulomb potential is the exchange term. It determines the specifics of the excitation spectrum. The K^d is the direct interaction term that is stemmed from the screened-exchange self-energy. This term represents the attractive nature of e^- - h^+ interaction and is also responsible for the formation of bound excitons. The K^d and K^x contain the (W) and (v) interactions, respectively.

The matrix elements of K are expressed as:

$$\begin{aligned}\langle vc|K^{AA,d}(\Omega_S)|v'c'\rangle = \int d\mathbf{r}d\mathbf{r}'\psi_c^*(\mathbf{r})\psi_{c'}(\mathbf{r})\psi_v(\mathbf{r}')\psi_{v'}^*(\mathbf{r}') \times \frac{i}{2\pi}\int d\omega e^{-i\omega 0^+}W(\mathbf{r},\mathbf{r}',\omega) \\ \times \left[\frac{1}{\Omega_S - \omega - \left(E_{c'}^{\mathrm{QP}} - E_v^{\mathrm{QP}}\right) + i0^+} \right. \\ \left. + \frac{1}{\Omega_S + \omega - \left(E_c^{\mathrm{QP}} - E_v^{\mathrm{QP}}\right) + i0^+}\right]\end{aligned} \tag{2.124}$$

and

$$\langle vc|K^{AA,x}(\Omega_S)|v'c'\rangle = \int d\mathbf{r}d\mathbf{r}'\psi_c^*(\mathbf{r})\psi_v(\mathbf{r})v(\mathbf{r},\mathbf{r}')\psi_{c'}(\mathbf{r}')\psi_{v'}^*(\mathbf{r}') \tag{2.125}$$

K^d achieves the frequency integration along with the real-space integration by plasmon-pole model that expands the screened Coulomb interaction.

$$W(\mathbf{r},\mathbf{r}',\omega) = \sum_l W_l(\mathbf{r},\mathbf{r}')\frac{\omega_l}{2}\left(\frac{1}{\omega - \omega_l + i0^+} - \frac{1}{\omega + \omega_l - i0^+}\right) \tag{2.126}$$

where ω_l is the plasmon frequency and $W_l(\mathbf{r},\mathbf{r}')$ is the spatial behavior of the plasmon mode l. Subsequent frequency integration deduces the Equation 2.124 to

$$\begin{aligned}\langle vc|K^{AA,d}(\Omega_S)|v'c'\rangle = \int d\mathbf{r}d\mathbf{r}'\psi_c^*(\mathbf{r})\psi_{c'}(\mathbf{r})\psi_v(\mathbf{r}')\psi_{v'}^*(\mathbf{r}')W_l(\mathbf{r},\mathbf{r}') \\ \times \frac{\omega_l}{2}\left[\frac{1}{\omega_l - (\Omega_S - (E_{c'}^{\mathrm{QP}} - E_v^{\mathrm{QP}}))} \right. \\ \left. + \frac{1}{\omega_l - (\Omega_S - (E_c^{\mathrm{QP}} - E_v^{\mathrm{QP}}))}\right]\end{aligned} \tag{2.127}$$

Now, the transition energies $(E_c^{\mathrm{QP}} - E_v^{\mathrm{QP}})$ often, approximates to the excitation energies Ω_S as in semiconductor crystals. As the $\Omega_S - (E_c^{\mathrm{QP}} - E_v^{\mathrm{QP}})$ is considerably smaller than ω_l the term can be negated thereby deducing the Equation 2.127 to:

$$\langle vc|K^{AA,d}(\Omega_S)|v'c'\rangle = \int d\mathbf{r}d\mathbf{r}'\psi_c^*(\mathbf{r})\psi_{c'}(\mathbf{r})\psi_v(\mathbf{r}')\psi_{v'}^*(\mathbf{r}')W(\mathbf{r},\mathbf{r}',\omega=0) \tag{2.128}$$

Here, the static properties of W are retained while omitting its dynamical properties. Note that the case above is for semiconductor crystals and will not hold for atoms and molecules as the difference $\Omega_S - (E_c^{\mathrm{QP}} - E_v^{\mathrm{QP}})$ might be significant. Hence, Equation 2.127 would evaluate the e^- - h^+ interaction kernel K. Since, K^d depends on excitation energies Ω_S, calculation of e^- - h^+ interaction and subsequently, solving the BSE self-consistently is challenging. The workflow is then as follows:

- Determination of the static screened Coulomb interaction W and K^d is evaluation from Equation 2.128
- Solving BSE for excitations $|S\rangle$ and first estimation of excitation energies $\Omega_S^{(0)}$
- Determination of K^d from Equation 2.124 by using the $\Omega_S^{(0)}$
- The difference of updated K^d and the previous step $K^{d,0}$ is a test for convergence. It is treated as a perturbation in first order and hence, Ω_S is updated.
- Iterate until Ω_S converges

2.7.5 Optical Spectrum

We obtain the optical response from the imaginary part ($\epsilon_2(\omega)$) of the macroscopic transverse dielectric function $\epsilon(\omega)$

$$\epsilon_2(\omega) = \frac{16\pi e^2}{\omega^2} \sum_S \left| \vec{\lambda} \cdot \langle 0|\vec{v}|S\rangle \right|^2 \delta(\omega - \Omega_S) \tag{2.129}$$

Here, $\vec{\lambda} = \frac{\vec{A}}{|\vec{A}|}$ is the polarization vector of the light and $\vec{v} = i/\hbar[H, \vec{r}]$ is the single-particle velocity operator. In case of independent hole and electron states (i.e., no e^- - h^+ interaction), the excitations correspond to the vertical transitions, thereby reducing Equation 2.129 to:

$$\epsilon_2^{(0)}(\omega) = \frac{16\pi e^2}{\omega^2} \sum_{v,c} \left| \vec{\lambda} \cdot \langle v|\vec{v}|c\rangle \right|^2 \delta(\omega - (E_c - E_v)) \tag{2.130}$$

Now, excitations correspond to the correlated e^- - h^+ states ($|S\rangle$) and hence, we obtain the optical transition matrix elements as:

$$\langle 0|\vec{v}|S\rangle = \sum_v^{\text{hole}} \sum_c^{\text{elec}} A_{vc}^s \langle v|\vec{v}|c\rangle \tag{2.131}$$

Evaluating transition matrix elements $\langle v|\vec{v}|c\rangle$ significantly depends on the pseudopotentials [78]. In the case of local pseudopotentials, the potential and position operator commutes, whereas this is not the case in non-local pseudopotentials.

2.8 Sham-Schlüter equation

Equation 2.132 is referred to as Sham-Schlüter equation (SSE) and represents the connection between DFT and MBPT [79, 80]. Hence, the link is between the xc potential (v_{xc}) and the

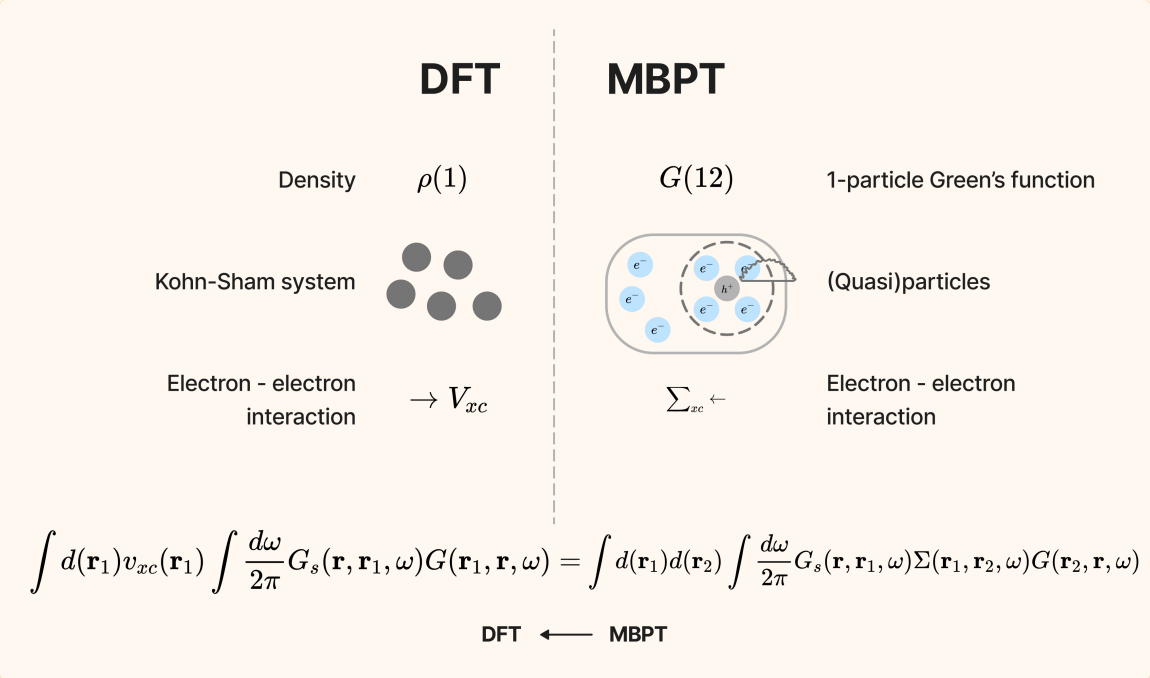

Figure 2.11: Connection of DFT and MBPT by Sham-Schlüter equation

self-energy (Σ). Here, G_s is the Green function of the Kohn-Sham system.

$$\int d(\mathbf{r}_1) v_{xc}(\mathbf{r}_1) \int \frac{d\omega}{2\pi} G_s(\mathbf{r}, \mathbf{r}_1, \omega) G(\mathbf{r}_1, \mathbf{r}, \omega) = \int d(\mathbf{r}_1) d(\mathbf{r}_2) \int \frac{d\omega}{2\pi} G_s(\mathbf{r}, \mathbf{r}_1, \omega) \Sigma(\mathbf{r}_1, \mathbf{r}_2, \omega) G(\mathbf{r}_2, \mathbf{r}, \omega) \tag{2.132}$$

In linearized form (replacing G by G_s) the equation becomes:

$$\int d(\mathbf{r}_1) v_{xc}(\mathbf{r}_1) \int \frac{d\omega}{2\pi} G_s(\mathbf{r}, \mathbf{r}_1, \omega) G_s(\mathbf{r}_1, \mathbf{r}, \omega) = \int d(\mathbf{r}_1) d(\mathbf{r}_2) \int \frac{d\omega}{2\pi} G_s(\mathbf{r}, \mathbf{r}_1, \omega) \Sigma(\mathbf{r}_1, \mathbf{r}_2, \omega) G_s(\mathbf{r}_2, \mathbf{r}, \omega) \tag{2.133}$$

One can derive v_{xc} approximations from Σ with the Equation 2.133, thereby avoiding the Dyson equation solution for determining G. For instance, Σ in Hartree-Fock approximation corresponds to the solution of local exact-exchange potential. However, this approach is not prominent due to the complexity of the equation and has been numerically solved only for a few isolated cases.

2.9 Density functional perturbation theory (DFPT)

Density functional perturbation theory (DFPT) approaches the system under small perturbation with one of the important parameters being lattice vibrations. This influences the physical properties such as heat conduction, elastic neutron scattering, specific heat and thermal expansion.

Also the electron-phonon coupling dominates the superconductivity and the temperature dependence of optical spectra [81]. This section discusses the underlying linear response framework for implementing the method.

2.9.1 Lattice dynamics from electronic structure theory

The Schrödinger equation under the Born–Oppenheimer approximation for the lattice dynamics is governed by the eigenstates Φ and eigenvalues $\mathcal{E}$ as:

$$\left(-\sum_I \frac{\hbar^2}{2M_I}\frac{\partial^2}{\partial \mathbf{R}_I^2} + E(\mathbf{R})\right)\Phi(\mathbf{R}) = \mathcal{E}\Phi(\mathbf{R}) \tag{2.134}$$

where M_I and $\mathbf{R}_I$ is the mass of the Ith nucleus and its coordinate, repectively. The $\mathbf{R} \equiv \{\mathbf{R}_I\}$ is the set of all the nuclear coordinates. $E(\mathbf{R})$ is referred to as Born–Oppenheimer energy surface. It evaluates the ground-state energy of a system of interacting electrons under the influence of the field of fixed nuclei. The equilibrium geometry of the system corresponds to the forces acting on individual nuclei to be zero.

$$\mathbf{F}_I \equiv -\frac{\partial E(\mathbf{R})}{\partial \mathbf{R}_I} = 0 \tag{2.135}$$

Equation 2.136 represents the Hessian of the Born–Oppenheimer energy. Its eigenvalues determine the vibrational frequencies ω of the system.

$$\det\left|\frac{1}{\sqrt{M_I M_J}}\frac{\partial^2 E(\mathbf{R})}{\partial \mathbf{R}_I \partial \mathbf{R}_J} - \omega^2\right| = 0 \tag{2.136}$$

The force as per the Hellmann-Feynman theorem conforming with Born–Oppenheimer Hamiltonian and $\Psi(\mathbf{r};\mathbf{R})$ as the electronic ground-state wave function is:

$$\mathbf{F}_I = -\frac{\partial E(\mathbf{R})}{\partial \mathbf{R}_I} = -\left\langle \Psi(\mathbf{R}) \left| \frac{\partial H_{BO}(\mathbf{R})}{\partial \mathbf{R}_I} \right| \Psi(\mathbf{R}) \right\rangle \tag{2.137}$$

where

$$\begin{aligned} H_{BO}(\mathbf{R}) = &-\sum_i \frac{\hbar^2}{2m_e}\frac{\partial^2}{\partial \mathbf{r}_i^2} - \sum_{i,I}\frac{Z_I e^2}{|\mathbf{R}_I - \mathbf{r}_i|} \\ &+ \frac{e^2}{2}\sum_{i\neq j}\frac{1}{|\mathbf{r}_i - \mathbf{r}_j|} + \frac{e^2}{2}\sum_{I\neq J}\frac{Z_I Z_J}{|\mathbf{R}_I - \mathbf{R}_J|} \end{aligned} \tag{2.138}$$

where, Z_I is the charge of the Ith nucleus. Subsequently, $\mathbf{F}_I$ is expressed as:

$$\mathbf{F}_I = -\int d\mathbf{r}\, n(\mathbf{r})\frac{\partial V_{ext}(\mathbf{r})}{\partial \mathbf{R}_I} - \frac{\partial E_{II}(\mathbf{R})}{\partial \mathbf{R}_I} \tag{2.139}$$

where

$$E_{II}(\mathbf{R}) = \frac{e^2}{2}\sum_{I\neq J}\frac{Z_I Z_J}{|\mathbf{R}_I - \mathbf{R}_J|} \quad , \quad V_{ext}(\mathbf{r}) = -\sum_{i,I}\frac{Z_I e^2}{|\mathbf{R}_I - \mathbf{r}_i|}$$
$$n(\mathbf{r}) \quad : \text{electronic ground state density} \tag{2.140}$$

Now differentiating the $\mathbf{F}_I$ w.r.t nuclear coordinates, we obtain the Hessian (Equation 2.136). This equation further deduces the requirement of $n(\mathbf{r})$ and its linear response upto of $\frac{\partial n(\mathbf{r})}{\partial \mathbf{R}_I}$.

$$\frac{\partial^2 E(\mathbf{R})}{\partial \mathbf{R}_I \partial \mathbf{R}_J} \equiv -\frac{\partial \mathbf{F}_I}{\partial \mathbf{R}_J} = \int d\mathbf{r}\,\frac{\partial n(\mathbf{r})}{\partial \mathbf{R}_J}\frac{\partial V_{ext}(\mathbf{r})}{\partial \mathbf{R}_I} + \int d\mathbf{r}\, n(\mathbf{r})\frac{\partial^2 V_{ext}(\mathbf{r})}{\partial \mathbf{R}_I \partial \mathbf{R}_J} + \frac{\partial^2 E_{II}(\mathbf{R})}{\partial \mathbf{R}_I \partial \mathbf{R}_J} \tag{2.141}$$

2.9.2 Linear response

Equation 2.141 determines the interatomic force constants. Incorporation of the same under the DFT workflow requires linearization w.r.t potential variations, density and wave function. The first-order perturbation theory determines the variation of Kohn-Sham orbitals as:

$$(H_{SCF} - \epsilon_n)|\Delta\psi_n\rangle = -(\Delta V_{SCF} - \Delta\epsilon_n)|\psi_n\rangle \tag{2.142}$$

The terms of the Equation 2.142 corroborate to:

$$\begin{aligned}
&\text{Unperturbed SCF Hamiltonian:} \quad H_{SCF} = -\frac{\hbar^2}{2m}\frac{\partial^2}{\partial \mathbf{r}^2} + V_{SCF}(\mathbf{r}) \\
&\text{SCF potential:} \quad V_{SCF}(\mathbf{r}) = V_{ext}(\mathbf{r}) + \int d\mathbf{r}'\,\frac{n(\mathbf{r}')}{|\mathbf{r} - \mathbf{r}'|} + v_{\text{xc}}(\mathbf{r}) \\
&\text{First-order correction to } V_{SCF}\text{:} \quad \Delta V_{SCF}(\mathbf{r}) = \Delta V_{ext}(\mathbf{r}) + \int d\mathbf{r}'\,\frac{\Delta n(\mathbf{r}')}{|\mathbf{r} - \mathbf{r}'|} + \left.\frac{dv_{\text{xc}}}{dn}\right|_{n=n(\mathbf{r})}\Delta n(\mathbf{r}) \\
&\text{First-order correction to } \epsilon_n\text{:} \quad \Delta\epsilon_n = \langle\psi_n|\Delta V_{SCF}|\psi_n\rangle
\end{aligned} \tag{2.143}$$

Here, $v_{\text{xc}}(\mathbf{r}) \equiv \frac{\delta E}{\delta n(\mathbf{r})}$ is the xc-potential and ϵ_n is the Kohn-Sham eigenstates. Considering nonmagnetic systems, the linearized charge density, $\Delta n(\mathbf{r})$ is expressed as:

$$\Delta n(\mathbf{r}) = 4\sum_{n=1}^{N/2}\psi_n^*(\mathbf{r})\Delta\psi_n(\mathbf{r}) \tag{2.144}$$

where finite-difference operator (Δ) is defined as:

$$\Delta(\equiv \Delta^\lambda) \Rightarrow \Delta^\lambda F = \sum_i \frac{\partial F_\lambda}{\partial \lambda_i}\Delta\lambda_i$$
$$\lambda \quad : \text{set of parameters, } \mathbf{R}_I \tag{2.145}$$

The first-order correction to the eigenfunction in Equation 2.142 is:

$$\Delta\psi_n(\mathbf{r}) = \sum_{m\neq n} \psi_m(\mathbf{r}) \frac{\langle\psi_m|\Delta V_{SCF}|\psi_n\rangle}{\epsilon_n - \epsilon_m} \tag{2.146}$$

where the summation includes all the occupied and unoccupied states. Hence, on deducing $\Delta n(\mathbf{r})$ from Equations 2.146 and 2.144, we obtain:

$$\Delta n(\mathbf{r}) = 4 \sum_{n=1}^{N/2} \sum_{m\neq n} \psi_n^*(\mathbf{r})\psi_m(\mathbf{r}) \frac{\langle\psi_m|\Delta V_{SCF}|\psi_n\rangle}{\epsilon_n - \epsilon_m} \tag{2.147}$$

We observe from Equation 2.147 that the terms corresponding to products of occupied states cancel. Therefore, the index m appears to be associating only to the conduction band states c. Now, in order to evaluate $\Delta\psi_n(\mathbf{r})$, the operator P_c i.e., the projector onto the unoccupied states, is employed in the Equation 2.142 as:

$$(H_{SCF} + \alpha P_v - \epsilon_v)|\Delta\psi_n\rangle = -P_c \Delta V_{SCF}|\psi_v\rangle \tag{2.148}$$

Here, $P_c = \sum_c |\psi_c\rangle\langle\psi_c| = 1 - \sum_v |\psi_v\rangle\langle\psi_v|$. A multiple of the projector operator P_v i.e., projector onto the occupied states, is also added to make the Equation 2.142 nonsingular. Equation 2.148, is solved by any iterative method with the trial solution being orthogonal to occupied states. As a result the incurred computational cost is similar to that of solving the Kohn-Sham equations.

2.10 Climbing image nudged elastic band method

The nudged elastic band (NEB) method obtains the saddle points and the minimum energy path (MEP) between the reactants and products. The approach involves optimizing several intermediary images along the reaction chain. The minimum energy configuration of each image is obtained while maintaining an equal distance from neighboring images. The optimization is constrained by adding spring forces along the band between the images and by the projection of the force component owing to the potential perpendicular to the band. The reaction coordinates of various transition processes such as chemical reactions, the conformation of molecules, and atomic exchange processes. The maximum energetic image configuration constitutes a saddle point on the MEP, which determines the activation energy barrier. The reactant and product are the local minima, and a set of images between them are obtained by linear interpolation. The spring forces between the images link them, forming an elastic band that optimizes the forces for MEP. However, there are two issues in this traditional elastic band approach: (i) sliding

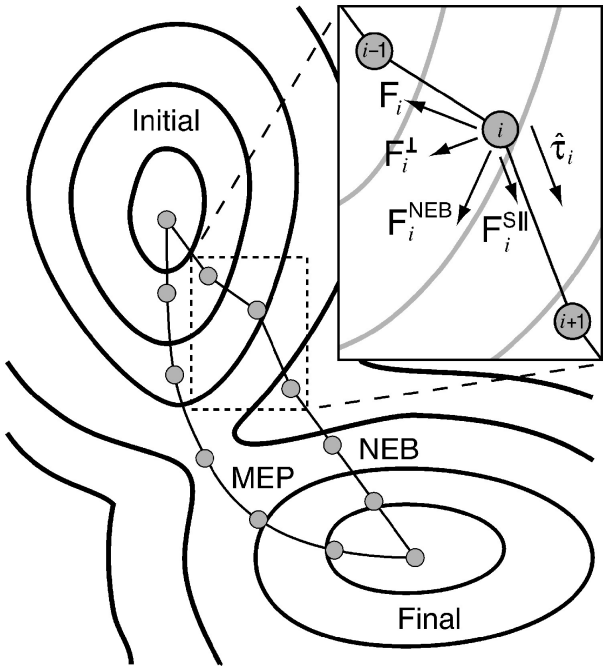

Figure 2.12: Schematic for various forces acting on the image while optimization [2]

down and (ii) corner-cutting problem. The former is due to the smaller spring constant, resulting in the shift of images towards minima due to the true force along the path. This reduces the resolution around the saddle point. In the case of corner-cutting, spring forces perpendicular to the path tend to shift the saddle point, thereby preventing the images from true MEP. Therefore, the saddle point convergence significantly depends on the spring constant. To cater to these issues, "nudging" scheme has been proposed, where the parallel and perpendicular components of the respective true force and spring force are eliminated. Hence, the total force is due to the perpendicular true force and spring force along the local tangent. Now, let us understand with an example where $\mathbf{R}_0$ and $\mathbf{R}_N$ are the initial and final states. On considering, the elastic band with N+1 images [$\mathbf{R}_1$, $\mathbf{R}_2$, ..., $\mathbf{R}_{N-1}$], the forces acting on the i-th image are expressed as follows:

$$F_i = F_i^s|_{\parallel} - \nabla E(\mathbf{R}_i)|_{\perp} \tag{2.149}$$

Here, E represents energy that is the function of atomic coordinates. The images on the MEP satisfies the condition: $\nabla E(\mathbf{R}_i)|_{\perp} = 0$. The correspondig true force expression is:

$$\nabla E(\mathbf{R}_i)|_{\perp} = \nabla E(\mathbf{R}_i) - \nabla E(\mathbf{R}_i).\hat{\tau}_i \tag{2.150}$$

The $\hat{\tau}_i$ is the normalized local tangent for image i. The corresponding spring force is:

$$F_i^s|_{\parallel} = k(|\mathbf{R}_{i+1} - \mathbf{R}_i| - |\mathbf{R}_i - \mathbf{R}_{i-1}|).\hat{\tau}_i \tag{2.151}$$

where k is the spring constant. The equal spacing between the images is due to the equal spring constant of the images. If the spring constant is a variable, more resolution can be attained near the saddle point. This is attributed to the spring constant being related to the energy of the images, where low-energy images are associated with a weaker spring constant, and that near the saddle point are linked with a stronger spring constant. A significant drawback still laid in the method is the non-capturing of the transition state in the MEP. Hence, a modification that finds the exact transition state and the precise barrier is incorporated into the climbing image NEB (CI-NEB) method. No significant change in the computational cost has been observed with this improvement.

In this approach, the highest energy image i_{max} is identified, where the image is not under the influence of spring force and acted upon by the reversed force, that is, the true force acting along the reversed direction of the elastic band. This image is defined as the climbing image and the force acting on the same is:

$$\begin{aligned} F_{i_{max}} &= -\nabla E(\mathbf{R}_{i_{max}}) + 2\nabla E(\mathbf{R}_{i_{max}})|_{\parallel} \\ &= -\nabla E(\mathbf{R}_{i_{max}}) + 2\nabla E(\mathbf{R}_{i_{max}}).\hat{\tau}_i\hat{\tau}_i \end{aligned} \tag{2.152}$$

As a result, we obtain the energetically maximum climbing image along the path and energetically minimum images perpendicular to the path in all directions. Hence, the precise location of the saddle point and the convergence of MEP is assured, thereby making the CI-NEB an appropriate choice for obtaining the activation barrier of chemical reactions.

CHAPTER 3

Effect of many body dispersion for efficient point defect tuning in monolayer MoS_2

3.1 Introduction

Transition metal dichalcogenides (TMDs) is a field of high research interest due to their unique properties [6, 7, 8]. These are the layered materials with interlayer van der Waals forces and intralayer covalent bond [82, 83]. They exhibit indirect to direct band gap transition, as the dimension is reduced from bulk to monolayer. Molybdenum disulfide (MoS_2) is the most studied TMD material, owing to its abundance and low cost [84]. Monolayer of MoS_2 features exceptional optical [85], electrical [86] and mechanical [87] properties. It has a tunable band gap and therefore, its electronic and optoelectronic properties can be controlled as per different requirements [88, 89]. Hence, MoS_2 is a promising material for future applications in device engineering, optoelectronics and sensors [90, 91, 92].

Monolayers are manufactured by various experimental state-of-the-art methods viz. chemical vapour deposition (CVD), sulfurization, chemical and mechanical exfoliation techniques, etc. [93, 94, 95, 96]. Similar to any other material, defects are inadvertently introduced during its manufacture. These imperfections affect the mechanical [97], electrical [98, 99], electronic, optical [100] and magnetic [101, 102] properties of the system. For instance, the electrical conductivity is largely affected as the defect constrains the mobility [103, 104]. The defects create different impact on the material of reduced dimensions than that on its bulk counterpart [105]. These issues have been the focus of many experimental and theoretical studies [106, 107, 108, 109]. Characteristics of the defects under a given condition is a matter of understanding on the basis of which we may want to eliminate or induce a defect [110]. Since defects alter the properties of the materials, these can be engineered for diverse appli-

cations [111, 112]. Defect engineering has its utilization in the field of spintronics, catalysis, electrochemical reactions and semiconductors [113, 114, 115, 116, 117].

Among many characteristics pertaining to this system, the often observed n-type doping of MoS_2 has also been the motivation for conducting defect studies on the material [118]. The stated observation is usually attributed to the large amount of native S vacancies. However, one needs to consider both n-type and p-type monolayers of MoS_2 for any requisite device application. Hence, the defect states that affect the thermodynamic stability of p-type monolayer are essential to be discussed [119, 120]. In addition, the van der Waals interactions do affect the stability and mobility of the point defects in the semiconductors [121, 122]. The polarization which results in van der Waals interactions might affect the defect states leading to a change in the free energy of formation and hence, in the stability. The field of defect studies on the TMD monolayers, though significantly studied, has not established a complete database.

In this work, we, therefore, intend to analyse the thermodynamic stability of native point defects using density functional theory (DFT). First, we have validated the xc-functionals viz. LDA, PBE and HSE06 for the MoS_2 monolayer. Subsequently, to determine the most stable defect states, with the ground state defect configurations we have calculated the formation energies of the neutral and charged defects. We have modeled eight possible defect configurations, which consist of three vacancies and five antisites [123]. Here, Mo, S and S_2 vacancies, and S_{Mo}, $S_{2_{Mo}}$, Mo_S, Mo_{S_2} and $2Mo_{S_2}$ antisites are shown in Fig. 3.1. Following this, in the expression of defect's formation energy, we have included the dispersion corrections as per (i) the two-body van der Waals interaction using Tkatchenko-Scheffler scheme (TS) [124] and (ii) many-body dispersion (MBD)[125, 126]. We have also shown results without including vdW effects just as a reference. The concentration of these defect states in the temperature range of 50-1000 K using *ab inito* atomistic thermodynamics approach [127, 67, 128] have established the most important defects in doped MoS_2 monolayer. Further, we have obtained the optical response of those stable defect states which have tuned the band gap that includes visible region of the spectrum.

3.2 Methodology

We have employed first-principles based methodology under the framework of DFT [27, 129, 130, 131]. The calculations are performed with all electron based code FHI-aims that uses

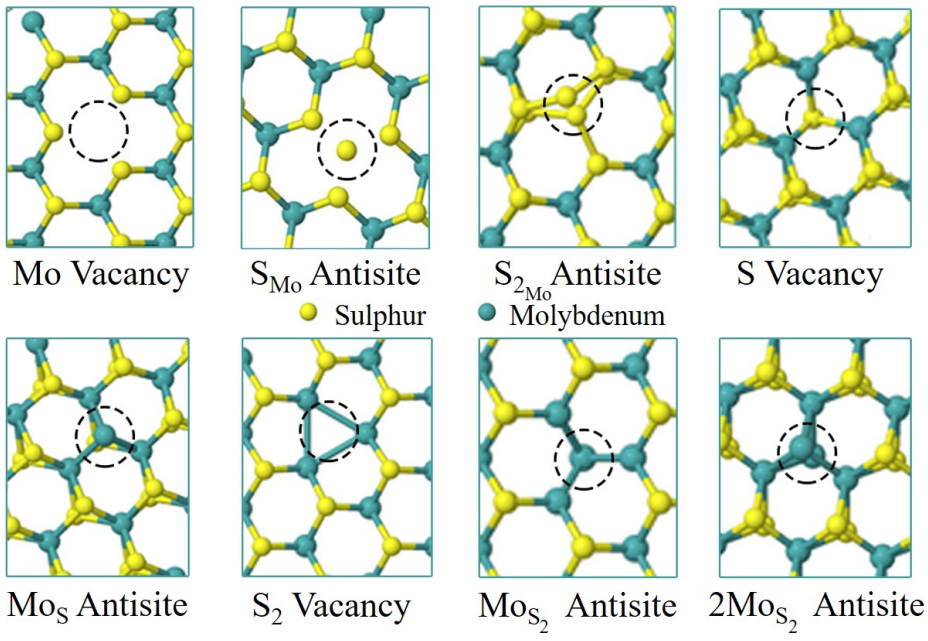

Figure 3.1: Optimized geometries of the defects within the MoS_2 monolayer.

numeric, atom-centered basis set [132, 133, 134, 135]. We have presented here an exhaustive scenario on the choice of exchange correlation functionals starting from local/semi-local functional to more advanced hybrid functional especially to capture the effect due to exact exchange [136, 137]. The respective functional that we have employed here are proposed by Perdew-Burke-Ernzerhof (PBE) [138] and Heyd-Scuseria-Ernzerhof (HSE06) [139]. The hybrid functional (HSE06) considers 25% mixing (α) of the short range Hartree-Fock exchange. Its long range part is described by GGA-PBE functional. The screening parameter (ω) of 0.21 bohr^{-1} is optimized for the calculations. The following equation defines the exchange energy for this functional.

$$E_{xc}^{HSE06} = \alpha E_{xc}^{HF}(\omega) + (1-\alpha)E_{xc}^{DFT}(\omega) + E_{c}^{DFT}(\omega) \tag{3.1}$$

In the bulk form, MoS_2 has trigonal prismatic structure [140]. A 6×6×1 supercell of MoS_2 monolayer, consisting 108 atoms, has been modeled. This size of the supercell is kept on increasing until it aptly localizes the defects. In the calculations, the Brillouin zone was sampled by 4×4×1 k-grid. Tier-2 basis sets for atoms with "tight" settings have been applied [132]. Note that, in order to avoid any artifact due to choice of DFT functionals, we have presented here the results obtained from PBE and HSE06 functionals for the rest of the study. This comparative study of the functionals has been undertaken to ensure the importance of hybrid functionals and the possible error one may come across from employing local/semi-local func-

tionals. Note that the two-body vdW interaction (TS scheme [124]) and many-body dispersion scheme [125, 126] are being thoroughly benchmarked on both the PBE and HSE06 functionals. The correction parameter is based on Hirshfeld partitioning of the electron density.

The absorption spectra has been obtained by HSE06 functional under the Vienna *ab initio* simulation package (VASP) [141] that implements PAW pseudopotential method [63]. Conjugate gradient minimization have been employed with $2\times2\times1$ K-mesh for optimizing the force in the structures upto 0.001 eV/Å . The energy calculation for the structure have been performed with brillouin zone sampling of $6\times6\times1$ Gamma centered K-mesh with 0.01 meV energy tolerance. The plane wave energy cut-off is set to 500 eV for ground state calculations. The imaginary part of the obtained dielectric function gives the optical absorption of the system.

3.3 Results and Discussions

3.3.1 Stability in defect states

The free energy of formation of charged defects can be calculated with the help of following expression:

$$\mathrm{E_f} = \mathrm{F}^{(q)}_{\mathrm{defect}} - \mathrm{F}^{(0)}_{\mathrm{pristine}} \pm \sum \mathrm{N_i}\mu_\mathrm{i} + q(\mu_\mathrm{e} + \Delta\mathrm{V} + \mathrm{VBM}) \tag{3.2}$$

Here, $\mathrm{E_f}$ is the free energy of formation of the defect state. F is the Helmohltz free energy, which is sum of total DFT energy and vibrational energy due to lattice vibration. Since the contribution of the latter term is not much, and we are taking differences of $\mathrm{F}^{(q)}_{\mathrm{defect}}$ and $\mathrm{F}^{(0)}_{\mathrm{pristine}}$, the effect due to lattice vibration will be insignificant. Therefore, the dominating term in F is total DFT energy. Hence, it's important to compute it accurately after thorough validation of DFT functionals. μ_i is the chemical potential of the component i, $\mathrm{N_i}$ is the number of vacancies or antisites, μ_e is the chemical potential of an electron, ΔV is the difference between core levels of pristine and defected supercell, and VBM denotes valence band maximum of the pristine neutral. The charge transition levels are given with respect to this VBM and μ_e is varied within the band gap (see discussion for charged defects later). However, in case of neutral defects (q=0), the free energy of formation reduces to the following expression:

$$\mathrm{E_f} = \mathrm{F}^{(0)}_{\mathrm{defect}} - \mathrm{F}^{(0)}_{\mathrm{pristine}} \pm \sum \mathrm{N_i}\mu_\mathrm{i} \tag{3.3}$$

MoS_2 layers act as a thermodynamic reservoir thereby making the chemical potentials of Mo and S interdependent [142]. Hence we have,

$$\Delta H_f(MoS_2) = \mu_{MoS_2} - (\mu_{Mo} + 2\mu_S) \tag{3.4}$$

where $\Delta H_f(MoS_2)$ is the formation enthalpy i.e. 2.44 eV at 300 K for this system [143, 66]. In equilibrium with the MoS_2 bulk, μ_{Mo} and μ_S are related through the following expression:

$$\mu_{Mo} + 2\mu_S = E_{MoS_2} \tag{3.5}$$

The chemical potentials can never exceed the value of the corresponding condensed pure element [27]. Therefore, we have physical permissible limits as $\mu_{Mo} \leq E_{Mo}$ (Mo-rich limit) and $\mu_S \leq E_S$ (S-rich limit). The Mo-rich limit can also be termed as S-poor limit with expression $\mu_{S,min} = (E_{MoS_2} - E_{Mo})/2$. The corresponding values are found from the formation enthalpy of MoS_2. Hence, we obtain the limiting conditions for the chemical potential of S (μ_S) as -1.22 $\leq \Delta\mu_S = \mu_S - E_S \leq 0$.

In equilibrium, the negative values of free energy of formation correspond to the stable defect configurations with respect to the pristine monolayer. No neutral defect states are more stable than the pristine monolayer. However, as previously discussed, defects are inevitable in the material, which further indicates the presence of extra charge in the system. Note that the formation energy of one isolated defect can be reduced significantly by several eVs, when the charge carriers (holes or electrons) are available in the material [127]. Therefore, we have analyzed the defects with -2, -1, +1 and +2 charged states by the two functionals (PBE and HSE06). We now analyze the variation of free energy of formation of the defect as a function of chemical potential of electron ($\Delta\mu_e$) within S rich ($\Delta\mu_S$= 0) and Mo rich ($\Delta\mu_S$= -1.22) limits. Consider, S vacancy stable defect states as obtained by HSE06 functional in Fig. 3.2a and Fig. 3.2b for understanding. Here, we observe that V_S^{-2} and V_S^{+2} are the most stable defect configurations near CBm (conduction band minimum) and VBM, respectively. However, these states were found to be more stable than pristine, only in the Mo-rich condition. These plots do give an idea about the stability of certain defect states over other but only at a fixed $\Delta\mu_S$ condition (viz. here plotted at S-rich and Mo-rich limiting conditions). In order to gain more clarity we have considered a 3D phase diagram (Fig. 3.2c), where along x, y, and z-axis we have respectively plotted $\Delta\mu_S$, $\Delta\mu_e$ and E_f. The x-y plane is being viewed here from the negative z-axis (lower the E_f more stable is the configuration). From Fig. 3.2c the most stable defect configurations amongst the neutral and all possible charged defects are determined (as

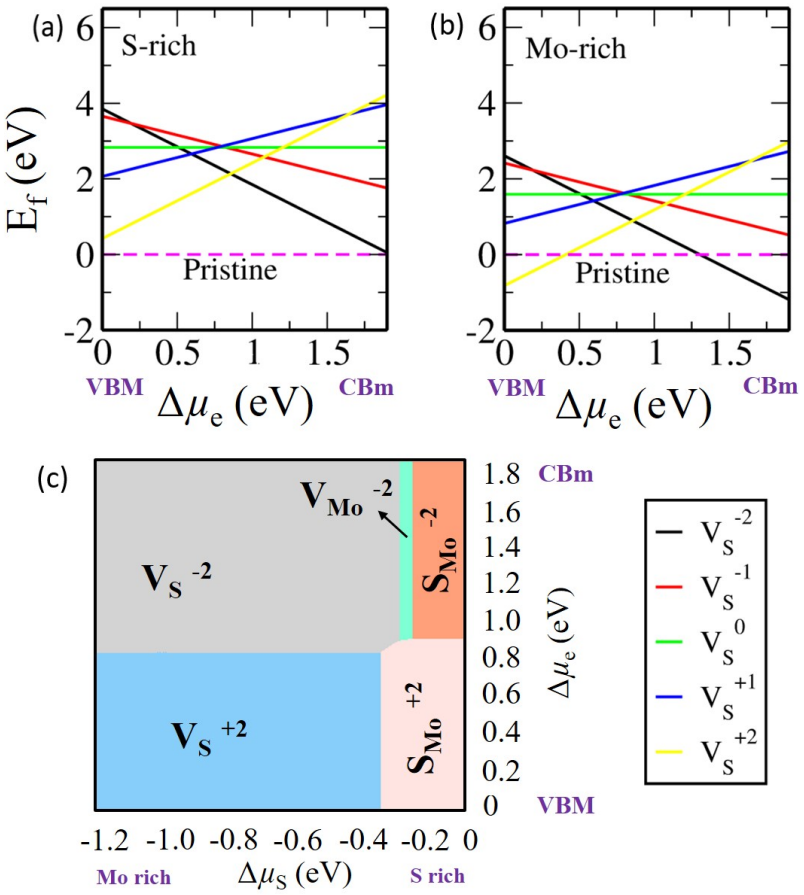

Figure 3.2: Variation of free energy of formation of S vacancy defect states observed at (a) S-rich limit, and (b) Mo-rich limit. (c) 3D phase diagram by HSE06 with no vdW interaction.

obtained from HSE06 functional). Each colour in the phase diagram is associated with a defect configuration and the region of a specific colour represents the range of $\Delta\mu_S$ and $\Delta\mu_e$, where the corresponding configuration is stable. This plot covers the full range of chemical potential of sulfur i.e. -1.22 $\leq \Delta\mu_S \leq$ 0 and chemical potential of electron i.e. 0 $\leq \Delta\mu_e \leq$ 1.8. Moreover, the phase diagram also considers the positive values of free energy of formation of defects, which might be probable in real situations. At the Mo-rich condition, we have observed V_S^{-2} and V_S^{+2} as the most stable states near CBm and VBM, respectively. This is in agreement with the observation from Fig. 3.2a and Fig. 3.2b.

This phase diagram helps to infer whether the stable defect states are acceptors or donors depending on the position of stability over the bandgap. If a defect accepts electron to gain stability, it will have negative charge associated with it and hence will act as electron acceptors. Similarly, positive charged defects have lost electrons to gain stability and hence acting as electron donors. Moreover, when $\Delta\mu_e$ is near to CBm, this situation can be stated as n-type

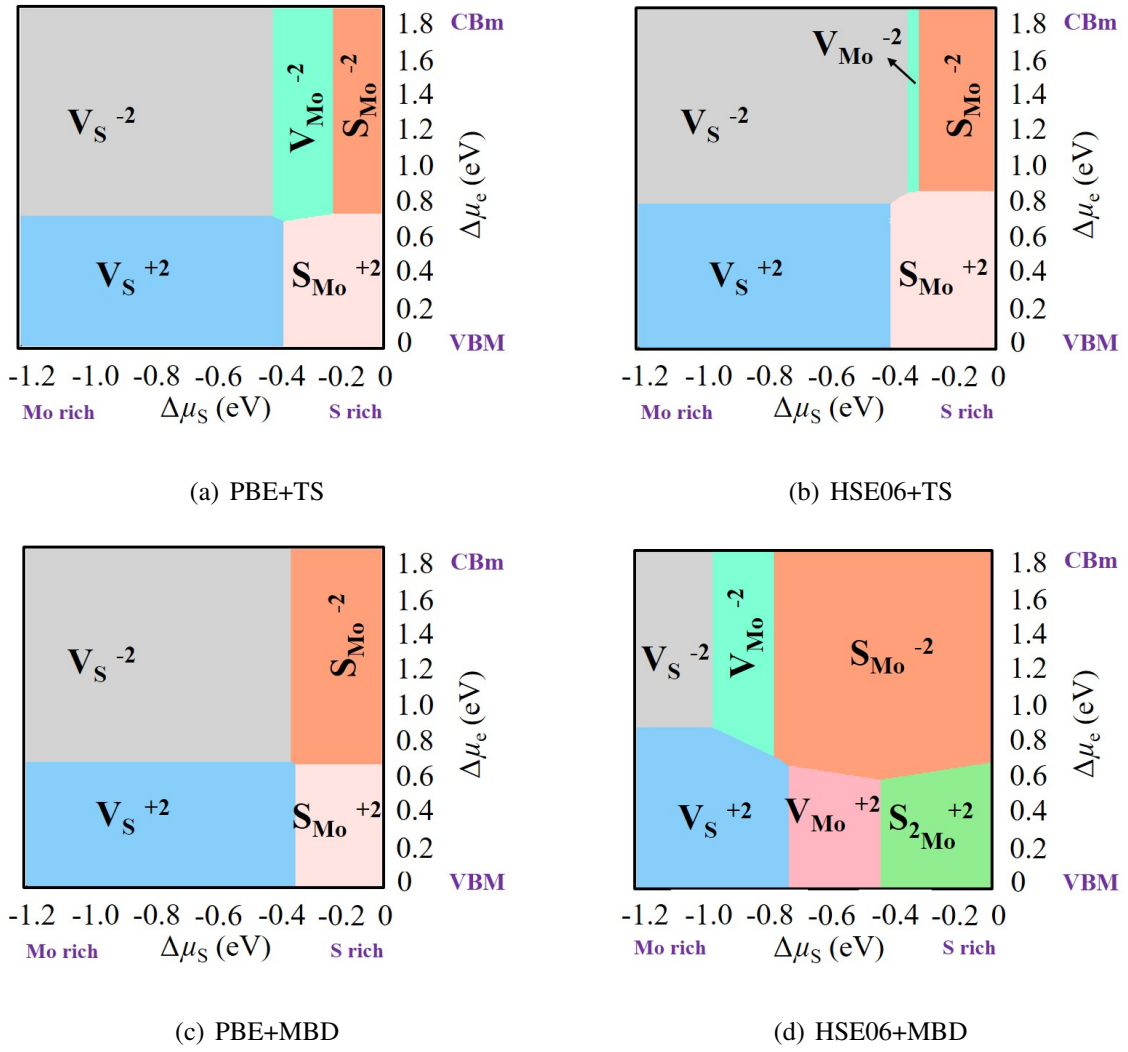

(a) PBE+TS

(b) HSE06+TS

(c) PBE+MBD

(d) HSE06+MBD

Figure 3.3: 3D Phase diagrams that show most stable defect states by the PBE and HSE06 functionals under the two-body vdW interaction (TS) and many-body dispersion (MBD).

MoS_2 monolayer. Similarly, $\Delta\mu_e$ nearer to VBM is the situation of p-type MoS_2 monolayer. In the phase diagrams, negative defect states are stable near CBm and positive defect states are stable near VBM, hence inferring their stability in n-type and p-type monolayer, respectively.

3.3.2 Effect of van der Waals interactions in the stability

The vdW interaction originates as a result of polarization in the material. It is a part of long range non-local correlation energy. The polarization refers to the induced dipole in the system, which will definitely affect the defect states and the charge associated with it. Hence, we have obtained the 3D phase diagrams (Fig. 3.3) for the most stable defect configurations, under two-body vdW interaction and many-body dispersion, with PBE and HSE06 functionals. We have

observed the same defect states as the most stable configurations, by PBE and HSE06 functional under two-body vdW interaction (i.e. PBE+TS and HSE06+TS). The n-type and p-type MoS_2 monolayers have V_S^{-2}, V_{Mo}^{-2}, S_{Mo}^{-2} and V_S^{+2}, S_{Mo}^{+2}, as the most stable states, respectively. Further, on analyzing the phase diagrams under many-body dispersion, we see considerable change in the stability pattern of the defect states. The phase diagram obtained by the HSE06 functional shows the emergence of the new defect states of V_{Mo}^{+2} and $S_{2_{Mo}}^{+2}$ in the S-rich limit, for the case of p-type MoS_2 monolayer. Moreover, the V_{Mo}^{-2} state is absent from the phase diagram obtained by the PBE functional for the case of n-type MoS_2 monolayer. The HSE06 functional incorporates the Hartree-Fock exchange term, which is not the case in PBE functional. Therefore, electron localization is efficient in the former case. Since, many-body dispersion incorporates beyond two-body interactions as well as polarizability screening [126] that has affected the stability of defected system configuration, we need to consider this for the prediction of most stable defect states. Moreover, as the Kohn-Sham eigenvalues is more accurate in the case of HSE06, we report here the inference corresponding to HSE06 functional with many-body dispersion (HSE06+MBD) correction.

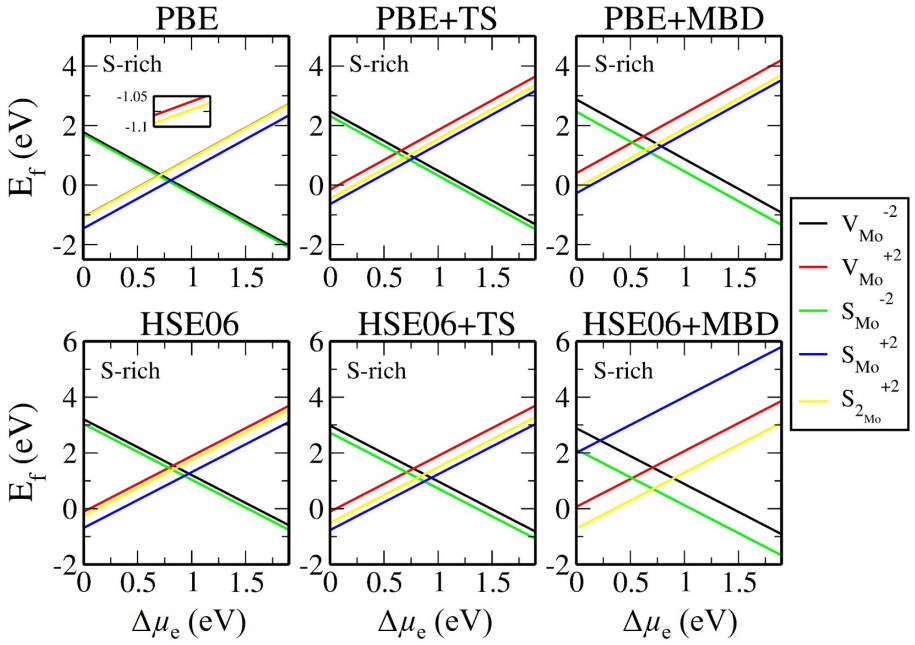

Figure 3.4: Variation of free energy of formation of defect states observed at S-rich limit in 3D phase diagrams by PBE (upper panel) and HSE06 (lower panel) functionals under the two body vdW interaction (TS) and many-body dispersion (MBD).

We now intend to get insight over the energetics of the two functionals under the situations

of no vdW interaction, TS and MBD. Hence, by visualizing the 2D phase diagram in Fig. 3.4 at S-rich limit we see that mostly S^{+2}_{2Mo}, S^{+2}_{Mo} and V^{+2}_{Mo} have very close values of free energy of formation, making these likely to occur in monolayer. The corresponding phase diagram of HSE06+MBD is an exception, where S^{+2}_{Mo} has comparatively high free energy of formation (i.e. less stable). Hence, on observing all the phase diagrams, we understand that there is definitely some competition in free energy of formation of few defects and in a real experiment all of them should have finite probability to occur simultaneously. It's therefore even more interesting to understand the concentration of such defects with varying temperatures.

3.3.3 Defect concentration

After the observation of varied range of stable defects, it becomes imperative to compute the concentration of defects at higher temperatures in order to understand the defect stability. The effect of environment is incorporated using *ab initio* atomistic thermodynamics [67] approach in the chemical potential of sulfur ($\mu_S(T,p) = \frac{1}{2}\mu_{S_2}(T,p_{S_2})$) as per the following expression:

$$\begin{aligned}\mu_{S_2}(T,p_{S_2}) = &-k_B T \ln\left[\left(\frac{2\pi m}{h^2}\right)^{\frac{3}{2}}(k_B T)^{\frac{5}{2}}\right] + k_B T \ln p_{S_2} \\ &- k_B T \ln\left(\frac{8\pi^2 I_A k_B T}{h^2}\right) + k_B T \ln\left[1-\exp\left(-\frac{h\nu_{SS}}{k_B T}\right)\right] \\ &- k_B T \ln \mathcal{M} + k_B T \ln \sigma\end{aligned} \tag{3.6}$$

where m is the mass, $\mathcal{M}$ is the spin multiplicity, and σ is the symmetry number [127, 144]. The above expression includes translational, rotational, vibrational, spin and symmetry degrees of freedom for gaseous molecule of S_2. We have considered two conditions for chemical potential of electrons, i.e., $\Delta\mu_e$ = 0 eV at VBM and $\Delta\mu_e$ = 1.8 eV at CBm, for calculating the concentration of defects under different functional energetics.

If N is the total number of atomic sites in the lattice and E_{fn} free energy of formation of any one kind of defect (let it specify as type-n), then the number of type-n defect states, N_n, is given as

$$N_n = (N - \Sigma_{m\neq n} N_m)\frac{1}{1+\exp(\beta E_{fn})} \tag{3.7}$$

where N_m is the number of the defect states (specified as type-m) other than type-n and $\beta = 1/k_B T$. An equation similar as above can be written for each defect type and their solution will provide the concentration at a finite temperature [127, 144].

$$\frac{N_n}{N} = \frac{\exp(-\beta E_{fn})}{1+\Sigma_{m\neq n}\exp(-\beta E_{fm})} \tag{3.8}$$

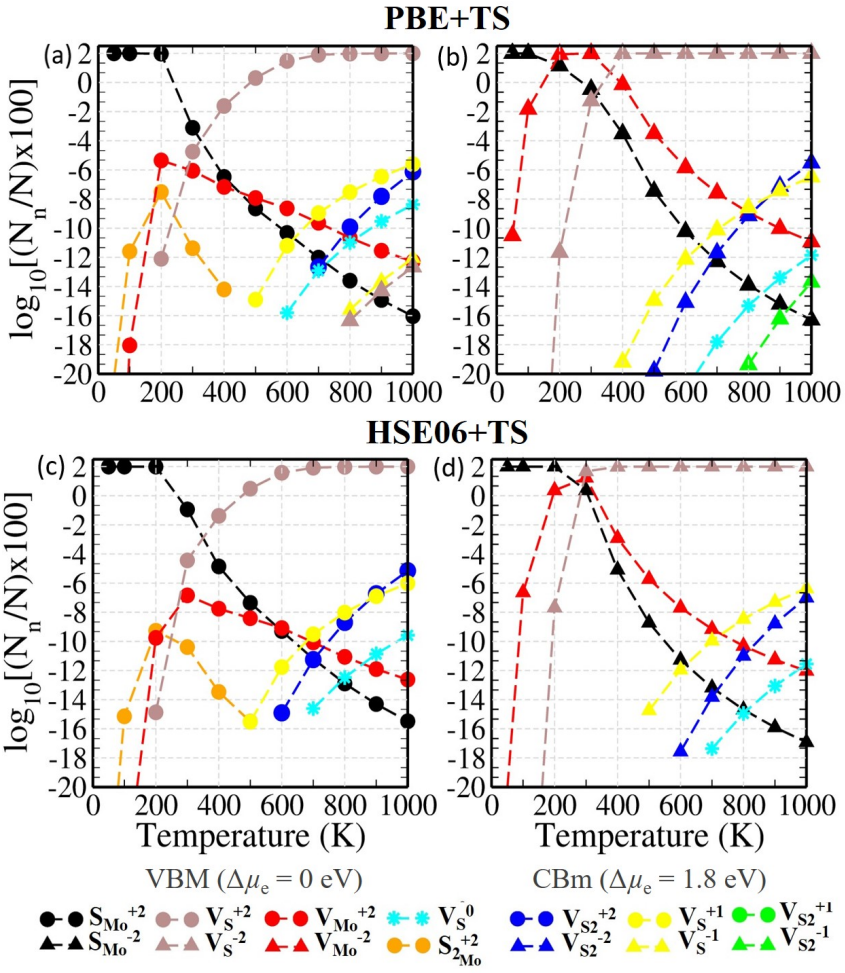

Figure 3.5: Logarithm of concentration (in %) of defects versus T by PBE (upper panel) and HSE06 (lower panel) functionals keeping μ_e at VBM (left panel) and CBm (right panel) under TS scheme of vdW.

We have computed equation (8) for analyzing the concentration of defect states at the finite temperatures. The plot gives the variation of logarithmic percentage concentration of various defects as a function of temperature. The 100% concentration of a defect in the system corresponds to the value of logarithmic percentage concentration as 2. The partial pressure p_{S_2} is fixed at 1 atm, and $\Delta\mu_e$ is set at VBM and CBm.

The concentration plots are obtained for PBE and HSE06 functional under the consideration of TS (Fig. 3.5) and MBD (Fig. 3.6). The earlier discussions stated that positive charges are stable near VBM and negative charges are stable near CBm, and the same is evident from the concentration plots as well. Fig. 3.5 is in correspondence with the 3D phase diagrams of PBE+TS and HSE06+TS. The most stable defect configurations have significant concentrations at the finite temperatures and are accompanied by the concentrations of other defect states viz.

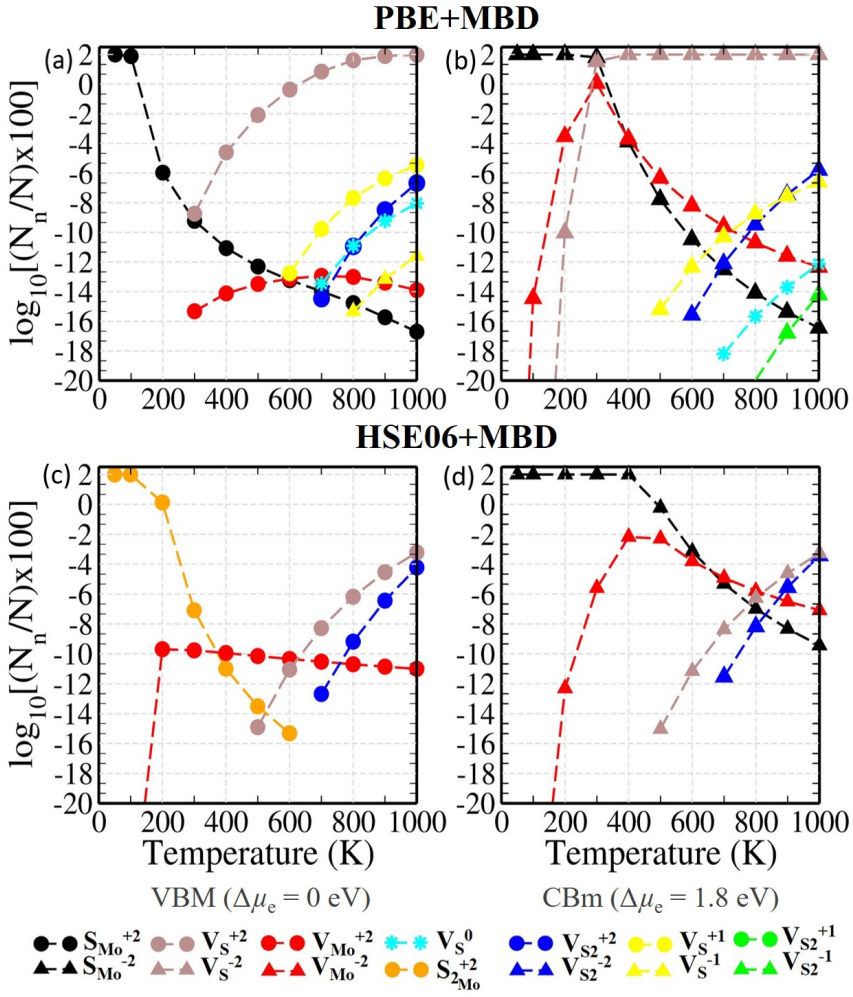

Figure 3.6: Logarithm of concentration (in %) of defects versus T by PBE (upper panel) and HSE06 (lower panel) functionals at VBM (left panel) and CBm (right panel) under many-body dispersion (MBD).

V_S^{+1}, V_S^{-1}, $V_{S_2}^{+2}$ and $V_{S_2}^{-2}$. These concentration plots will help in indicating the occurrence of the defect states, when the monolayer is exposed to the corresponding environmental conditions.

We observe from the Fig. 3.6 that the S_{Mo}^{-2}, V_S^{-2}, V_{Mo}^{-2} achieve significant concentration in the n-type monolayer. The 3D phase diagram for the case of PBE+MBD does not display V_{Mo}^{-2} as most stable state, however, it achieves a significant concentration comparable to that of S_{Mo}^{-2} and V_S^{-2}. Hence, unanimously we observe that, the stable defect states which have significant probability at finite temperatures for n-type monolayer are S_{Mo}^{-2}, V_S^{-2} and V_{Mo}^{-2}. In the p-type case, we see +2 charged state of the defects as stable. The stability of +2 and -2 charged states can be possibly attributed to the electronic configuration of the S ($3s^2 3p^4$) and Mo ($4d^5 5s^1$). They both have six valence electrons, therefore, the antisite (S_{Mo}) and the vacancies (V_S and

V_{Mo}), can be both donor and acceptor at VBM and CBm, respectively. However, S vacancies are observed to be the abundant defects. These could be created with S^{-2} ions leaving the site and hence, as per charge neutrality S vacancy would be stable at -2 charged state. It is clear from the phase diagrams and concentration plots that Mo vacancy is stable for a short range of $\Delta\mu_S$. This may be attributed to larger atomic radius and greater atomic mass of Mo than that of S.

The general trend of the defect states in n-type monolayer are in sync with the existing literatures. The improbability of Mo antisites have also been inferred in the works of Hong *et al.*[93]. However, the obtained stable charged state differs from the previous works. The corresponding explanation have been attributed to the valence electronic configuration of the Mo and S atoms. Moreover, the $S^{+2}_{2_{Mo}}$ defect state is visible as the stable state in phase diagram with HSE06+MBD. The $S_{2_{Mo}}$ phase has been discussed in the experiment cum theoretical work of Zhou *et al.*[145]. Hence, this also gives an indication that HSE06+MBD correlates well with the experimental finding. The aspect of defect states in p-type MoS_2 monolayer and inclusion of many body dispersion adds to the broader defect literature of MoS_2 monolayer. Further, the wide applicability of our inference is ascertained by obtaining the optical response of the defect states in comparison with the pristine, as discussed in the following section.

3.3.4 Absorption spectra

Table 3.1 contains the information about the band gaps corresponding to stable defect states as obtained by HSE06 functional. We observe that S^{-2}_{Mo} and $S^{+2}_{2_{Mo}}$ have band gap in range 1.1 to 1.8 eV, which implies its application in photovoltaics. We have commented on its applicability by obtaining the absorption spectra (Fig. 3.7) by HSE06 functional. The imaginary part of the frequency dependent complex dielectric function, $\varepsilon(\omega) = \mathrm{Re}(\varepsilon) + \mathrm{Im}(\varepsilon)$, gives the absorption. The real part is calculated by the Kramers-Kronig relation. The basic contribution to the analysis of optical properties is achieved by the interband process that includes transitions to an unoccupied higher band. Hence, it is this interband matrix elements in the momentum space that results in imaginary part of the dielectric function The defect states display red shift that implies enhanced optical response in visible region. Hence, in case these defect states are created or induced in the system, it may be utilized in the aforementioned applications. A small bump seen at 0.6 eV in the spectra corresponding to S^{-2}_{Mo}, is attributed to the partial charges that occupy the orbitals.

Table 3.1: Band gap corresponding to stable defect states as obtained by HSE06 functional

Defect	Pristine	V_S^{-2}	V_S^{+2}	V_{Mo}^{-2}	V_{Mo}^{+2}	S_{Mo}^{-2}	$S_{2_{Mo}}^{+2}$
Band gap (eV)	1.96	0.75	0.02	0.47	0.60	1.34	1.14

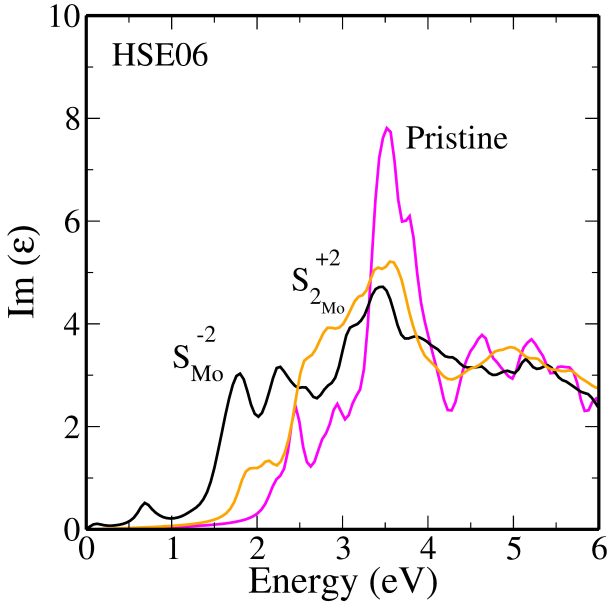

Figure 3.7: Imaginary part of dielectric function (Absorption spectra) as obtained by HSE06 functional

3.4 Conclusions

An exhaustive study has been undertaken for understanding the stability of defect configurations in MoS_2 monolayer. We have observed that defect configurations are not stable in the neutral state and the Mo antisites are improbable to occur due to their high formation energies. The results have indicated that the stability of defect configurations depend on the many body dispersion and therefore, for accurate experimental correlation this should be incorporated in the studies. The most probable defect configurations as obtained by the HSE06+MBD are V_S^{-2}, V_{Mo}^{-2} and S_{Mo}^{-2} for n-type monolayer; and V_S^{+2}, V_{Mo}^{+2} and $S_{2_{Mo}}^{+2}$ for p-type monolayer. The $S_{2_{Mo}}^{+2}$ that appeared to be stable by HSE06 functional with MBD, also showed significant concentration by HSE06 functional with TS scheme of vdW. Further, the computed concentration of all the stable defect states verifies their presence at finite temperatures. In addition, we have observed red shift in the optical response of S_{Mo}^{-2} and $S_{2_{Mo}}^{+2}$ from that of pristine, extending their applicability in photovoltaics. Since, a defect free MoS_2 monolayer is practically impossible, harnessing

these defect states for absorption in photovoltaics is considerable. Moreover, there is enough scope of experimental understanding of the discussed point defects in p-type MoS_2 monolayer, which would pose an important inference for applications in device industry.

CHAPTER 4

Role of adsorbed water in the negative differential resistance observed in the 2D MoS_2 thin films

4.1 Introduction

The layered 2D van der Waals (2D vdW) materials have established versatility and massive potential for various applications owing to their mechanical, electrical, chemical, and optical properties [146, 147]. The property under consideration of research here is the negative differential resistance (NDR) effect using 2D vdW materials. This is achieved by forming hybrid/standard heterojunctions with huge potential for signal processing, amplifiers, data storage technology, and neuromorphic computing [148]. The NDR effect corresponds to the decrease in device current with increased applied bias voltage. This non-linear effect was first observed in the tunnel diode by Leo Esaki in 1958 [149]. The material under consideration was the heavily doped narrow p-n junction of germanium. Obtaining the NDR effect in thin-film-based devices has been an exciting topic. NDR effect has been subsequently investigated for devices based on hybrid perovskite, 2D vdW heterostructures, and 2D vdW/organic hybrid heterojunction [150, 151, 152, 153, 154]. When conducting electrical characterizations, the tunnelling of electrons frequently plays a crucial part in demonstrating the NDR effect. However, apart from theoretical prediction, there is no literature evidence of a planar 2D vdW device displaying the well-known NDR phenomenon [155].

Developing proton-conductive materials for applications such as fuel cells, batteries, and sensors has enormous potential [156, 157, 158]. Proton-conductors have (H^+) as primary charge carriers. One of the mechanisms that explain proton conduction via hydroxide (OH^-) and hydronium (H_3O^+) is the Grotthuss mechanism that was proposed 200 years ago [159, 160]. Since 2013 first principles approaches have indulged in understanding the same. However, the

water-chain network, structure, and in-plane protonic conduction are elusive in literature. Recent studies have reported the Grotthuss proton transfer in zinc oxide-water interfacial systems favoring the multiple water molecules [161]. In addition, first-principles calculations have also reported a phase diagram of water confined in nanoscale with a hexatic phase showing high electrical conductivity [162]. The discovery also observed monolayer of water being extremely sensitive to temperature and van der Waals pressure. It is desirable to demonstrate this experimentally in a proper context to see real-world variations from theoretical predictions.

Here, the work is based on the thin film growth of MoS_2 by the self-assembly at the junction of two immiscible liquids of hexane and water. The electrical characteristics examined on the thin film deposited on glass substrates have observed NDR with a peak-to-valley current ratio (PVCR) of 6.3 at the ambient environment and room temperature. The NDR peaks obtained have been consistent and reproducible in the positive and negative sweep directions. Further, moisture is critical in observing the property indicating the absorbed water at defect sites to promote electrochemical redox processes. The computational studies have verified the adsorption of atmospheric moisture and the subsequent electrolysis. Results indicate the defect sites to be more prone to adsorb OH^- ions. Hence, this promotes the H^+ ions transfer and the NDR. This work, therefore, highlights the NDR in the liquid-phase exfoliated (LPE) thin film of MoS_2 on desired substrates without availing the sophisticated instruments. This is the first time such an effect is observed in the LPE based MoS_2 thin films at room temperature ambient conditions.

4.2 Computational Methodology

The first-principles based density functional theory (DFT) calculations as have been employed in the present work [27, 129, 130, 131, 136, 137]. The associated code chosen is Vienna *ab initio* simulation package (VASP) [141, 63, 132] with projector augmented wave (PAW) pseudopotentials using plane wave basis. The generalized gradient approximation (GGA) that accounts for the exchange-correlation (xc) interaction amongst electrons is incorporated by PBE xc functional (as proposed by Perdew-Burke-Ernzerhof (PBE) [163, 138]). The conjugate gradient minimization with energy tolerance of 0.001 meV and the force tolerance of 0.01 eV/Å. The plane wave cut-off energy is set to 500 eV. The Tkatchenko-Scheffler vdW scheme has been employed for obtaining optimized structures [124, 125]. We have employed climbing-image nudged elastic band (CI-NEB) method to obtain minimum energy path [164, 165]. The

modelled systems are S vacancy in 4 × 4 MoS_2 monolayer and (4 × 4) MoS_2/(5 × 5) Cu (111) HTS.

4.3 Results and Discussion

Experimentally, the NDR property is observed irrespective of the electrodes used, in the ambient condition and at room temperature. The optimum presence of moisture or water molecules have been deduced to be crucial. Also, the observation confirmed the effect at each sweep of the applied voltages. Therefore, it is pertinent to understand the mechanism behind the observed NDR in the few-layer MoS_2 as grown by the bi-phasic method under liquid phase exfoliation. The emergence of the effect can be correlated with the protonic conduction between the two electrodes. Also, the synthesis route plays a massive role in the formation and type of defects. The liquid-phase exfoliated MoS_2 nanoflakes are prone to defect sites at the edges and basal planes, thereby facilitating the adsorption of water molecules and their thin layer formed from the environment. The calculation strongly favors the physisorption of water molecules to the defect sites of MoS_2 nanoflakes. It predicts a higher adsorption possibility of OH^- ions compared to H^+ ions, resulting in the increased mobility of H^+ ions. This indicates the subsequent Grotthuss mechanism between the electrodes upon the application of bias voltage.
Now, a positive bias to the left copper electrode ipromoting the oxidation of water molecules is expressed as:

$$2H_2O \rightarrow O_2 + 4H^+ + 4e^- \tag{4.1}$$

Similarly, at right copper electrode the electrons thus produced facilitate the reduction of water molecules:

$$2H_2O + 2e^- \rightarrow H_2 + 4OH^- \tag{4.2}$$

These redox reactions at both electrodes initiate the protonic conduction through the chain of water molecules indicating the Grotthuss protonic conduction mechanism. The transfer of H^+ ions changes the intermolecular covalent bond between hydrogen and oxygen to the intramolecular hydrogen bond. The underlying process initiates and subsequently increases the device current with the bias voltage due to the protonic conduction. After that, it reaches a peak value and the corresponding NDR peak current. The depletion width reaches a maximum

at peak current, following which the device current starts decreasing with an increase in the bias voltage. The protonic conduction is therefore restricted. Further increased applied voltage leads to the device current towards the NDR valley region. Finally, the trend of I-V beyond the NDR valley region depends on the thermally generated carriers alone, which cannot be avoided in all cases. The calculations performed for the device Cu/MoS_2/Cu with adsorbed

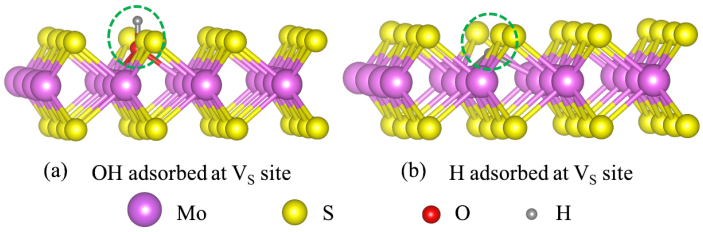

Figure 4.1: Optimized geometries of the defects within the MoS_2 monolayer.

water molecules at the sulfur (S) defect sites of MoS_2 supports the proposed mechanism above. Firstly, the Schottky-type contact between the Cu and MoS_2 have been verified. Now, MoS_2 in its natural form contains point defects that are usually S vacancies and antisites. The synthesis route further adds to the formation and type of these defects. In either case, S vacancies (V_S) are prominent in MoS_2 monolayer and bulk. We obtained the optimized structure of the adsorbed H^+ and OH^- at the defect sites as shown in Fig. 4.1, respectively. The binding energy (E_b) strength of the same was obtained by equation 3 below:

$$E_b = E_{DS} - E_{SP} - E_{AS} \tag{4.3}$$

where E_{DS}, E_{SP}, and E_{AS} represent the energy of the defected system (Cu/MoS_2) with adsorbed species, energy of the system (Cu/MoS_2) with point defect V_S, and energy of adsorbed species, respectively. We found the E_b of H^+ and OH^- are –0.37 eV and –3.47 eV, respectively. The higher E_b of the OH^- is accompanied by more charge transfer in their neighbouring Mo and S atoms, as seen through the Hirshfeld charges (Table 4.1). This indicates that OH adsorption affects electron conduction as these are prominent on the vacancy S sites. Further, it is imperative to understand that at a specific temperature, V_S would not exist in neutral form but in charge states, in both monolayer and multilayer. Therefore, the V_S^{+2} being abundant and stable with +2 charged state adsorbs OH^-. Hence, these charged state leads to the dissociation of H_2O to H^+ and OH^-. The H^+ exists in the form of hydronium (H_3O^+) in the water layer. Thus, active sites prefer OH^- adsorption, thereby facilitating the H^+ to transfer and conduct between electrodes through the water molecular chain. This defect mediated H^+ transfer as

Table 4.1: Hirshfeld charges (e) at S vacancy neighboring atoms.

Site	S vacancy	With H^+ adsorbed	With OH^- adsorbed
Mo_1	0.207	0.235	0.261
Mo_2	0.206	0.219	0.261
Mo_3	0.207	0.236	0.260
S	-0.137	-0.120	-0.123
H	—	-0.108	0.146
O	—	—	-0.223

shown in Fig. 4.2 creates a gradient between OH^- and H_3O^+ species, thus supporting NDR effect in MoS_2 device in the presence of adsorbed water molecules. The previous studies, such as Manoranjan Ghosh et al. have also indicated the dissociation of H_2O and adsorption of OH^- on the O vacancy sites, that facilitates the proton conduction, thereby affecting the NDR seen in the system [166]. Further, we have obtained the minimum energy path by performing CI-

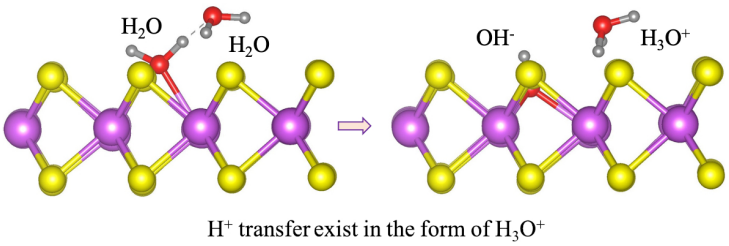

Figure 4.2: Optimized geometries of the defects within the MoS_2 monolayer.

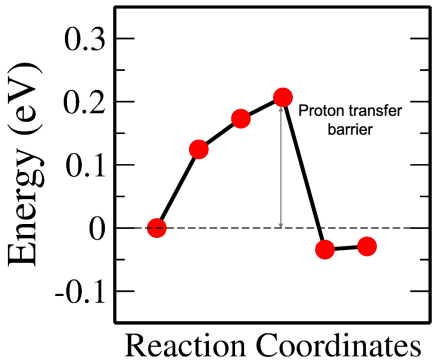

Figure 4.3: Minimum energy path for proton transfer on the single layer of MoS_2

NEB calculations for proton transfer leading to OH^- and H_3O^+ species from $2H_2O$ molecules.

The corresponding system consists of two V_S in the MoS_2 monolayer. We observe a barrier height of 0.21 eV which indicates the requirement of bias to overcome the barrier for proton to transfer from one H_2O molecule to another, thereby forming H_3O^+. Hence, this strongly supports the proposed Grotthuss mechanism on proton diffusion through the water molecular channel between the electrodes as previously discussed.

4.4 Conclusion

In conclusion, the solution-processed few-layered 2D MoS_2 nanoflakes (NFs) using the biphasic (BPM) method have efficiently deposited the high-quality thin films. The corresponding thin film devices with metal/MoS_2/metal structures were made with the interdigitated electrodes of copper (Cu) or gold (Au). The system exhibited NDR property with PVCR of 6.6 and >10.0 with Cu and Au electrodes, respectively. The property observed is robust and highly reproducible under the ambient conditions, presence of moisture and room temperature, thereby indicating the crucial role of moisture in the MoS_2 thin film device. The underlying mechanism is controlled by the protons (H^+) that are produced by the electrolysis of adsorbed water molecules at the edges, basal planes or defect sites of MoS_2. These protons transfer between two metal electrodes through the adsorbed water molecular wire kind of structure under bias-controlled favourable MoS_2 valence band. The depletion layer broadening between the metal electrode and MoS_2 constrains the in-plane protonic conduction that lowers the device current. The Hirshfeld analysis and the minimum energy profile show that OH^- ions interact more strongly than H^+ at the atomic sites on the MoS_2 surface, indicating higher protons' mobility. Hence, the layered van der Waals (vdW) materials can be utilized for NDR-based applications like signal processing, neuromorphic computing, amplifiers, and multi-valued logic devices.

CHAPTER 5

Designing MoS_2 and MoSSe (Janus) based van der Waals heterostructures for photocatalytic hydrogen evolution reaction

Pollutant degradation and water splitting is an urgent necessity for sustainability [167, 168, 169, 170]. 2D materials as discussed in previous sections is widely researched upon especially MoS_2 from transition metal dichalcogenides (TMD) family. These materials have been engineered and studied for photovoltaics and optoelectronics [171, 172, 173, 85]. Apart from $MoSe_2$, WS_2, MoS_2 and WSe_2, other TMDs such as ZrS_2, HfS_2, and TiS_2 have also generated interest in engineering and tuning the properties for aforementioned applications [174, 175, 176]. Now as per Lebègue *et al.* [177] the stable bulk phases of transition metal oxides are rare thereby affecting their low experimental synthesis [178]. These material have put forth a huge potential. Recently, Janus materials (MXY; M = Mo and X,Y = O, S, Se and Te; X$\neq$Y) have drawn a lot of interest for phototcatalytic applications [179, 180]. They have vertical dipole moment and lack mirror symmetry [181, 182]. van der Waals heterostructures (HTSs) have exemplified valley physics and interlayer screening effects thereby evident in the present work [140, 183, 184, 185, 186, 187, 188, 189, 190, 191, 192, 193].

MoS_2 monolayer have direct band gap and its redox potentials are apt for a photocatalyst [194, 195]. However, the carriers (electron (e^-), hole (h^+)) is generated in the same spatial region, hence incresed recombination [196]. vdW HTSs with type II band alignment have established itself as successful alternative due to the spatial separation of e^- - h^+ carriers on different layers. vdW HTSs showcase two types of photocatalytic mechanisms:

(a) Simple heterojunction photocatalysts: In this case the CBm and VBM, that are associated with two different monolayers of the vdW HTSs, straddle the redox potential [197, 198]. Hence, the spatial charge separation is facilitated with reduction and oxidation reactions on

different monolayer, respectively.

(b) Z-scheme systems: This is natural photocatalysis [199, 200, 201], where also the type II alignment is mandatory. In this case the CBm and VBM does not straddle the redox potentials. Infact, the layer with its CBm straddling the reduction level is utilized for hydrogen evolution reaction (HER) and another layer with VBM straddling the oxidation level is utilized for oxygen evolution reaction (OER), respectively (Fig. 5.1).Therefore, high number of interlayer e^{-} - h^{+} recombination as compared to that of intralayer is necessary for the process [202, 203, 204].

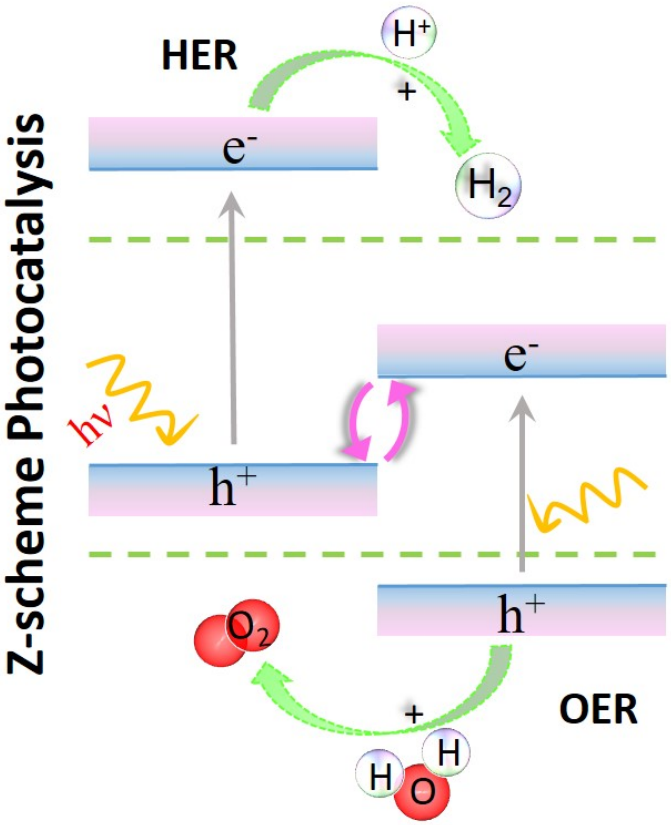

Figure 5.1: Schematic of Z-scheme photocatalysis.

The lubricancy due to weak vdW forces facilitates the interlayer movement that assists the Z-scheme photocatalysis [205]. There exists vdW HTSs under this regime [206, 205, 199, 207], but no extensive study on MoS_2 based bilayer vdW HTSs with TMOs (viz. HfO_2, T-PtO_2, T-SnO_2) and TMDs (viz. HfS_2, ZrS_2, TiS_2) as second layer is observed so far. Also the database of Janus (MoSSe) based bilayer vdW HTSs is at an initial stage. There are two possible stacking arrangements for MoSSe based vdW HTSs. Hence, it is crucial to compare the possible stacking configurations of MoSSe based vdW HTSs with the MoS_2 based vdW HTSs, for the

photocatalytic application.

In reference to the Rasmussen *et al.* we have started our research with the alignment of type II vdW HTSs [208] for photocatalytic applications. Analysis for both the monolayers of TMDs and TMOs are present in this work. In further sections, we have studied the vdW HTSs of MoS_2 (and MoSSe) with (i) TMOs viz. HfO_2, T-PtO_2, T-SnO_2 and (ii) TMDs viz. WS_2, HfS_2, ZrS_2, TiS_2. The present literature, have not discussed the these vdW HTSs for the Z-scheme photocatalysis. We have synchronously studied the pertinent parameters such as band gap, Hirshfeld charge, absolute band edge positions, recombination and optical response.

5.1 Computational Methodology

We have employed first-principles based methodology under the framework of DFT [27, 129, 130, 131, 136, 137]. The PAW pseudopotentials are used in our calculations using plane wave basis set as employed in Vienna *Ab initio* Simulation Package (VASP) [141, 63, 132]. The xc interaction amongst electrons are accounted by Generalized Gradient Approximation (GGA) with the functional form as proposed by Perdew-Burke-Ernzerhof (PBE) [163, 138]. The hybrid density functional have also been employed to account for the same with the functional proposed by Heyd-Scuseria-Ernzerhof (HSE06) [139]. The hybrid functional (HSE06) considers 25% mixing (α) of the short range Hartree-Fock (HF) exchange. Its long range part is described by GGA-PBE functional.

The vdW HTSs are optimized using PBE functional and HSE06 is used to determine single point energy. The Conjugate Gradient Minimization is performed with the Brillouin Zone (BZ) sampling of $2 \times 2 \times 1$ K-grid and the energetics are obtained by the BZ sampling of $16 \times 16 \times 1$ K-grid. The energy tolerance of 0.001 meV and force tolerance of 0.001 eV/Å have been used for optimization. In the ground state calculations, the plane wave cut-off energy is set to 600 eV. The vdW HTSs are modelled with 20 Å vacuum in order to avoid electrostatic interactions between the periodic images. The two-body vdW interaction as devised by Tkatchenko-Scheffler has been employed [124, 125]. The correction parameter is based on Hirshfeld partitioning of the electron density. Note that, we have not included spin-orbit coupling (SOC) in our calculations, since the previous literatures have reported only slight change in band gap due to the same [199, 209, 210]. The optical properties are calculated using the GW approach [211, 212]. We have performed hybrid calculations (HSE06), as an initial step for single shot GW calcula-

tions [i.e. G_0W_0@HSE06].

5.2 Results and Discussion

5.2.1 Heterostructure stacking

We have constructed commensurate bilayer vdW HTSs [213] with minimum lattice mismatch between the layers. The vdW HTSs have been formed with monolayer of MoS_2 (or MoSSe) along with that of WS_2, ZrS_2, HfS_2, TiS_2, HfO_2, T-PtO_2 and T-SnO_2, in vertical alignment. The specifications of the monolayers (Table 5.1) corroborate with the existing literature [214, 208, 215]. All the monolayers are constituted as $2\times2\times1$ supercell (24 atoms) except ZrS_2 and HfS_2 with $\sqrt{3}\times\sqrt{3}\times1$ supercell (21 atoms). Here, the stacking styles between two monolayers have not been varied in each vdW HTS. This is due to the fact that, the binding energy change of merely few meV is observed with the change in stacking styles of two monolayers in a particular vdW HTS [216, 217].

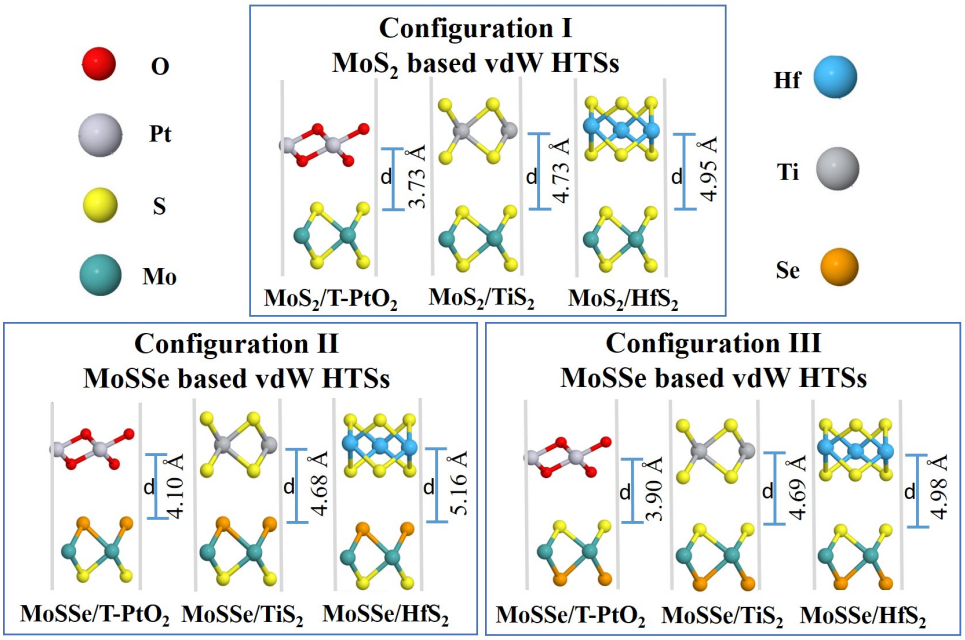

Figure 5.2: vdW HTSs with configuration I, II and III. MoS_2/BX_2 (configuration I), MoSSe/BX_2 (configuration II), where Se atomic layer is at interface and MoSSe/BX_2 (configuration III), where S atomic layer is at interface.

We have calculated the binding energy of vdW HTSs by the expression [216],

$$E_b = E(\text{vdW HTSs}) - E(MoS_2 \text{ or MoSSe}) - E(BX_2) \tag{5.1}$$

where E_b is the binding energy of the vdW HTS MoS_2/BX_2 (or $MoSSe/BX_2$); $E(MoS_2)$ is the energy of monolayer MoS_2; E(MoSSe) is the energy of monolayer MoSSe and $E(BX_2)$ is the energy of monolayer BX_2 (where B = W, Hf, Zr, Pt, Sn and X = S or O).

Table 5.1: Lattice constants (l) of 2×2 monolayers

BX_2	MoS_2	WS_2	ZrS_2	HfS_2	TiS_2	HfO_2	T-PtO_2	T-SnO_2
l	6.321	6.321	7.120	7.019	6.660	6.243	6.296	6.450

Table 5.2: The corresponding bilayer vdW HTS lattice mismatch and binding energies of different configurations (MoS_2/BX_2(I), $MoSSe/BX_2$(II and III)) are enlisted

BX_2	Lattice mismatch (%)	Binding Energy (eV)		
		I	II	III
WS_2	0.0	-1.04	-1.05	-1.02
ZrS_2	2.5	-0.49	-0.54	-0.52
HfS_2	3.9	-0.30	-0.35	-0.33
TiS_2	2.5	-0.45	-1.00	-0.94
HfO_2	1.2	-0.40	-0.54	-0.47
T-PtO_2	0.4	-0.83	-0.63	-0.68
T-SnO_2	1.8	-2.19	-2.24	-2.22

Fig. 5.2 shows the three configuration of vdW HTSs as considered in the present work. Configuration I is of the type MoS_2/BX_2. The stacking type of MoS_2/T-SnO_2, MoS_2/ZrS_2 and MoS_2/WS_2(or HfO_2) are same as that of MoS_2/T-PtO_2, MoS_2/HfS_2 and MoS_2/TiS_2, respectively. On replacing MoS_2 with MoSSe, we have constituted configuration II and III. The former consists of Se atomic layer of MoSSe at the interface, whereas the latter has S atomic layer at the interface. Configuration II and III also follow the same analogy as configuration I. Table 5.2 enlists the lattice mismatch and the binding energy of all the vdW HTS configurations. We define the mismatch as $(l(MoS_2) - l(BX_2))/l(BX_2)$, where l is the lattice constant of MoS_2 and BX_2 respectively.

5.2.2 Band edge alignment

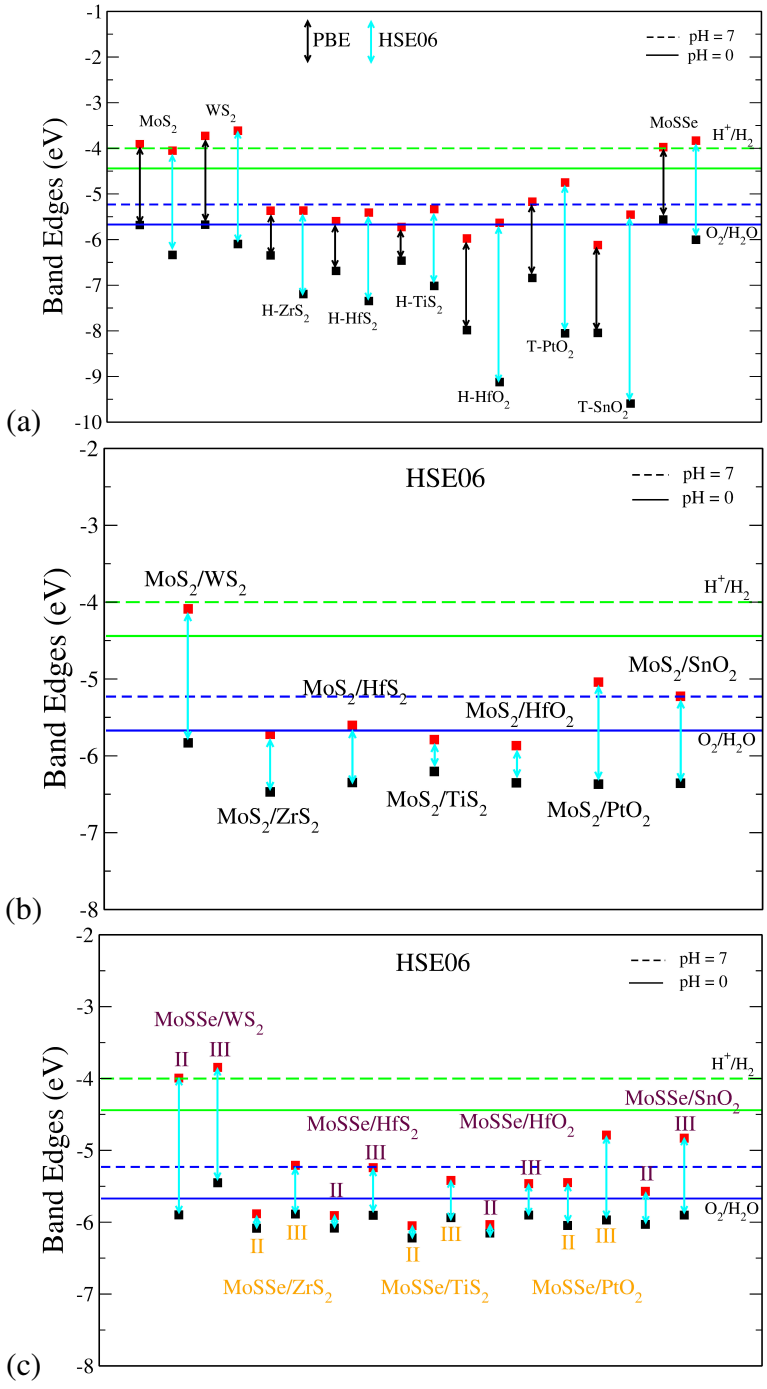

Figure 5.3: Band edge alignment with respect to water redox potentials of (a) individual monolayers, (b) MoS_2/BX_2 vdW HTSs (configuration I), (c) $MoSSe/BX_2$ vdW HTSs (configuration II and III), where BX_2 refers to WS_2, ZrS_2, HfS_2, TiS_2, HfO_2, PtO_2 and SnO_2.

The photocatalytic applications require the understanding of band gaps and absolute band edge positions. We have calculated these with both PBE and HSE06 functionals. Fig. 5.3(a) provides

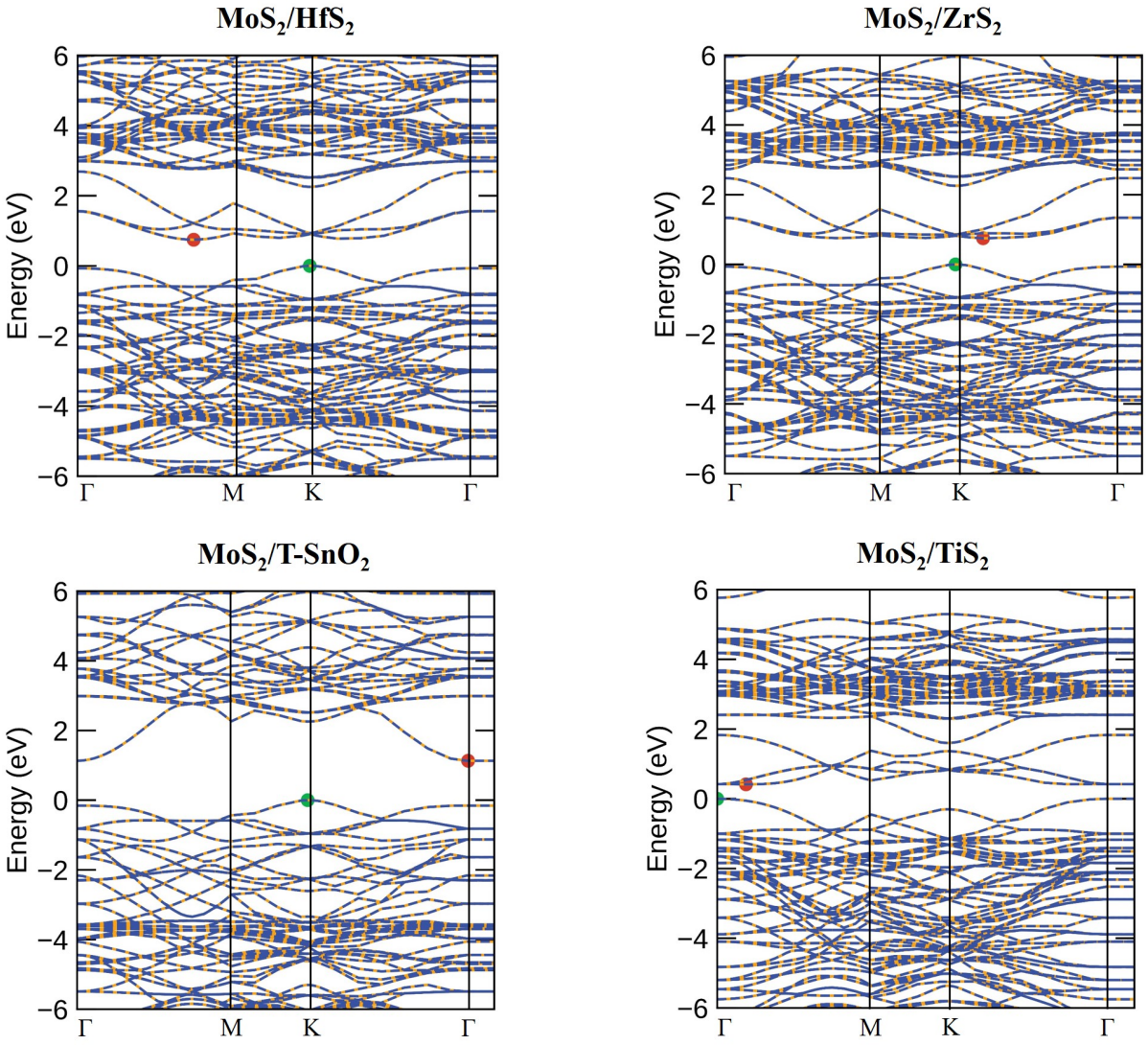

Figure 5.4: Bandstructures corresponding to the supercell of MoS_2/BX_2 HTSs (configuration I) where MoS_2/ZrS_2 has similar bandstructure as that of MoS_2/HfS_2. The bandstructures corresponding to the MoSSe based vdW HTSs (configurations II and III) are similar with slight change in energetics. The red and green points correspond to the conduction band minimum and valence band maximum.

Table 5.3: Band gaps of the monolayers and their corresponding vdW HTSs.

BX_2	Band Gap (eV) (Indirect/Direct)			
	Monolayer	I	II	III
MoS_2	-/2.257	-	-	-
MoSSe	-/2.172	-	-	-
WS_2	-/2.447	1.636/2.038	1.879/1.885	1.589/1.928
ZrS_2	1.829/1.892	0.752/0.809	0.123/0.177	0.676/0.729
HfS_2	1.937/2.019	0.746/0.863	0.079/0.185	0.663/0.773
TiS_2	1.672/1.769	0.414/0.418	0.047/0.056	0.520/0.525
HfO_2	3.516/3.520	0.486/0.499	0.072/0.090	0.440/0.453
T-PtO_2	3.304/3.313	1.323/1.525	0.595/0.846	1.178/1.423
T-SnO_2	4.143/4.297	1.130/1.285	0.460/0.882	1.069/1.473

band edge alignment of the monolayers. We observe here that the chosen monolayers for vdW HTSs have type II heterojunction. In the figure, H^+/H_2 and O_2/H_2O correspond to the reduction and oxidation potential of water splitting, respectively, both for pH(0) (solid line) and pH(7) (dashed line). Fig. 5.3(a), therefore, shows that HSE06 and PBE show sufficient discrepancies in estimating band edge positions. Calculations with HSE06 functional incorporate HF exact exchange term resulting due to self-interaction error of e^-, which is not well taken care of in the case of PBE functional. Hence, the results presented in further plots are carried out by the HSE06 functional. Fig. 5.3(b) and Fig. 5.3(c) depict the absolute band edge positions of the MoS_2 and MoSSe based vdW HTSs, respectively. Fig. 5.3(b) indicates that individual band alignment approximately predicts the combined alignment of the vdW HTSs. The weak vdW interaction between 2D monolayers is attributed to the aforementioned indication. Here, the type II alignment can be seen with VBM of MoS_2 (or MoSSe) monolayer and CBm of HfS_2, ZrS_2, TiS_2, HfO_2, T-PtO_2 and T-SnO_2 monolayers. The band gaps of the monolayers and vdW HTSs are listed in Table 5.3. Now, the CBm and VBM should lie a few eVs above and below the redox potentials for the material to be good for photocatalysis. However, in our case the vdW HTS band gap does not straddle the photocatalytic water splitting potentials. Hence, we analyze these bilayer vdW HTSs for their applicability as Z-scheme photocatalyst.

The vdW HTSs deduced for further analysis from Fig. 5.3 are the configurations consisting HfS_2, ZrS_2, TiS_2, HfO_2, T-PtO_2 and T-SnO_2. Note that MoS_2 (or MoSSe) monolayer (CBm) does form type II alignment with WS_2 (VBM) as well and the HTS is observed to be capable for photocatalysis (but not via Z-scheme). However, we have included this in our manuscript as a reference, with an intention to showcase clear distinction w.r.t Z-scheme photocatalysts. Moreover, on observing Fig. 5.3(c) a unanimously similar trend infers that the band gap of vdW HTSs of configuration II is significantly different than that of configuration III.

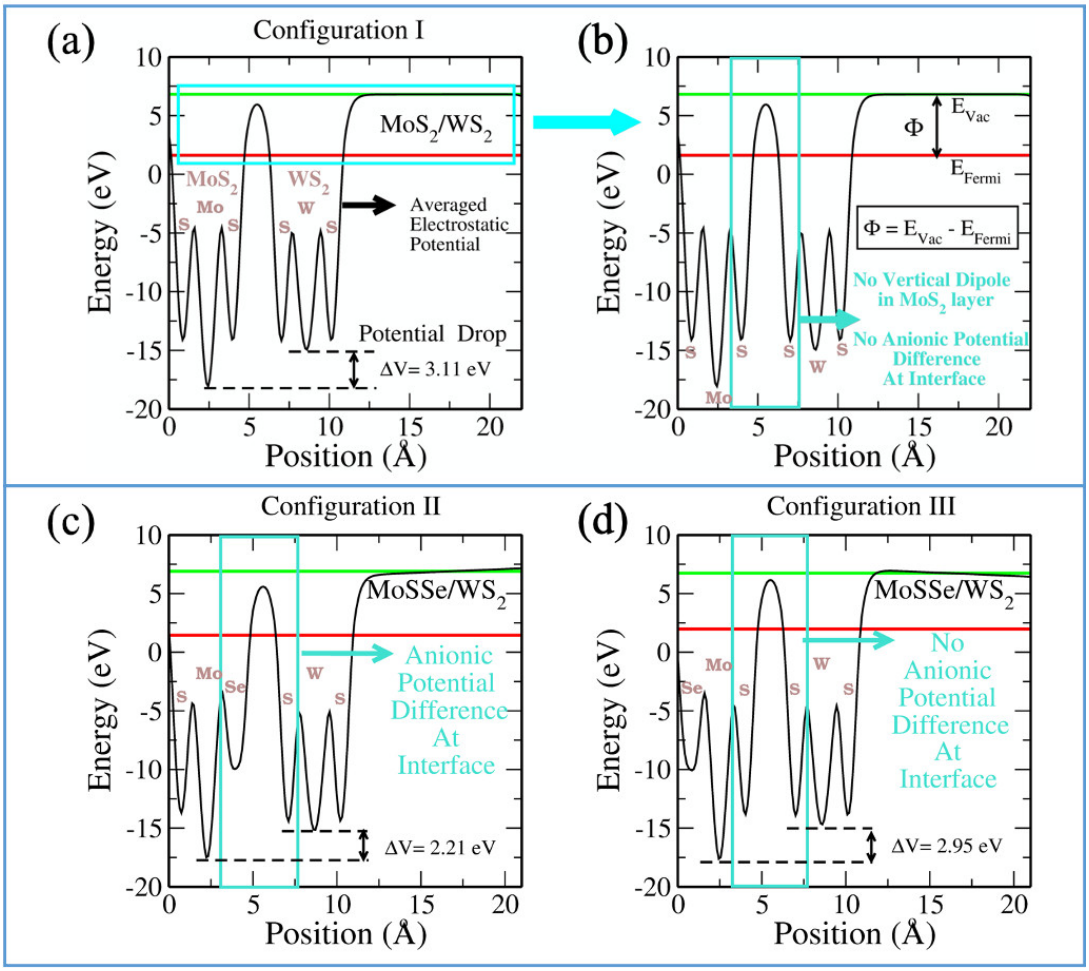

Figure 5.5: Electrostatic potential plot of MoS_2/WS_2 depicting (a) the potential difference, (b) the work function in configuration I, (c) cationic and anionic potential difference in configuration II, and (d) configuration III.

It should be noted that the absolute band edge alignment is obtained with respect to the zero vacuum level. The associated E_{Vac} (vacuum level) of each calculation is obtained from the electrostatic potential of the system. As is evident from the term, the plot explains the electrostatic potential corresponding to each atomic layer (Fig. 5.5). It is pertinent to understand the plot

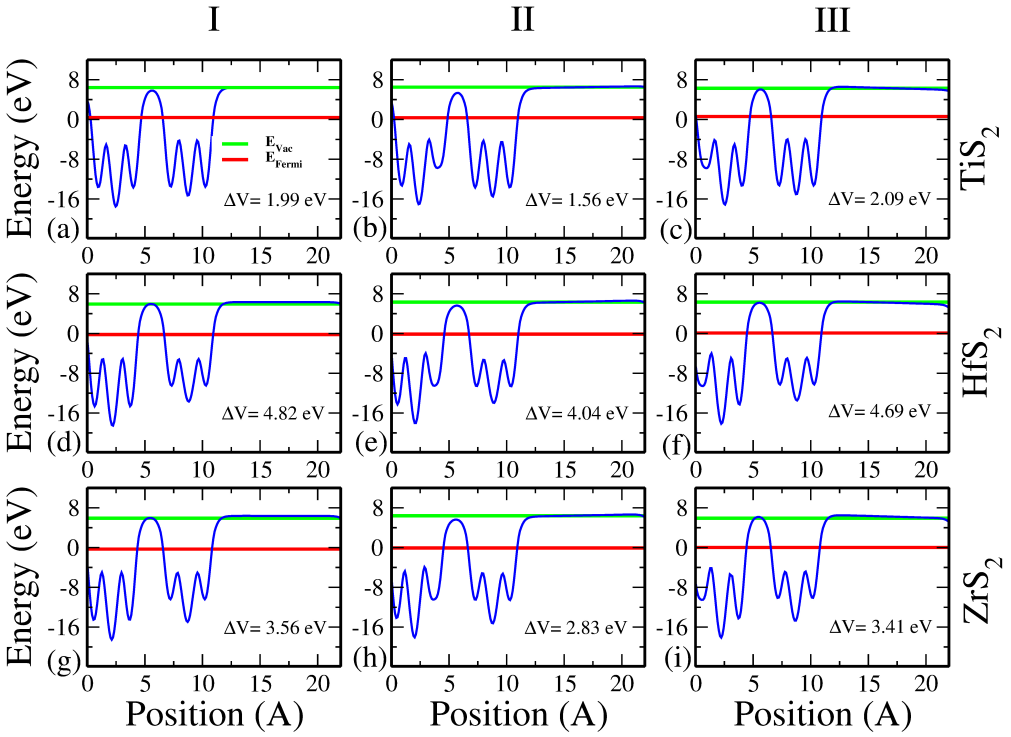

Figure 5.6: Averaged electrostatic potential corresponding to TMDs viz. TiS_2 (upper panel), HfS_2 (middle panel) and ZrS_2 (lower panel) for I, II and III configurations.

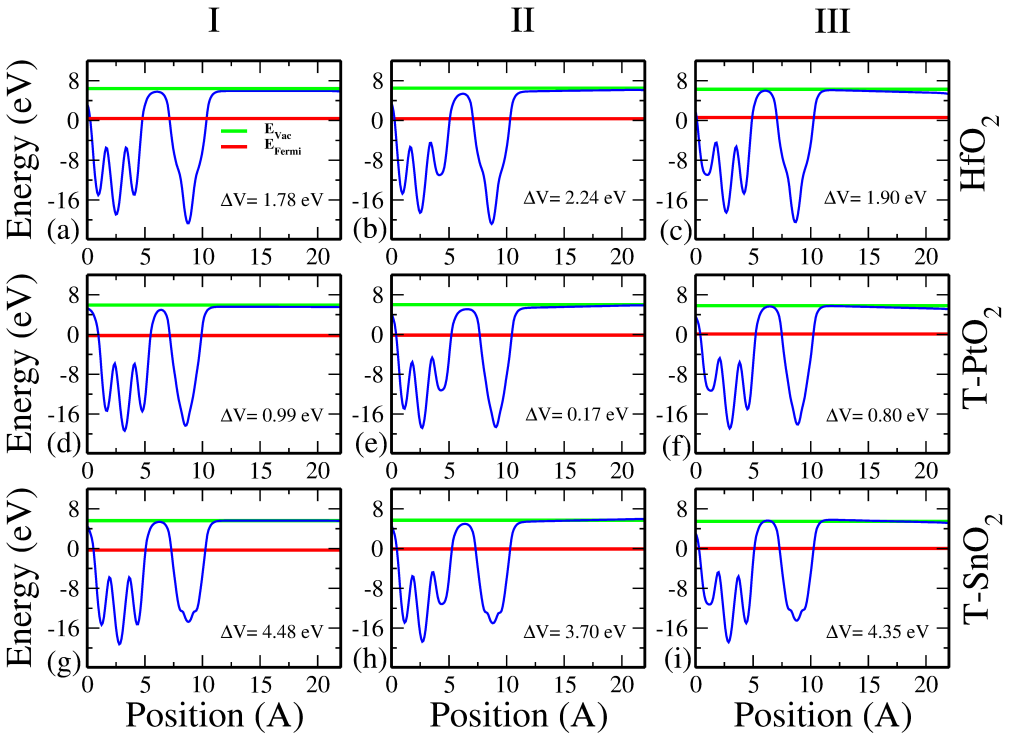

Figure 5.7: Averaged electrostatic potential corresponding to TMOs viz. HfO_2 (upper panel), T-SnO_2 (middle panel) and T-PtO_2 (lower panel) for I, II and III configurations.

as it informs about the work function and potential difference between the monolayers. Thus, we are able to analyze the interlayer charge transfer that indicates the photocatalytic strength. Fig. 5.5 corresponds to the electrostatic potential plot of MoS_2/WS_2. Considering left to right chronology in Fig. 5.5(a), we observe the potential of S, Mo, S atomic layers of MoS_2 monolayer and S, W, S atomic layers of WS_2 monolayer. We see a clear difference in the potentials of cationic layers viz. Mo and W atomic layers. The gradient between the monolayers facilitate the charge separation between them. Fig. 5.5(b) shows the method of work function calculation. Fig. 5.5(c) and (d), show the plots for MoSSe/WS_2 configuration II and III, respectively. We observe, that in configuration II (Fig. 5.5(c)) there is an additional potential gradient between Se atomic layer of MoSSe and S atomic layer of the WS_2 at the interface, along with the cationic potential difference. In case of configuration III, the interface has no anionic gradient and hence, charge separation is mainly the result of cationic gradient. Therefore, we see different band gaps in configuration III and configuration II. Further, one should always remember, that these configurations are type II and the band edge levels are on two different layers. Therefore, any potential gradient at interface will definitely effect the corresponding band edge levels. Fig. 5.6- 5.7 discuss the electrostatic potential for other vdW HTSs and further, explains the change in band gap on the basis of dipole direction. Dipole direction is seen from S to Se i.e. from lower to higher potential. So, we observe opposite dipole directions in configurations II and III, thereby affecting the interfacial interactions. Thus, the vdW HTSs with TMOs is also inline with the above discussion and inference.

5.2.2.1 Planar Averaged Charged Density

We have also calculated the associated charge density on the layers and the work function of the vdW HTSs. The work function (ϕ) is significant parameter to understand the charge separation or transfer at the interface. It is defined as follows:

$$\phi = \mathrm{E_{Vac}} - \mathrm{E_{Fermi}}, \tag{5.2}$$

where $\mathrm{E_{Vac}}$ and $\mathrm{E_{Fermi}}$ are the electrostatic potential corresponding to the vacuum level and Fermi level, respectively (Fig. 5.5). Table 5.4 gives the total Hirshfeld charge (of all the atoms in the monolayer of the HTS) and the work function of vdW HTSs. The estimated values of the work function of free standing monolayer (ϕ_{M} as in Table 5.7), have been corroborated with the

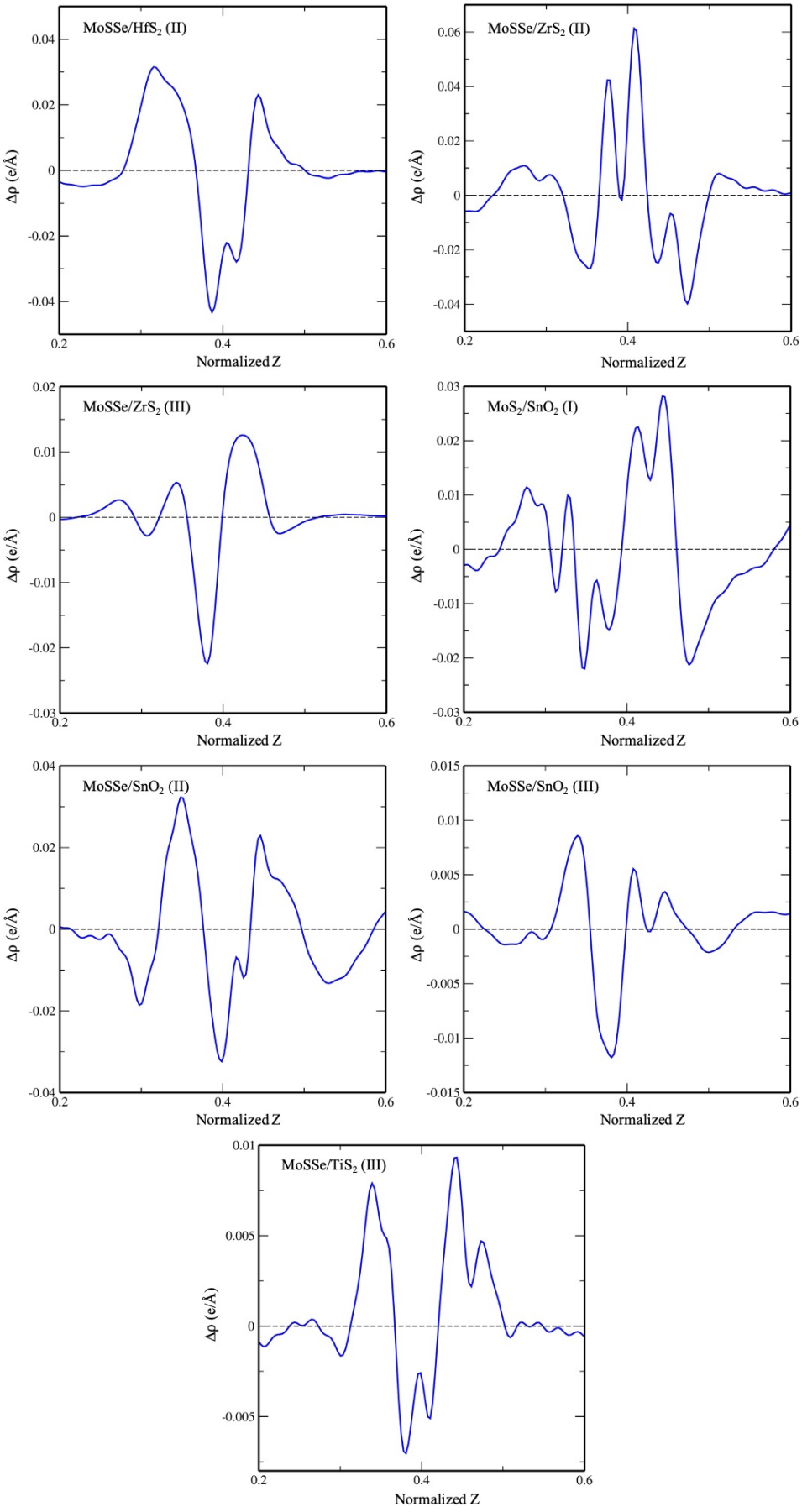

Figure 5.8: Planar averaged charge density

Table 5.4: The Hirshfeld charge and work function of different configurations (I: MoS_2/BX_2, II: $MoSSe/BX_2$ (Se interfacial layer), III: $MoSSe/BX_2$ (S interfacial layer))

BX_2	Hirshfeld charge (e)			Work function (ϕ) (eV)		
	I	II	III	I	II	III
WS_2	0.64	0.19	3.00	5.19	5.34	4.76
ZrS_2	-0.26	-0.25	-0.16	5.98	6.02	5.56
HfS_2	-0.08	-0.14	-0.07	5.98	6.01	5.58
TiS_2	-0.09	-0.25	-0.12	6.02	6.15	5.69
HfO_2	-0.04	-0.12	-0.09	6.12	6.13	5.70
T-PtO_2	0.03	-0.08	-0.04	5.78	5.75	5.53
T-SnO_2	-0.10	-0.16	-0.06	5.91	5.79	5.46

existing literature [215][1]. The Hirshfeld charge in case of configuration II show greater charge transfer than that of as in the case of configuration I and III. This is attributed to the anionic and cationic potential difference at the interface. The lesser charge transfer corresponds to the lower work function in configurations I and III. The plane averaged charge density difference $\Delta\rho$ has been calculated (Fig. 5.8) by:

$$\Delta\rho = \rho(\text{vdW HTSs}) - \rho(\text{MoS}_2 \text{ or MoSSe}) - \rho(\text{BX}_2) \tag{5.3}$$

where ρ(vdW HTSs), $\rho(\text{MoS}_2)$, ρ(MoSSe) and $\rho(\text{BX}_2)$ is the charge density of the vdW HTS, monolayer MoS_2, monolayer MoSSe and monolayer BX_2, respectively.

We can understand the charge transfer by calculating the band bending as well. This parameter is estimated by the Fermi-level difference between the vdW HTSs and the corresponding free-standing monolayer, with the expression as follows [218]:

$$\Delta\text{E} = \phi - \phi_{\text{M}} \tag{5.4}$$

where ϕ is the work function of vdW HTSs and ϕ_{M} is the work function of free standing monolayer. The $\Delta\text{E} < 0$ indicates charge transfer from the vdW HTSs to the monolayer. All the vdW HTSs, display $\Delta\text{E} < 0$ i.e. charge gained by the monolayer (Table 5.5). The observation is in

[1]Note that the mentioned reference has considered 15 Å vacuum, which we have found to be converged at 20 Å vacuum. The slight difference (i.e. not exact match) may be due to this change.

Table 5.5: The estimated band bending between vdW HTSs and free-standing monolayer (ϕ_M is the work function of free standing monolayer, I: MoS_2/BX_2, II: $MoSSe/BX_2$ (Se interfacial layer), III: $MoSSe/BX_2$ (S interfacial layer))

BX_2	ϕ_M (eV)	ΔE (eV)		
		I	II	III
WS_2	5.53	-0.34	-0.19	-0.77
ZrS_2	6.95	-0.97	-0.93	-1.39
HfS_2	7.13	-1.15	-1.12	-1.55
TiS_2	7.01	-0.99	-0.86	-1.32
HfO_2	8.86	-2.74	-2.73	-3.16
T-PtO_2	7.86	-2.08	-2.11	-2.33
T-SnO_2	9.06	-3.15	-3.27	-3.60

sync with the calculated Hirshfeld charges as noted in Table 5.4. It is to be noted that in case of WS_2, ΔE is more negative with $\phi_M(MoS_2)$ = 5.82 eV than that with $\phi_M(WS_2)$. Hence, the associated Hirshfeld charge on the WS_2 monolayer is positive. The above observations indicate MoSSe based configurations (II and III) to play a crucial role in photocatalytic applications.

The aforementioned discussion along with Fig. 5.3(a) have showcased the spatial charge separation due to the work function difference. Therefore, with the e^- - h^+ pair generation in the individual monolayers of vdW HTSs, the MoS_2 (or MoSSe) monolayer will be positively charged as it contributes to the VBM of vdW HTS, which will restrict the flow of e^- to other layer (BX_2). Moreover, BX_2 monolayer that contributes to the CBm of vdW HTS, does not straddle the reduction potential. Hence, MoS_2 (or MoSSe) monolayer will observe restricted e^- motion from its CBm to BX_2 CBm, thereby facilitating the e^- - h^+ recombination path of BX_2 CBm to MoS_2 VBM and promoting the standard Z-scheme mechanism.

5.2.3 Recombination in vdW HTSs

Considering the case of photocatalysts that straddle the potentials, slower recombination rate is synchronous with the effective photocatalytic capability. However, vdW HTSs for applicability as Z-scheme potocatalysts, require higher recombination in them as compared to their constituent monolayers. Hence, the layer with CBm above the reduction potential can facilitate HER, while, the layer with VBM below the oxidation potential can facilitate OER. In view of this, we have analyzed the recombination rate, which is indicated by the effective mass of electrons and holes. The effective mass has been calculated by the parabolic fitting at CBm and VBM in the bandstructure obtained by the hybrid calculations [219]. The bandstructure of MoS_2/ZrS_2 have been found to be previously reported [220] and is in sync with that reported in the present work. The similar database of other vdW HTSs discussed here are previously unreported.

Table 5.6: The effective mass ratio (D) of the monolayers (BX_2) except MoS_2 and MoSSe (both have same value of D = 1.21)

BX_2	WS_2	ZrS_2	HfS_2	TiS_2	HfO_2	T-PtO_2	T-SnO_2
D	1.29	1.58	1.17	0.03	5.88	4.66	9.00

The recombination rate can be estimated by relative ratio (D) that is defined as follows [221]:

$$D = m_h^*/m_e^* \tag{5.5}$$

The higher the variance of D from 1, the lesser is the recombination. Since, D refers to the relative ratio of the effective masses of hole (m_h^*) and electron (m_e^*), its value closer to 1 (i.e low variance) is ideal for high recombination in the system. This is obvious as value closer to 1 indicates similar electron and hole effective masses, resulting in easier recombination. On the contrary, large difference in the effective masses pose significant difference in carrier mobilities leading to the separation of carriers and hindrance in their recombination. Consider, Table 5.7 that enlists the value of D for monolayers and their corresponding vdW HTSs. The effective mass of carriers at CBm (i.e. m_e^*) and VBM (i.e. m_h^*) have been obtained along the designated direction in the high symmetry path Γ - M - K - Γ (see bandstructures i.e. Fig. 5.4). Also, it

Table 5.7: The effective mass ratio (D) of the vdW HTSs (I: MoS_2/BX_2, II: $MoSSe/BX_2$ (Se interfacial layer), III: $MoSSe/BX_2$ (S interfacial layer))

BX_2	Effective Mass Ratio (D)		
	I	II	III
WS_2	2.50	0.85	10.19
ZrS_2	0.13	0.64	0.62
HfS_2	0.65	0.87	0.71
TiS_2	0.50	0.20	0.80
HfO_2	0.32	0.34	0.34
T-PtO_2	0.49	0.50	0.49
T-SnO_2	0.91	1.15	1.14

should be noted that the parameter is calculated from the bandstructures of the supercell than the primitive cells. Since, the supercell is small, the density of the bands near the VBM and CBm is not very high and hence, the band folding is not an issue here.

Further, since we are considering Z-scheme photocatalysis, we require monolayer with lesser recombination as compared to that of their corresponding vdW HTSs. In order to review this we have checked the variance of D values from 1 for monolayers and vdW HTSs. Therefore, the vdW HTSs with lesser variance as compared to that of their respective monolayer can be considered probable for Z-scheme photocatalysis. As per the discussed approach, we have deduced $MoSSe/ZrS_2$ (configuration II and III), $MoSSe/HfS_2$ (configuration II), $MoSSe/TiS_2$ (configuration III), MoS_2/SnO_2 and $MoSSe/SnO_2$ (configuration II and III) as the probable Z-scheme vdW HTSs. Amongst these, the MoS_2/SnO_2, $MoSSe/HfS_2$ (configuration II) and $MoSSe/TiS_2$ (configuration III) have shown least variance from 1. Their respective carrier mobilities [222] have been approximately calculated to 46×10^2 $cm^2V^{-1}s^{-1}$, 21×10^2 $cm^2V^{-1}s^{-1}$ and 2×10^2 $cm^2V^{-1}s^{-1}$. The corresponding expression is as follows:

$$\mu = \frac{2e\hbar^3 C}{3k_B T|m^*|^2 E_1^2} \tag{5.6}$$

In this expression C is defined as C = $[\partial^2 E/\partial\delta^2]/S^0$. E refers to the total energy of the system, δ is the applied uniaxial strain, and S^0 is the area of the optimized vdW HTS. m* is the effective

mass, expressed as $m^* = \hbar^2 (\partial E/\partial k^2)^{-1}$. T represents temperature, and E_1 is the deformation potential constant that is defined as $\Delta E = E_1(\Delta l/l_0)$. Here, ΔE is the energy shift of the band edge position with respect to the lattice strain $\Delta l/l_0$. The energies of the band edges (CBm or VBM) are obtained with vacuum level as the reference.

Moreover, we have also estimated their exciton binding energy which showed comparatively smaller exciton binding energy of vdW HTSs as compared to that of MoS_2 and MoSSe monolayers. However, the value D is an indicative approach and should not be considered as the sole criteria for any deductions. The future scope definitely lies in the carrier dynamics to understand the excitonic physics in these materials.

5.2.4 Absorption spectra

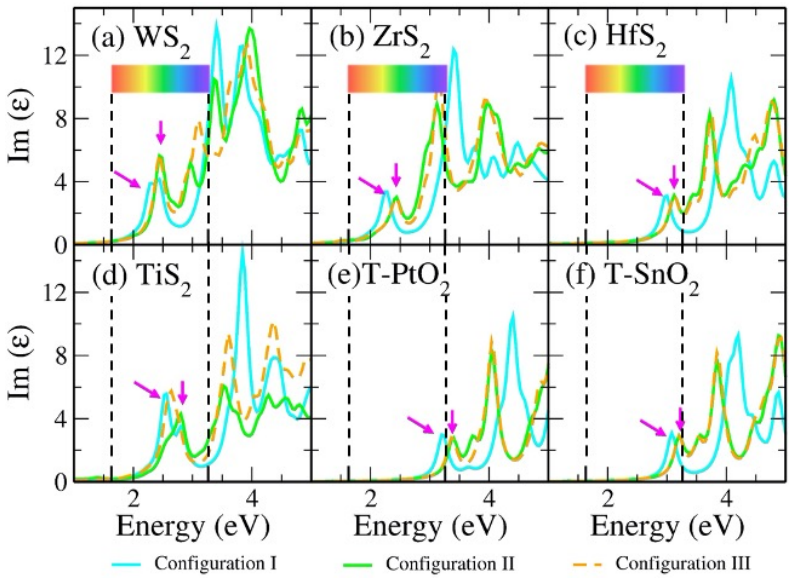

Figure 5.9: Imaginary part of dielectric function vs. energy plot depicting the optical response of the vdW HTS configurations I, II and III by G_0W_0@HSE06. Here, the arrow indicates the initial peak position that is associated with the absorption onset.

Optical response is amongst the important parameters involved in constructing the photocatalytic devices. Therefore, we have obtained the same for previously discussed vdW HTSs, that can be considered for the photocatalytic applications. Fig. 5.9 gives the absorption spectra obtained from imaginary part of the dielectric function as computed by GW method (G_0W_0@HSE06). The dielectric function is a frequency dependent complex function ($\epsilon(\omega) = \mathrm{Re}(\epsilon) + \mathrm{Im}(\epsilon)$) where the real part ($\mathrm{Re}(\epsilon)$) is computed from the Kramers-Kronig relation and the imaginary part

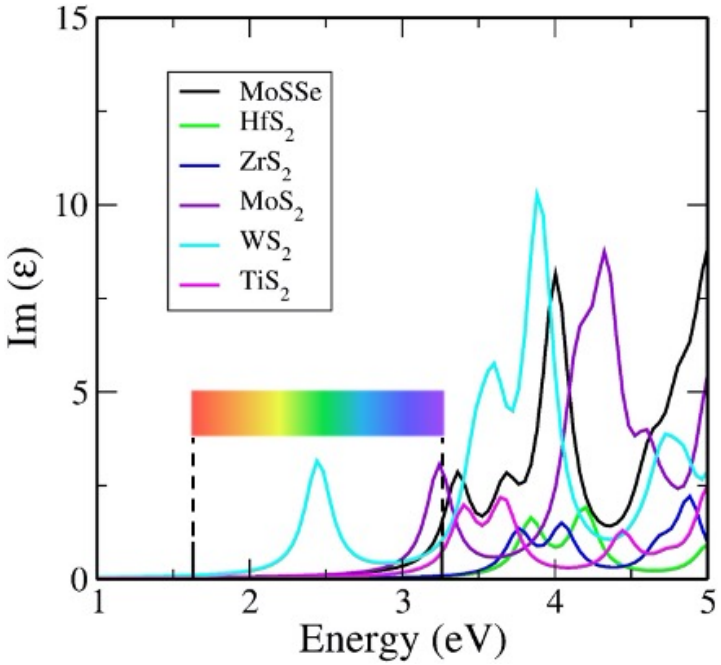

Figure 5.10: Absorption spectra of Janus (MoSSe) and monolayer TMDs i.e MoS_2, WS_2, TiS_2, HfS_2 and ZrS_2

(Im(ϵ)) is obtained from the interband matrix elements in the momentum space [223]. Since, the interband process consists of transitions to the unoccupied orbitals, the Im(ϵ) gives the absorption spectra. The first peak will, therefore, indicate the onset of absorption process. We observe that the vdW HTSs of MoS_2/TMD and MoS_2/TMO have response in the visible region. The spectra corresponding to MoSSe vdW HTSs (configuration II and III) have shown minute blue shift as compared to that of MoS_2 vdW HTSs. Further, we observe from Fig. 5.9(b) that the vdW HTSs with ZrS_2 and TiS_2 monolayer show red shift as compared to other vdW HTSs (i.e., Fig. 5.9(a), (c), (d)-(f)). The spectra, thus, indicate the use of MoS_2/ZrS_2, MoSSe/ZrS_2, MoS_2/TiS_2 and MoSSe/TiS_2 for harnessing the overlap region of Im(ϵ) with the solar spectrum in order to construct the photocatalytic devices.

5.2.4.1 Exciton Binding Energy

We have performed mBSE calculations, with an intention to simply compare the exciton binding energy (E_{exc}) of vdW HTSs with MoS_2 and MoSSe. We have included four valence and conduction bands for mBSE on top of hybrid functional. However, there is a huge scope in understanding the excitonic transitions in these systems with different computational approaches. Presently, considering the Z-scheme application, the smaller E_{exc} of vdW HTSs as compared to

MoS_2 (or MoSSe) would allow more e^- - h^+ recombination in vdW HTS thereby facilitating MoS_2 (or MoSSe) for HER.

Table 5.8: Exciton binding energies of vdW HTSs, MoS_2 and MoSSe monolayers

	MoS_2	MoSSe	MoSSe/ HfS_2(II)	MoSSe/ TiS_2(III)	MoS_2/ SnO_2(I)	MoSSe/ ZrS_2(II)	MoSSe/ ZrS_2(III)	MoSSe/ SnO_2(III)
E_{exc} (eV)	1.5	1.8	0.44	0.37	1.3	0.42	0.41	1.3

5.2.5 H_2O Adsorption

Table 5.9: H_2O adsorption on the monolayer surface

BX_2	Adsorption Energy (eV)	Distance (Å)
WS_2	-0.09	2.88
ZrS_2	-0.24	2.59
HfS_2	-0.23	2.75
TiS_2	-0.25	2.74
T-PtO_2	-0.28	2.08
T-SnO_2	-0.29	2.31

We have further calculated the H_2O adsorption in these vdW HTSs to confirm that the adsorption is supported for further redox reactions. The associated methodology is as per the following equation:

$$E_{ads} = E(\text{adsorbed } H_2O) - E(\text{vdW HTSs}) - E(H_2O) \tag{5.7}$$

Here, E_{ads} is the adsorption energy (Table 5.9) of the H_2O on the vdW HTSs; E(adsorbed H_2O) is the energy of the vdW HTSs with adsorbed H_2O, E(vdW HTSs) is the energy of the vdW HTSs and E(H_2O) is the energy of the water molecule. From the Table 5.9 we observe, H_2O is physisorbed in the system and its binding strength in all the monolayers is higher than that in

case of WS_2. Also, the transition metal oxides show higher binding strength than the transition metal dichalcogenides. The data supplements the analysis for considering the monolayers for Z-scheme photocatalysis.

In addition, we have calculated the Gibb's free energy change (ΔG) of the intermediate in the HER as per the expression:

$$\Delta G = \Delta E + \Delta E_{zpe} - T\Delta S \tag{5.8}$$

where ΔE is the intermediate adsorption energy on the vdW HTSs, ΔE_{zpe} and ΔS represent the difference of the zero-point energy and the difference of entropy between the ground state and the adsorbed system, respectively. T is the temperature, herein considered as 300K. The HER diagram along the reaction pathway $H^+ + e^- \rightarrow H^* \rightarrow 1/2\ H_2$ is illustrated in the Fig. 5.11. Here, H* represents the adsorbed intermediate. Under the consideration of pH = 0 and Standard Hydrogen Electrode (SHE) potential of 0 V the $H^+ + e^-$ is equivalent to the 1/2 H_2.

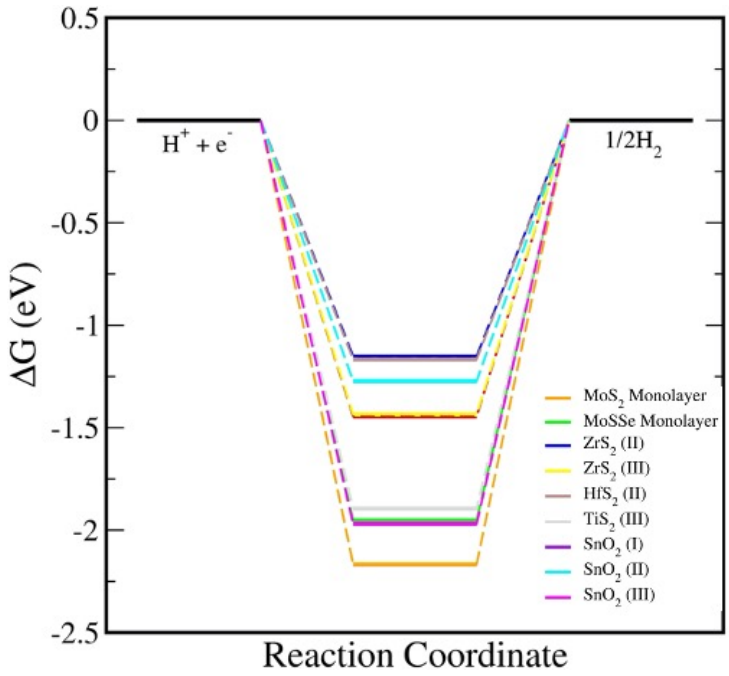

Figure 5.11: The HER reaction free energy diagrams on monolayer and vdW HTSs at an electrode potential E_{SHE} = 0 V and pH = 0. At zero potential, ($H^+ + e^-$) can be expressed as 1/2 H_2.

Now, upon systematically revisiting all the aforementioned factors, we have observed vdW HTSs to be type II with their work function being affected by the interfacial potential difference. This further influences the charge separation. Another point is that the smaller conduction band offset between the two monolayer systems would promote efficient charge separation at

the interface [224]. Therefore, in reference to Fig. 3, with comparatively large difference in two conduction band levels along with type II alignment, the consideration for interlayer recombination in vdW HTSs for Z-scheme process seems plausible. Effective mass being the important factor for the same, we have indicated the recombination probability by the effective mass ratio (D). Since, the approach is qualitative we have included the results of optical response, H_2O adsorption and HER , that implies MoSSe/HfS_2, MoSSe/TiS_2, MoS_2/T-SnO_2, MoSSe/T-SnO_2, MoS_2/ZrS_2 and MoSSe/ZrS_2 as probable Z-scheme photocatalysts. We have, in addition, complied to the inferences with the study of optical response, carrier mobility, H_2O adsorption and HER.

5.3 Conclusion

An exhaustive study has been undertaken for understanding different MoS_2 and MoSSe based vdW HTSs. As per the band edge alignment, it is observed that these vdW HTSs does not facilitate the normal photocatalytic process as they do not straddle the redox potential. However, these are predicted to be implementing the natural photocatalysis by Z-scheme. The band edge alignment of the MoSSe vdW HTSs has inferred large band gap in configuration III than in case of configuration II. This has been attributed to the additional anionic potential gradient due to Se atomic layer at the interface in configuration II. The recombination rate as implicated by the effective mass ratio (D) have corroborated the MoSSe/HfS_2, MoSSe/TiS_2, MoS_2/T-SnO_2, MoSSe/T-SnO_2, MoS_2/ZrS_2 and MoSSe/ZrS_2 as favourable Z-scheme photocatalyst. The absorption spectra further confirms the response of these vdW HTSs and hence, their applicability in the photocatalytic devices. Finally, the H_2O adsorption and HER indicates their interaction with water, thus, helping in the photocatalytic process.

CHAPTER 6

Hydrogen evolution reaction in acidic media for MoS_2/BP and MoSSe/BP van der Waals heterostructure

6.1 Introduction

The availability of clean and renewable energy source governs the tenable development. Innovation in systems like fuel cells, metal-air batteries and water electrolysis positively impacts the environment [225]. The cleanest alternative for the same is the molecular hydrogen (H_2) and hence, in the present context, we consider materials that support its production [226, 227]. The electrochemical reactions that are in sync with the clean environment aim involve hydrogen oxidation reaction (HOR), oxygen reduction reaction (ORR), hydrogen evolution reaction (HER) and oxygen evolution reaction (OER) [228]. The former two are associated with fuel cells, while the latter two are associated with water splitting or water electrolysis. There exists wide range of materials that can catalyze these electrochemical reactions by photocatalytic or electrocatalytic pathways [229, 230, 231]. The present work focuses on HER by the electrocatalysts. HER requires large overpotential to be initiated, and therefore catalysts are required to lower the overpotential [232]. In this respect, Pt has established itself to be an efficient catalyst [233]. However, its high cost and low abundance have urged the scientific community to find new materials for catalytic applications [234]. In fact, any heterogeneous catalysis under periodic boundary conditions faces the challenge of possessing an apt catalytic material that decreases the reaction barrier [235].

HER can occur in both acidic and alkaline media. In either of the media, the reaction steps follow (i) adsorption of H, (ii) its reduction and (iii) desorption as H_2 [236]. Now, HER has been reported to have sluggish kinetics in alkaline media with ambiguous active sites [237].

Since the electrolytic reactions at the electrode are acidic, we are focusing on the acidic media in the present study. The adsorption step is very fast and is termed as the Volmer step [42]:

Volmer reaction (fast): $H^+ + e^- \rightarrow H_{ad}$

The subsequent steps take place either as Tafel or Heyrovsky paths.

Tafel reaction: $2H_{ad} \rightarrow H_2$

Heyrovsky reaction: $H_{ad} + H^+ + e^- \rightarrow H_2$

As previously mentioned, the concept is to obtain material for the reaction that does not include

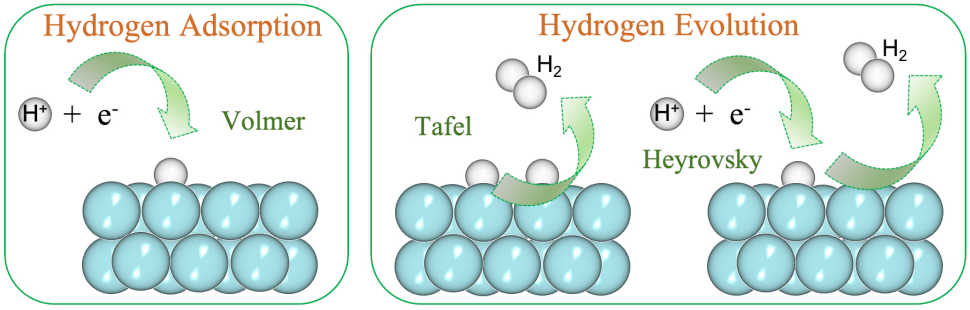

Figure 6.1: (Color online) HER Steps: Volmer is the adsorption step, and Tafel/Heyrovsky is the evolution step.

precious metals like Pt. The literature has shown the transition metals (Fe, Ni, Co), carbides, metal oxides (RuO_2, IrO_2), graphene, non-layered 2D materials, metal–organic frameworks (MOFs) and transition metal dichalcogenides (TMDs) as effective HER catalysts [238, 236, 239, 232, 240, 241, 242]. We restrict our study to the 2D materials that showcase quantum confinement effects with increased carrier mobility and large surface area [243, 244, 245]. This results in their increased catalytically active sites. The monolayer TMDs (in place of graphene) have established themselves as a potent material with optimal band gap suitable for optoelectronics, photocatalysis and electrocatalysis [246, 247, 171, 172, 173, 85]. In addition, due to their flexibility, these are widely studied for flexible electronic devices. Literature has reported their use as catalysts for HER, especially on the surface of 1T′-MoS_2 and edge sites of 2H-MoS_2 [248, 249]. MoS_2 being acid-stable is an added advantage [250]. Furthermore, its heterojunctions have also shown promising HER catalytic behaviour [251, 84, 252, 237]. It is pertinent to mention here that the tunability of 2D materials for specific applications is prevalent by defect engineering, strain engineering, stacking order, external field implementation, alloying and forming heterojunctions [253, 254, 255, 256, 257]. Amongst them, formation of heterojunctions with van der Waals forces in between the constituent monolayers are classified

under van der Waals heterostructures (vdW HTSs). These have proved a real boon to the field of work because the constituent monolayers retain their properties simultaneously with their combined vdW HTS properties [258]. In addition, the electronegativity difference between the constituent monolayers actuates electron transfer, thereby affecting the HER [259]. Even if the constituent monolayers have inactive sites, the resulting vdW HTS can be obtained as an active electrocatalyst due to an inbuilt electric field at the interface [41].

Presently, we explore Boron Phosphide (BP) monolayer, MoS_2/BP and MoSSe/BP vdW HTSs for HER. Recent works have reported vdW HTSs with BP instead of graphene as it has a similar single atomic layered hexagonal structure, however, along with a band gap [260]. BP monolayer has been reported with low carrier effective mass, high carrier mobility, good mechanical strength, and stability in water environments [261, 262]. Since the lattice parameter of MoS_2 and BP is similar, the MoS_2/BP vdW HTS becomes a plausible system with minimal lattice mismatch [263]. BP monolayer has also been synthesized experimentally [264]. In addition, since Janus (MoSSe) has established itself with more catalytically active sites than MoS_2, we have also analyzed MoSSe/BP vdW HTS. Any prior investigations for HER on these systems are hitherto unknown; hence we have considered these systems for our work.

The aforementioned HER reaction path should be accounted for the proton and electron free energies [265]. These are incorporated by the computational hydrogen electrode model as proposed by Norskov *et al.* [42]. The model caters to the fundamental problem of large-scale calculation of a real system along with electrolyte by following the electrochemical double layer approach rather than external charge formation. The underlying approximation considers solvated proton upto first bilayer. Until now, no study has been reported with the analysis of vdW HTSs by computational hydrogen electrode model for HER in acidic media to the best of our knowledge [266]. We have initially discussed the stacking configuration and electronic structure. Subsequently, the computational hydrogen electrode model is discussed. Thereafter, Tafel and Heyrovsky reaction paths are analyzed. Finally, we discuss the electrode potential, and the reaction and activation energies.

6.2 Methodology

The first-principles based density functional theory (DFT) calculations have been employed in the present work [27, 129, 130, 131, 136, 137]. The associated code chosen is Vienna

ab initio simulation package (VASP) [141, 63, 132] with projector augmented wave (PAW) pseudopotentials using plane wave basis. The generalized gradient approximation (GGA) that accounts for the exchange-correlation (xc) interaction amongst electrons is incorporated by PBE xc functional (as proposed by Perdew-Burke-Ernzerhof (PBE) [163, 138]). The Brillouin zone (BZ) sampling of 2×2 K-mesh is used for conjugate gradient minimization with an energy tolerance of 0.001 meV and the force tolerance of 0.001 eV/Å. The intermediate, initial and final energetics are obtained by the BZ sampling of 6×6 K-mesh. The plane wave cut-off energy is set to 500 eV. All the structures are built with 20 Å vacuum that avoids the electrostatic interactions among the periodic images. The two-body Tkatchenko-Scheffler vdW scheme has been employed for obtaining optimized structures [124, 125]. This is an iterative scheme based on Hirshfeld partitioning of the electron density. We have employed climbing-image nudged elastic band (CI-NEB) method to obtain minimum energy path for HER [164, 165]. Note that we have not explicitly considered entropic calculations, as in approximation of solvated proton on first layer, 0.2 - 0.3 eV can be added all along the energetics [42]. In reference to the previous literature, we have not included the spin-orbit coupling (SOC) in our calculations [199, 209, 210].

6.3 Results and Discussions

6.3.1 Heterostructure

The present work features BP monolayer, MoS_2/BP and MoSSe/BP vdW HTSs for HER assessment. The lattice parameter of BP monolayer is 3.20 Å and that of MoS_2 is 3.16 Å. Since the lattice mismatch between them is less (1.2% as obtained by (l(MoS_2) - l(BP))/l(BP), where l(MoS_2) and l(BP) is the lattice constant of MoS_2 and BP, respectively), the corresponding MoS_2/BP vdW HTS formed is commensurate [213]. Its corresponding structural, electronic and optical properties are obtained by unit cell configuration (Fig. 6.2- 6.5), whereby, MoS_2/BP and MoSSe/BP form type 1 and type 2 alignment and it corroborates with the prior research [267, 263]. In case of MoSSe/BP, BP contributes to the CBm (Conduction Band Minimum) and MoSSe contributes to the VBM (Valence Band Maximum).

The optical properties have also been calculated by the GW approach (Many Body Perturbation Theory (MBPT)). Fig. 6.4 shows the optical response using GW@BSE method that calculates the dielectric function. This is a complex function where the expression for interband process is

the imaginary part thereby giving the absorption spectra. The real part (Re(ϵ)) is deduced from the Kramers-Kronig relation. We observe both the vdW HTSs (MoS_2/BP and MoSSe/BP) having response in the visible region. We have calculated the exciton binding energy (E_{exc}) using the Bethe-Salpeter Equation. We observe small E_{exc} that indicates its applicability in photo-electrochemical processes.

Note that, initially, two stacking styles (Fig. 6.2 (a) and (b)) between the constituent monolayers were considered, wherein the stacking corresponding to Fig. 6.2 (b) has minimum binding energy [251]. Therefore, we have proceeded with this stacking in our work.

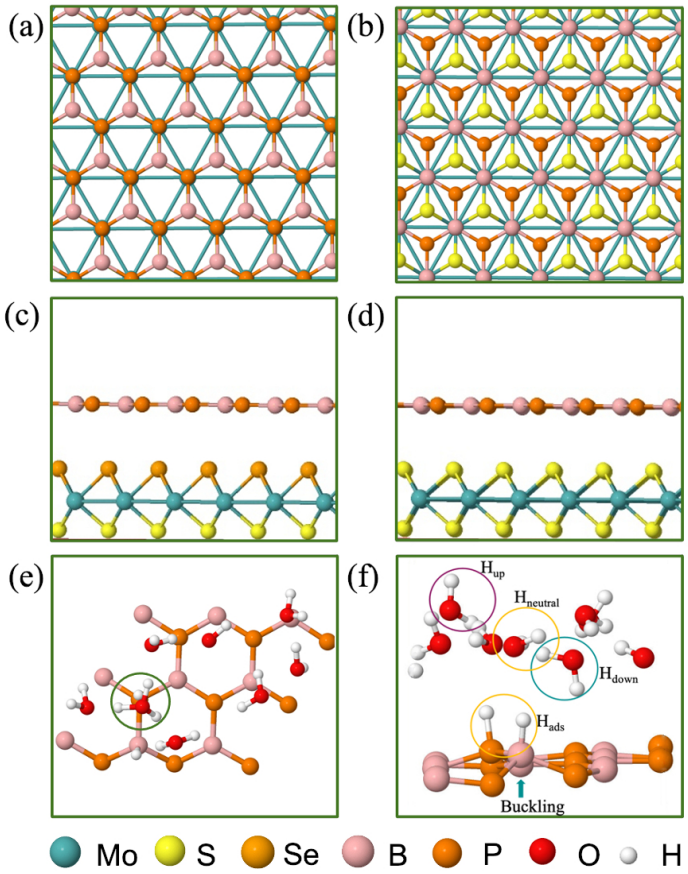

Figure 6.2: (Color online) (a) and (b) Top view of MoS_2/BP vdW HTS stacking configurations, (c) and (d) Side view of minimum energy stacking configuration for MoSSe/BP and MoS_2/BP vdW HTSs, respectively, (e) 3×3 supercell of BP monolayer schematic with 1/3 H^+ conc. i.e., 1 $H^+/3H_2O$, (f) Water molecule orientations of H_{up}, H_{down} and $H_{neutral}$. Buckling on BP can be observed at the H_{ads} site.

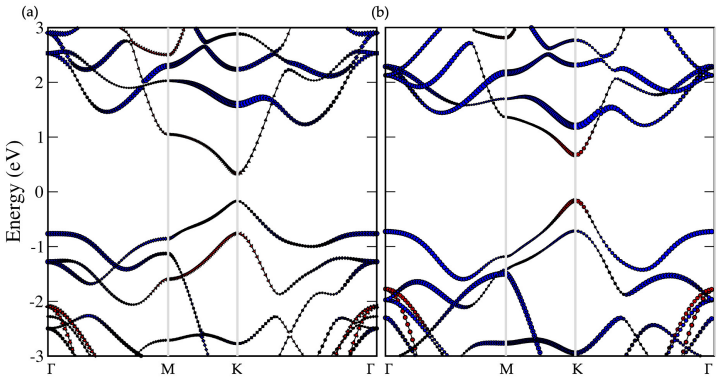

Figure 6.3: (Color online) (a) Type II bandstructure obtained for MoSSe/BP vdW HTS; (b) Type I bandstructure obtained for MoS_2/BP vdW HTS. (xc functional: PBE)

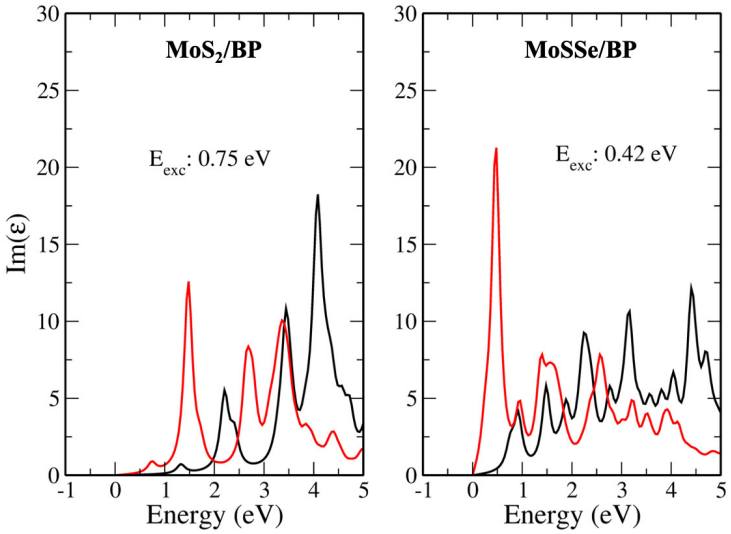

Figure 6.4: (Color online) Exciton binding energy obtained for MoS_2/BP and MoSSe/BP vdW HTS.

We have obtained the binding energies per atom (BE) and work of adhesion (W_{ad}) for each bilayer model (MoS_2/BP and MoSSe/BP) with the supercells of 2×2, 3×3, 4×4, 5×5 and 6×6. The equation for work of adhesion is as follows:

$$W_{ad} = \frac{E_{BP} - E_{MoS_2} - E_{MoS_2/BP}}{2A}$$

The values are consistent with all the cases as observed in the Table 6.1.

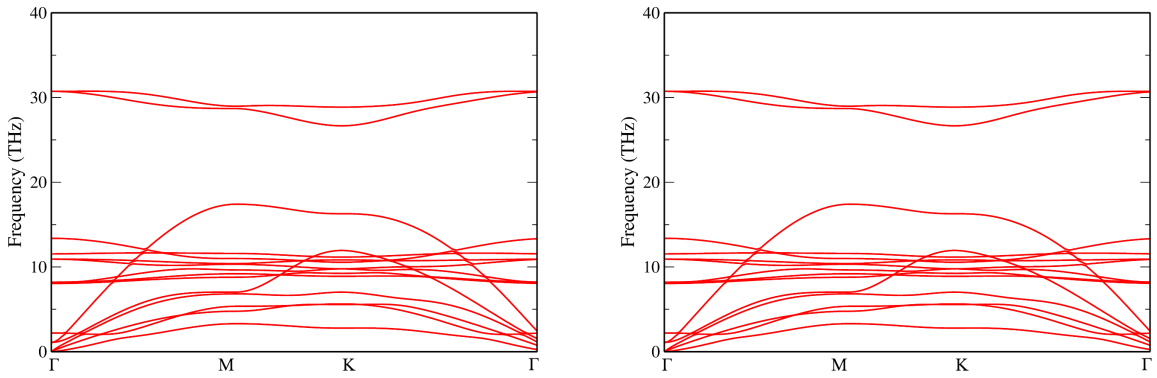

(a) MoS_2/BP (b) MoSSe/BP

Figure 6.5: Phonon dispersion plots

Table 6.1: BE and W_{ad} for MoS_2/BP and MoSSe/BP with and without H^+ in water layer.

System	BE/W_{ad}				
	2×2 eV	3×3 eV	4×4 eV	5×5 eV	6×6 eV
MoS_2/BP	-0.047/-0.014	-0.048/-0.014	-0.048/-0.015	-0.048/-0.016	-0.048/-0.016
MoSSe/BP	-0.050/-0.015	-0.051/-0.015	-0.051/-0.015	-0.051/-0.015	-0.051/-0.015

The planar averaged charge density difference $\Delta\rho$ is calculated by:

$$\Delta\rho = \rho(\text{vdW HTSs}) - \rho(\text{MoS}_2 \text{ or MoSSe}) - \rho(\text{BP}) \tag{6.1}$$

where ρ(vdW HTSs), $\rho(MoS_2)$, ρ(MoSSe) and ρ(BP) are the charge densities of the vdW HTS, monolayer MoS_2, monolayer MoSSe and monolayer BP, respectively.

Fig. 6.6 shows the planar averaged charge density plot and the corresponding electrostatic potential plot for MoS_2/BP with 1 solvated H^+. The electrostatic potential plot explains the electrostatic potential corresponding to each atomic layer. We observe significant charge transfer at the BP and water interface.

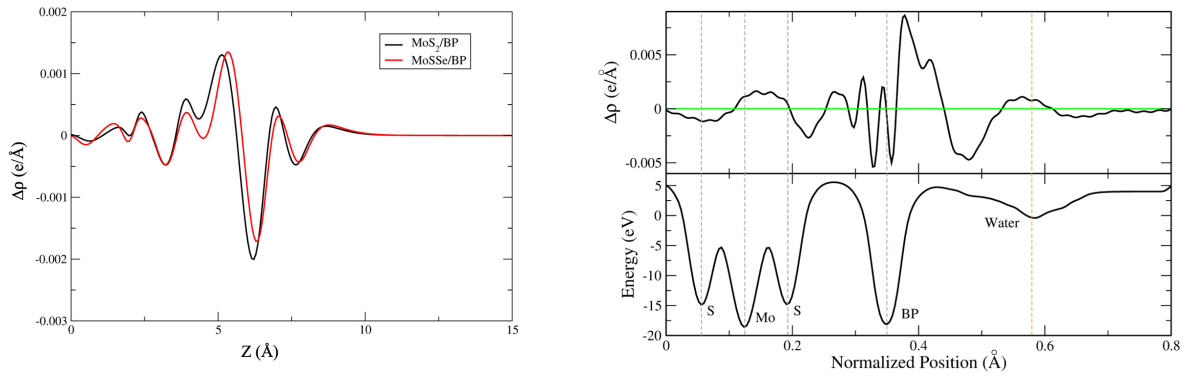

(a) vdW HTSs (b) with 1 H^+

Figure 6.6: Phonon dispersion plots

6.3.2 HER Study

Now, we advance on HER study, for which we have constituted 2×2, 3×3 and 4×4 supercells. The former being smaller restricts the proton concentration (conc.) variability, therefore we need larger supercells. In view of this, we are analyzing 2×2 supercell along with 3×3 and 4×4, because unlike monolayer, the vdW HTS with further large supercell size becomes computationally demanding. The subsequent paragraphs discuss the concepts of coverage and proton conc. for clarity.

The first step is to obtain the coverage that gives $\Delta G_H \simeq 0$ for our study. The number of adsorbed hydrogen (H_{ads}) per surface atoms is defined as the coverage. ΔG_H is the free energy of atomic hydrogen adsorption and is expressed as:

$$\Delta G_H = \Delta E_H + \Delta E_{ZPE} - T\Delta S_H$$

where,

$$\Delta E_H = E[nH] - E[(n\text{-}1)H] - 1/2E[H_2]$$

In the aforementioned equations, ΔE_H is the hydrogen binding energy on the surface of vdW HTS, E[nH] (or E[(n-1)H]) is the energy of the configuration with n (or n-1) number of H_{ads}, ΔE_{ZPE} is the zero-point energy of H_{ads} and ΔS_H is the entropy of H_2 in the gas phase. At 298 K, $\Delta E_{ZPE} - T\Delta S_H = 0.25$ eV is well established in literature [250].

We observe 2×2 supercell with 25% H coverage ($2H_{ads}$ per 8 surface atoms) and 3×3 supercell with 11% H coverage ($2H_{ads}$ per 18 surface atoms) with ΔG_H equal to -0.024 eV and 0.049 eV, respectively. We have deduced these coverages after trials upto 38%. The 4×4

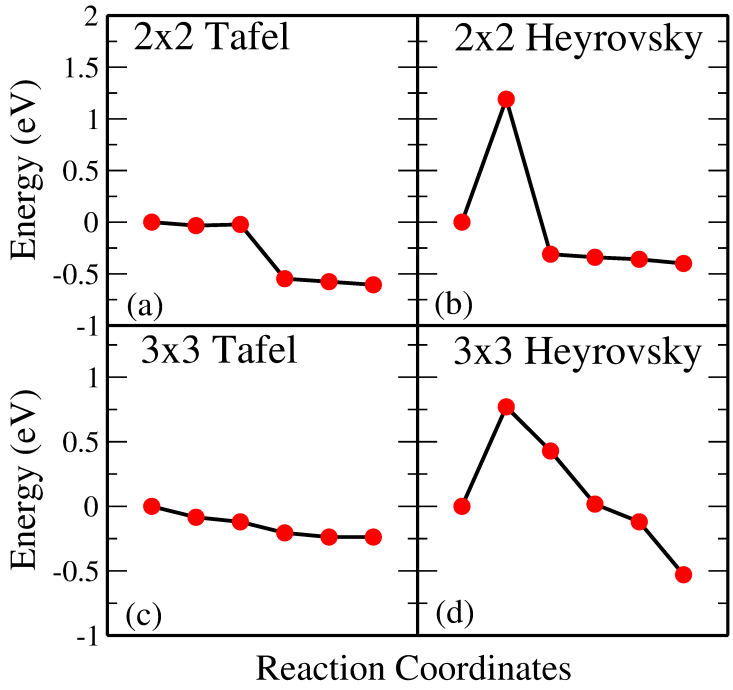

Figure 6.7: (Color online) 2×2 supercell of BP monolayer showing (a) Tafel reaction path and (b) Heyrovsky reaction path. 3×3 supercell of BP monolayer showing (c) Tafel reaction path and (d) Heyrovsky reaction path.

supercell shares the same coverage and H^+ conc. as in the case of 2×2 supercell. We have chosen consecutive B and P atomic sites for H_{ads} as this configuration was found to be the most stable. Also, we observed buckling at the site of H_{ads} (Fig. 6.2 (f)).

We now discuss the optimized systems consisting of water layer (water-solid interface with 3 Å thick water layer) without and with solvated protons (i.e., H^+). Fig. 6.2 (e) shows the BP monolayer ($2H_{ads}$) with H^+ in 3×3 supercell. Note that the H^+ is in the form of hydronium (H_3O) in the water layer. 2×2 supercell is a small supercell and therefore, only 1 H^+ is been considered. However, the corresponding H_2O molecules in the water layer are varied, thereby constituting 1/3 (i.e., 1 $H^+/3H_2O$) and 1/4 (i.e., 1 $H^+/4H_2O$) H^+ conc. The configuration corresponding to 3×3 supercell size has been studied for 1/8 (i.e., 1 $H^+/8H_2O$) H^+ conc. The 4×4 supercell size with 12 and 16 H_2O has been studied for 1/3 and 1/4 H^+ conc. The water orientation (Fig. 6.2 (f)) over the H_{ads} species is flat and H_{up} orientation is usually seen on the topmost layer. Further, all H_2O molecules are not H_{down}, rather, they are at some angular orientations other than strict H_{up} and H_{down} configurations. These orientations are essential because the electrostatic potential, as seen from the solid surface, also depends on the same. The stability of the vdW HTS along with water layer orientation is established by the similar

profile of radial distribution plot at 0K and 300K (Fig. 6.8). The radial distribution function

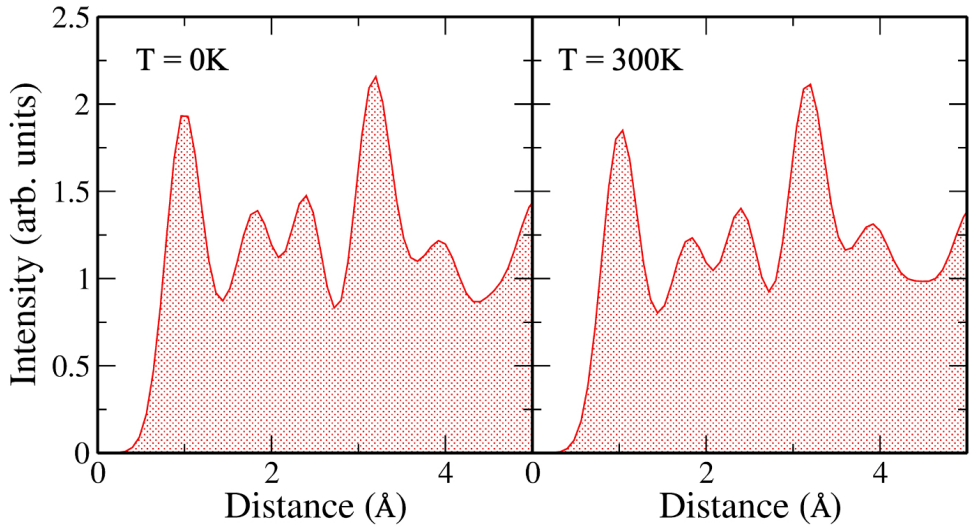

Figure 6.8: (Color online) Radial distribution function of MoS_2/BP at two different temperatures T= 0K and T= 300K.

here indicates the structural similarity of the MoS_2/BP with water layer at 0K and 300K. The water orientation thus obtained corroborates with the initial optimized configuration.

6.3.3 Tafel Reaction Step

Fig. 6.7(a) and 6.7(b) give Tafel and Heyrovsky reaction steps, respectively on the BP monolayer. This corresponds to the 2×2 supercell with 3 H_2O molecules and 1/3 H^+ conc., respectively. The BP monolayer acts as a reference to analyze the reactions for the MoS_2/BP and MoSSe/BP vdW HTSs. Here, we observe a reaction barrier in Heyrovsky reaction step (1.19 eV) and not in case of the Tafel reaction step. The reaction steps for 3×3 supercell and 1/8 H^+ conc. are given in Fig. 6.7(c) and 6.7(d), whereby the Tafel reaction steps show no barrier and Heyrovsky reaction steps show reduced reaction barrier as compared to that in 2×2 supercell. Further, we first discuss the Tafel reaction step analysis for the vdW HTSs. Fig. 6.9 highlights the Tafel reaction step on the MoS_2/BP ((a) and (c)) and MoSSe/BP ((b) and (d)) vdW HTSs. Firstly, no significant difference is observed between MoS_2/BP and MoSSe/BP vdW HTSs for 2×2 supercell. The overview of the Tafel reaction analysis is consistent with Tafel being surface reaction, thereby, less or no observed reaction barrier. We observed that the minimum energy profile in Tafel reaction is not continuously decreasing; instead, a slight hump is present. This corresponds to the buckling in the BP monolayer. As previously mentioned,

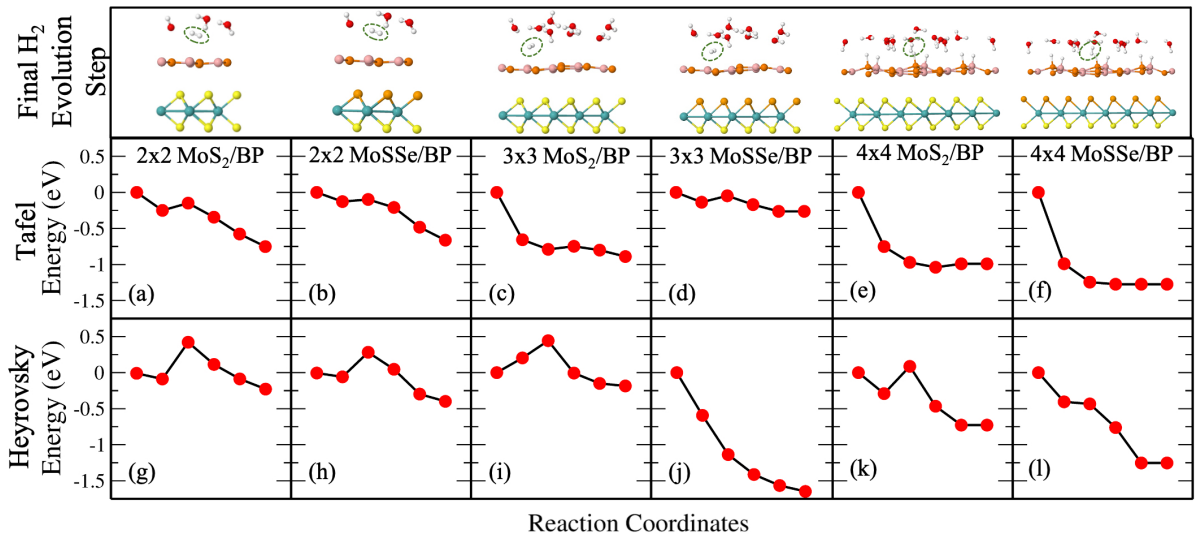

Figure 6.9: (Color online) (a)-(f) Tafel reaction path (upper row) on MoS_2/BP and MoSSe/BP vdW HTSs for 2×2, 3×3 and 4×4 supercell. (g)-(l) Heyrovsky reaction path (lower row) on MoS_2/BP and MoSSe/BP vdW HTSs for 2×2, 3×3 and 4×4 supercell.

the site of H_{ads} is buckled with respect to other sites, and during the H_2 evolution process, the corresponding BP site adjusts itself to the planar configuration (Fig. 6.10). Note that BP surface is considered for the reaction analysis as basal plane of MoS_2 is not catalytically active.

Now, the Tafel reaction path discussed in manuscript is for two adjacent H-atoms desorption as a molecular H_2. We have also performed the calculations on the 2×2 supercell to check the sites and the corresponding activation barrier (Volmer step). The first step consists of the transfer of H^+ to H adsorbed at P (H_{adsP}) or B (H_{adsB}) site, where the H_{adsB} shows less barrier than H_{adsP}. The second step is the H adsorption when the surface already has H_{ads} at any other site. In case of second H_{adsB}, with already existing H_{adsP} we obtain a barrier in the range 0.05 eV - 0.08 eV. However, when the H_{adsB} precedes H_{adsP}, the final structure is at a higher ground energy state than the initial structure. Hence, this reaction path is not possible. The aforementioned observation is for both MoS_2/BP and MoSSe/BP vdW HTSs (Fig. 6.11).

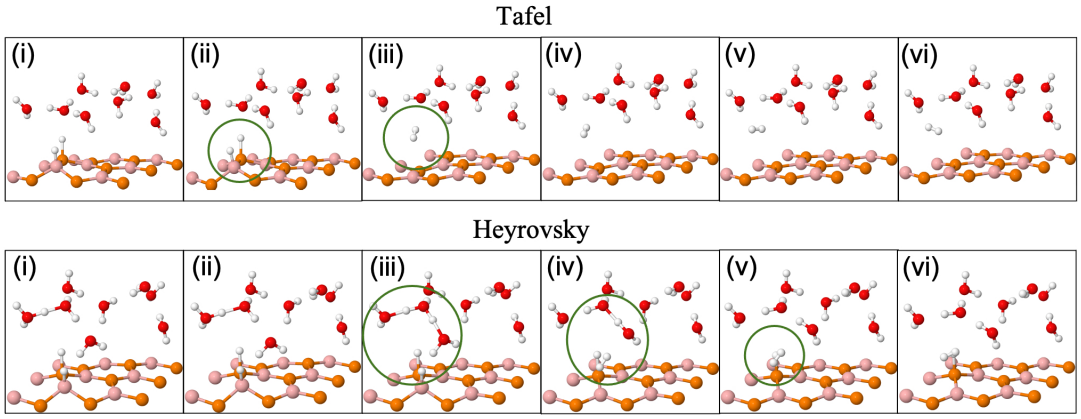

Figure 6.10: (Color online) Tafel (upper row) and Heyrovsky (lower row) reaction profile snapshots on 3×3 BP surface.

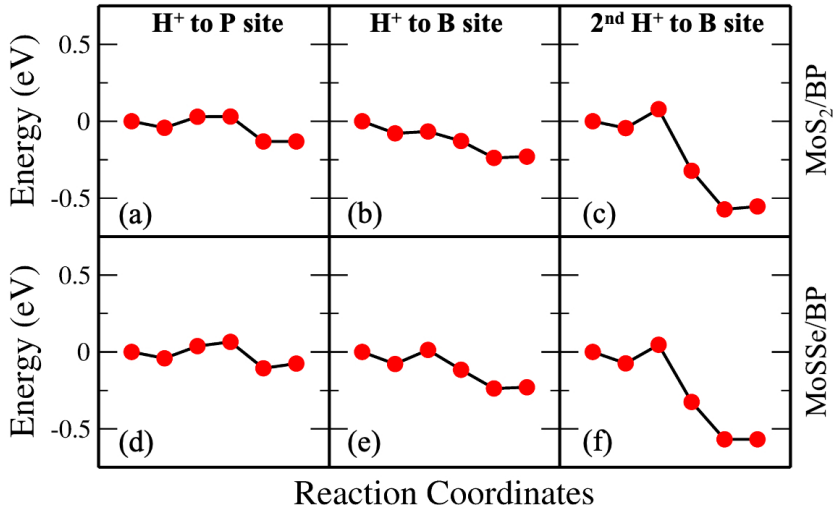

Figure 6.11: (Color online) Volmer reaction path for $H_{adsorbed}$ at P site ((a) and (d)), B site ((b) and (e)) on MoS_2/BP and MoSSe/BP vdW HTSs. (c) and (f) H^+ adsorbed on P site along already H adsorbed on B site.

6.3.4 Heyrovsky Reaction Step

Unlike Tafel, the Heyrovsky reaction step is not a pure surface reaction. It involves charge transfer, thereby affecting the reaction barrier and Fig. 6.9 (e)-(h) substantiates the same. We have observed reduction in reaction barrier in the vdW HTSs as compared to that in BP monolayer (Fig. 6.7 and Fig. 6.9). The 4×4 supercell configuration puts forth lowest reaction barrier amongst three supercell configurations. The MoS_2/BP and MoSSe/BP demonstrates this reduction from 0.43 eV (Fig. 6.9 (g)) to 0.08 eV (Fig. 6.9 (k)) and 0.28 eV (Fig. 6.9 (h)) to 0 eV (Fig. 6.9 (l)), respectively. Apart from previously discussed, we also considered the 4×4

supercell corresponding to the 15.6% H coverage ($5H_{ads}$ per 32 surface atoms) with ΔG_H equal to 0.026 eV and 1/3 H^+ conc., for the Heyrovsky reaction step. In this case, 0.09 eV reaction barrier is observed for MoS_2/BP, whereas MoSSe/BP showed 0 eV. Further, we observe significant change in case of MoSSe and this may be attributed to the combined effect of the coverage and the electronegativity difference within the MoSSe layer that affects the charge transfer at the interface.

Apart from the factors that are discussed above, there are structural parameters that affect the reaction steps. The H bonds in H_3O^+ stretch before combining with the H_{ads}. At the transition state, H_2 is formed. After that, the atoms adjust themselves to low energy configuration. After the intermediate step, the B and P atoms adjust, corresponding to H_{ads}, along with the other H_2O molecules. As in the Tafel scenario, the steps post H_2 formation optimize the H_2 molecule in the water layer. The reaction barrier, therefore, depends on the buckling in the monolayer, the water molecule's orientation, and the coexisting water molecules with H^+ (Fig. 6.10).

Finally, we discuss the Heyrovsky reaction in MoS_2/BP for 1/4 H^+ conc. in the cases of

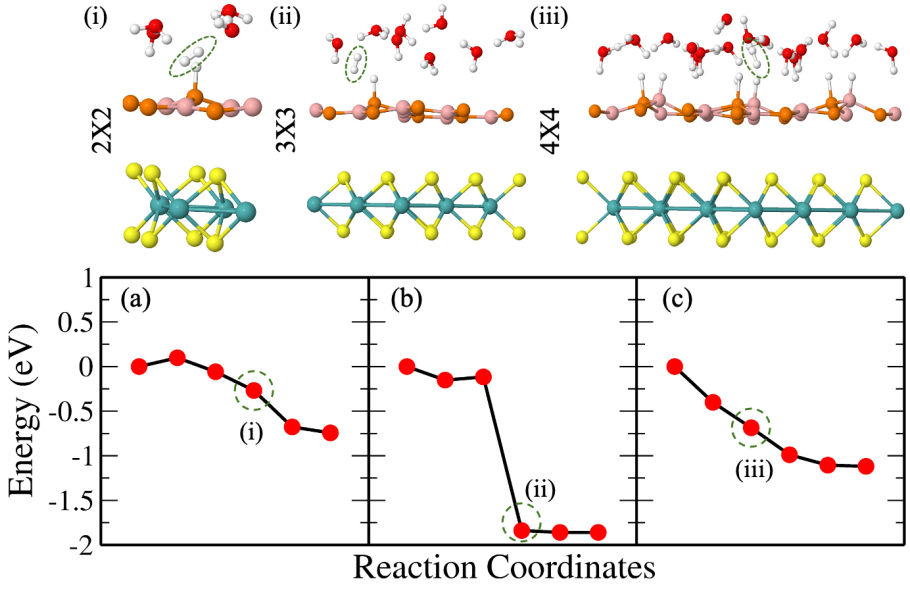

Figure 6.12: (Color online) Heyrovsky reaction path for MoS_2/BP vdW HTS with 1/4 H^+ conc. in (a) 2×2 supercell, (b) 3×3 supercell and (c) 4×4 supercell.

2×2 (i.e., 1 $H^+/4H_2O$), 3×3 (i.e., 2 $H^+/8H_2O$) and 4×4 (i.e., 4 $H^+/16H_2O$) supercells. We observed reaction barrier decreases from 0.43 eV (Fig. 6.9 (g)) to 0.09 eV (Fig. 6.12 (a)), 0.44 eV (Fig. 6.9 (i)) to 0 eV (Fig. 6.12 (b)) and 0.08 eV (Fig. 6.9 (k)) to 0 eV (Fig. 6.12 (c)) in 2×2, 3×3 and 4×4 supercells, respectively. This indicates that high coverage prefers low H^+ conc. and vice versa for reduction in reaction barrier. Note that till now we discussed

the H_2 evolution that includes H^+ and H_{adsB}. The trend with supercell size is same in case of H_{adsP} as well (Fig. 6.13 and 6.13). However, for a particular supercell the reaction barrier for the latter is smaller than the former, indicating that H^+ would initially prefer combining with H_{adsP}. We correlate this with the overpotential of the reaction, as discussed in the following section. Overpotential is the difference between the experimentally obtained reaction potential and the electrode potential. The electrode potential is analyzed only in the Heyrovsky reaction as it involves proton transfer. Therefore, this affects the work function and the potential at which the reaction takes place.

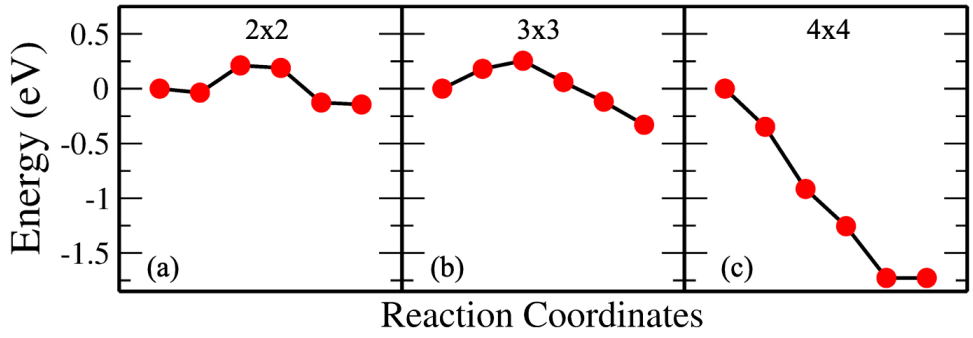

Figure 6.13: (Color online) Heyrovsky reaction path for $H_{adsorbed}$ at P site on MoS_2/BP vdW HTSs for (a) 2×2, (b) 3×3 and(c) 4×4 supercell.

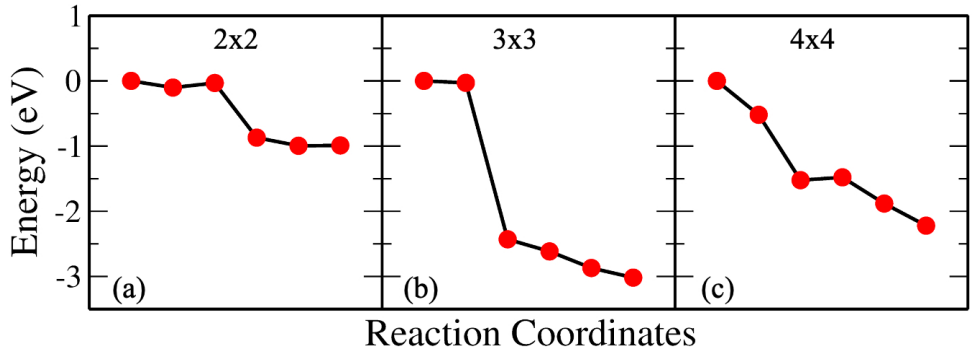

Figure 6.14: (Color online) Heyrovsky reaction path for $H_{adsorbed}$ at P site on MoS_2/BP vdW HTSs for (a) 2×2, (b) 3×3 and(c) 4×4 supercell for 1/4 H^+ conc.

6.3.5 Electrode Potential

The electrode potential (U) of the slab is reported relative to the normal hydrogen electrode (NHE):

$$U = \phi - \phi_{NHE}$$

Here ϕ (E_{vac} - E_{fermi}) is the work function, and ϕ_{NHE} is taken to be 4.44 eV[42, 268, 250]. The work function depends on the surface H coverage, the thickness or number of water bilayers, the water molecule orientation, and the system size.

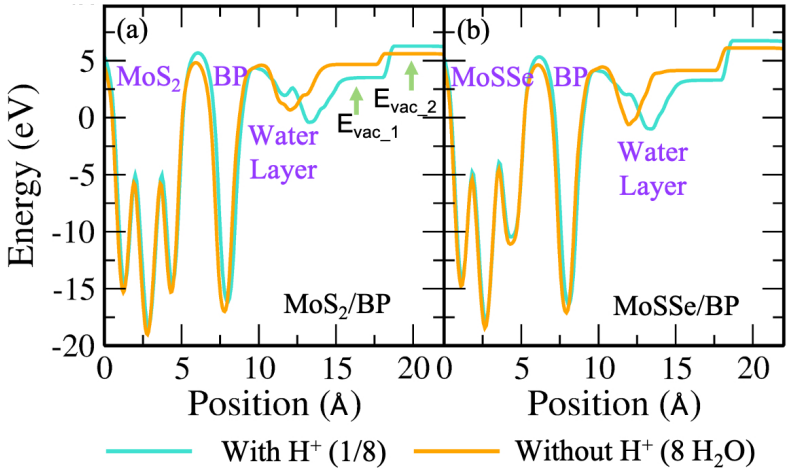

Figure 6.15: (Color online) Electrostatic potential plot of MoS_2/BP and MoSSe/BP vdW HTSs depicting water layer with and without H^+. (a) and (b) 3×3 supercell with 1/8 H^+ conc. and 8 H_2O molecules.

In small systems (here 2×2), the range of electrode potential analysis is limited to a few H^+ conc. considerations. Fig. 6.15 presents the electrostatic potential plot where we have deduced the work function of 3×3 MoS_2/BP and MoSSe/BP. The same for 2×2 and 4×4 is shown in Fig. 6.16 and 6.17. The potential drops are evident in Fig. 6.15, with a significant drop at the interface of BP and the water layer. The values of U corresponding to water layer with and without H^+ are reported in Table 6.2, which are in the range of -2.5 V to 1.3 V. We have incorporated dipole corrections as the vdW HTSs with two different surfaces maintain two potentials. Moreover, the H_{ads} and, therefore, the coverage affects the dipole-dipole interactions. As a result, we report the two values of U, i.e., U_1 and U_2, corresponding to two vacuum levels of E_{vac_1} and E_{vac_2}, respectively.

Table 6.2: Electrode potential (U) of MoS_2/BP and MoSSe/BP with and without H^+ in water layer.

vdW HTSs	With H^+		Without H^+	
	U_1 (V)	U_2 (V)	U_1 (V)	U_2 (V)
MoS_2/BP (2×2)	-2.31	0.48	1.04	0.70
MoSSe/BP (2×2)	-1.83	1.07	-0.68	1.31
MoS_2/BP (3×3)	-2.09	-0.05	-0.09	0.84
MoSSe/BP (3×3)	-2.55	0.90	-0.79	1.19
MoS_2/BP (4×4)	-2.12	0.39	-0.20	-0.75
MoSSe/BP (4×4)	-2.08	1.02	1.27	1.27

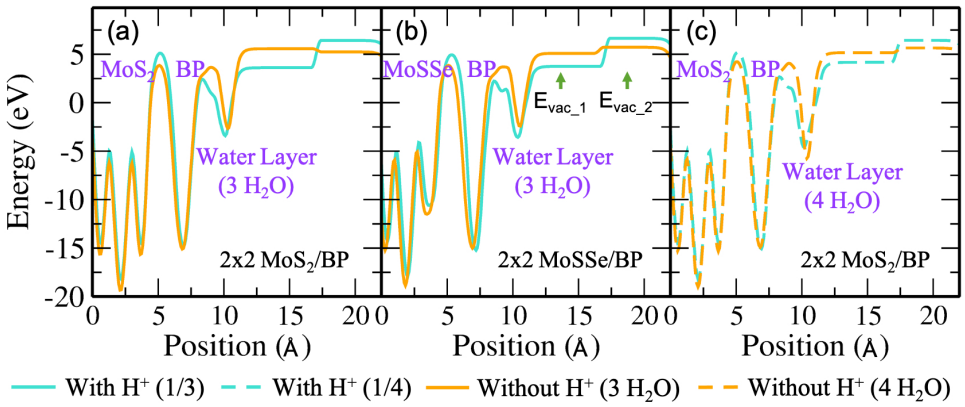

Figure 6.16: (Color online) (a) Electrode potential for 2×2 MoS_2/BP with and without H^+ corresponding to 1/3 proton concentration and 3 H_2O, respectively. (b) Electrode potential for 2×2 MoSSe/BP with and without H^+ corresponding to 1/3 proton concentration and 3 H_2O, respectively. (c) Electrode potential for 2×2 MoS_2/BP with and without H^+ corresponding to 1/4 proton concentration and 4 H_2O, respectively.

As previously discussed the dependence of ϕ on water orientation, we have explicitly optimized the H_{down} configuration for H_2O molecules. The Heyrovsky reaction path for the same in MoS_2/BP and MoSSe/BP 3×3 supercells can be seen in Fig. 6.18 (a) and (b). The obtained barrier is reduced as compared to the 2×2 supercells of MoS_2/BP, MoSSe/BP and 3×3 supercell of MoS_2/BP. The corresponding electrode potential is also reported in Fig. 6.18 (c) and (d).

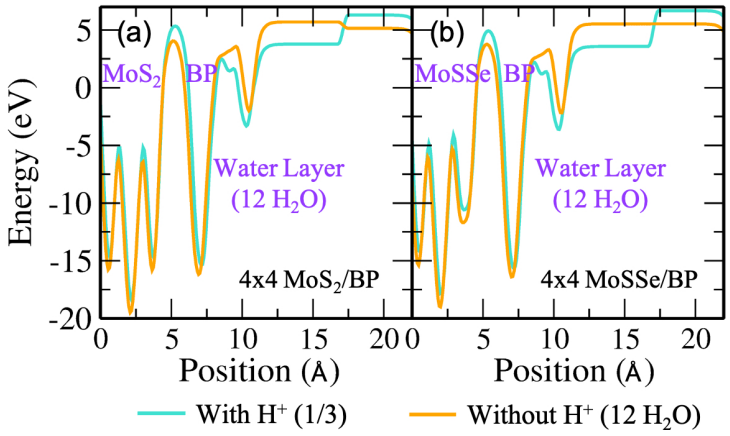

Figure 6.17: (Color online) (a) Electrode potential for 4×4 MoS_2/BP with and without H^+ corresponding to 1/3 proton concentration and 12 H_2O, respectively. (b) Electrode potential for 4×4 MoSSe/BP with and without H^+ corresponding to 1/3 proton concentration and 12 H_2O, respectively.

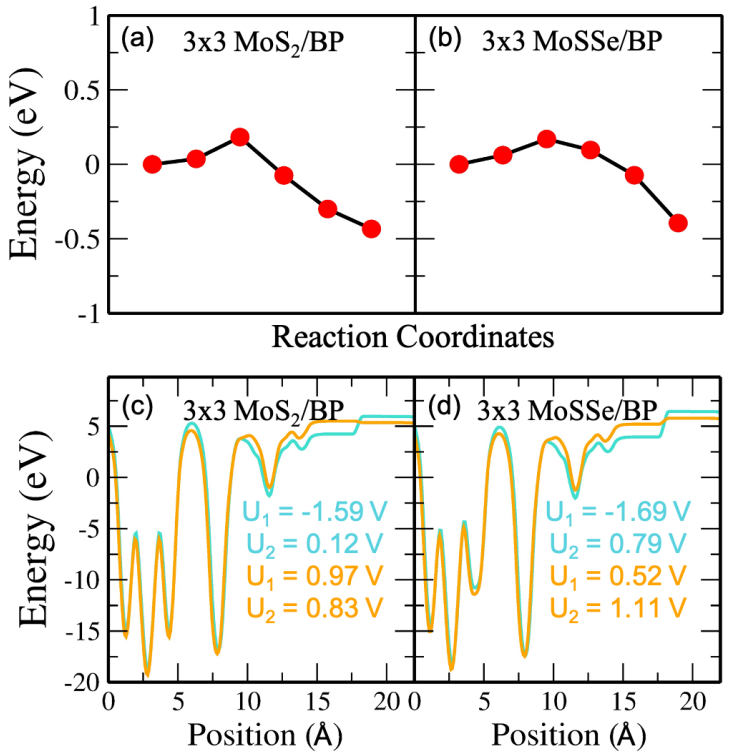

Figure 6.18: (Color online) (a) and (b) Heyrovsky reaction step for MoS_2/BP and MoSSe/BP vdW HTS in 3×3 supercell with 1/8 proton concentration (c) and (d) Electrostatic potential plot of MoS_2/BP and MoSSe/BP vdW HTSs depicting water layer with and without H^+ in 3×3 supercell with 1/8 proton concentration and 8 water molecules, respectively.

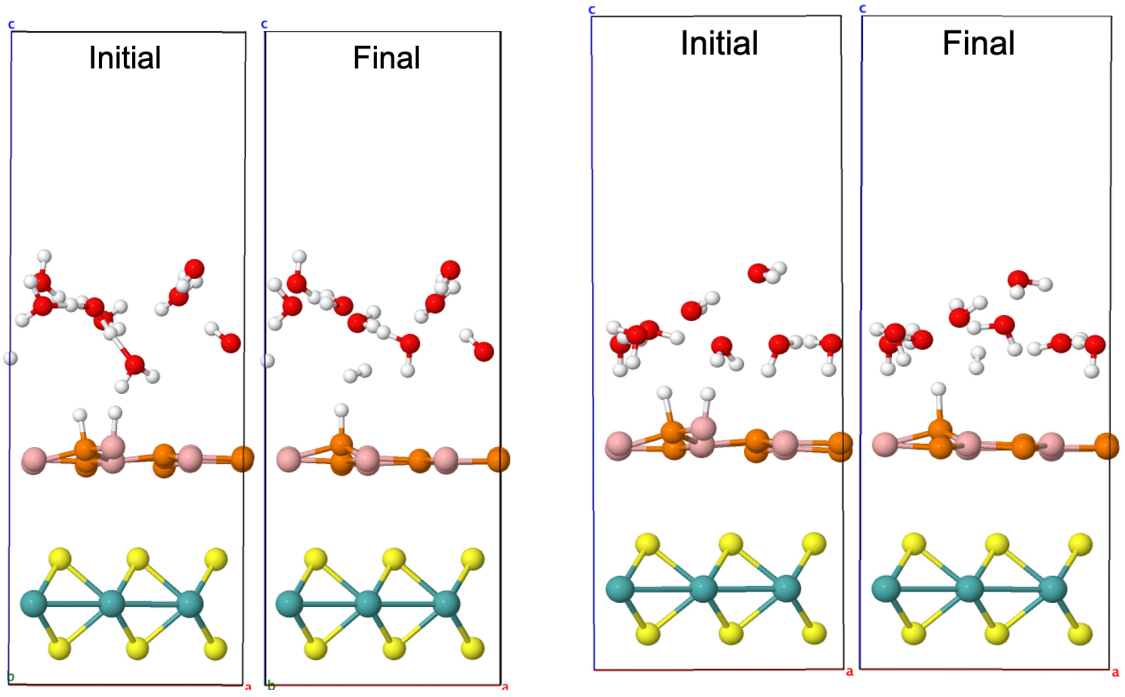

(a) 3×3 MoS_2/BP (b) With H_{down}

Figure 6.19: Initial and final configuration of 3×3 MoS_2/BP for Heyrovsky reaction water layer orientation.

Now, we progress towards the extrapolation approach to cater the problem of potential change from initial to final in case of proton transfer Heyrovsky reaction. In this approach, we obtain reaction energies and activation energies of system with different supercell sizes and H^+ conc. The former represents the energy difference between initial and final states, while the latter is the amount of energy required to overcome the reaction barrier.

Thereafter, we obtain ΔE_R and E_a vs ΔU plot. The ΔU signifies change in electrode potential from initial to final. Moreover, the change in U_1 (corresponding to water layer potential) is significant as compared to the change in U_2 (corresponding to MoS_2 layer potential). The potential drop and charge transfer would accordingly affect the U_1 and U_2. Hence, the reaction taking place at BP layer surface is crucial and we must consider U_1 for our analysis of electrode potential. Therefore, the ΔU represented in the plot is corresponding to the U_1. On extrapolating the ΔE_R to $\Delta U = 0$, we obtain -1.24 eV. The negative value indicates the spontaneity of the Heyrovsky reaction step. In case of positive ΔE_R, the Heyrovsky reaction would have been the rate determining step. The corresponding E_a is obtained at 0.05 eV. Hence, on comparing vdW HTS with monolayer, the synergistic effect of the two layers play role in affecting the

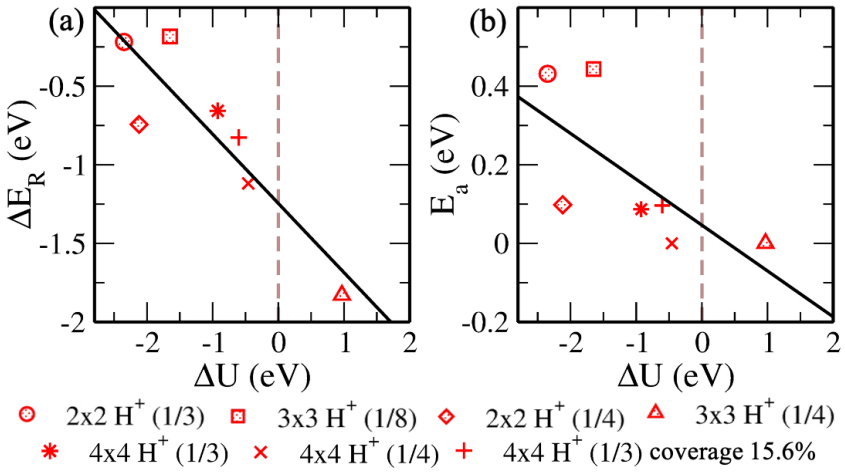

Figure 6.20: (Color online) Variation of (a) reaction energy ($\Delta E_R = E_{final} - E_{initial}$) and (b) activation energy (E_a), of configurations with respect to the change in electrode potential ($\Delta U = U_{1_{initial}} - U_{1_{final}}$) from initial to final.

overpotential and hence the reaction mechanism.

Now, we revisit the observations systematically. The H_{adsB} shows lower ground state energy and reaction barrier than the H_{adsP}. Also, we obtain a barrier in the range 0.05 eV - 0.08 eV when H_{adsP} precedes the H_{adsB} at the surface. The vice versa observes higher ground state energy of the final structure state than the initial structure. Therefore, though the Tafel reaction path shows no reaction barrier, above mentioned proton transfer (Volmer step) is restricted on sites. Subsequently, for the Heyrovsky reaction path, we observe the lower barrier for H_2 evolution that includes H^+ and H_{adsP}. Hence, the extrapolated Heyrovsky E_a of 0.05 eV further indicates the Heyrovsky reaction path to be plausible.

6.4 Conclusion

In summary, we have modelled a dynamically stable MoS_2/BP and MoSSe/BP vdW HTSs. They have been studied for HER by computational hydrogen electrode model. The optimized structure with the water layer showed a significant potential drop at the surface-water interface. The electrostatic potential is further affected by the proton solvated in water layer and the H_{ads} constituting coverage over the surface. 2×2, 3×3 and 4×4 supercells with 25%, 11% and 25% H coverage have been deduced for the calculations. Firstly, the MoS_2/BP and MoSSe/BP vdW HTSs show reduced barrier height for both Tafel and Heyrovsky reactions in comparison to the

BP monolayer. Tafel reaction, being a surface reaction does not require charge transfer, herein corroborates with no or less barrier observed in the MoS_2/BP and MoSSe/BP vdW HTSs. The analysis of H adsorption at B and P sites, infers H_{adsB} with lower ground state energy. The second Volmer step restricts the path of H_{adsB} preceding the H_{adsP}. In case of Heyrovsky reaction, reduced reaction barrier has been reported for H_{adsP}. Further, there is no significant difference between the MoSSe/BP and MoS_2/BP vdW HTS, as observed from the minimum energy reaction paths, except in the case of 11% coverage of MoSSe/BP with no reaction barrier. Hence, the MoSSe based vdW HTS has shown Heyrovsky reaction favoured HER for low coverage. On comparing the supercells (and hence different coverages) with respect to the same H^+ conc., we observe high coverage to favour low H^+ conc. and vice versa for reduced reaction barrier. Finally, as per the extrapolation approach for ΔE_R vs ΔU, the Heyrovsky reaction mechanism is established as favourable.

CHAPTER 7

Epilogue and outlook

The MoS_2 monolayer exhibits atypical optical, electrical, and mechanical properties. Its electrical and optoelectronic properties can be adjusted to meet various needs because of its tunable band gap. Moreover, defects, strain, and vdW HTSs further affect the properties, and understanding the same is crucial. In this thesis, we have observed the effect of defects and van der Waals heterostructure on the optical and catalytic properties.

The defect engineering on a monolayer for eliminating or inducing a defect depends on the applicability in various fields, viz., electrochemical reactions, spintronics, and semiconductors. The thermodynamic stability of defects is requisite for the analysis. In addition, the polarization that results in van der Waals interaction affects the free energy of formation. The change is more pronounced in monolayers than in bulk. We have modeled eight native point defect configurations consisting of vacancies (Mo, S, and S_2) and antisites (S_{Mo}, $S_{2_{Mo}}$, Mo_S, Mo_{S_2} and $2Mo_{S_2}$). The exhaustive study undertaken has indicated the accurate experimental correlation with the defect configuration obtained by hybrid functional and many-body dispersion. The plausible defect configurations of V_S^{-2}, V_{Mo}^{-2}, S_{Mo}^{-2}, V_S^{+2}, V_{Mo}^{+2} and $S_{2_{Mo}}^{+2}$ are also significant at the finite temperatures. In addition, the applicability of S_{Mo}^{-2} and $S_{2_{Mo}}^{+2}$ can be extended to the optoelectronics due to red shift in their optical response as compared to that of pristine. Moreover, the device industry can utilize the prominence of point defects in p-type MoS_2 monolayer along with the naturally known defect states in n-type.

The layered 2D vdW materials are versatile in terms of tunability and applicability. These, too, can be utilized for negative differential resistance (NDR). The NDR effect is the phenomenon where the device current decreases with the increase in applied bias voltage. Leo Esaki first observed this in the tunnel diode, i.e., heavily doped germanium p-n junction. The thin-film-based devices for observing the effect are an active area of study. Moreover, proton conductors have potential in the occurrence of the effect where the primary charge carriers here are protons

(H^+). The oxidation of water molecules generates O_2, H^+, and electrons. The electrons thus produced facilitate the reduction of water molecules. Hence, the protonic conduction mechanism has significance in the NDR effect. This work has thus proposed the generation of H^+ due to the bias voltage-induced electrolysis of the adsorbed water molecules in the ambient environment. The diffusion of H^+ is restricted by the broadening of the depletion width, thereby reducing the device current. The Hirshfeld analysis and minimum energy profile further indicate the stronger binding of OH^- ions than the H^+ ions at the MoS_2 S vacancy sites. This supports the higher mobility of protons and, thus, the NDR effect. This can be utilized in NDR-based applications like signal processing, amplifiers, and multi-valued logic devices.

$MoSe_2$, WS_2, MoS_2 and WSe_2 are the most researched TMDs. In an ever-increasing database of 2D materials, other members of the TMD family, such as ZrS_2, HfS_2, TiS_2, and transition metal oxides, have gained interest. Further, no photocatalytic study of MoS_2 based bilayer vdW HTSs exists with the combinations above of constituent monolayers. Along with these materials, the Janus materials (MXY; M = Mo and X, Y = O, S, Se, and Te; X$\neq$Y) have developed an interest in photocatalysis. Hence, a comparative study is conducted for MoSSe-based vdW HTSs with the MoS_2 based vdW HTSs. These vdW HTSs cannot proceed through the normal photocatalytic process as their band edges do not straddle the water-splitting redox potential. However, these have been studied for Z-scheme photocatalytic capability. Initially, we observed significant band gap differences in MoSSe-based vdW HTSs between the configurations of the interfacial S atomic layer and Se atomic layer. This is attributed to the anionic potential difference at the interface for the two configurations. The recombination rate by the effective mass ratio, exciton binding energy, carrier mobility, and optical response have corroborated the MoSSe/HfS_2, MoSSe/TiS_2, MoS_2/T-SnO_2, MoSSe/T-SnO_2, MoS_2/ZrS_2 and MoSSe/ZrS_2 as plausible Z-scheme photocatalyst. Finally, the HER and H_2O adsorption explains their interaction with water.

The HER is also widely studied by electrocatalytic pathways. We have modeled the Boron Phosphide (BP) monolayer, MoS_2/BP and MoSSe/BP vdW HTSs. BP monolayer has a single atomic layered structure with a lattice mismatch similar to MoS_2. It has been reported with stability in water environments, high carrier mobility, and good mechanical strength. Any prior investigations for HER on these systems are still being determined; hence we have considered these systems for our work. The optimized structures, along with the water layer, have shown significant potential drops at the interface of the surface and water. The factors further affect-

ing the electrostatic potential are the solvated protons in the water layer, the H_{ads} constituting coverage, and water orientations. The vdW HTSs show reduced barrier height for both Tafel and Heyrovsky reactions compared to the BP monolayer. The Heyrovsky reaction reports the reduced reaction barrier in the MoSSe/BP compared to that in MoS_2/BP. Subsequently, we observe a reduced barrier for high coverage low H^+ conc. and vice versa. Finally, the extrapolation for ΔE_R vs. ΔU established the Heyrovsky reaction mechanism to be plausible.

Among various designing alternatives, we have conducted our study in the field of defect engineering and vdW HTSs. These have been apposite due to significant control upon researcher for tuning the properties. The present work has exemplified the utilization of TMD-based monolayers and vdW HTSs for optical and catalytic properties that can be employed in photovoltaic, device, and catalytic industries. However, the systems and parameters have the scope of improvement. The different stable defect states (point and interfacial defects) and strain require analysis. These corroborate the synthesis techniques employed, further affecting the scalability of the monolayer production. Also, many materials in the TMD family still need to be explored. Often, the selection problem is essential and considerable research is ongoing to build the library. The parameters that affect the accuracy are large system size, long simulation time, and sophisticated methodologies like GW, which increase the computational expense. Therefore, machine learning approaches are attracting interest to predict material properties without expensive calculations. Overall, the parameters and applicability discussed in the thesis can guide future endeavors to design TMD-based photovoltaics, devices, and catalytic applications.

Bibliography

[1] John P. Perdew and Karla Schmidt. Jacob's ladder of density functional approximations for the exchange-correlation energy. *AIP Conference Proceedings*, 577:1–20, 2001.

[2] Daniel Sheppard, Rye Terrell, and Graeme Henkelman. Optimization methods for finding minimum energy paths. *The Journal of chemical physics*, 128(13):134106, 2008.

[3] Ramkrishna Sahoo, Anjali Pal, and Tarasankar Pal. 2d materials for renewable energy storage devices: outlook and challenges. *Chemical Communications*, 52(93):13528–13542, 2016.

[4] AH Castro Neto, Francisco Guinea, Nuno MR Peres, Kostya S Novoselov, and Andre K Geim. The electronic properties of graphene. *Reviews of modern physics*, 81(1):109, 2009.

[5] Xin Li, Jiaguo Yu, S Wageh, Ahmed A Al-Ghamdi, and Jun Xie. Graphene in photocatalysis: a review. *Small*, 12(48):6640–6696, 2016.

[6] Sajedeh Manzeli, Dmitry Ovchinnikov, Diego Pasquier, Oleg V Yazyev, and Andras Kis. 2d transition metal dichalcogenides. *Nature Reviews Materials*, 2(8):17033, 2017.

[7] Deep Jariwala, Vinod K Sangwan, Lincoln J Lauhon, Tobin J Marks, and Mark C Hersam. Emerging device applications for semiconducting two-dimensional transition metal dichalcogenides. *ACS nano*, 8(2):1102–1120, 2014.

[8] Tasuku Onodera, Yusuke Morita, Ai Suzuki, Michihisa Koyama, Hideyuki Tsuboi, Nozomu Hatakeyama, Akira Endou, Hiromitsu Takaba, Momoji Kubo, and Fabrice Dassenoy. A computational chemistry study on friction of h-mos2. part i. mechanism of single sheet lubrication. *The Journal of Physical Chemistry B*, 113(52):16526–16536, 2009.

[9] Kostya S Novoselov. Discovery of 2d van der waals layered mosi2n4 family. *National Science Review*, 7(12):1842–1844, 2020.

[10] Andre K Geim and Irina V Grigorieva. Van der waals heterostructures. *Nature*, 499(7459):419–425, 2013.

[11] Wei Zhao, Jie Pan, Yuqiang Fang, Xiangli Che, Dong Wang, Kejun Bu, and Fuqiang Huang. Metastable mos2: crystal structure, electronic band structure, synthetic approach and intriguing physical properties. *Chemistry–A European Journal*, 24(60):15942–15954, 2018.

[12] Changli Li, Qi Cao, Faze Wang, Yequan Xiao, Yanbo Li, Jean-Jacques Delaunay, and Hongwei Zhu. Engineering graphene and tmds based van der waals heterostructures for photovoltaic and photoelectrochemical solar energy conversion. *Chemical Society Reviews*, 47(13):4981–5037, 2018.

[13] Zongyou Yin, Jixin Zhu, Qiyuan He, Xiehong Cao, Chaoliang Tan, Hongyu Chen, Qingyu Yan, and Hua Zhang. Graphene-based materials for solar cell applications. *Advanced energy materials*, 4(1):1300574, 2014.

[14] Chaoliang Tan, Xiehong Cao, Xue-Jun Wu, Qiyuan He, Jian Yang, Xiao Zhang, Junze Chen, Wei Zhao, Shikui Han, Gwang-Hyeon Nam, et al. Recent advances in ultrathin two-dimensional nanomaterials. *Chemical reviews*, 117(9):6225–6331, 2017.

[15] Kin Fai Mak, Changgu Lee, James Hone, Jie Shan, and Tony F Heinz. Atomically thin mos 2: a new direct-gap semiconductor. *Physical review letters*, 105(13):136805, 2010.

[16] Rafael Besse, Matheus P Lima, and Juarez LF Da Silva. First-principles exploration of two-dimensional transition metal dichalcogenides based on fe, co, ni, and cu groups and their van der waals heterostructures. *ACS Applied Energy Materials*, 2(12):8491–8501, 2019.

[17] Wei Zhou, Huimin Gong, Xiaohe Jin, Yang Chen, Huimin Li, and Song Liu. Recent progress of two-dimensional transition metal dichalcogenides for thermoelectric applications. *Frontiers in Physics*, page 67, 2022.

[18] Gang Zhang and Yong-Wei Zhang. Thermoelectric properties of two-dimensional transition metal dichalcogenides. *Journal of Materials Chemistry C*, 5(31):7684–7698, 2017.

[19] Stefan K Estreicher. Hydrogen-related defects in crystalline semiconductors: a theorist's perspective. *Materials Science and Engineering: R: Reports*, 14:319–412, 1995.

[20] Chris G Van de Walle and Jörg Neugebauer. First-principles calculations for defects and impurities: Applications to III-nitrides. *Journal of applied physics*, 95:3851–3879, 2004.

[21] David A Drabold and Stefan K Estreicher. Defect theory: An armchair history. In *Theory of Defects in Semiconductors*, pages 11–28. Springer, 2007.

[22] Audrius Alkauskas and Alfredo Pasquarello. Band-edge problem in the theoretical determination of defect energy levels: The O vacancy in ZnO as a benchmark case. *Physical Review B*, 84:125206, 2011.

[23] Robert A Evarestov. *Quantum chemistry of solids: LCAO treatment of crystals and nanostructures*, volume 153. Springer Science & Business Media, 2013.

[24] Christoph Freysoldt, Blazej Grabowski, Tilmann Hickel, Jörg Neugebauer, Georg Kresse, Anderson Janotti, and Chris G. Van de Walle. First-principles calculations for point defects in solids. *Rev. Mod. Phys.*, 86:253–305, 2014.

[25] Jürgen Spitaler and Stefan K. Estreicher. Perspectives on the theory of defects. *Frontiers in Materials*, 5, 2018.

[26] W.D. Callister and D.G. Rethwisch. *Materials Science and Engineering*. Wiley, 2014.

[27] Richard M Martin. *Electronic structure: basic theory and practical methods*. Cambridge university press, 2004.

[28] Riccardo Frisenda, Efrén Navarro-Moratalla, Patricia Gant, David Pérez De Lara, Pablo Jarillo-Herrero, Roman V Gorbachev, and Andres Castellanos-Gomez. Recent progress in the assembly of nanodevices and van der waals heterostructures by deterministic placement of 2d materials. *Chemical Society Reviews*, 47(1):53–68, 2018.

[29] Valeria Nicolosi, Manish Chhowalla, Mercouri G Kanatzidis, Michael S Strano, and Jonathan N Coleman. Liquid exfoliation of layered materials. *Science*, 340(6139):1226419, 2013.

[30] Feng Wang, Zhenxing Wang, Tofik Ahmed Shifa, Yao Wen, Fengmei Wang, Xueying Zhan, Qisheng Wang, Kai Xu, Yun Huang, Lei Yin, et al. Two-dimensional non-layered materials: synthesis, properties and applications. *Advanced Functional Materials*, 27(19):1603254, 2017.

[31] JW Niemantsverdriet and I Chorkendorff. *Concepts of modern catalysis and kinetics*. John Wiley & Sons, 2006.

[32] Marco Piumetti. A brief history of the science of catalysis-i: From the early concepts to single-site heterogeneous catalysts. *Chim. Oggi*, 32:22–27, 2014.

[33] Stanisław Wacławek, Vinod VT Padil, and Miroslav Černík. Major advances and challenges in heterogeneous catalysis for environmental applications: a review. *Ecological Chemistry and Engineering S*, 25(1):9–34, 2018.

[34] Liangxu Lin, Peter Sherrell, Yuqing Liu, Wen Lei, Shaowei Zhang, Haijun Zhang, Gordon G Wallace, and Jun Chen. Engineered 2d transition metal dichalcogenides—a vision of viable hydrogen evolution reaction catalysis. *Advanced Energy Materials*, 10(16):1903870, 2020.

[35] Qiangmin Yu, Yuting Luo, Azhar Mahmood, Bilu Liu, and Hui-Ming Cheng. Engineering two-dimensional materials and their heterostructures as high-performance electrocatalysts. *Electrochemical Energy Reviews*, 2:373–394, 2019.

[36] Cheng Tang, Ling Zhong, Bingsen Zhang, Hao-Fan Wang, and Qiang Zhang. 3d mesoporous van der waals heterostructures for trifunctional energy electrocatalysis. *Advanced Materials*, 30(5):1705110, 2018.

[37] Alain R Puente Santiago, Tianwei He, Oscar Eraso, Md Ariful Ahsan, Aruna N Nair, Venkata SN Chava, Ting Zheng, Srikanth Pilla, Olivia Fernandez-Delgado, Aijun Du, et al. Tailoring the interfacial interactions of van der waals 1t-mos2/c60 heterostructures for high-performance hydrogen evolution reaction electrocatalysis. *Journal of the American Chemical Society*, 142(42):17923–17927, 2020.

[38] Thomas F Jaramillo, Kristina P Jørgensen, Jacob Bonde, Jane H Nielsen, Sebastian Horch, and Ib Chorkendorff. Identification of active edge sites for electrochemical h2 evolution from mos2 nanocatalysts. *science*, 317(5834):100–102, 2007.

[39] Dhanasekaran Vikraman, Sajjad Hussain, Supriya A Patil, Linh Truong, Alvira Ayoub Arbab, Sung Hoon Jeong, Seung-Hyun Chun, Jongwan Jung, and Hyun-Seok Kim. Engineering mose2/ws2 hybrids to replace the scarce platinum electrode for hydrogen evolution reactions and dye-sensitized solar cells. *ACS applied materials & interfaces*, 13(4):5061–5072, 2021.

[40] Jürgen Spitaler and Stefan K Estreicher. Perspectives on the theory of defects. *Frontiers in Materials*, 5:70, 2018.

[41] Sumit Bawari, Nisheal M Kaley, Shubhadeep Pal, Thazhe Veettil Vineesh, Shamasree Ghosh, Jagannath Mondal, and Tharangattu N Narayanan. On the hydrogen evolution reaction activity of graphene–hbn van der waals heterostructures. *Physical Chemistry Chemical Physics*, 20(22):15007–15014, 2018.

[42] Egill Skúlason, Gustav S Karlberg, Jan Rossmeisl, Thomas Bligaard, Jeff Greeley, Hannes Jónsson, and Jens K Nørskov. Density functional theory calculations for the hydrogen evolution reaction in an electrochemical double layer on the pt (111) electrode. *Physical Chemistry Chemical Physics*, 9(25):3241–3250, 2007.

[43] Llewellyn H Thomas. The calculation of atomic fields. In *Mathematical proceedings of the Cambridge philosophical society*, volume 23, pages 542–548. Cambridge University Press, 1927.

[44] Enrico Fermi. Statistical method to determine some properties of atoms. *Rend. Accad. Naz. Lincei*, 6(602-607):5, 1927.

[45] P. Hohenberg and W. Kohn. Inhomogeneous electron gas. *Phys. Rev.*, 136:B864–B871, 1964.

[46] W. Kohn and L. J. Sham. Self-consistent equations including exchange and correlation effects. *Phys. Rev.*, 140:A1133–A1138, 1965.

[47] David C. Langreth and M. J. Mehl. Beyond the local-density approximation in calculations of ground-state electronic properties. *Phys. Rev. B*, 28:1809–1834, 1983.

[48] John P. Perdew, Kieron Burke, and Matthias Ernzerhof. Generalized gradient approximation made simple. *Phys. Rev. Lett.*, 77:3865–3868, 1996.

[49] John P Perdew, Stefan Kurth, Aleš Zupan, and Peter Blaha. Accurate density functional with correct formal properties: A step beyond the generalized gradient approximation. *Physical review letters*, 82(12):2544, 1999.

[50] Jochen Heyd, Gustavo E. Scuseria, and Matthias Ernzerhof. Hybrid functionals based on a screened coulomb potential. *The Journal of Chemical Physics*, 118:8207–8215, 2003.

[51] Aliaksandr V. Krukau, Oleg A. Vydrov, Artur F. Izmaylov, and Gustavo E. Scuseria. Influence of the exchange screening parameter on the performance of screened hybrid functionals. *The Journal of Chemical Physics*, 125:224106, 2006.

[52] Neil W. Ashcroft and N David Mermin. Solid state physics, 1976.

[53] Peter Kratzer and Jörg Neugebauer. The basics of electronic structure theory for periodic systems. *Frontiers in Chemistry*, 7:106, 2019.

[54] D. J. Chadi and Marvin L. Cohen. Special points in the brillouin zone. *Phys. Rev. B*, 8:5747–5753, 1973.

[55] Hendrik J. Monkhorst and James D. Pack. Special points for brillouin-zone integrations. *Phys. Rev. B*, 13:5188–5192, 1976.

[56] Juana Moreno and José M. Soler. Optimal meshes for integrals in real- and reciprocal-space unit cells. *Phys. Rev. B*, 45:13891–13898, 1992.

[57] M. C. Payne, M. P. Teter, D. C. Allan, T. A. Arias, and J. D. Joannopoulos. Iterative minimization techniques for ab initio total-energy calculations: molecular dynamics and conjugate gradients. *Rev. Mod. Phys.*, 64:1045–1097, 1992.

[58] D. R. Hamann, M. Schlüter, and C. Chiang. Norm-conserving pseudopotentials. *Phys. Rev. Lett.*, 43:1494–1497, 1979.

[59] Michael Teter. Additional condition for transferability in pseudopotentials. *Physical Review B*, 48(8):5031, 1993.

[60] David Vanderbilt. Soft self-consistent pseudopotentials in a generalized eigenvalue formalism. *Phys. Rev. B*, 41:7892–7895, 1990.

[61] O. Krogh Andersen. Linear methods in band theory. *Phys. Rev. B*, 12:3060–3083, 1975.

[62] J. C. Slater. Wave functions in a periodic potential. *Phys. Rev.*, 51:846–851, 1937.

[63] Peter E Blöchl. Projector augmented-wave method. *Physical review B*, 50(24):17953, 1994.

[64] Dorothea Golze, Marc Dvorak, and Patrick Rinke. The GW compendium: A practical guide to theoretical photoemission spectroscopy. *Frontiers in Chemistry*, 7:377, 2019.

[65] Richard Phillips Feynman. Forces in molecules. *Physical review*, 56:340, 1939.

[66] Hannu-Pekka Komsa and Arkady V Krasheninnikov. Native defects in bulk and monolayer mos_2 from first principles. *Physical Review B*, 91(12):125304, 2015.

[67] Saswata Bhattacharya, Sergey V Levchenko, Luca M Ghiringhelli, and Matthias Scheffler. Efficient ab initio schemes for finding thermodynamically stable and metastable atomic structures: Benchmark of cascade genetic algorithms. *New Journal of Physics*, 16(12):123016, 2014.

[68] L. J. Sham and W. Kohn. One-particle properties of an inhomogeneous interacting electron gas. *Phys. Rev.*, 145:561–567, 1966.

[69] John P. Perdew, Robert G. Parr, Mel Levy, and Jose L. Balduz. Density-functional theory for fractional particle number: Derivative discontinuities of the energy. *Phys. Rev. Lett.*, 49:1691–1694, 1982.

[70] Dahvyd Wing, Jonah B Haber, Roy Noff, Bradford Barker, David A Egger, Ashwin Ramasubramaniam, Steven G Louie, Jeffrey B Neaton, and Leeor Kronik. Comparing time-dependent density functional theory with many-body perturbation theory for semiconductors: Screened range-separated hybrids and the g w plus bethe-salpeter approach. *Physical Review Materials*, 3(6):064603, 2019.

[71] Giovanni Onida, Lucia Reining, and Angel Rubio. Electronic excitations: density-functional versus many-body green's-function approaches. *Rev. Mod. Phys.*, 74:601–659, 2002.

[72] Lars Hedin. New method for calculating the one-particle green's function with application to the electron-gas problem. *Phys. Rev.*, 139:A796–A823, 1965.

[73] Maxim Shishkin and Georg Kresse. Self-consistent g w calculations for semiconductors and insulators. *Physical Review B*, 75(23):235102, 2007.

[74] M Shishkin and G Kresse. Implementation and performance of the frequency-dependent g w method within the paw framework. *Physical Review B*, 74(3):035101, 2006.

[75] Sergey V. Faleev, Mark van Schilfgaarde, and Takao Kotani. All-electron self-consistent GW approximation: Application to Si, MnO, and NiO. *Phys. Rev. Lett.*, 93:126406, 2004.

[76] Manuel Grumet, Peitao Liu, Merzuk Kaltak, Ji ří Klimeš, and Georg Kresse. Beyond the quasiparticle approximation: Fully self-consistent GW calculations. *Phys. Rev. B*, 98:155143, 2018.

[77] G. Strinati. Effects of dynamical screening on resonances at inner-shell thresholds in semiconductors. *Phys. Rev. B*, 29:5718–5726, 1984.

[78] Michael Rohlfing and Steven G. Louie. Electron-hole excitations and optical spectra from first principles. *Phys. Rev. B*, 62:4927–4944, 2000.

[79] Lu J Sham and Michael Schlüter. Density-functional theory of the energy gap. *Physical review letters*, 51(20):1888, 1983.

[80] Yann Michel Niquet, Martin Fuchs, and Xavier Gonze. Asymptotic behavior of the exchange-correlation potentials from the linear-response sham–schlüter equation. *The Journal of chemical physics*, 118(21):9504–9518, 2003.

[81] Stefano Baroni, Stefano de Gironcoli, Andrea Dal Corso, and Paolo Giannozzi. Phonons and related crystal properties from density-functional perturbation theory. *Rev. Mod. Phys.*, 73:515–562, 2001.

[82] AH Castro Neto, Francisco Guinea, Nuno MR Peres, Kostya S Novoselov, and Andre K Geim. The electronic properties of graphene. *Reviews of modern physics*, 81(1):109, 2009.

[83] Rudren Ganatra and Qing Zhang. Few-layer mos2: a promising layered semiconductor. *ACS nano*, 8(5):4074–4099, 2014.

[84] Faling Ling, Wei Kang, Huirong Jing, Wen Zeng, Yankun Chen, Xiaoqing Liu, Yixin Zhang, Lin Qi, Liang Fang, and Miao Zhou. Enhancing hydrogen evolution on the basal plane of transition metal dichacolgenide van der waals heterostructures. *npj Computational Materials*, 5(1):20, 2019.

[85] Chung-Yu Wang and Guang-Yu Guo. Nonlinear optical properties of transition-metal dichalcogenide mx2 (m= mo, w; x= s, se) monolayers and trilayers from first-principles calculations. *The Journal of Physical Chemistry C*, 119(23):13268–13276, 2015.

[86] Branimir Radisavljevic, Aleksandra Radenovic, Jacopo Brivio, i V Giacometti, and A Kis. Single-layer mos 2 transistors. *Nature nanotechnology*, 6(3):147, 2011.

[87] Andres Castellanos-Gomez, Menno Poot, Gary A Steele, Herre SJ van der Zant, Nicolás Agraït, and Gabino Rubio-Bollinger. Elastic properties of freely suspended mos_2 nanosheets. *Advanced Materials*, 24(6):772–775, 2012.

[88] Mohapatra Prakash Kumar Sahoo, Jie Wang, Yajun Zhang, Takahiro Shimada, and Takayuki Kitamura. Modulation of gas adsorption and magnetic properties of monolayer-mos_2 by antisite defect and strain. *The Journal of Physical Chemistry C*, 120(26):14113–14121, 2016.

[89] C Ataca, H Sahin, E Akturk, and S Ciraci. Mechanical and electronic properties of mos_2 nanoribbons and their defects. *The Journal of Physical Chemistry C*, 115(10):3934–3941, 2011.

[90] Wenzhuo Wu, Lei Wang, Yilei Li, Fan Zhang, Long Lin, Simiao Niu, Daniel Chenet, Xian Zhang, Yufeng Hao, Tony F Heinz, and et al. Piezoelectricity of single-atomic-layer mos_2 for energy conversion and piezotronics. *Nature*, 514(7523):470, 2014.

[91] Lanzhong Hao, Yunjie Liu, Wei Gao, Zhide Han, Qingzhong Xue, Huizhong Zeng, Zhipeng Wu, Jun Zhu, and Wanli Zhang. Electrical and photovoltaic characteristics of mos2/si pn junctions. *Journal of Applied Physics*, 117(11):114502, 2015.

[92] Song-Lin Li, Kazuhito Tsukagoshi, Emanuele Orgiu, and Paolo Samorì. Charge transport and mobility engineering in two-dimensional transition metal chalcogenide semiconductors. *Chemical Society Reviews*, 45(1):118–151, 2016.

[93] Jinhua Hong, Zhixin Hu, Matt Probert, Kun Li, Danhui Lv, Xinan Yang, Lin Gu, Nannan Mao, Qingliang Feng, Liming Xie, and et al. Exploring atomic defects in molybdenum disulphide monolayers. *Nature communications*, 6:6293, 2015.

[94] Yong Xie, Zhan Wang, Yongjie Zhan, Peng Zhang, Ruixue Wu, Teng Jiang, Shiwei Wu, Hong Wang, Ying Zhao, Tang Nan, and et al. Controllable growth of monolayer mos_2 by chemical vapor deposition via close moo_2 precursor for electrical and optical applications. *Nanotechnology*, 28(8):084001, 2017.

[95] Yi-Hsien Lee, Xin-Quan Zhang, Wenjing Zhang, Mu-Tung Chang, Cheng-Te Lin, Kai-Di Chang, Ya-Chu Yu, Jacob Tse-Wei Wang, Chia-Seng Chang, Lain-Jong Li, and et al. Synthesis of large-area mos_2 atomic layers with chemical vapor deposition. *Advanced materials*, 24(17):2320–2325, 2012.

[96] Yu-Chuan Lin, Wenjing Zhang, Jing-Kai Huang, Keng-Ku Liu, Yi-Hsien Lee, Chi-Te Liang, Chih-Wei Chu, and Lain-Jong Li. Wafer-scale mos_2 thin layers prepared by moo_3 sulfurization. *Nanoscale*, 4(20):6637–6641, 2012.

[97] Simone Bertolazzi, Jacopo Brivio, and Andras Kis. Stretching and breaking of ultrathin mos_2. *ACS nano*, 5(12):9703–9709, 2011.

[98] Jing Yang, Hiroyo Kawai, Calvin Pei Yu Wong, and Kuan Eng Johnson Goh. Electrical doping effect of vacancies on monolayer mos_2. *The Journal of Physical Chemistry C*, 123(5):2933–2939, 2019.

[99] Stephen McDonnell, Rafik Addou, Creighton Buie, Robert M Wallace, and Christopher L Hinkle. Defect-dominated doping and contact resistance in mos_2. *ACS nano*, 8(3):2880–2888, 2014.

[100] Tobias Korn, Stefanie Heydrich, Michael Hirmer, Johannes Schmutzler, and Christian Schüller. Low-temperature photocarrier dynamics in monolayer mos_2. *Applied Physics Letters*, 99(10):102109, 2011.

[101] Sang Wook Han, Young Hun Hwang, Seon-Ho Kim, Won Seok Yun, Jae Dong Lee, Min Gyu Park, Sunmin Ryu, Ju Sang Park, Dae-Hwang Yoo, Sang-Pil Yoon, and et al. Controlling ferromagnetic easy axis in a layered mos_2 single crystal. *Physical review letters*, 110(24):247201, 2013.

[102] Nan Gao, Yu Guo, Si Zhou, Yizhen Bai, and Jijun Zhao. Structures and magnetic properties of mos_2 grain boundaries with antisite defects. *The Journal of Physical Chemistry C*, 121(22):12261–12269, 2017.

[103] Sefaattin Tongay, Joonki Suh, Can Ataca, Wen Fan, Alexander Luce, Jeong Seuk Kang, Jonathan Liu, Changhyun Ko, Rajamani Raghunathanan, and Jian Zhou. Defects activated photoluminescence in two-dimensional semiconductors: interplay between bound, charged, and free excitons. *Scientific reports*, 3:2657, 2013.

[104] Mahdi Ghorbani-Asl, Andrey N Enyashin, Agnieszka Kuc, Gotthard Seifert, and Thomas Heine. Defect-induced conductivity anisotropy in mos_2 monolayers. *Physical Review B*, 88(24):245440, 2013.

[105] Mingsheng Xu, Tao Liang, Minmin Shi, and Hongzheng Chen. Graphene-like two-dimensional materials. *Chemical reviews*, 113(5):3766–3798, 2013.

[106] KC Santosh, Roberto C Longo, Rafik Addou, Robert M Wallace, and Kyeongjae Cho. Impact of intrinsic atomic defects on the electronic structure of mos_2 monolayers. *Nanotechnology*, 25(37):375703, 2014.

[107] C González, Yannick J Dappe, and B Biel. Reactivity enhancement and fingerprints of point defects on a mos_2 monolayer assessed by ab initio atomic force microscopy. *The Journal of Physical Chemistry C*, 120(30):17115–17126, 2016.

[108] Leonardo Vicarelli, Stephanie J Heerema, Cees Dekker, and Henny W Zandbergen. Controlling defects in graphene for optimizing the electrical properties of graphene nanodevices. *ACS nano*, 9(4):3428–3435, 2015.

[109] Bo Peng, Zeyu Ning, Hao Zhang, Hezhu Shao, Yuanfeng Xu, Gang Ni, and Heyuan Zhu. Beyond perturbation: Role of vacancy-induced localized phonon states in thermal transport of monolayer mos_2. *The Journal of Physical Chemistry C*, 120(51):29324–29331, 2016.

[110] Ji-Young Noh, Hanchul Kim, and Yong-Sung Kim. Stability and electronic structures of native defects in single-layer mos 2. *Physical Review B*, 89(20):205417, 2014.

[111] Zhong Lin, Bruno R Carvalho, Ethan Kahn, Ruitao Lv, Rahul Rao, Humberto Terrones, Marcos A Pimenta, and Mauricio Terrones. Defect engineering of two-dimensional transition metal dichalcogenides. *2D Materials*, 3(2):022002, 2016.

[112] Yongqing Cai, Hangbo Zhou, Gang Zhang, and Yong-Wei Zhang. Modulating carrier density and transport properties of mos_2 by organic molecular doping and defect engineering. *Chemistry of Materials*, 28(23):8611–8621, 2016.

[113] Haiyan Nan, Zilu Wang, Wenhui Wang, Zheng Liang, Yan Lu, Qian Chen, Daowei He, Pingheng Tan, Feng Miao, and Xinran Wang. Strong photoluminescence enhancement of mos2 through defect engineering and oxygen bonding. *ACS nano*, 8(6):5738–5745, 2014.

[114] Guoping Gao, Qiao Sun, and Aijun Du. Activating catalytic inert basal plane of molybdenum disulfide to optimize hydrogen evolution activity via defect doping and strain engineering. *The Journal of Physical Chemistry C*, 120(30):16761–16766, 2016.

[115] Gonglan Ye, Yongji Gong, Junhao Lin, Bo Li, Yongmin He, Sokrates T Pantelides, Wu Zhou, Robert Vajtai, and Pulickel M Ajayan. Defects engineered monolayer mos_2 for improved hydrogen evolution reaction. *Nano letters*, 16(2):1097–1103, 2016.

[116] Yuzi Xu, Longlu Wang, Xia Liu, Shuqu Zhang, Chengbin Liu, Dafeng Yan, Yunxiong Zeng, Yong Pei, Yutang Liu, and Shenglian Luo. Monolayer mos_2 with s vacancies from interlayer spacing expanded counterparts for highly efficient electrochemical hydrogen production. *Journal of Materials Chemistry A*, 4(42):16524–16530, 2016.

[117] Gayatree Barik and Sourav Pal. Defect induced performance enhancement of monolayer mos_2 for li-and na-ion batteries. *The Journal of Physical Chemistry C*, 2019.

[118] Seung Hyun Song, Min-Kyu Joo, Michael Neumann, Hyun Kim, and Young Hee Lee. Probing defect dynamics in monolayer mos_2 via noise nanospectroscopy. *Nature communications*, 8(1):2121, 2017.

[119] Kapildeb Dolui, Ivan Rungger, and Stefano Sanvito. Origin of the n-type and p-type conductivity of mos_2 monolayers on a sio_2 substrate. *Physical review B*, 87(16):165402, 2013.

[120] Shaoxiong Wu, Yang Zeng, Xiangbin Zeng, Shibo Wang, Yishuo Hu, Wenzhao Wang, Sheng Yin, Guangtong Zhou, Wen Jin, Tingting Ren, and et al. High-performance p-type mos_2 field-effect transistor by toroidal-magnetic-field controlled oxygen plasma doping. *2D Materials*, 6:025007, 2019.

[121] Wang Gao and Alexandre Tkatchenko. Electronic structure and van der waals interactions in the stability and mobility of point defects in semiconductors. *Physical review letters*, 111(4):045501, 2013.

[122] Henrik Rydberg, Max Dion, Niclas Jacobson, Elsebeth Schröder, Per Hyldgaard, SI Simak, David C Langreth, and Bengt I Lundqvist. Van der waals density functional for layered structures. *Physical review letters*, 91(12):126402, 2003.

[123] C González, B Biel, and Yannick J Dappe. Theoretical characterisation of point defects on a mos_2 monolayer by scanning tunnelling microscopy. *Nanotechnology*, 27(10):105702, 2016.

[124] Alexandre Tkatchenko and Matthias Scheffler. Accurate molecular van der waals interactions from ground-state electron density and free-atom reference data. *Physical review letters*, 102(7):073005, 2009.

[125] Alexandre Tkatchenko, Robert A DiStasio Jr, Roberto Car, and Matthias Scheffler. Accurate and efficient method for many-body van der waals interactions. *Physical review letters*, 108(23):236402, 2012.

[126] Alberto Ambrosetti, Anthony M Reilly, Robert A DiStasio Jr, and Alexandre Tkatchenko. Long-range correlation energy calculated from coupled atomic response functions. *The Journal of chemical physics*, 140(18):18A508, 2014.

[127] Saswata Bhattacharya, Daniel Berger, Karsten Reuter, Luca M Ghiringhelli, and Sergey V Levchenko. Theoretical evidence for unexpected o-rich phases at corners of mgo surfaces. *Physical Review Materials*, 1(7):071601, 2017.

[128] Karsten Reuter, Catherine Stampf, and Matthias Scheffler. Ab initio atomistic thermodynamics and statistical mechanics of surface properties and functions. In *Handbook of materials modeling*, pages 149–194. Springer, 2005.

[129] Richard M Martin, Lucia Reining, and David M Ceperley. *Interacting Electrons*. Cambridge University Press, 2016.

[130] Christoph Freysoldt, Blazej Grabowski, Tilmann Hickel, Jörg Neugebauer, Georg Kresse, Anderson Janotti, and Chris G Van de Walle. First-principles calculations for point defects in solids. *Reviews of modern physics*, 86(1):253, 2014.

[131] Li-ping Feng, Jie Su, Shuai Chen, and Zheng-tang Liu. First-principles investigations on vacancy formation and electronic structures of monolayer mos2. *Materials Chemistry and Physics*, 148(1-2):5–9, 2014.

[132] Volker Blum, Ralf Gehrke, Felix Hanke, Paula Havu, Ville Havu, Xinguo Ren, Karsten Reuter, and Matthias Scheffler. Ab initio molecular simulations with numeric atom-centered orbitals. *Computer Physics Communications*, 180(11):2175–2196, 2009.

[133] Andreas Marek, Volker Blum, Rainer Johanni, Ville Havu, Bruno Lang, Thomas Auckenthaler, Alexander Heinecke, Hans-Joachim Bungartz, and Hermann Lederer. The elpa library: scalable parallel eigenvalue solutions for electronic structure theory and computational science. *Journal of Physics: Condensed Matter*, 26(21):213201, 2014.

[134] Thomas Auckenthaler, Volker Blum, H-J Bungartz, Thomas Huckle, Rainer Johanni, Lukas Krämer, Bruno Lang, Hermann Lederer, and Paul R Willems. Parallel solution of partial symmetric eigenvalue problems from electronic structure calculations. *Parallel Computing*, 37(12):783–794, 2011.

[135] Ville Havu, Volker Blum, Paula Havu, and Matthias Scheffler. Efficient o (n) integration for all-electron electronic structure calculation using numeric basis functions. *Journal of Computational Physics*, 228(22):8367–8379, 2009.

[136] Pierre Hohenberg and Walter Kohn. Inhomogeneous electron gas. *Physical review*, 136(3B):B864, 1964.

[137] Walter Kohn and Lu Jeu Sham. Self-consistent equations including exchange and correlation effects. *Physical review*, 140(4A):A1133, 1965.

[138] John P Perdew, Kieron Burke, and Matthias Ernzerhof. Generalized gradient approximation made simple. *Physical review letters*, 77(18):3865, 1996.

[139] Jochen Heyd, Gustavo E Scuseria, and Matthias Ernzerhof. Hybrid functionals based on a screened coulomb potential. *The Journal of chemical physics*, 118(18):8207–8215, 2003.

[140] Agnieszka Kuc and Thomas Heine. The electronic structure calculations of two-dimensional transition-metal dichalcogenides in the presence of external electric and magnetic fields. *Chemical Society Reviews*, 44(9):2603–2614, 2015.

[141] Georg Kresse and Jürgen Furthmüller. Efficient iterative schemes for ab initio total-energy calculations using a plane-wave basis set. *Physical review B*, 54(16):11169, 1996.

[142] Karsten Reuter and Matthias Scheffler. Composition, structure, and stability of ruo 2 (110) as a function of oxygen pressure. *Physical Review B*, 65(3):035406, 2001.

[143] WM Haynes. Crc handbook of chemistry and physics, (internet version 2011). *Taylor Francis Group: Boca Raton, FL*, 2011.

[144] Ekta Arora, Shikha Saini, Pooja Basera, Manish Kumar, Arunima Singh, and Saswata Bhattacharya. Elucidating the role of temperature and pressure to the thermodynamic stability of charged defects in complex metal-hydrides: A case study of naalh4. *The Journal of Physical Chemistry C*, 123(1):62–69, 2018.

[145] Wu Zhou, Xiaolong Zou, Sina Najmaei, Zheng Liu, Yumeng Shi, Jing Kong, Jun Lou, Pulickel M Ajayan, Boris I Yakobson, and Juan-Carlos Idrobo. Intrinsic structural defects in monolayer molybdenum disulfide. *Nano letters*, 13(6):2615–2622, 2013.

[146] Manish Chhowalla, Hyeon Suk Shin, Goki Eda, Lain-Jong Li, Kian Ping Loh, and Hua Zhang. The chemistry of two-dimensional layered transition metal dichalcogenide nanosheets. *Nature chemistry*, 5(4):263–275, 2013.

[147] Xiaobo Yin, Ziliang Ye, Daniel A Chenet, Yu Ye, Kevin O'Brien, James C Hone, and Xiang Zhang. Edge nonlinear optics on a mos2 atomic monolayer. *Science*, 344(6183):488–490, 2014.

[148] Jaewoo Shim, Seyong Oh, Dong-Ho Kang, Seo-Hyeon Jo, Muhammad Hasnain Ali, Woo-Young Choi, Keun Heo, Jaeho Jeon, Sungjoo Lee, Minwoo Kim, et al. Phosphorene/rhenium disulfide heterojunction-based negative differential resistance device for multi-valued logic. *Nature communications*, 7(1):13413, 2016.

[149] Leo Esaki. New phenomenon in narrow germanium p- n junctions. *Physical review*, 109(2):603, 1958.

[150] Hanlu Ma, Wei Wang, Haiyang Xu, Zhongqiang Wang, Ye Tao, Peng Chen, Weizhen Liu, Xintong Zhang, Jiangang Ma, and Yichun Liu. Interface state-induced negative differential resistance observed in hybrid perovskite resistive switching memory. *ACS applied materials & interfaces*, 10(25):21755–21763, 2018.

[151] Sina Yeganeh, Michael Galperin, and Mark A Ratner. Switching in molecular transport junctions: polarization response. *Journal of the American Chemical Society*, 129(43):13313–13320, 2007.

[152] Kei Kinoshita, Rai Moriya, Shota Okazaki, Yijin Zhang, Satoru Masubuchi, Kenji Watanabe, Takashi Taniguchi, Takao Sasagawa, and Tomoki Machida. Resonant tunneling between quantized subbands in van der waals double quantum well structure based on few-layer wse2. *Nano Letters*, 22(12):4640–4645, 2022.

[153] Chen Xu, Chuanping Li, and Yongdong Jin. Programmable organic-free negative differential resistance memristor based on plasmonic tunnel junction. *Small*, 16(34):2002727, 2020.

[154] Kil-Su Jung, Keun Heo, Min-Je Kim, Maksim Andreev, Seunghwan Seo, Jin-Ok Kim, Ji-Hye Lim, Kwan-Ho Kim, Sungho Kim, Ki Seok Kim, et al. Double negative differential resistance device based on hafnium disulfide/pentacene hybrid structure. *Advanced Science*, 7(19):2000991, 2020.

[155] Adam V Bruce, Shuanglong Liu, James N Fry, and Hai-Ping Cheng. Insights into negative differential resistance in mos 2 esaki diodes: A first-principles perspective. *Physical Review B*, 102(11):115415, 2020.

[156] Mohammad Razaul Karim, Kazuto Hatakeyama, Michio Koinuma, and Shinya Hayami. Proton conductors produced by chemical modifications of carbon allotropes, perovskites and metal organic frameworks. *Journal of Materials Chemistry A*, 5(16):7243–7256, 2017.

[157] Jian Su, Wen He, Xiao-Min Li, Lei Sun, Hai-Ying Wang, Ya-Qian Lan, Mengning Ding, and Jing-Lin Zuo. High electrical conductivity in a 2d mof with intrinsic superprotonic conduction and interfacial pseudo-capacitance. *Matter*, 2(3):711–722, 2020.

[158] Fabian M Draber, Christiane Ader, John P Arnold, Sebastian Eisele, Steffen Grieshammer, Shu Yamaguchi, and Manfred Martin. Nanoscale percolation in doped bazro3 for high proton mobility. *Nature materials*, 19(3):338–346, 2020.

[159] Dominik Marx. Proton transfer 200 years after von grotthuss: Insights from ab initio simulations. *ChemPhysChem*, 7(9):1848–1870, 2006.

[160] Ali Hassanali, Federico Giberti, Jérôme Cuny, Thomas D Kühne, and Michele Parrinello. Proton transfer through the water gossamer. *Proceedings of the National Academy of Sciences*, 110(34):13723–13728, 2013.

[161] Matti Hellström, Vanessa Quaranta, and Jörg Behler. One-dimensional vs. two-dimensional proton transport processes at solid–liquid zinc-oxide–water interfaces. *Chemical Science*, 10(4):1232–1243, 2019.

[162] Venkat Kapil, Christoph Schran, Andrea Zen, Ji Chen, Chris J Pickard, and Angelos Michaelides. The first-principles phase diagram of monolayer nanoconfined water. *Nature*, 609(7927):512–516, 2022.

[163] C Stampfl and CG Van de Walle. Density-functional calculations for iii-v nitrides using the local-density approximation and the generalized gradient approximation. *Physical Review B*, 59(8):5521, 1999.

[164] Graeme Henkelman, Blas P Uberuaga, and Hannes Jónsson. A climbing image nudged elastic band method for finding saddle points and minimum energy paths. *The Journal of Chemical Physics*, 113(22):9901–9904, 2000.

[165] Graeme Henkelman and Hannes Jónsson. Improved tangent estimate in the nudged elastic band method for finding minimum energy paths and saddle points. *The Journal of Chemical Physics*, 113(22):9978–9985, 2000.

[166] Manoranjan Ghosh, SC Gadkari, and SK Gupta. Redox reaction based negative differential resistance and bistability in nanoparticulate zno films. *Journal of Applied Physics*, 112(2), 2012.

[167] Meng Ni, Michael KH Leung, Dennis YC Leung, and K Sumathy. A review and recent developments in photocatalytic water-splitting using tio2 for hydrogen production. *Renewable and Sustainable Energy Reviews*, 11(3):401–425, 2007.

[168] Hongbao Yao, Maohong Fan, Yujun Wang, Guangsheng Luo, and Weiyang Fei. Magnetic titanium dioxide based nanomaterials: synthesis, characteristics, and photocatalytic application in pollutant degradation. *Journal of Materials Chemistry A*, 3(34):17511–17524, 2015.

[169] Francis Opoku, Krishna Kuben Govender, Cornelia Gertina Catharina Elizabeth van Sittert, and Penny Poomani Govender. Role of mos 2 and ws 2 monolayers on photocatalytic hydrogen production and the pollutant degradation of monoclinic bivo 4: A first-principles study. *New Journal of Chemistry*, 41(20):11701–11713, 2017.

[170] Changlin Yu, Fanyun Chen, Debin Zeng, Yu Xie, Wanqin Zhou, Zhen Liu, Longfu Wei, Kai Yang, and Dehao Li. A facile phase transformation strategy for fabrication of novel z-scheme ternary heterojunctions with efficient photocatalytic properties. *Nanoscale*, 11(16):7720–7733, 2019.

[171] CNR Rao, K Gopalakrishnan, and Urmimala Maitra. Comparative study of potential applications of graphene, mos2, and other two-dimensional materials in energy devices, sensors, and related areas. *ACS applied materials & interfaces*, 7(15):7809–7832, 2015.

[172] Eric Singh, Pragya Singh, Ki Seok Kim, Geun Young Yeom, and Hari Singh Nalwa. Flexible molybdenum disulfide (mos2) atomic layers for wearable electronics and optoelectronics. *ACS Applied Materials & Interfaces*, 11(12):11061–11105, 2019.

[173] Hualing Zeng, Gui-Bin Liu, Junfeng Dai, Yajun Yan, Bairen Zhu, Ruicong He, Lu Xie, Shijie Xu, Xianhui Chen, Wang Yao, et al. Optical signature of symmetry variations and spin-valley coupling in atomically thin tungsten dichalcogenides. *Scientific reports*, 3:1608, 2013.

[174] Nina Glebko, Irina Aleksandrova, Girish C Tewari, Tripurari S Tripathi, Maarit Karppinen, and Antti J Karttunen. Electronic and vibrational properties of tis2, zrs2, and hfs2: Periodic trends studied by dispersion-corrected hybrid density functional methods. *The Journal of Physical Chemistry C*, 122(47):26835–26844, 2018.

[175] Ka Wai Lau, Caterina Cocchi, and Claudia Draxl. Electronic and optical excitations of two-dimensional zrs 2 and hfs 2 and their heterostructure. *Physical Review Materials*, 3(7):074001, 2019.

[176] Miika Mattinen, Georgi Popov, Marko Vehkama ki, Peter J King, Kenichiro Mizohata, Pasi Jalkanen, Jyrki Ra isa nen, Markku Leskela , and Mikko Ritala. Atomic layer deposition of emerging 2d semiconductors, hfs2 and zrs2, for optoelectronics. *Chemistry of Materials*, 31(15):5713–5724, 2019.

[177] Sébastien Lebègue, T Björkman, Mattias Klintenberg, Risto M Nieminen, and Olle Eriksson. Two-dimensional materials from data filtering and ab initio calculations. *Physical Review X*, 3(3):031002, 2013.

[178] Juan Yang, Zhiyuan Zeng, Jun Kang, Sophia Betzler, Cory Czarnik, Xiaowei Zhang, Colin Ophus, Chang Yu, Karen Bustillo, Ming Pan, et al. Formation of two-dimensional transition metal oxide nanosheets with nanoparticles as intermediates. *Nature materials*, 18(9):970–976, 2019.

[179] Xiangchao Ma, Xin Wu, Haoda Wang, and Yucheng Wang. A janus mosse monolayer: a potential wide solar-spectrum water-splitting photocatalyst with a low carrier recombination rate. *Journal of Materials Chemistry A*, 6(5):2295–2301, 2018.

[180] Yi Luo, Sake Wang, Huabing Shu, Jyh-Pin Chou, Kai Ren, Jin Yu, and Minglei Sun. A mosse/blue phosphorene vdw heterostructure with energy conversion efficiency of 19.9% for photocatalytic water splitting. *Semiconductor Science and Technology*, 35(12):125008, 2020.

[181] Bing Song, Limin Liu, and ChiYung Yam. Suppressed carrier recombination in janus mosse bilayer stacks: A time-domain ab initio study. *The journal of physical chemistry letters*, 10(18):5564–5570, 2019.

[182] Yajing Sun, Zhigang Shuai, and Dong Wang. Janus monolayer of wsete, a new structural phase transition material driven by electrostatic gating. *Nanoscale*, 10(46):21629–21633, 2018.

[183] Rajeev Kumar, Ivan Verzhbitskiy, Francesco Giustiniano, Themistoklis PH Sidiropoulos, Rupert F Oulton, and Goki Eda. Interlayer screening effects in ws2/wse2 van der waals hetero-bilayer. *2D Materials*, 5(4):041003, 2018.

[184] YC Huang, X Chen, C Wang, L Peng, Q Qian, and SF Wang. Layer-dependent electronic properties of phosphorene-like materials and phosphorene-based van der waals heterostructures. *Nanoscale*, 9(25):8616–8622, 2017.

[185] Humberto Terrones, Florentino López-Urías, and Mauricio Terrones. Novel hetero-layered materials with tunable direct band gaps by sandwiching different metal disulfides and diselenides. *Scientific reports*, 3(1):1–7, 2013.

[186] Qingyun Zhang and Udo Schwingenschlögl. Rashba effect and enriched spin-valley coupling in ga x/m x 2 (m= mo, w; x= s, se, te) heterostructures. *Physical Review B*, 97(15):155415, 2018.

[187] Pasqual Rivera, Kyle L Seyler, Hongyi Yu, John R Schaibley, Jiaqiang Yan, David G Mandrus, Wang Yao, and Xiaodong Xu. Valley-polarized exciton dynamics in a 2d semiconductor heterostructure. *Science*, 351(6274):688–691, 2016.

[188] Pengfei Li, Wei Zhang, Dongdong Li, Changhao Liang, and Xiao Cheng Zeng. Multifunctional binary monolayers ge x p y: Tunable band gap, ferromagnetism, and photocatalyst for water splitting. *ACS applied materials & interfaces*, 10(23):19897–19905, 2018.

[189] Pengfei Li, Wei Zhang, Changhao Liang, and Xiao Cheng Zeng. Two-dimensional mgx 2 se 4 (x= al, ga) monolayers with tunable electronic properties for optoelectronic and photocatalytic applications. *Nanoscale*, 11(42):19806–19813, 2019.

[190] Yi Luo, Kai Ren, Sake Wang, Jyh-Pin Chou, Jin Yu, Zhengming Sun, and Minglei Sun. First-principles study on transition-metal dichalcogenide/bse van der waals heterostructures: A promising water-splitting photocatalyst. *The Journal of Physical Chemistry C*, 123(37):22742–22751, 2019.

[191] Yi Luo, Sake Wang, Kai Ren, Jyh-Pin Chou, Jin Yu, Zhengming Sun, and Minglei Sun. Transition-metal dichalcogenides/mg (oh) 2 van der waals heterostructures as promising

water-splitting photocatalysts: a first-principles study. *Physical Chemistry Chemical Physics*, 21(4):1791–1796, 2019.

[192] Kai Ren, Sake Wang, Yi Luo, Jyh-Pin Chou, Jin Yu, Wencheng Tang, and Minglei Sun. High-efficiency photocatalyst for water splitting: a janus mosse/xn (x= ga, al) van der waals heterostructure. *Journal of Physics D: Applied Physics*, 53(18):185504, 2020.

[193] Sake Wang, Chongdan Ren, Hongyu Tian, Jin Yu, and Minglei Sun. Mos 2/zno van der waals heterostructure as a high-efficiency water splitting photocatalyst: a first-principles study. *Physical Chemistry Chemical Physics*, 20(19):13394–13399, 2018.

[194] Yunguo Li, Yan-Ling Li, Carlos Moyses Araujo, Wei Luo, and Rajeev Ahuja. Single-layer mos 2 as an efficient photocatalyst. *Catalysis Science & Technology*, 3(9):2214–2220, 2013.

[195] Eric Parzinger, Bastian Miller, Benno Blaschke, Jose A Garrido, Joel W Ager, Alexander Holleitner, and Ursula Wurstbauer. Photocatalytic stability of single-and few-layer mos2. *ACS nano*, 9(11):11302–11309, 2015.

[196] Zhen-Kun Tang, Wen-Jin Yin, Le Zhang, Bo Wen, Deng-Yu Zhang, Li-Min Liu, and Woon-Ming Lau. Spatial separation of photo-generated electron-hole pairs in biobr/bioi bilayer to facilitate water splitting. *Scientific reports*, 6:32764, 2016.

[197] Kai Ren, Chongdan Ren, Yi Luo, Yujing Xu, Jin Yu, Wencheng Tang, and Minglei Sun. Using van der waals heterostructures based on two-dimensional blue phosphorus and xc (x= ge, si) for water-splitting photocatalysis: a first-principles study. *Physical Chemistry Chemical Physics*, 21(19):9949–9956, 2019.

[198] Bao-Ji Wang, Xiao-Hua Li, Ruiqi Zhao, Xiao-Lin Cai, Wei-Yang Yu, Wei-Bin Li, Zhen-Shen Liu, Li-Wei Zhang, and San-Huang Ke. Electronic structures and enhanced photocatalytic properties of blue phosphorene/bse van der waals heterostructures. *Journal of Materials Chemistry A*, 6(19):8923–8929, 2018.

[199] Cen-Feng Fu, Qiquan Luo, Xingxing Li, and Jinlong Yang. Two-dimensional van der waals nanocomposites as z-scheme type photocatalysts for hydrogen production from overall water splitting. *Journal of Materials Chemistry A*, 4(48):18892–18898, 2016.

[200] Yue Liu, Xiangkang Zeng, Christopher D Easton, Qinye Li, Yun Xia, Yichun Yin, Xiaoyi Hu, Jian Hu, Dehua Xia, David T McCarthy, et al. An in situ assembled wo 3–tio 2 vertical heterojunction for enhanced z-scheme photocatalytic activity. *Nanoscale*, 12(16):8775–8784, 2020.

[201] Xinyuan Xia, Mengjiao Song, Hua Wang, Xiangtong Zhang, Ning Sui, Qingbo Zhang, Vicki L Colvin, and W Yu William. Latest progress in constructing solid-state z scheme photocatalysts for water splitting. *Nanoscale*, 11(23):11071–11082, 2019.

[202] Kazuhiko Maeda. Z-scheme water splitting using two different semiconductor photocatalysts. *ACS Catalysis*, 3(7):1486–1503, 2013.

[203] Haijin Li, Wenguang Tu, Yong Zhou, and Zhigang Zou. Z-scheme photocatalytic systems for promoting photocatalytic performance: recent progress and future challenges. *Advanced Science*, 3(11):1500389, 2016.

[204] Allen J Bard. Photoelectrochemistry and heterogeneous photocatalysis at semiconductors. *Journal of Photochemistry*, 10(1):59–75, 1979.

[205] Ruiqi Zhang, Lili Zhang, Qijing Zheng, Pengfei Gao, Jin Zhao, and Jinlong Yang. Direct z-scheme water splitting photocatalyst based on two-dimensional van der waals heterostructures. *The journal of physical chemistry letters*, 9(18):5419–5424, 2018.

[206] Junyu Lang and Yun Hang Hu. Phosphorus-based metal-free z-scheme 2d van der waals heterostructures for visible-light photocatalytic water splitting: a first-principles study. *Physical Chemistry Chemical Physics*, 22(17):9250–9256, 2020.

[207] Lin Ju, Ying Dai, Wei Wei, Mengmeng Li, and Baibiao Huang. Dft investigation on two-dimensional ges/ws2 van der waals heterostructure for direct z-scheme photocatalytic overall water splitting. *Applied Surface Science*, 434:365–374, 2018.

[208] Filip A Rasmussen and Kristian S Thygesen. Computational 2d materials database: electronic structure of transition-metal dichalcogenides and oxides. *The Journal of Physical Chemistry C*, 119(23):13169–13183, 2015.

[209] Junhui Weng and Shang-Peng Gao. A honeycomb-like monolayer of hfo 2 and the calculation of static dielectric constant eliminating the effect of vacuum spacing. *Physical Chemistry Chemical Physics*, 20(41):26453–26462, 2018.

[210] Kai Ren, Wencheng Tang, Minglei Sun, Yongqing Cai, Yuan Cheng, and Gang Zhang. A direct z-scheme pts 2/arsenene van der waals heterostructure with high photocatalytic water splitting efficiency. *Nanoscale*, 12(33):17281–17289, 2020.

[211] Giovanni Onida, Lucia Reining, and Angel Rubio. Electronic excitations: density-functional versus many-body green's-function approaches. *Reviews of modern physics*, 74(2):601, 2002.

[212] Hong Jiang, Patrick Rinke, and Matthias Scheffler. Electronic properties of lanthanide oxides from the g w perspective. *Physical Review B*, 86(12):125115, 2012.

[213] Altaf Ur Rahman, Juliana M Morbec, Gul Rahman, and Peter Kratzer. Commensurate versus incommensurate heterostructures of group-iii monochalcogenides. *Physical Review Materials*, 2(9):094002, 2018.

[214] Carlos MO Bastos, Rafael Besse, Juarez LF Da Silva, and Guilherme M Sipahi. Ab initio investigation of structural stability and exfoliation energies in transition metal dichalcogenides based on ti-, v-, and mo-group elements. *Physical Review Materials*, 3(4):044002, 2019.

[215] Sten Haastrup, Mikkel Strange, Mohnish Pandey, Thorsten Deilmann, Per S Schmidt, Nicki F Hinsche, Morten N Gjerding, Daniele Torelli, Peter M Larsen, Anders C Riis-Jensen, et al. The computational 2d materials database: high-throughput modeling and discovery of atomically thin crystals. *2D Materials*, 5(4):042002, 2018.

[216] Congxin Xia, Wenqi Xiong, Wenbo Xiao, Juan Du, Lizhen Fang, Jingbo Li, and Yu Jia. Enhanced carrier concentration and electronic transport by inserting graphene into van der waals heterostructures of transition-metal dichalcogenides. *Physical Review Applied*, 10(2):024028, 2018.

[217] Xiaohui Hu, Liangzhi Kou, and Litao Sun. Stacking orders induced direct band gap in bilayer mose 2-wse 2 lateral heterostructures. *Scientific reports*, 6:31122, 2016.

[218] JE Padilha, A Fazzio, and Antônio JR da Silva. van der waals heterostructure of phosphorene and graphene: tuning the schottky barrier and doping by electrostatic gating. *Physical review letters*, 114(6):066803, 2015.

[219] Alex Ganose, Adam Jackson, and David Scanlon. sumo: Command-line tools for plotting and analysis of periodic* ab initio* calculations. *Journal of Open Source Software*, 3(28):717, 2018.

[220] Anh Khoa Augustin Lu, Michel Houssa, Mathieu Luisier, and Geoffrey Pourtois. Impact of layer alignment on the behavior of mos 2- zrs 2 tunnel field-effect transistors: An ab initio study. *Physical Review Applied*, 8(3):034017, 2017.

[221] Haijun Zhang, Lu Liu, and Zhen Zhou. First-principles studies on facet-dependent photocatalytic properties of bismuth oxyhalides (bioxs). *RSC advances*, 2(24):9224–9229, 2012.

[222] Jun Dai and Xiao Cheng Zeng. Titanium trisulfide monolayer: theoretical prediction of a new direct-gap semiconductor with high and anisotropic carrier mobility. *Angewandte Chemie*, 127(26):7682–7686, 2015.

[223] Pooja Basera, Shikha Saini, and Saswata Bhattacharya. Self energy and excitonic effect in (un) doped tio 2 anatase: a comparative study of hybrid dft, gw and bse to explore optical properties. *Journal of Materials Chemistry C*, 7(45):14284–14293, 2019.

[224] Sunita Khanchandani, Pawan Kumar Srivastava, Sandeep Kumar, Subhasis Ghosh, and Ashok K Ganguli. Band gap engineering of zno using core/shell morphology with environmentally benign ag2s sensitizer for efficient light harvesting and enhanced visible-light photocatalysis. *Inorganic Chemistry*, 53(17):8902–8912, 2014.

[225] Xu Zhang, An Chen, Letian Chen, and Zhen Zhou. 2d materials bridging experiments and computations for electro/photocatalysis. *Advanced Energy Materials*, 12(4):2003841, 2022.

[226] Steven Chu and Arun Majumdar. Opportunities and challenges for a sustainable energy future. *Nature*, 488(7411):294–303, 2012.

[227] Zhi Wei Seh, Jakob Kibsgaard, Colin F Dickens, IB Chorkendorff, Jens K Nørskov, and Thomas F Jaramillo. Combining theory and experiment in electrocatalysis: Insights into materials design. *Science*, 355(6321):4998, 2017.

[228] Varun Vij, Siraj Sultan, Ahmad M Harzandi, Abhishek Meena, Jitendra N Tiwari, Wang-Geun Lee, Taeseung Yoon, and Kwang S Kim. Nickel-based electrocatalysts for energy-related applications: oxygen reduction, oxygen evolution, and hydrogen evolution reactions. *ACS Catalysis*, 7(10):7196–7225, 2017.

[229] Qipeng Lu, Yifu Yu, Qinglang Ma, Bo Chen, and Hua Zhang. 2d transition-metal-dichalcogenide-nanosheet-based composites for photocatalytic and electrocatalytic hydrogen evolution reactions. *Advanced Materials*, 28(10):1917–1933, 2016.

[230] Lingyun Cao and Cheng Wang. Metal–organic layers for electrocatalysis and photocatalysis. *ACS Central Science*, 6(12):2149–2158, 2020.

[231] Huanyu Jin, Taeseup Song, Ungyu Paik, and Shi-Zhang Qiao. Metastable two-dimensional materials for electrocatalytic energy conversions. *Accounts of Materials Research*, 2(7):559–573, 2021.

[232] Han Zhang, Xiaohui Yang, Huijuan Zhang, Jinling Ma, Zhengyong Huang, Jian Li, and Yu Wang. Transition-metal carbides as hydrogen evolution reduction electrocatalysts: Synthetic methods and optimization strategies. *Chemistry–A European Journal*, 27(16):5074–5090, 2021.

[233] Johannes Novak Hansen, Hector Prats, Karl Krøjer Toudahl, Niklas Mørch Secher, Karen Chan, Jakob Kibsgaard, and Ib Chorkendorff. Is there anything better than pt for her? *ACS Energy Letters*, 6(4):1175–1180, 2021.

[234] Guoqiang Zhao, Jian Chen, Wenping Sun, and Hongge Pan. Non-platinum group metal electrocatalysts toward efficient hydrogen oxidation reaction. *Advanced Functional Materials*, 31(20):2010633, 2021.

[235] Yi Shi, Zhi-Rui Ma, Yi-Ying Xiao, Yun-Chao Yin, Wen-Mao Huang, Zhi-Chao Huang, Yun-Zhe Zheng, Fang-Ya Mu, Rong Huang, Guo-Yue Shi, et al. Electronic metal–support interaction modulates single-atom platinum catalysis for hydrogen evolution reaction. *Nature Communications*, 12(1):1–11, 2021.

[236] Huanyu Jin, Chunxian Guo, Xin Liu, Jinlong Liu, Anthony Vasileff, Yan Jiao, Yao Zheng, and Shi-Zhang Qiao. Emerging two-dimensional nanomaterials for electrocatalysis. *Chemical Reviews*, 118(13):6337–6408, 2018.

[237] Jumeng Wei, Min Zhou, Anchun Long, Yanming Xue, Hanbin Liao, Chao Wei, and Zhichuan J Xu. Heterostructured electrocatalysts for hydrogen evolution reaction under alkaline conditions. *Nano-Micro Letters*, 10(4):1–15, 2018.

[238] Yizhan Wang, Ziyi Zhang, Yanchao Mao, and Xudong Wang. Two-dimensional nonlayered materials for electrocatalysis. *Energy & Environmental Science*, 13(11):3993–4016, 2020.

[239] Y Wang, H Zhang, X Yang, J Ma, Z Huang, and J Li. Recent advances in transition-metal carbides: from controlled preparation to hydrogen evolution reaction application. *Chemistry (Weinheim an der Bergstrasse, Germany)*, 118(13):5074–5090, 2020.

[240] Jian Du, Fei Li, and Licheng Sun. Metal–organic frameworks and their derivatives as electrocatalysts for the oxygen evolution reaction. *Chemical Society Reviews*, 50(4):2663–2695, 2021.

[241] Daniel V Esposito, Sean T Hunt, Yannick C Kimmel, and Jingguang G Chen. A new class of electrocatalysts for hydrogen production from water electrolysis: metal monolayers supported on low-cost transition metal carbides. *Journal of the American Chemical Society*, 134(6):3025–3033, 2012.

[242] Sergio Trasatti. Physical electrochemistry of ceramic oxides. *Electrochimica Acta*, 36(2):225–241, 1991.

[243] Showkat Hassan Mir, Vivek Kumar Yadav, and Jayant Kumar Singh. Recent advances in the carrier mobility of two-dimensional materials: a theoretical perspective. *ACS Omega*, 5(24):14203–14211, 2020.

[244] Xiwen Zhang, Bing Wang, Xianghong Niu, Yunhai Li, Yunfei Chen, and Jinlan Wang. Bi2os2: a direct-gap two-dimensional semiconductor with high carrier mobility and surface electron states. *Mater. Horiz.*, 5:1058–1064, 2018.

[245] Karim Khan, Ayesha Khan Tareen, Muhammad Aslam, Yupeng Zhang, Renheng Wang, Zhengbiao Ouyang, Zhongyi Gou, and Han Zhang. Recent advances in two-dimensional materials and their nanocomposites in sustainable energy conversion applications. *Nanoscale*, 11(45):21622–21678, 2019.

[246] Arunima Singh, Pooja Basera, Shikha Saini, Manish Kumar, and Saswata Bhattacharya. Importance of many-body dispersion in the stability of vacancies and antisites in free-standing monolayer of mos2 from first-principles approaches. *The Journal of Physical Chemistry C*, 124(2):1390–1397, 2020.

[247] Yan Chen, Shengxi Huang, Xiang Ji, Kiran Adepalli, Kedi Yin, Xi Ling, Xinwei Wang, Jianmin Xue, Mildred Dresselhaus, Jing Kong, et al. Tuning electronic structure of single layer mos_2 through defect and interface engineering. *ACS Nano*, 12(3):2569–2579, 2018.

[248] Hao Wang, Xu Xiao, Shuyuan Liu, Chao-Lung Chiang, Xiaoxiao Kuai, Chun-Kuo Peng, Yu-Chang Lin, Xing Meng, Jianqing Zhao, Jinho Choi, et al. Structural and electronic optimization of mos2 edges for hydrogen evolution. *Journal of the American Chemical Society*, 141(46):18578–18584, 2019.

[249] Jiu Chen, Fuhua Li, Yurong Tang, and Qing Tang. Tuning the phase stability and surface her activity of $1t^{/}$-mos_2 by covalent chemical functionalization. *Journal of Materials Chemistry C*, 8(44):15852–15859, 2020.

[250] Qing Tang and De-en Jiang. Mechanism of hydrogen evolution reaction on 1t-mos2 from first principles. *ACS Catalysis*, 6(8):4953–4961, 2016.

[251] Arunima Singh, Manjari Jain, and Saswata Bhattacharya. Mos_2 and janus (mosse) based 2d van der waals heterostructures: emerging direct z-scheme photocatalysts. *Nanoscale Advances*, 3(10):2837–2845, 2021.

[252] Farhad Keivanimehr, Sajjad Habibzadeh, Alireza Baghban, Amin Esmaeili, Ahmad Mohaddespour, Amin Hamed Mashhadzadeh, Mohammad Reza Ganjali, Mohammad Reza Saeb, Vanessa Fierro, and Alain Celzard. Electrocatalytic hydrogen evolution on the noble metal-free mos2/carbon nanotube heterostructure: a theoretical study. *Scientific Reports*, 11(1):1–9, 2021.

[253] Jiayu Wan, Steven D Lacey, Jiaqi Dai, Wenzhong Bao, Michael S Fuhrer, and Liangbing Hu. Tuning two-dimensional nanomaterials by intercalation: materials, properties and applications. *Chemical Society Reviews*, 45(24):6742–6765, 2016.

[254] Jiong Zhao, Qingming Deng, Alicja Bachmatiuk, Gorantla Sandeep, Alexey Popov, Jürgen Eckert, and Mark H Rümmeli. Free-standing single-atom-thick iron membranes suspended in graphene pores. *Science*, 343(6176):1228–1232, 2014.

[255] Wenzhong Bao, Lei Jing, Jr Velasco, Y Lee, Gang Liu, D Tran, B Standley, M Aykol, SB Cronin, D Smirnov, et al. Stacking-dependent band gap and quantum transport in trilayer graphene. *Nature Physics*, 7(12):948–952, 2011.

[256] Ji Feng, Xiaofeng Qian, Cheng-Wei Huang, and Ju Li. Strain-engineered artificial atom as a broad-spectrum solar energy funnel. *Nature Photonics*, 6(12):866–872, 2012.

[257] Feng Wang, Yuanbo Zhang, Chuanshan Tian, Caglar Girit, Alex Zettl, Michael Crommie, and Y Ron Shen. Gate-variable optical transitions in graphene. *Science*, 320(5873):206–209, 2008.

[258] Gayatri Swain, Sabiha Sultana, and Kulamani Parida. A review on vertical and lateral heterostructures of semiconducting 2d-mos_2 with other 2d materials: A feasible perspective for energy conversion. *Nanoscale*, 13(22):9908–9944, 2021.

[259] Guoqiang Zhao, Kun Rui, Shi Xue Dou, and Wenping Sun. Heterostructures for electrochemical hydrogen evolution reaction: a review. *Advanced Functional Materials*, 28(43):1803291, 2018.

[260] Hasan Şahin, Seymur Cahangirov, Mehmet Topsakal, E Bekaroglu, Ethem Akturk, R Tugrul Senger, and Salim Ciraci. Monolayer honeycomb structures of group-iv elements and iii-v binary compounds: First-principles calculations. *Physical Review B*, 80(15):155453, 2009.

[261] Jie Wu, Jia-Hui Li, and Yang-Xin Yu. Single nb or w atom-embedded bp monolayers as highly selective and stable electrocatalysts for nitrogen fixation with low-onset potentials. *ACS Applied Materials & Interfaces*, 13(8):10026–10036, 2021.

[262] Tuan V Vu, AI Kartamyshev, Nguyen V Hieu, Tran DH Dang, Sy-Ngoc Nguyen, NA Poklonski, Chuong V Nguyen, Huynh V Phuc, and Nguyen N Hieu. Structural, elastic, and electronic properties of chemically functionalized boron phosphide monolayer. *RSC Advances*, 11(15):8552–8558, 2021.

[263] Manish Kumar Mohanta, Ashima Rawat, Nityasagar Jena, Dimple, Raihan Ahammed, and Abir De Sarkar. Interfacing boron monophosphide with molybdenum disulfide for an ultrahigh performance in thermoelectrics, two-dimensional excitonic solar cells, and nanopiezotronics. *ACS Applied Materials & Interfaces*, 12(2):3114–3126, 2019.

[264] Balabalaji Padavala, CD Frye, Xuejing Wang, Zihao Ding, Ruifen Chen, Michael Dudley, Balaji Raghothamachar, Peng Lu, BN Flanders, and JH Edgar. Epitaxy of boron phosphide on aluminum nitride (0001)/sapphire substrate. *Crystal Growth & Design*, 16(2):981–987, 2016.

[265] Yi Xiao and Weibin Zhang. High throughput screening of m_3c_2 mxenes for efficient co_2 reduction conversion into hydrocarbon fuels. *Nanoscale*, 12(14):7660–7673, 2020.

[266] Joshua D Wiensch, Jimmy John, Jesus M Velazquez, Daniel A Torelli, Adam P Pieterick, Matthew T McDowell, Ke Sun, Xinghao Zhao, Bruce S Brunschwig, and Nathan S Lewis. Comparative study in acidic and alkaline media of the effects of ph and crystallinity on the hydrogen-evolution reaction on mos2 and mose2. *ACS Energy Letters*, 2(10):2234–2238, 2017.

[267] Kai Ren, MingLei Sun, Yi Luo, SaKe Wang, Jin Yu, and WenCheng Tang. First-principle study of electronic and optical properties of two-dimensional materials-based heterostructures based on transition metal dichalcogenides and boron phosphide. *Applied Surface Science*, 476:70–75, 2019.

[268] Qiaoqiao He, Xiaobo Chen, Shiqi Chen, Lu Liu, Fangwang Zhou, Xi-Bo Li, and Guangjin Wang. Electrochemical hydrogen evolution at the interface of monolayer vs2 and water from first-principles calculations. *ACS Applied Materials & Interfaces*, 11(3):2944–2949, 2018.